

Dissertation

submitted to the
Combined Faculties for the Natural Sciences and for Mathematics
of the Ruperto-Carola University of Heidelberg, Germany
for the degree of

Doctor of Natural Sciences

Put forward by

Dipl. Phys. Thomas Schubert
Born in York, Great Britain

Oral examination: 28th October 2009

INFLUENCE OF MOLECULAR STRUCTURE ON ORDERING AND DYNAMICS OF LIPIDS AND PROTEINS IN BIOLOGICAL MEMBRANE MODELS

Referees: Prof. Dr. Motomu Tanaka
Prof. Dr. Ulrich Schwarz

Einfluss molekularer Struktur auf die Ordnung und die Dynamik von Proteinen und Lipiden in Modellen biologischer Membranen

In dieser Arbeit wird die Struktur und die Dynamik von Modellmembranen mit einer Kombination aus Experimenten und Simulationen untersucht. Die laterale Diffusion an Lipide gekoppelter Prionproteine (PrP^c) in planaren Lipidmembranen ("Festkörper-gestützte Membranen") wird in Kapitel 5 mit einem selbstkonstruierten Einzelmolekül-Fluoreszenzmikroskop untersucht. Molekulare Variationen der PrP^c konnten durch ihren Einfluss auf die Diffusionskoeffizienten anhand von Simulationen der thermischen Zufallsbewegung erkannt werden. Zur Erweiterung des Verständnisses vom Überleben von Archaeen unter extremen Bedingungen werden in Kapitel 6 Archaea-mimetische Lipide und Membranen untersucht. Die Struktur, Ordnung und laterale Diffusion dieser zyklischen transmembranen Lipide wird durch optische Methoden und Röntgenstreuung untersucht. In Kapitel 7 werden Molekulardynamiksimulationen verwendet um Membranen bestehend sowohl aus konventionellen als auch aus einzigartigen zyklischen Lipiden mit atomarer Genauigkeit zu untersuchen, wobei eine hervorragende Übereinstimmung mit den experimentellen Ergebnissen beobachtet wird. Eine optimierte Darstellung der geordneten Membranen in der Gelphase erlaubt erstmals die erfolgreiche Simulation von Schmelzübergängen erster Ordnung. Es wird ersichtlich, dass die Kombination optischer Techniken im Realraum mit Streumethoden im reziproken Raum und ergänzenden Computersimulationen ein mächtiges Werkzeug zur Entschlüsselung der Ordnung und Dynamik biologischer Systeme auf verschiedenen Längen- und Zeitskalen ist.

Influence of Molecular Structure on Ordering and Dynamics of Lipids and Proteins in Biological Membrane Models

In this thesis, the structure and dynamics of model membranes are probed using a combination of experiments and simulations. The lateral diffusion of prion proteins (PrP^c) coupled to lipid headgroups in planar lipid membranes (supported membranes) are investigated in Chapter 5 using a self-constructed single-molecule fluorescence microscope. Using random walk simulations, molecular variations of the PrP^c were detected by their influence on the lateral diffusion. In order to improve understanding of archaea survival under extreme conditions, archaea-mimetic lipids and membranes are investigated in Chapter 6. The structure, ordering, and lateral diffusion of these cyclic transmembrane lipids are investigated by optical and X-ray scattering techniques. In Chapter 7, molecular dynamics (MD) simulations are used to study membranes of conventional phospholipids and unique cyclic lipids on the level of atomic detail, showing excellent agreement with the experimental findings. An optimized representation of the ordered gel phase allows for the first successful simulation of first order melting transitions. Thus, the combination of optical techniques in real space and scattering experiments in reciprocal space with complementary computer simulations is a powerful tool to unravel the ordering and dynamics of biological systems in different length and time scales.

ACKNOWLEDGMENTS

I would like to thank

Prof. Motomu Tanaka for guidance and ideas throughout this thesis,

Prof. Ulrich Schwarz for kindly refereeing this thesis,

Emanuel Schneck for day and night discussions about science and lots of support for this thesis,

Pit Seitz for the IGOR alliance and bringing consistency to this thesis,

Harden Rieger and **Tom Kaindl** for suffering through proofreading,

Stefan Kaufman for finally letting me win some sets in badminton,

Alberto Zibetti for help with the transmembrane lipids,

Diana Stoycheva, **Kai Hock** and **Wasim Abuillan** for help with single-molecule experiments,

Michael Bärmann and **Monika Rusp** for preparation of proteins,

and everybody else for the enjoyable working atmosphere.

Contents

1	Introduction	1
2	Theoretical Background	7
2.1	Physics of Lipid Membrane Models	7
2.1.1	Phases and Phase Transitions of Lipid Membranes	7
2.1.2	Diffusion in Lipid Membranes	9
2.2	Optics for Visible Light and X-Rays	12
2.2.1	Diffraction of X-Rays	12
2.2.2	Diffraction of Visible Light	14
2.2.3	Total Reflection of Visible Light and X-Rays	15
3	Methods	17
3.1	Total Internal Reflection Fluorescence (TIRF) Microscopy	17
3.2	Single-Molecule Localization Microscopy	18
3.3	Analysis of Single-Molecule Random Walks	20
3.4	Fluorescence Recovery after Photobleaching (FRAP)	22
3.5	X-Ray Reflectivity of Oriented Stratified Systems	23
3.6	X-Ray Scattering of Unoriented Samples (SAXS/WAXS)	24
3.7	Grazing-Incidence X-Ray Diffraction (GID)	26
3.8	Modeling of GID and WAXS Data	27
3.9	Molecular Dynamics (MD) Simulations of Lipid Membranes	30
4	Materials and Experiments	33
4.1	Materials	33
4.2	Preparation of Samples	35
4.3	Optical Instruments	36
4.3.1	Single-Molecule TIRF Microscopy	36
4.3.2	FRAP	39
4.3.3	Epi-Fluorescence Microscopy	39
4.4	X-Ray and Neutron Scattering Experiments	40
4.5	MD Software and Simulations	41
5	Diffusion of Membrane-Anchored Prion Protein	43
5.1	Introduction	43
5.2	Single Dye Tracking (SDT) of Membrane-Anchored Prion-Protein (PrP ^c)	45
5.2.1	SDT Results	45
5.2.2	Simulation-Based Analysis of the Diffusion Coefficients	46
5.2.3	Discussion	50
5.3	Construction of a Two-Color Dual-Imaging TIRF Microscope	52
5.3.1	Target Application of Instrument Design	52
5.3.2	Localization Accuracy and Noise	52
5.3.3	Image Registration for Two-Color Co-Localization Microscopy	54
6	Structure and Dynamics of Archaea-Mimetic Cyclic Lipid Membranes	61
6.1	Introduction	61

6.2	Supported Membranes of Cyclic Lipids	63
6.2.1	Macroscopic Homogeneity	63
6.2.2	Fluidity of Cyclic Lipid Membranes (FRAP)	64
6.3	X-Ray Reflectivity of Supported Monolayer Membranes	70
6.3.1	Results	70
6.3.2	Discussion	72
6.4	X-Ray Scattering of Unoriented Samples (SAXS/WAXS)	73
6.4.1	Results	73
6.4.2	Electron Density Modeling	75
6.4.3	Discussion	79
6.5	X-Ray and Neutron Scattering of Oriented Multilayer Samples	81
6.5.1	Results	81
6.5.2	Discussion	83
6.6	Grazing Incidence X-Ray Diffraction (GID) of Oriented Samples	85
6.6.1	Results	85
6.6.2	Discussion	93
7	Structure and Thermodynamics of Lipid Membranes in Molecular Dynamics Simulations with Atomistic Detail	95
7.1	Introduction	95
7.2	3D-Autocorrelation for Membrane Simulations	97
7.3	DPPC	99
7.3.1	Creating Highly Ordered Gel Phase Membranes	99
7.3.2	Unit Cell of Gel Phase Membranes	102
7.3.3	Chain Melting Transitions	105
7.3.4	Pre-Transition and Ripple Phase	109
7.3.5	Discussion	110
7.4	C20 Cyclic Lipids	113
7.4.1	Structure and Ordering in the Gel Phase	113
7.4.2	Electron Density Profiles	115
7.4.3	Comparison to Experiments	116
7.4.4	Outlook to Fluid Phase Simulations of Cyclic Lipid Membranes	118
8	Conclusions	119
9	Outlook	123
A	Appendix	125
A.1	Stereochemistry of Archaeol and Related Lipids	125
A.2	SAXS/WAXS of DMPC	126
A.3	DSC Measurement of DPPC	127
A.4	Prion Protein Preparation	128
	References	131

1 Introduction

All cells of living organisms possess various types of membranes like the plasma membrane of eukaryotic cells which provides confinement and separation from the environment, or the membranes separating internal organelles from the cytosol [1]. Membranes define the global shape of cells, and together with the cytoskeleton are responsible for their mechanical stability. They also take part in transport of nutrients and waste, regulate communication with the surroundings, and support many other functions.

The core structural feature of most membranes is the lipid bilayer. Lipids are amphiphilic molecules, which in their most common configuration possess one hydrophilic region (the headgroup) and a hydrophobic region consisting of two hydrocarbon chains. The lipid molecules form the lamellar double-leaflet bilayer by self-assembly through the entropy-driven hydrophobic effect [2]. This lipid bilayer provides a quasi-2D matrix to the membrane-associated proteins (see Figure 1.1), which impart most of the “functionality” to a membrane. They have many roles, as active or passive transporters and ion channels [3], signal receptors, and cell adhesion molecules (e.g. integrin [4] or ICAM [5]). Several models have been proposed to describe the roles of lipids and proteins in biological membranes, where the most well-known is the classic *fluid mosaic model* of Singer and Nicolson [6].

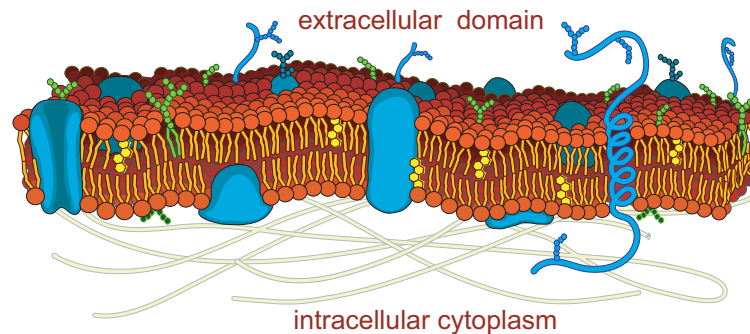


Figure 1.1: A sketch of a biological membrane [7] showing the lipid bilayer matrix, membrane-associated proteins and cytoskeleton components on the inner (cytoplasmic) side.

In general, fluidity of the membranes is vital to all organisms. Only in a fluid state can the membrane heal defects and maintain its isolating properties. Importantly, lateral diffusion in the membrane drives many protein interaction processes, like the ubiquitous membrane-anchored G-protein-coupled cell signaling step [8]. Membrane fluidity is achieved and maintained by the cells through the composition and the structure of the lipid molecules. For instance, the presence of unsaturated double bonds in the hydrocarbon chains drastically lowers the melting temperature [9], thus increasing fluidity.

Recently, an increasing number of studies have evidenced [10, 11] that several diseases

such as Creutzfeldt-Jakob (in humans) or bovine spongiform encephalitis (BSE) and scrapie (in animals) are caused by infectious proteins (prions). The currently known prion proteins are a family of membrane-associated proteins with a close homology across species and a lipid-like GPI-anchor [12]. The normally benign cellular prion proteins (called PrP^c) can be converted to the misfolded pathogenic isoform PrP^{sc} (*sc* for scrapie) by already misfolded PrP^{sc} , as illustrated in Figure 1.2. The PrP^{sc} aggregate in amyloid plaques during the course of the disease. Similar pathogenic aggregation of proteins is also observed in non-prion diseases such as Parkinson and Alzheimer. Several studies have shown the necessity of membrane anchoring and lateral mobility for development and infectiousness of prion-based diseases [13–15]. Thus, lateral diffusion and protein interaction in the fluid membrane appear to be a crucial step in the chain of infection and an important target for further studies.

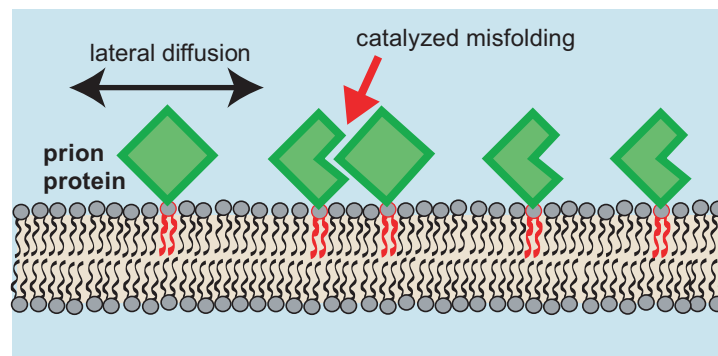


Figure 1.2: The prion protein (PrP^c) has been established as the causative agent of diseases such as bovine spongiform encephalitis (BSE). PrP^c is a membrane anchored protein which becomes pathogenic when converted to a misfolded isoform by contact with already misfolded prions.

Regulating the physical properties of their membranes is an important aspect of how living organisms adapt to their environment [16]. In fact, some organisms possess membranes which are very stable and robust even under extreme environmental conditions. One example are archaea [17], which are considered a separate domain of life next to eucaryotes and bacteria [18]. Even though these organisms are abundant in the environment, they were only recognized recently as being different from bacteria [19, 20]. Many archaea are extremophiles [21] and can be found in habitats such as hot springs, deep sea vents or hypersaline water.

One of the unique distinctions of the archaea domain lies in the cell membrane [22]. Strikingly, the glycerol junction of archaea lipids uniquely has the opposite stereochemistry than in lipids of other organisms¹, as the alkyl chains are linked at the *sn*-2,3 positions of glycerol rather than *sn*-1,2. Most archaea lipids are derived from the diphytanyl glycerol diether lipid *archaeol* and its cyclic² tetraether dimer *caldarchaeol*. Caldarchaeol is a bipolar lipid, with two polar headgroups connected by the hydrocarbon chains. Such bipolar lipids lead to the formation of membrane monolayers, in

¹See Appendix A.1 for a more detailed illustration of the stereochemistry.

²The term “cyclic” refers to the closed carbon chain ring which is formed, and is used interchangeably with the term “bola” lipid.

contrast to conventional lipids which assemble into bilayers³. These two fundamentally different membrane configurations are illustrated in Figure 1.3.

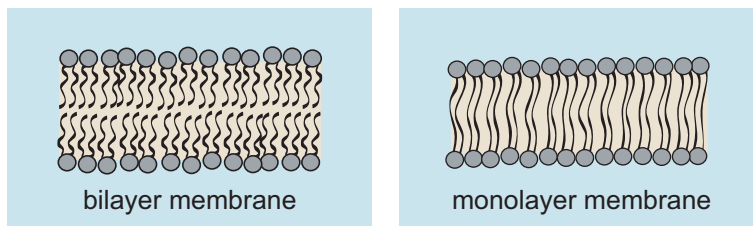


Figure 1.3: An illustration of a lipid bilayer (left) as seen in the membranes of most organisms, and a lipid monolayer (right) of transmembrane bipolar lipids as seen in members of the Archaea domain. Membrane monolayers are thought to be more rigid, more thermostable and less permeable than their bilayer counterparts.

The correlation between extreme habitats and unique plasma membrane architecture of archaea is intriguing. For instance, some studies have found monolayers of ether-lipids to be more rigid, more thermostable and less permeable to ions and protons than lipid bilayers [21, 23–25]. The archaeol fatty acid building block phytanyl possesses methyl sidechains, which have been shown to preserve fluidity between -120°C and $+120^{\circ}\text{C}$ [26, 27]. However, full characterization of the biophysical properties of archaea membranes is still lacking.

The complexity of biological membranes can make investigations of their fundamental physical properties challenging. Therefore, various types of simplified and well-defined lipid model membranes have been used to quantitatively study the fundamental structural and dynamical properties of membranes [16, 28] (see Figure 1.4). Unoriented membrane multilayers in dispersion [29] have for instance been used to study the structure of the well-known “standard” lipid DPPC in great detail by small- and wide-angle X-ray scattering [30, 31]. Often, higher resolution is achieved by using specular reflectivity with oriented multilayer stacks [32], which can also be used to reveal information about membrane mechanics in off-specular X-ray or neutron scattering [33, 34]. Other commonly employed techniques to probe lipid and membrane dynamics include nuclear magnetic resonance [35] and fourier transform infrared spectroscopy [36].

Single lipid bilayers deposited on planar solid supports (*solid-supported membranes*) [37, 38] have proven to be very versatile models of biological membranes and the cell surface due to their mechanical and thermodynamical stability over large areas ($\sim\text{cm}^2$). The most commonly applied method to deposit solid-supported membranes uses small unilamellar vesicles (SUVs), which rupture easily on a hydrophilic solid surface such as glass or silicon and fuse to form a continuous membrane [39–42]. Without a solid support only extremely delicate optical and electrochemical experiments on single membranes are possible using black lipid membranes or the patch-clamp technique.

Due to the planar geometry, many experimental methods such as fluorescence recovery after photobleaching (FRAP) [43–45], the quartz crystal microbalance [42], and X-ray/neutron scattering [46–51] are especially well suited for experiments with supported

³In this work, the term “lipid membrane” is used for both monolayer and bilayer membranes.

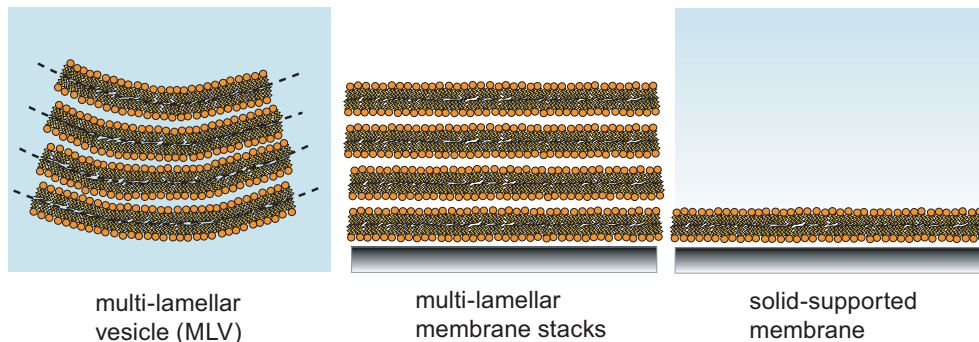


Figure 1.4: Model membrane geometries used in this thesis. The lipid bilayers (or monolayer in the case of archaea-type lipids) can be configured as large relaxed multi-lamellar vesicles in dispersion, as oriented multi-lamellar membrane stacks in controlled humidity or under water, or as a single solid-supported membranes under water.

membranes. Fluorescence microscopy is widely used, ranging from simple wide-field microscopy to advanced single-molecule and even single-dye fluorescence experiments [52]. The planar membranes enable the application of surface-sensitive fluorescence techniques such as total internal reflection fluorescence (TIRF) [53]. In practice, supported membranes have been used in studies ranging from fundamental questions of lateral lipid diffusion and friction [45] to complex experiments modeling immune response and cell adhesion [54–60].

Proteins can be incorporated in supported lipid membranes by fusion of reconstituted vesicles containing membrane proteins (proteoliposomes). For large transmembrane proteins contact with the solid support can pose the risk of denaturation and loss of mobility and functionality. Alternatively, functional lipid anchors can be added to the supported membrane which bind specific protein motifs (e.g. His-tags). Recently, more sophisticated supported model membranes were established by using ultrathin polymer interlayers that mimic generic roles of ECM and glycocalix [61]. It has been demonstrated that they can be used to fine-adjust the lateral diffusivity and functionality of transmembrane cell receptors [62–64]. However, since this thesis focuses on diffusion and dynamics of lipids and lipid-anchored proteins, simple solid-supported membrane systems are used in the following chapters.

The central aim of this thesis is to investigate the influence that molecular variations of lipids and proteins have on structural and dynamic properties of model membranes. Towards this aim, the membrane systems of interest are probed on various length and time scales with complementary techniques including single-molecule fluorescence microscopy, X-ray scattering, and molecular dynamics simulations. A more detailed introduction to all topics is given at the beginning of each chapter.

The lateral diffusion of individual prion proteins in fluid supported membranes is studied in Chapter 5 using single-molecule microscopy. There have been studies reporting variations in glycosylation of prion proteins [65, 66], as well as the existence of a

monomer/dimer equilibrium [67]. Thus, special emphasis is placed on the exact quantitative evaluation of the distribution of the diffusion coefficients. The full potential of single-molecule experiments is utilized to investigate the effects that apparent variations of membrane-anchored proteins (e.g. of their glycosylation) can have on the frictional coupling to the surrounding media. For these experiments, a single-molecule fluorescence TIRF microscope was constructed and additionally extended for use in high-resolution two-color single-molecule colocalization experiments.

Selective structural variations of lipids and their influence on membrane ordering and dynamics are studied in Chapter 6 for a series of synthetic archaea-mimetic cyclic bipolar lipids [68]. A central theme is the study of the effects of a diacetylenic core (triple bonds in the hydrocarbon chains), which has been proposed as a rigidification element for cyclic lipids with long and flexible chains. Supported monolayer formation using cyclic lipids is investigated by fluorescence microscopy and X-ray reflectivity. The lateral diffusion of cyclic lipids in supported monolayer membranes is quantified by FRAP at various temperatures. Small and wide-angle X-ray scattering (SAXS/WAXS) of vesicles in suspensions as well as grazing-incidence X-ray diffraction (GID) of oriented supported membranes are used to further investigate the lateral and vertical structure of the monolayer membranes on various length scales, as well as their phases and melting transitions. In all experiments the influence of a diacetylenic core as well as variations of the chain length and of the headgroup chemistry are investigated systematically.

For computer modeling of experimental data with atomistic detail, molecular dynamics (MD) simulations of lipid bilayer and monolayer membranes are performed in Chapter 7. First, new approaches to simulations of membranes in the gel phase are developed using conventional phospholipids with the aim of reproducing well-known fundamental structural and thermodynamic parameters (including melting transitions) from experiments. The autocorrelation of the atomic coordinates is used as a new tool for quantification of ordering in MD simulations of membranes. The strategies are then transferred to simulations of the cyclic lipids with unique chemical motifs, which are investigated Chapter 6. Simulation-based modeling of experimental data is demonstrated, aiming towards better analysis and deeper understanding of experimental results.

2 Theoretical Background

2.1 Physics of Lipid Membrane Models

2.1.1 Phases and Phase Transitions of Lipid Membranes

Lipid membranes can undergo several thermotropic and lyotropic phase transitions [9, 28, 69]. For pure single-component systems, the lamellar phases in excess water can be separated into a fluid phase and several solid phases. In Figure 2.1 the major *thermotropic* phases for DPPC in excess water are shown in an experimental differential scanning calorimetry (DSC) scan.

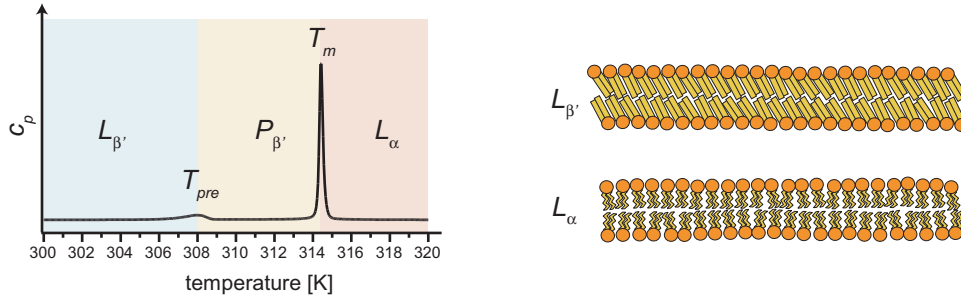


Figure 2.1: Important thermotropic phase transitions of phosphatidylcholine (PC) lipids in excess water, shown for the example of DPPC. Left: An experimental DSC scan, where the peaks of excess heat capacity C_p mark the transitions from the gel phase $L_{\beta'}$ to the ripple phase $P_{\beta'}$ (at T_{pre}) and to the fluid phase L_{α} (at T_m). The low temperature L_c phase is not covered in this scan. Right/Top: In the solid $L_{\beta'}$ phase the chains are stretched in an all-trans configuration and possess lateral long-range ordering. The molecules are tilted due to the mismatch of the cross-sectional area of large headgroups and smaller chains. Right/Bottom: In the L_{α} phase the chains are disordered, giving the membrane fluid-like properties.

The lowest-temperature phase of DPPC and related PC lipids is the crystalline (L_c) phase, with lateral ordering (correlation) of the chains as well as the headgroups [32]. However, for PC lipids the typically observed solid phase is the gel phase $L_{\beta'}$, characterized by nearly all-*trans* chain conformation and sharply reduced lateral and rotational mobility, as well as the existence of lateral chain-chain ordering without headgroup ordering. Measurements of the chain-correlation peak width in wide-angle X-ray scattering of gel phase DPPC have suggested correlation lengths (or crystallite sizes) of up to 290 nm [30]. A further solid phase observed for phosphatidylcholine (PC) lipids between the $L_{\beta'}$ and L_{α} phases is the ripple phase $P_{\beta'}$, exhibiting a static out-of-plane undulation with wavelengths on the order of ~ 15 nm. Some structural details of this phase such as lipid orientation are still under discussion, as it does not lend itself well to experimental analysis by X-ray scattering or similar techniques [70, 71].

In a solid ordered phase, the chains are in principle ordered in a 2D hexagonal lattice. However, the unit cell is often referred to as orthorhombic which strictly speaking only applies to a 3D lattice. If the cross-sectional area for the headgroups is larger than for the chains, then the chains tilt to maintain contact. By convention one denotes a phase with tilted chains with a prime “ ’ ”. For fully hydrated PC lipid membranes the molecular tilt vector usually lies in the direction of the nearest neighbor (nn), which distorts the unit cell by stretching parallel to the tilt.

Above T_m , lipid membranes exist in the fluid L_α phase, characterized by disordered hydrocarbon chains with a high number of *gauche* bond rotations and a high lateral and rotational mobility. This is commonly regarded as the biologically most relevant phase.

The main thermotropic transition at T_m ($P_{\beta'} \rightarrow L_\alpha$ for PC lipids, $L_\beta \rightarrow L_\alpha$ for the general case) is considered a first-order cooperative chain-melting transition [72], where the associated melting enthalpy can be measured by calorimetric measurements such as differential scanning calorimetry (DSC). There is little volumetric change at T_m , but large area and thickness changes, so that the area per molecule is a suitable and commonly used order parameter to describe this transition. The cooperativity can be described based on the interfacial line energy between melted and frozen lipids, as minimizing the mismatch (number of interfacial lipids) favors large domains of lipids melting/freezing simultaneously. In general, a higher cooperativity leads to a smaller transition width over temperature. For PC lipids, the cooperativity is especially high, leading to transition widths smaller than 0.1 °C. However, the equilibrium size of the cooperative unit is a material parameter which cannot be predicted in a simple fashion. The transition between the gel and the ripple phase ($L_{\beta'} \rightarrow P_{\beta'}$) is also of first order, but possesses much lower transition enthalpy and occurs over a broader temperature range [9, 73, 74].

In the laboratory system with constant pressure and temperature the Gibbs free energy is the appropriate thermodynamic ensemble:

$$\Delta G(P, T) = \Delta H - T \Delta S. \quad (2.1)$$

At the transition temperature T_m the free energies of the melted/frozen states are equal, thus the free energy difference ΔG is zero:

$$\Delta G(T_m) = 0 \implies \Delta S_t = \Delta H_t / T_m. \quad (2.2)$$

Consequently, with knowledge of the melting temperature, measuring the transition enthalpy ΔH_t (e.g. by DSC) also gives knowledge about the transition entropy. Additionally, Equation 2.2 shows that the melting temperature T_m is linked the “material parameters” ΔH_t and ΔS_t :

$$T_m = \frac{\Delta H_t}{\Delta S_t}. \quad (2.3)$$

2.1.2 Diffusion in Lipid Membranes

2.1.2.1 Self-diffusion and the Free Volume Model

When a particle in solution experiences collisions with thermally excited solvent molecules, the instantaneous imbalance of the net force causes the well-known Brownian motion and underlies all diffusion processes. The fundamental Einstein relation [75]

$$D = \mu k_B T \quad (2.4)$$

links the diffusion coefficient D with the mobility μ of the particle and the temperature T . In general, the mobility $\mu = 1/f$ is the inverse of the friction coefficient f and is defined from the terminal velocity v_t under a force F as $\mu = v_t/F$. For a spherical particle of radius r in low Reynolds condition the Stokes friction coefficient f is $f = 6\pi\eta r$ for a liquid with viscosity η .

The friction of a particle embedded in a lipid membrane can be described from a continuum or an atomistic viewpoint. In a continuum model, the diffusing particle is large against the solvent molecules (the lipids). Then, the friction experienced by the embedded particle is a function of membrane and bounding solvent viscosity as well as particle size and shape. Such a model is the well-known Saffmann-Delbrück model [76]. It describes the diffusion of an idealized cylindrical particle and is valid e.g. for integral membrane proteins in free-standing membranes [77] and in supported membranes with modifications [78].

A different situation is present when looking at the self-diffusion of the solvent molecules themselves or particles of comparable size, where the continuum assumption of the solvent breaks down [79–82]. As a consequence, the diffusion of lipids in a lipid matrix is best described using a free-volume model. Such a model states that random thermal density fluctuations can create a free volume into which a neighboring lipid molecule will move with a certain probability and activation energy. Based on the free-volume theory for liquids of Cohen & Turnbull [83], Macedo & Litovitz [84] derived a general expression for thermally activated self-diffusion:

$$D = D' \exp \left(-\frac{\gamma a^*}{a_f(T)} - \frac{E_a}{k_B T} \right), \quad (2.5)$$

where D' is a pre-factor, $0.5 < \gamma < 1.0$ is a geometric constant, a^* is the critical free area, $a_f(T)$ is the temperature-dependent average molecular free area, and E_a is the activation energy for the lipid to move into the free volume¹. Equation 2.5 is a suitable description for the long-range diffusion of lipids or lipid-anchored proteins with small interfacial or hydrodynamic drag as measured by FRAP (see Section 3.4) or similar methods [85].

¹Almeida *et al.* [81] give a modified description which also rigorously derives D' and γ .

2.1.2.2 Random Walks

Free Random Walk Diffusion Whatever the nature of the friction, the thermally excited diffusion of a molecule in a membrane (further than a few lipid diameters) is described by a 2D random walk [79, 86]. The probability distribution function p_d of the 2D random walk endpoint displacement d after a certain time t is given by

$$p_t(d) = \frac{d}{\sigma^2} \exp\left(-\frac{1}{2} \left(\frac{d}{\sigma}\right)^2\right), \quad (2.6)$$

where the probability maximum is at the distance σ and the inflection point is at $\sigma\sqrt{3}$ (see Figure 2.2). The maximum position is related to the diffusion coefficient through $\sigma = \sqrt{2Dt}$, while the root-mean-square (RMS) average of the endpoint distribution is $\text{RMS}(d) = \sigma\sqrt{2} = \sqrt{4Dt}$.

The mean square displacement (MSD) $\langle d^2 \rangle$ of such a 2D random walk is linear in time, given by

$$\langle d^2 \rangle = 4Dt \quad (2.7)$$

where D is the molecular diffusion coefficient and t the time.

The central limit theorem states that all random walks with step size distributions having the same RMS average will have the same endpoint distribution in the limit of long walks, independent of the exact functional shape of the step size distribution (see Figure 2.3). Consequently, a computer-generated 2D random walk with a desired two-dimensional diffusion coefficient D can be obtained in a simple fashion by calculating each step with a random direction and a fixed step size $d = \sqrt{4D \times \Delta t}$ for a given time step Δt .

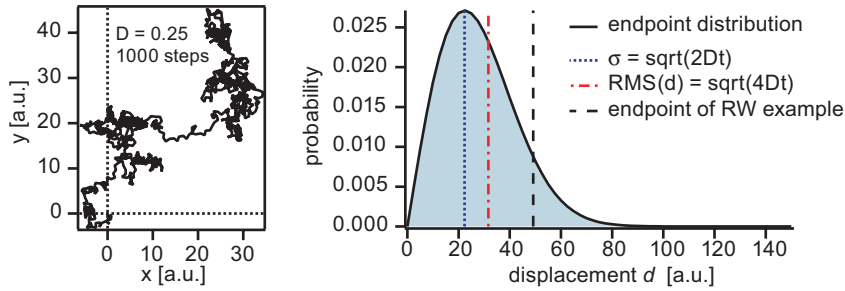


Figure 2.2: Left: A computer generated random walk of 1000 steps, with stepsize 1 and timestep 1 (arbitrary units). Right: The endpoint distribution for many random walks with these parameters has its probability maximum at $\sigma = \sqrt{2Dt}$ (see Equation 2.6).

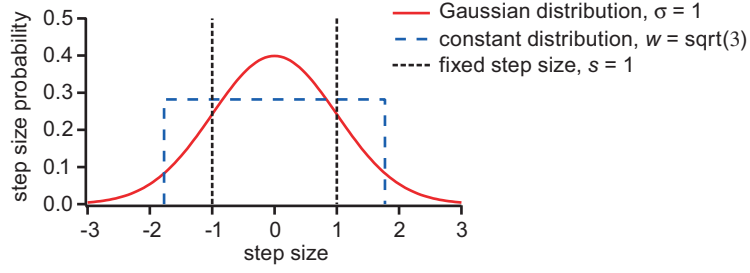


Figure 2.3: Three different step size distributions which result in random walks with the same average properties: Fixed step sizes with $s_{fix} = 1$, Gaussian probability distribution with $\sigma_{gauss} = 1$, and a constant probability distribution between $\pm(w = \sqrt{3})$.

Non-free Diffusion Experimentally obtained single molecule diffusion data often deviates from free diffusion, especially in native biomembranes [87–90]. To detect this, the square displacement is typically fitted by a power law of the form $\langle d \rangle^2 \sim t^\alpha$, where $\alpha = 1$ indicates free Brownian motion. The case $\alpha > 1$ indicates ballistic processes or directed transport, and $\alpha < 1$ indicates *subdiffusion*. Subdiffusion is most often due to obstacles, which can be inert, attractive (well-type pinning) or repellent (mountain-type), and the degree of subdiffusion α is dependent on the obstacle concentration. In other words, if a particle is free on short length and time scales but hindered in covering large distances because of obstacles, then the average displacement at short times will be high, while it will appear reduced and slowed down at long times. Furthermore, especially in live cell membranes, diffusion in a sharply confined space (corrals) is sometimes observed as well as transitions between confinements (called hop-diffusion) [82, 91–94], necessitating careful analysis. At the obstacle percolation threshold [95], the long range diffusion coefficient will go to zero. These modes of motion are illustrated in Figure 3.4 on page 21.

2.2 Optics for Visible Light and X-Rays

2.2.1 Diffraction of X-Rays

Diffraction (or scattering) of X-rays is extensively described in many textbooks, for instance [50]. Here, a short summary is given of basic concepts and equations relevant to the methods employed in this thesis. For these descriptions, the impinging wave vector is \vec{k} , where $k = |\vec{k}| = 2\pi n/\lambda$ with the refractive index n and the wavelength λ , and the scattered vector is \vec{k}' with $\Delta k = k' - k$. X-ray diffraction is usually described in reciprocal space based on the momentum transfer $q = \Delta k$.

For scattering at crystalline objects with periodicity in at least one dimension, there are special q values (i.e. scattering angles) with high intensity peaks, whereas the intensity is negligibly small in between. This is the *Bragg* condition, which can be geometrically visualized using constructive and destructive interference of reflections at lattice planes, or described with the reciprocal lattice vectors G where $q = G$ for any such peak. The real space periodicity lengths corresponding to these q values are

$$d = 2\pi/q. \quad (2.8)$$

In the approximation of weak scattering (*kinematic* approximation), the scattering pattern of X-rays from a given arbitrarily shaped electron density (such as a molecule) is described by the Fourier transform of this electron density $\rho(x, y, z)$. It is well-known that these patterns can only be recorded as intensities, leading to a loss of the phase information. This so-called phase problem fundamentally prevents direct reconstructing of electron density maps from recorded scattering patterns.

The X-ray scattering intensity can be separated into the lattice structure factor $S(q)$ and the unit cell form factor $F(q)$. The structure factor describes the Bragg-type scattering of the crystal, whereas the form factor F is the fourier transform of the electron density $\rho(z)$ in the unit cell. For crystal-like stratified samples with periodicity in z direction, the form factor is

$$F(q) = \int \rho(z) e^{iqz} dz. \quad (2.9)$$

Due to crystal imperfections the structure factor peaks are broadened. For multi-layer systems this is described in the form of interface roughness, as implemented in Section 3.6. For the scattered intensity one finds

$$I(q) \sim \frac{1}{q^4} |S(q)|^2 \cdot F(q). \quad (2.10)$$

For X-ray optics at interfaces in oriented stratified systems the diffractive index of X-rays in matter is important. The complex refractive index describes the elastic scattering and (mainly photoelectric) absorption, and is usually given as $n = 1 - \delta + i\beta$. It can also be given as

$$n = 1 - \frac{\lambda^2}{2\pi} r_o \rho_e + i \frac{\lambda}{4\pi} \mu, \quad (2.11)$$

with the electron density ρ_e and the linear absorption coefficient $\mu = 4\pi\beta/\lambda$. Here, we can define the scattering length density (SLD) of the material through $\text{SLD} = r_o \rho_e$. We

can then calculate the penetration depth of X-rays from

$$I = I_0 \exp(-(4\pi/\lambda)\beta d) = I_0 \exp(-\mu d) \quad (2.12)$$

From Equation 2.11 and tabulated values of μ in water one finds for 22 keV $\mu \approx 0.72 \text{ cm}^{-1}$ (penetration length is $l \sim 1.4 \text{ cm}$), whereas for 8 keV $\mu \approx 10.4 \text{ cm}^{-1}$ ($l \sim 0.1 \text{ cm}$). This is equivalent to saying that for 22 keV 50% intensity absorption has occurred after $\sim 1 \text{ cm}$, and for 8 keV after $\sim 700 \mu\text{m}$. Only high energy X-rays allow sufficient transmission through macroscopic aqueous sample volumes. These observations motivate the choice of 22 keV X-ray energies in experiments with transmission through bulk water.

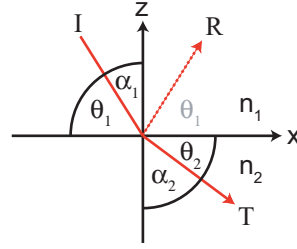


Figure 2.4: Geometry used in this section, where α angles are for the visible light convention, Θ angles for the X-ray convention.

X-ray diffraction at interfaces is often described with *dynamic* calculations, as opposed to the kinematic approximation. Here, the reflection and transmission at each interface are described with the Fresnel equations. A dynamic calculation can account for effects such as total reflection (see Section 2.2.3). In the X-ray convention (see Figure 2.4), the Fresnel equations are usually expressed in terms of wave vectors $k_z = k_{z,0}n \sin \Theta$. Using the relative refractive index $n = n_t/n_i$ one can write for the perpendicular amplitude reflection coefficient

$$r_{\perp} = \frac{n_i \sin \Theta_i - n_t \sin \Theta_t}{n_i \sin \Theta_i + n_t \sin \Theta_t} = \frac{k_i - k_t}{k_i + k_t} \quad (2.13)$$

and with $n^2 \approx 1$ for X-rays it follows that

$$r_{\parallel} = \frac{n_t \sin \Theta_i - n_i \sin \Theta_t}{n_t \sin \Theta_i + n_i \sin \Theta_t} = \frac{n^2 k_i - k_t}{n^2 k_i + k_t} \approx r_{\perp} \quad (2.14)$$

One can see that the difference between the parallel and perpendicular reflection coefficients is small for X-rays, and a single reflection coefficient $r := r_{\parallel} = r_{\perp}$ is used (the same holds for the transmission coefficient t). The reflected and transmitted intensities are

$$R = |r|^2 \quad \text{and} \quad T = |t|^2. \quad (2.15)$$

Energy transport is conserved, so that for the geometrically normalized transmittance $T^* = T(n_t \sin \Theta_t / n_i \sin \Theta_i)$ always $R + T^* = 1$ is valid. The amplitude reflection and transmission coefficients are used to calculate the total reflectivity of a layered model system for evaluation of experimental reflectivity experiments (see Section 3.5).

2.2.2 Diffraction of Visible Light

In very simplified terms diffraction can be understood by the Huygens principle of forward-propagating elementary waves [96]. Huygens-Fresnel diffraction (correctly considering interference of scattered elementary waves) can explain diffraction effects at boundaries, apertures, diffractive index gradients and interfaces of a general size d where $\lambda/d \ll 1$. Diffraction of visible light by arbitrary shapes is covered within some approximations by the extended framework of Kirchhoff's scalar diffraction theory.

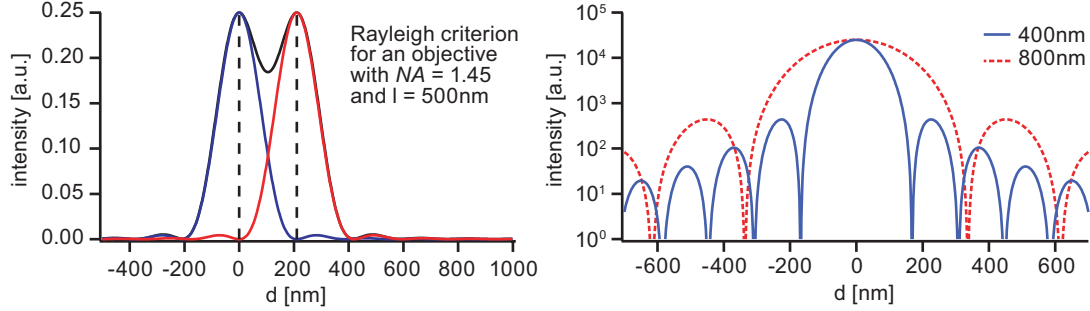


Figure 2.5: Illustration of lateral resolution in microscopy. Left: Two point-like objects are within a distance d . For the two objects to be still identifiable according to the Rayleigh criterion, the second object must be at least as far away as the position of first minimum of the first object's Airy function. Under this condition there is still a distinct minimum in the additive signal with $\sim 75\%$ of the maximum intensity. Right: The Airy function for two wavelengths in a log plot, using $NA = 1.45$.

Most relevant for optical microscopy is the well-known diffraction pattern of a circular aperture for parallel incident light and large image distance (Fraunhofer diffraction), which can be obtained by Fourier-transformation of the aperture. This function is commonly called the Airy function $A(\varphi)$ and is given in an angle-dependent form as

$$A(\varphi) \sim \left(\frac{J_1 \left(\frac{2\pi}{\lambda} R \sin \varphi \right)}{\frac{2\pi}{\lambda} R \sin \varphi} \right)^2. \quad (2.16)$$

Here J_1 is a first order Bessel function, λ is the wavelength, R is the radius of the circular aperture and φ is the angle under which the diffraction image is observed. For the case of microscopy, one finds for the diameter of the diffraction spot (its first minimum):

$$D = 1.22 \frac{\lambda}{NA} \quad (2.17)$$

with the numerical aperture NA of the objective. An illustration is given in Figure 2.5, calculated for a microscope with $NA = 1.45$ and $\lambda = 500\text{ nm}$. We see that under these conditions a point-like object is broadened by diffraction to a spot with a diameter of $\sim 420\text{ nm}$, which is commonly called the Airy disc. Under the somewhat arbitrary but widely used Rayleigh definition, two objects can still be resolved separately when the the intensity maximum of one object lies in the first minimum of the other, defining the resolution $r = 0.61\lambda/NA$. This is the diffraction limit that restricts the maximum resolution of a conventional microscope to approximately $r \sim 200\text{ nm}$. The effect of the

wavelength is also illustrated in Figure 2.5. The use of shorter wavelengths and larger NA increases the resolution of the microscope². In general, the z -resolution of an optical system is lower than its xy -resolution in the image plane. The 3D image of a point-like object is referred to the instrument point-spread-function (PSF).

2.2.3 Total Reflection of Visible Light and X-Rays

The angle of refraction of transmitted light at an interface between two media 1 and 2 of refractive indices n_1 and n_2 is given by Snell's law $\sin \alpha_i / \sin \alpha_t = n_2 / n_1$. For $n_2 > n_1$ there exists an angle α_c for which $\sin \alpha_t = 1$. Beyond that critical angle α_c the angle of refraction of the transmitted beam has a complex solution. The reflectance is $R = 1$ so that there is total reflection of the incident beam and there is no energy transported in z -direction into the medium 2 (see Figure 2.6). However, the Fresnel equations predict non-zero complex transmission coefficients, consistent with Maxwell's equations at an interface requiring continuity for the parallel component of the incident wave.

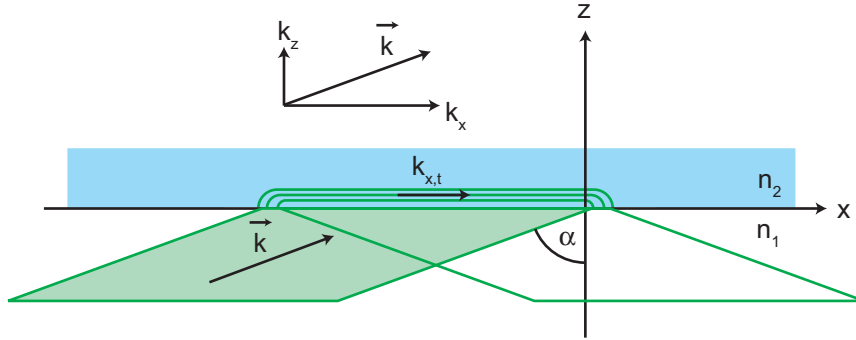


Figure 2.6: Total reflection of an incident beam at an angle $\alpha > \alpha_c$, drawn in the geometry typically used in visible light optics. The beam is incident on the interface from the medium with $n_1 > n_2$. The parallel component of the electric field is conserved at the interface and no energy is transported into medium 2 in z -direction.

Detailed analysis shows that an exponentially decaying field (standing wave) forms at the interface in medium 2, with a decay length depending on refractive indices, wavelength

²However for samples in water distant from the substrate, lower- NA water-immersion objectives can actually achieve higher resolution than high- NA oil-immersion objectives due to better refractive index matching. In the study here, the samples are always close to the substrate interface, so that oil-immersion is the method of choice.

and incident angle³. The correct calculations give the evanescent field decay length d as

$$\begin{aligned} d &= \frac{1}{2k_t} \left[(\sin \alpha_i / \sin \alpha_c)^2 - 1 \right]^{-1/2} \\ &= \frac{\lambda}{4\pi} \left[n_1^2 \sin^2(\alpha_i) - n_2^2 \right]^{-1/2}. \end{aligned} \quad (2.18)$$

For the case of (fluorescence) microscopy using visible light at the glass/water interface the penetration depth is plotted in Figure 2.7 for two wavelengths used in this study. Calculations made with $n_{water} = 1.33$ and $n_{glass} = 1.52$ result in the angle of total reflection $\alpha_c \approx 61^\circ$ and show that illumination of the sample in medium 2 (water) is restricted to ~ 100 nm depth from the surface.

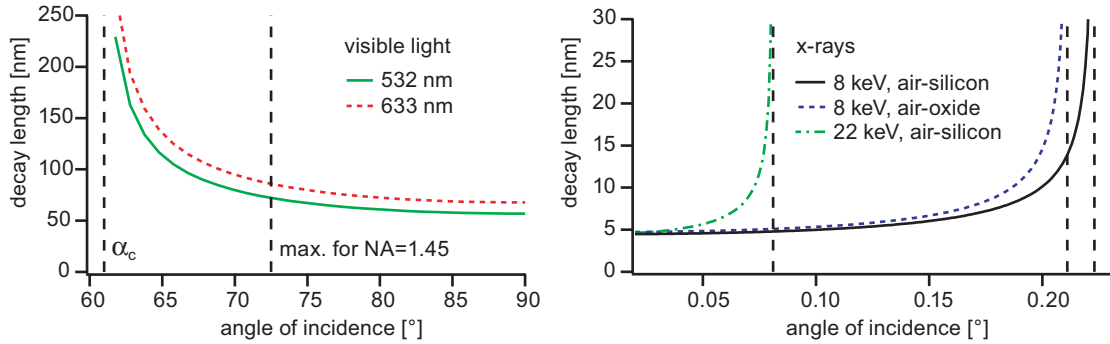


Figure 2.7: Left: Decay length (penetration depth) of the evanescent field under total reflection for visible light. Calculations are made with $n_{water} = 1.33$ and $n_{glass} = 1.52$ for the two laser lines at 532 nm and 633 nm. Dotted lines indicate the angle of total reflection $\alpha_c \sim 61^\circ$ and the maximum illumination angle attainable $\alpha_{max} \sim 72^\circ$ in through-the-objective TIRF with a $NA = 1.45$ objective using standard immersion oil and glass. Right: Decay lengths of the evanescent field for 8 keV and 22 keV X-rays into silicon at the air-silicon and air-oxide interface. Dotted lines indicate angles of total reflection.

Total reflection is also encountered in X-ray scattering experiments. Attention has to be given to the coordinate system, which now gives the angle between the incident beam and the interface. In the geometry for X-rays the condition for total reflection is met when $\cos \Theta_c = (1 - \delta)$, often approximated by $\Theta_c[\text{rad}] \approx \sqrt{2\delta}$. In fact, in the limit of small angles the evanescent field penetration of X-rays is wavelength independent and similar for most materials (see Figure 2.7). As with visible light, for surface sensitive experiments the background scattering from a bulk substrate is minimized by using total reflection.

³Detailed investigations show that diffraction at the edges of the finite beam footprint lead to energy flowing into medium 2 as a surface wave, and leaving medium 2 at the other edge, with the reflected beam offset by a distance d on order of the wavelength (Goos-Hänchen Effect). A geometric illustration for the transmission under total reflection can be made with a plane wave with a transmitted wave vector \vec{k}_t and an imaginary refraction angle α_t which necessarily has a real sine and an imaginary cosine. We see that there is an exponential decay in z-direction with an angle-dependent depth, and a wave solution in x-direction: $\exp(i\vec{k}_t\vec{r} - \omega t) = \exp(ik_t(x \sin \alpha_t + z \cos \alpha_t) - \omega t) = \exp(ik_t(\sin \alpha_i / \sin \alpha_c)x - \omega t) \times \exp(-k_t z \sqrt{(\sin \alpha_i / \sin \alpha_c)^2 - 1})$.

3 Methods

3.1 Total Internal Reflection Fluorescence (TIRF) Microscopy

In this study, through-the-objective total internal reflection fluorescence (TIRF) microscopy was implemented. This principle utilizes a high NA objective which has a front lens exit angle greater than the angle of total reflection of the sample interface (see Figure 3.1 and Section 2.2.3). Focusing a narrow laser beam into the back focal plane of the objective results in a parallel beam exiting at the front lens (Figure 3.1 inset) at an angle to the central axis which depends on the amount of off-axis displacement on entrance into the objective. Standard wide-field epi-illumination can be achieved by moving the beam back into the central axis. Also, the epi-illumination at the sample can be changed between parallel and focused illumination by either entering the objective focused into the backplane or focused to infinity (Figure 3.1 inset). The sample emission light is collected by the objective and separated from the excitation light with a dichroic mirror as in a conventional fluorescence microscope.

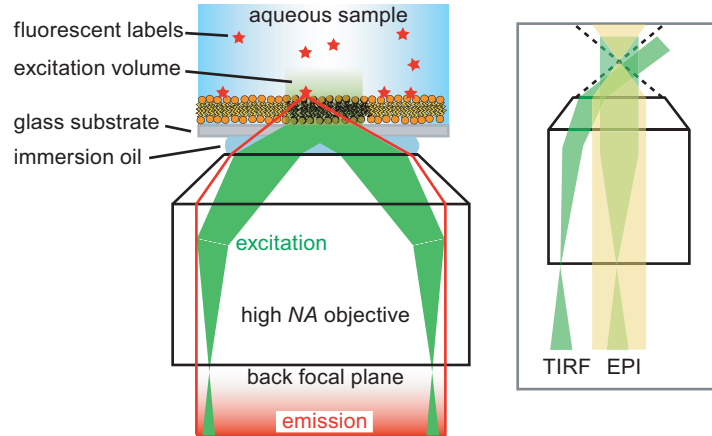


Figure 3.1: Illustration of through-the-objective total internal reflection fluorescence (TIRF) microscopy. Left: For infinity-corrected objectives, light which is focused into the back focal plane exits the front lens as a parallel beam. This is used for TIRF microscopy where the parallel beam impinges upon the sample interface (glass-water) at an angle greater than the critical angle for total reflection. Right: Standard epi-illumination (wide-field) can be achieved by central on-axis illumination.

In order to calculate the experimentally minimum necessary NA one has to consider the maximum exit angle of light from an objective. This is given by the numerical aperture through $NA = n_1 \sin \alpha$. If total reflection is desired at an interface going from the refractive index n_1 to n_2 we require $n_1 > n_2$ and $\alpha_i > \alpha_c$, so that $n_1 \sin \alpha_i > n_1 \sin \alpha_c = n_2$. From this one can see that for through-the-objective TIRF $NA \geq n_2$ is required.

For example, TIRF imaging of tightly adhered cells with a cytosolic $n_2 = 1.36$ require an objective with $NA > 1.36$. With an objective of $NA = 1.45$ the maximum attainable illumination angle is $\alpha_{max} \approx 72^\circ$, further limited by practical details including effects of a finite beam diameter and imperfect refractive index matching.

3.2 Single-Molecule Localization Microscopy

As discussed in Section 2.2.2, the image of an object smaller than the light wavelength is diffraction limited and for a circular aperture takes the form of the Airy function. Recently, several techniques have been established to overcome the resolution limit with visible light fluorescence. For instance, 4π -microscopy [97] improves the axial resolution, while stimulated emission depletion (STED) microscopy [98, 99] improves lateral resolution. Both techniques operate in a mode similar to conventional confocal imaging allowing fast acquisition times. Techniques using single-molecule localization such as photoactivation-localization microscopy (PALM) [100] require more time to acquire an image but can use simpler optical setups.

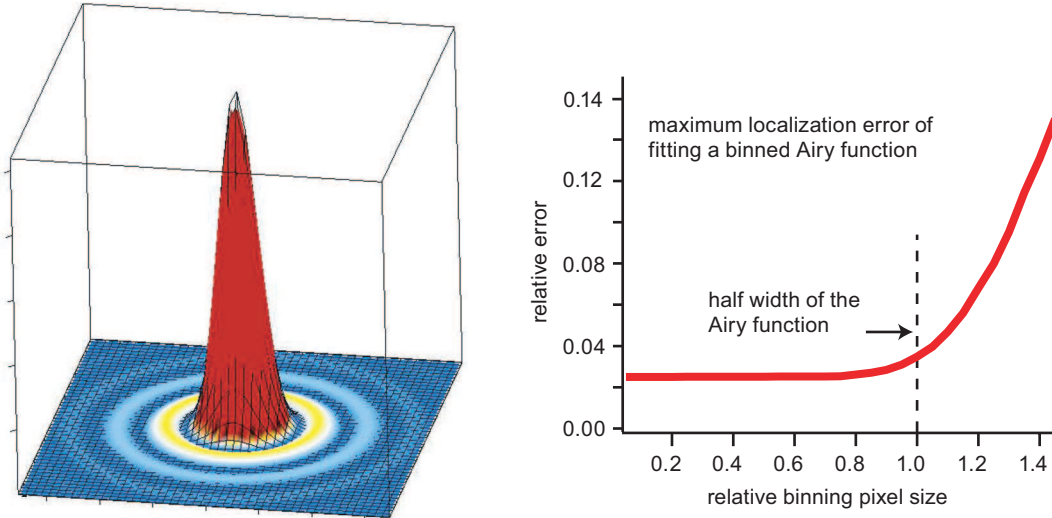


Figure 3.2: Left: A 2D-Airy function with a Gaussian fit of the central peak. Right: The relative error in localization of the central peak when fitting a binned Airy function (e.g. from CCD camera pixels). The calculation was performed by binning a given analytical 2D Airy function in a certain pixel size, applying a Gaussian fit and then comparing the center of the fit to the original position. Depending on the relative position of the Airy function to the pixel boundaries, a maximum fitting error is found.

In this thesis, single chemical dye molecules are used in order to minimize label effects when labeling membrane-bound proteins. However, chemical dye molecules have limited photostability [101] and single-dye imaging still poses a great challenge. In general, many other types of labels could be used in single molecule fluorescence microscopy. Quantum-dots have excellent photostability at a significantly larger size (>10 nm with functionalization) [102]. Even brighter but larger are labels such as latex beads with incorporated and protected/stabilized chemical dyes. As an alternative to fluorescent

labels, nanoscopic colloidal gold labels can be imaged based on optical light scattering, have no photostability issues and can be used for high-speed imaging at very high illumination intensity [92]. Such labels were not chosen in this thesis due to their large physical sizes.

Single-molecule localization microscopy relies on the fact that even if an object itself cannot be resolved, its central position is well defined by the peak position of the Airy disc. Consequently, single molecule localization is commonly performed with a 2D fit (Figure 3.2) to the diffraction limited spot, usually with a Gaussian function¹. The accuracy of the position obtained from the fit will be limited by the photon emission statistics and background noise. Ober *et al.* [103] derived an expression that describes the fundamental stochastic limit of localization accuracy δ of a single fluorescent molecule in the absence of noise:

$$\delta = \frac{\lambda_{em}}{2\pi NA\sqrt{\gamma At}}, \quad (3.1)$$

where λ_{em} is the wavelength of the emitted light, A is the photon emission rate of the molecule, NA is the numerical aperture, γ is the total detection efficiency of the system, and t is the acquisition time. The results of Bobroff [104] base similar calculations on Gaussian profiles and some further assumptions. Alternatively, a simple estimate often given (e.g. [105]) is

$$\delta = \frac{\sigma}{N}, \quad (3.2)$$

where $\sigma = \sigma(\lambda_{em}, NA)$ is the Gaussian standard deviation of the observed diffraction limited spot and N the total number of recorded photons. The total number of collected photons $N = \gamma At$ is the most useful experimental parameter to improve localization accuracy. In single molecule fluorescence experiments, this usually requires increasing illumination laser power to increase the number of emitted photons from each fluorescent label. This is explored in detail in Section 5.3.

However, in practice noise strongly degrades the accuracy for low signal-to-noise (S/N) ratios. Noise sources are typically laser background signal (through imperfect filters and dichroic mirrors), sample autofluorescence (incl. cellular and glass autofluorescence), and several types of noise present in the detector and its electronics (thermal dark noise, readout noise, etc). Detector noise is strongly reduced in deeply cooled electron multiplying CCDs (EMCCDs). A related observation is that noise can produce apparent sub-diffusion for short tracks of moving particles by adding errors to displacements measured at very short times [106].

To a lesser extent accuracy is also influenced by the xy-resolution of the Airy disc image, limited by pixelation of the detector. In Figure 3.2 the result of a maximum error calculation is shown for a range of pixel sizes. The maximum localization error obtained for a given image resolution (i.e. nm per pixel) should only increase significantly when the pixel size exceeds the Airy function half-width (measured from zero to the position of the first minimum). For the case of light with 500 nm wavelength, this would allow an

¹The Airy disc diameter is $\sim 2.9\times$ the Gaussian width (standard deviation). A fit directly with a 2D Airy function is of course possible as well.

xy-resolution as low as ~ 300 nm per pixel without introducing significant localization error (see Section 5.3).

Further limits in precision are imposed by effects such as mechanical stability (vibrations, thermal drift) of the setup. The accuracy including all error sources combined has to be determined from the experimental positional fluctuation when tracking a single stationary particle over time. In moving particles, a further effect to be considered is the smearing out the Airy disc during a single frame acquisition, also reducing its positional accuracy.

3.3 Analysis of Single-Molecule Random Walks

When evaluating an experimental set of diffusion traces it is often of great interest to understand the distribution of the obtained diffusion coefficients D . However, the statistical fluctuations in evaluating experimental random walks can be large, especially for short traces as expected in single molecule fluorescence experiments, emphasizing the importance of understanding scatter and distributions in the obtained results [107].

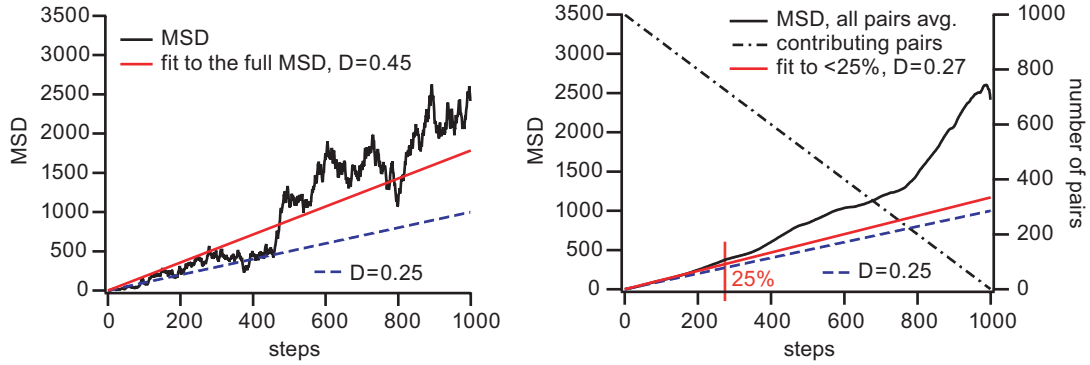


Figure 3.3: Left: The MSD of a random walk example. A linear fit to the whole MSD with Equation 2.7 results in $D = 0.45$, whereas a stepsize equivalent to $D = 0.25$ was used in calculating the random walk (blue line). Right: Averaging over all pairs in the RW. The fit to the first 25% of the MSD (250 steps) results in $D = 0.27$.

In order to extract the diffusion coefficient of a single random walk using Equation 2.7 one could conceivably

1. evaluate only the endpoint position, or
2. make a linear fit to the mean square displacement (MSD), or
3. make a linear fit to an *internally averaged* MSD.

Obviously, evaluating just the endpoints (1) will use only a single data point of each random walk. A linear fit to the unaveraged MSD (2) at least uses all data points, but is still subject to the large displacement fluctuations of a random walk (see Figure 3.3, left). In practice, the best way [107] to obtain D from a single trace is by *internal averaging* (3), which relies on the fact that any segment within a random walk has on average the same properties as any other segment. These strategies result in increasingly sharp

distributions of diffusion coefficients D when analyzing a population, ranging from the broad endpoint distribution function (Equation 2.6) to a narrow Gaussian distribution in the best cases.

In most cases one obtains the narrowest distribution of D from a set of traces by *averaging over all pairs* in each trace, where for a given Δt each existing displacement (between a pair of xy-points separated in time by Δt) in a trace is used for averaging the displacement at $t = \Delta t$ in order to obtain the averaged MSD(t) (see Figure 3.3, right). Independent from the trace length, the width of the distribution of D is determined by the maximum fraction of the trace length used in averaging. Values of Δt with few contributing displacement data points should be avoided, so that a linear fit to the averaged MSD should be performed only for short times (e.g. <25% of trace length) or with appropriate weighting (using the variance). The shorter the evaluated fraction, the more independent data points contribute, and the closer the fit result D will be to the “real” D . Consequently, the distribution of D will be sharper.

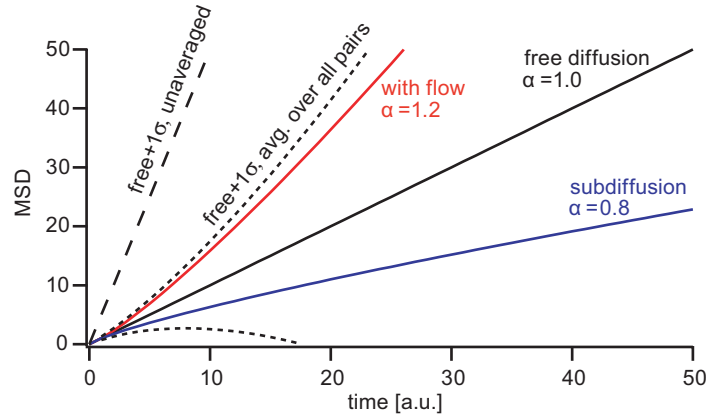


Figure 3.4: Modes of diffusion. Shown is free diffusion ($\alpha = 1.0$), diffusion with flow ($\alpha = 1.2$), and subdiffusion ($\alpha = 0.8$). Broken lines indicate the MSD for free diffusion plus its standard deviation σ in the case of no internal MSD averaging, and with MSD averaging over all pairs.

Due to the strong fluctuations of any random walk, the mode of diffusion can be difficult to determine in a single trace, illustrated in Figure 3.4. Both the flow and subdiffusion examples cannot be distinguished from free diffusion in a single trace within one standard deviation certainty. The standard deviation of the MSD of free diffusion is calculated according to refs. [107, 108]. From this example illustration it is clear that the modes of motion can only reliably be detected from the analysis of a whole population of diffusing particles.

3.4 Fluorescence Recovery after Photobleaching (FRAP)

A classical experiment to measure fluidity and diffusion in a membrane is *fluorescence recovery after photobleaching* (FRAP). A strong laser is used to bleach fluorescent marker molecules such as labeled lipids in a well-defined area and the fluorescence recovery in the bleached region by diffusion is observed. In a defined geometry, this enables quantitative determination of the diffusion coefficient as well the mobile fraction of the fluorescent markers. In a good approximation these markers represent the properties of the matrix. For the case of a circular and homogeneous bleaching beam and observation beam, the recovery of the total fluorescence intensity $F(t)$ can be described as [44, 109]:

$$F(t) = F(\infty) - (F_0 - F(0)) \left\{ 1 - \exp\left(-\frac{2\tau}{t}\right) \left[I_0\left(\frac{2\tau}{t}\right) + I_1\left(\frac{2\tau}{t}\right) \right] \right\}. \quad (3.3)$$

F_0 denotes the initial fluorescence intensity, $F(0)$ is the intensity at time $t = 0$ directly after bleaching and $F(\infty)$ is the equilibrium intensity reached in the infinite limit, as shown in Figure 3.5. I_0 and I_1 are modified Bessels functions of zero and first order.

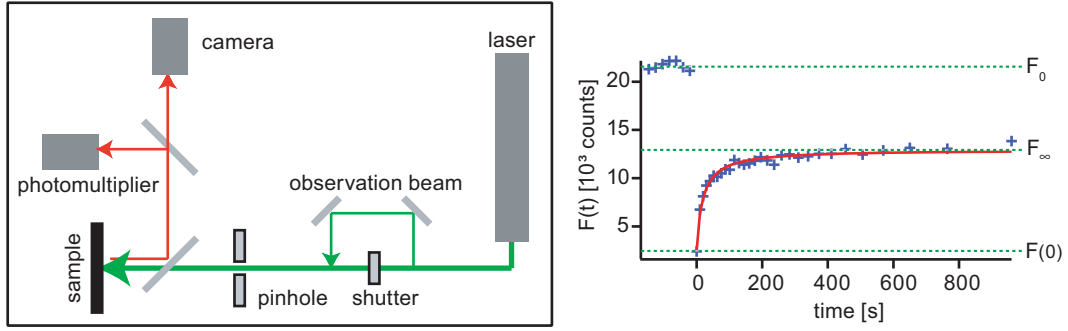


Figure 3.5: Left: Sketch of the experimental FRAP setup. Right: Typical intensity data ($F(t)$, markers) with fit (red curve) of a fluorescence recovery experiment after bleaching at $t = 0$.

Fitting the analytical expression Equation 3.3 to the recorded intensity allows evaluation of the characteristic time constant τ . With the known diameter of the bleached spot r , one can calculate the diffusion coefficient D and the recovery rate R_{rel} (the mobile fraction) from the fit according to:

$$D = \frac{r^2}{4\tau}, \quad (3.4)$$

$$R_{rel} = \frac{F(\infty) - F(0)}{F_0 - F(0)}. \quad (3.5)$$

3.5 X-Ray Reflectivity of Oriented Stratified Systems

A specular $\Theta - 2\Theta$ scan of an oriented sample (an *X-ray reflectivity* experiment [50]) as illustrated in Figure 3.6 gives structural information in z -direction on a similar length scale as SAXS (see Section 3.6). The scattering is recorded specularly and is mainly elastic ($k_f = k_i$) so that the momentum transfer is in direction of the z -axis

$$\vec{k}_f - \vec{k}_i = \vec{q} = \vec{q}_z \quad (3.6)$$

and

$$q_z = 2k \sin \Theta \quad (3.7)$$

with $k = k_f = k_i = 2\pi n/\lambda$. When an X-ray beam impinges on a stratified system, there will be reflection and transmission at each occurring interface as described by the Fresnel equations. In direction of the reflected beam the phase-correct sum of all interface reflections is the total system reflectivity R at a certain incident angle. Below the critical angle Θ_c there is full reflectivity $R \equiv 1$. For a single interface we observe the *Fresnel Reflectivity* $R_f = |r|^2$ (see Figure 3.6 and Section 2.2.1).

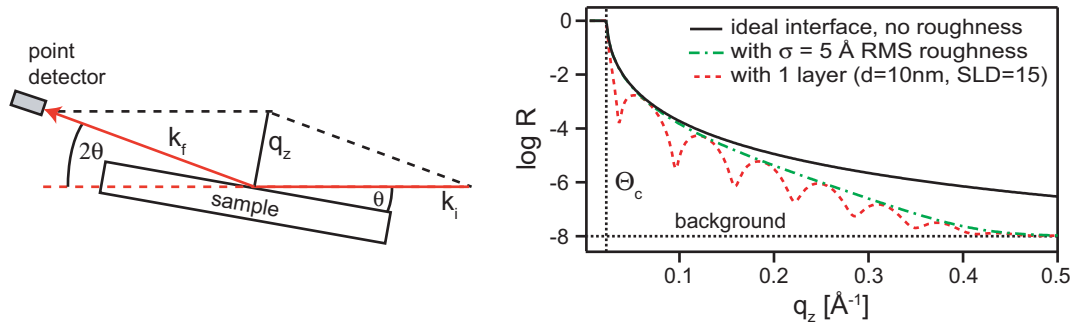


Figure 3.6: Left: Experimental geometry for $\Theta - 2\Theta$ specular X-ray reflectivity. Right: Theoretical reflectivity curves for a water/silicon interface ($\text{SLD}[\text{water}] = 9.4$, $\text{SLD}[\text{Si}] = 20$, in units of 10^{-6} \AA^{-2}) without roughness, with roughness, and with an additional layer .

In experiment and theory it is found that interfacial roughness damps the reflectivity. Sources of roughness can be static (topological, gradients) or dynamic (fluctuations). The roughness (with Gaussian width σ of the interface position distribution) is described as a refractive index gradient using the error function, and results in a damping factor of the Fresnel amplitude reflection and transmission coefficients. For roughness resulting from a Gaussian distribution of the interface position (with width σ) we can write

$$n(z) = \frac{n_1 + n_2}{2} - \frac{n_1 - n_2}{2} \text{erf} \left(\frac{z - z_0}{\sqrt{2}\sigma} \right) \quad (3.8)$$

with the error function

$$\text{erf}(z) = \frac{2}{\sqrt{\pi}} \int_0^z \exp(-t^2) dt. \quad (3.9)$$

The reflection coefficient between two layers j and $j + 1$ is modified by the *Névt-Croce*

damping factors:

$$r_{j,j+1} = \frac{k_j - k_{j+1}}{k_j + k_{j+1}} \exp(-2k_j k_{j+1} \sigma_{j,j+1}^2). \quad (3.10)$$

Systems with multiple interfaces (layers) display more complex reflectivity curves. The reflectivity of a single homogeneous layer on a substrate displays pronounced interference oscillations called the *Kiessig fringes*, with the periodicity Δq_z of the minima corresponding to the layer thickness d through

$$d = 2\pi/\Delta q_z. \quad (3.11)$$

There are different ways and approximations to calculate the reflectivity R of a layered system. In this thesis, reflectivity is calculated using slab models with the transfer matrix method of Abelès [110], analogous to the commonly used recursive algorithm for phase-correct summation of Fresnel reflectivities and transmittivities given by Parratt [111]. The latter is a *dynamic* calculation (as opposed to *kinematic*) which takes the preservation of intensity into account for a system of n layers and correctly includes effects such as total reflection. According to Parratt, the effective amplitude reflection coefficient of the stratified system with N layers is calculated recursively starting from the from the last interface between the media N and $N - 1$. The calculations use the Fresnel coefficients r^F (Equation 2.13) and the wave vector k_j in the layer j with thickness d_j :

$$\begin{aligned} r_{N-1,N} &= r_{N-1,N}^F \text{ (last interface)} \\ r_{j,N} &= \frac{r_{j,j+1}^F + r_{j+1,N}^F \cdot \exp(2ik_{j+1}d_{j+1})}{1 + r_{j,j+1}^F \cdot r_{j+1,N}^F \cdot \exp(2ik_{j+1}d_{j+1})} \text{ for } N - 2 \geq j \geq 0 \end{aligned} \quad (3.12)$$

The effective system reflectivity is then

$$R(q_z) = |r_{0,N}|^2. \quad (3.13)$$

3.6 X-Ray Scattering of Unoriented Samples (SAXS/WAXS)

In X-ray scattering experiments large structures are resolved in a small angle regime, while small structures scatter into wide angles. For membrane multilayer samples in dispersion, the vertical membrane structure and inter-membrane forces can be investigated in small-angle X-ray scattering (SAXS) [112], while the length-scales of the chain-chain correlation are visible in the wide-angle regime (WAXS) (see Figure 3.7, left).

As the sample is unoriented, scattering is radially averaged in Debye-Scherrer rings (see Figure 3.7, right), equivalent to powder scattering. Only crystallites with “correct” orientation to the incident beam fulfill the Bragg condition (see Section 2.2.1). The scattering angle α is related to the incident angle Θ at a sample “crystallite” through $\Theta = \alpha/2$, and

$$q_r = 4\pi\lambda/\sin(\Theta). \quad (3.14)$$

For SAXS, peaks at equidistant q -values indicate lamellar periodicity of the membrane

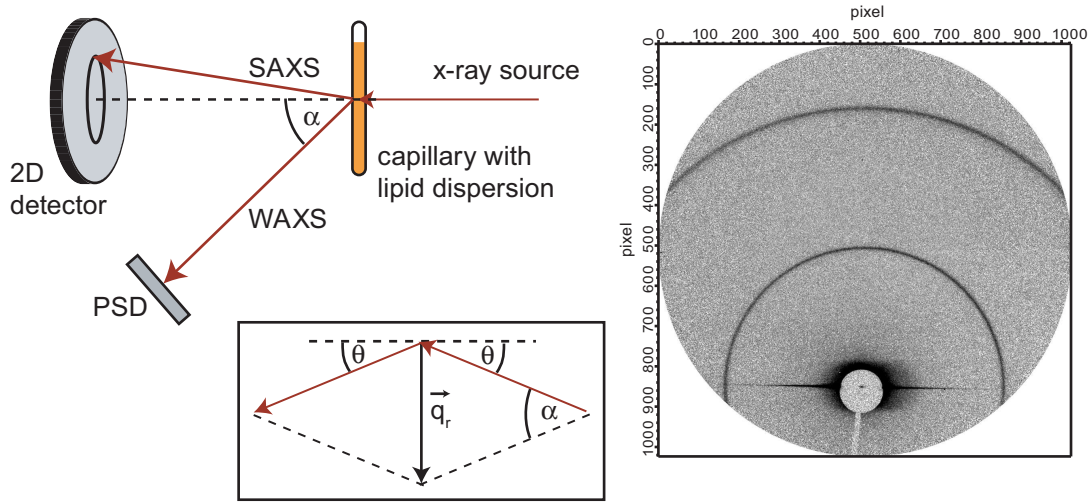


Figure 3.7: Left: SAXS/WAXS experimental setup and scattering geometry. SAXS is recorded on a 2D detector, WAXS on a position-sensitive detector (PSD). Right: Example of 2D raw data (1000 \times 1000 pixels) for unoriented (powder-type) X-ray scattering in SAXS.

multilayers. The q -value of the n^{th} order peak with lamellar spacing D is

$$q_n = \frac{2\pi n}{D} \quad (3.15)$$

D by itself can already give valuable information about membrane thickness and inter-membrane interaction. The detailed vertical structure (electron density) can be reconstructed by recording many orders of peaks (which sample the form factor), assigning phases and applying a Fourier reconstruction [113].

However, in this study an alternative method is applied. In the following, the description of the theoretical model for SAXS scattering follows the work of Pabst, Rappolt *et al.* [114, 115]. This model “classically” separates form and structure factor and SAXS data is analyzed with a full q -range fit (see also Section 2.2.1 and Figure 6.14 in Section 6.4). Even with only few orders of peaks available, this versatile method is found to give quantitative structural information. Especially information about layer thicknesses and the inter-membrane water gap can be obtained.

To facilitate analytical modeling, the electron density profile $\rho(z)$ can be chosen to consist of a sum of Gaussians. However, in this thesis $\rho(z)$ is described using a slab model with error functions (see Section 3.5 Equation 3.9), which also translate analytically under Fourier transformation when calculating the form factor $F(q)$ (see Equation 2.9).

The structure factor S is calculated with roughness according to paracrystalline perturbation theory, as the model is only applied to rigid gel phase membranes in this thesis. For fluid bilayers this may not apply [116]. It considers finite crystals with N correlated layers of thickness d and a stacking disorder described by the roughness Δ (the mean square fluctuation of the bilayer position). The structure factor is then given as

$$S(q) = N + 2 \sum_{n=1}^{N-1} (N - n) \cos(nqd) \exp\left(\frac{-nq^2\Delta}{2}\right). \quad (3.16)$$

The intensity is then calculated from S and F according to Equation 2.10.

WAXS is sensitive at small correlation distances on the order of the chain-chain spacing. In a lipid membrane in a solid phase (e.g. the gel phase) the hydrocarbon chains are hexagonally packed and their chain-chain spacing gives rise to one or more wide-angle peaks (see also Section 3.8). For tilted molecules, the spacing seen in WAXS corresponds to the spacing perpendicular to the chains, not to the membrane plane.

On the one hand, ordered solid phases of lipid membranes can be easily distinguished from a disordered liquid phase in WAXS, and thermal scans can investigate phase transitions and chain melting. On the other hand, the WAXS peak shape and spacing gives information about the type of packing, the repeat distance and the correlation distance in an ordered phase.

3.7 Grazing-Incidence X-Ray Diffraction (GID)

Grazing-incidence X-ray diffraction (GID) as used in this thesis records scattering at large angles and gives information on small length scales on the order of chain-chain correlation distances (similar to WAXS). Furthermore, due to the oriented sample geometry, scattering in q_z and q_{xy} can be resolved independently, which is impossible in the isotropic powder scattering of WAXS (see Figure 3.9). Experimentally, an upright linear position-sensitive detector (PSD) is used to scan the horizontal angle 2δ and record the out-of-plane scattering at the angle Θ . For grazing incidence and large scattering angles, we find

$$q_z \simeq k \sin \Theta \quad \text{and} \quad q_{xy} \simeq 2k \sin \delta, \quad (3.17)$$

for the angles as defined in Figure 3.8.

GID experiments are performed at incident angles φ_i below the critical angle of total reflection to achieve high surface sensitivity and avoid signal from scattering in the bulk. As a consequence of all material refractive indices being less than unity (and air/vacuum) for X-rays, X-ray total reflection at an air/sample interface occurs if the X-ray beam impinges on the sample from the side of air. The penetration depth under total reflection into the silicon calculated by Equation 2.18 is $d \sim 5$ nm, meaning that

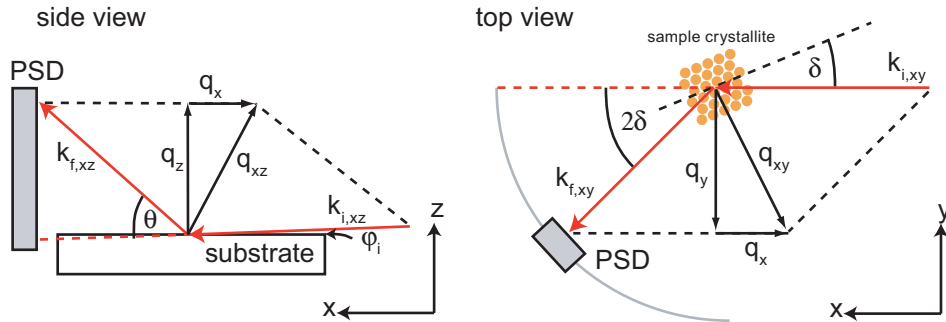


Figure 3.8: GID scattering geometry in xz (side view) and xy (top view) projection. Of all membrane crystallites (with random in-plane orientation), only those with correct orientation to the incident beam fulfill the Bragg condition.

the X-ray scattering signal is extremely surface sensitive below the critical angle Θ_c . For the air/silicon interface one finds $\Theta_c = 0.22^\circ$ and $\Theta_c = 0.08^\circ$ for 8 keV and 22 keV respectively.

3.8 Modeling of GID and WAXS Data

Due to the oriented sample geometry, GID q_z/q_{xy} maps can give quantitative information about the in-plane ordering as well as the molecular tilt in a lipid membrane. By contrast, WAXS data evaluation is more limited due to the powder averaged signal. Here, the radial q_r position of a peak gives information about the chain-chain correlation distance perpendicular to the chain orientation, not the membrane normal. The GID and WAXS q -values are related through $q_r = \sqrt{q_{xy}^2 + q_z^2}$ (see Figure 3.9).

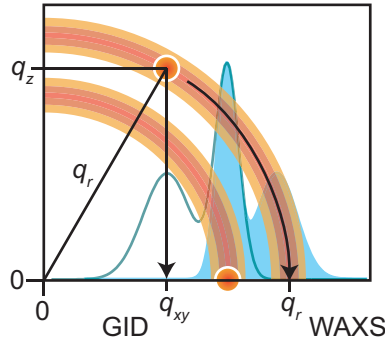


Figure 3.9: Illustration of the signal integration for GID compared to WAXS. With GID of oriented samples an integration is typically performed parallel to q_z , so that reflections with $q_z > 0$ retain their integrated peak position at their q_{xy} value, while for WAXS of unoriented samples the Debye-Scherrer rings only provide information on q_r .

In a qualitative manner, a distinct reflection with $q_z > 0$ indicates the presence of a molecular tilt. The position of a peak in q_{xy} give information about the in-plane projection of the chain-chain correlation distance and the corresponding correlation length. The Scherrer equation can be used to determine in-plane correlation lengths from peak widths [117, 118]. Assuming that the instrument resolution is high compared to the peak widths, one finds

$$L = 0.9 \times \frac{2\pi}{\sigma}, \quad (3.18)$$

where L is the in-plane correlation length and σ is the GID peak full width at half-maximum (FWHM). The geometric factor 0.9 accounts for crystallite shape.

To understand and evaluate wide-angle chain-chain correlation peaks in more detail, a simple model is used where the lipid molecules in an ordered solid phase are described as cylinders (see Figure 3.10) [119]. Up to three distinct first order reflections can occur in this model. Some possible scenarios are illustrated in Figure 3.11 with two kinds of distortion of the basic hexagonal unit cell, based on nearest-neighbor (nn) tilt and next-nearest-neighbor (nnn) tilt.

A membrane in a solid phase with a stretched orthorhombic unit cell and a molecular tilt $\alpha > 0$ has two distinct plane spacings d_{20} and d_{11} corresponding to two reflections

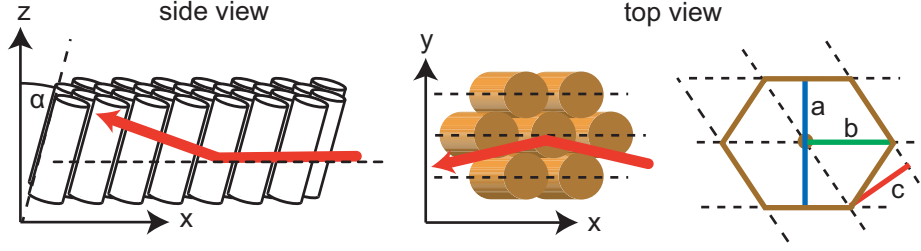


Figure 3.10: Left and Center: The model of hexagonally packed cylindrical molecules (here with nearest-neighbor nn tilt and a molecular tilt angle α) and the impinging X-ray beam (solid red arrow) at grazing-incidence. Right: A nn -tilt typically introduces an orthorhombic unit cell distortion (stretching) in direction of the tilt. In this case the 2D unit cell can be defined by the orthorhombic vectors a and b , where the undistorted plane spacing is $a/2 = d_{20}$, and b corresponds to the stretched nearest-neighbor distance. The vector $c = d_{11} \neq d_{20}$ is equal to the stretched plane spacing (its symmetrical counterpart is not indicated).

at $q_z = 0$ and at $q_z > 0$, respectively (see Figure 3.11). The nomenclature d_{20}/d_{11} refers to the reciprocal space Miller indices, and is illustrated and defined in detail in refs. [30, 119].

For upright hexagonal packing, exactly one reflection at $q_z = 0$ is expected. The orthorhombic unit cell vectors a and b as defined in Figure 3.10 can be calculated from the two experimentally obtained spacings through [31]

$$a = 2d_{20} \text{ and } b = \frac{d_{11}}{\sqrt{1 - \left(\frac{d_{11}}{d_{20}}\right)^2}}. \quad (3.19)$$

Furthermore, one can then calculate the interfacial area per headgroup (and per molecule) as

$$A_H = \frac{a \cdot b}{2}. \quad (3.20)$$

Also one can define a distortion order parameter ϵ from the vectors a and b as [120]

$$\epsilon = 1 - \frac{a}{\sqrt{3}b}, \quad (3.21)$$

where stretching along the vector b (parallel to the tilt vector) leads to a positive sign for ϵ . For a perfectly hexagonal undistorted unit cell $a = \sqrt{3}b$ and $\epsilon = 0$, while a stretching distortion leads to $\epsilon > 0$. One can also define the distortion ϵ_{chain} perpendicular to the chains, using $b \rightarrow b \cos \alpha$ with the molecular tilt angle α (ϵ and ϵ_{chain} are illustrated in Figure 3.12). For ϵ_{chain} deviations of the molecular shape from an ideal cylinder play a role.

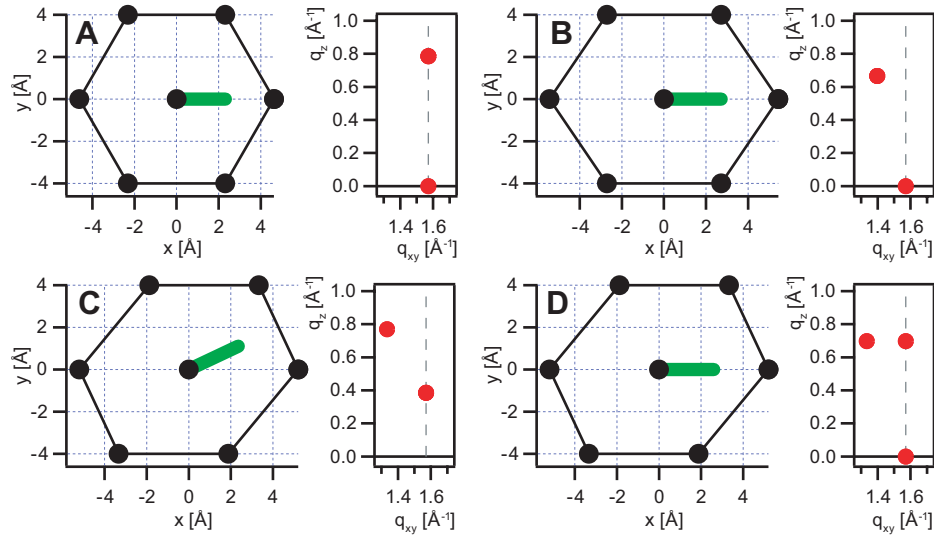


Figure 3.11: Illustration of reflections expected for an chain-chain spacing of 4.0 Å and a 30° molecular tilt, depending on the tilt direction with respect to the unit cell. A) Nearest-neighbor tilt (nn), no distortion. B) Nearest-neighbor tilt, orthorhombic (rectangular) distortion. C) Next-nearest-neighbor tilt (nnn), oblique distortion. D) Nearest-neighbor tilt, but oblique distortion (atypical).

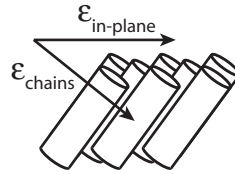


Figure 3.12: Illustration of the distortions in the plane of the membrane and perpendicular to the chains.

3.9 Molecular Dynamics (MD) Simulations of Lipid Membranes

Molecular dynamics (MD) simulations are a commonly used method to model small systems on a molecular length scale. In MD, the equations of motion for each atom are integrated with respect to the forces exerted on it from its environment. These instantaneous forces acting on an atom are derived from a set of potentials with certain functional forms and associated parameters (as an approximation of reality). With modern computing hardware, system dimensions can be in the range of 10-20 nm with hundred thousands of atoms. Some MD applications and examples as well as alternative or complementary simulation methods are discussed in Chapter 7. In the following, some implementation details from the software package GROMACS [121–129] are discussed, as used in this thesis.

The spherical atomic representations can be fully atomistic (all atoms including hydrogens), or represent different levels of coarse-graining. In this thesis, the *united-atom* concept of GROMACS is used. In such a model, non-polar hydrogen atoms are considered to interact mainly through minor contributions to van der Waals forces and are thus included in modified heavy atom types (heavy atoms being anything other than hydrogens). Polar hydrogens contribute specifically to hydrogen bonding and local dipoles and are explicitly included².

The force field employed in this thesis is based on GROMOS87 with GROMACS specific modifications (*ffgmx*) [130–133]. This force field is not the most recent implementation, but is well matched to the specialized lipid parameters used in addition (see Section 4.5). The term *force field* refers to the set of interaction functions and associated parameters used in a specific simulations.

Forces (potentials) in GROMACS are based on non-bonded and bonded interactions as well as long-range electrostatics. Non-bonded interactions are pair-additive and centrosymmetric, and include a dispersion-repulsion (van der Waals and hard-core repulsion) force as well as short-range electrostatics (Coulomb’s law). The simulation box and all interaction potentials are treated with periodic boundary conditions.

The dispersion-repulsion component is modeled with a Lennard-Jones 6-12 potential. Interactions with first and second nearest-neighbor bonded atoms are considered to be dominated by quantum (bonding) effects, and are explicitly excluded from dispersion interactions. The dispersion is typically cut off³ at ~ 1 nm. If desired, long-range effective dispersion corrections can be applied.

Long-range electrostatics are calculated without cut-offs using an Ewald sum [134]. This method splits the infinite and slowly-converging sum over all Coulomb interactions (and over infinite periodic simulation volumes) into a direct space and a reciprocal space sum. Very fast calculation of the reciprocal space sum can be made with the Particle-Mesh-Ewald (PME) method [123, 135]. Instead of a summation, a Fourier-transform is used

²In GROMACS, hydrogen bonds are formed through the general electrostatic interactions.

³Besides choosing the functional forms for the interaction potentials, interaction range cut-offs are the most critical step when balancing model complexity and calculation speed. Cut-offs in general are necessary to reduce the fundamental “all-to-all”-nature of MD with $O(n^2)$ scaling to a more manageable $O(n)$.

on a reciprocal space grid, which can be implemented very efficiently with a Fast Fourier transform (FFT) in practice. PME scales as $O(n \log n)$.

The bonded interactions are bond stretching (2 body), bond angle vibrations (3 body) and dihedral torsion (4 body), see Figure 3.13, left. In this thesis, bond length and angle potentials are harmonic. Three types of dihedral torsion potential are used: rotational, Ryckaert-Bellemans, and improper (fixed). In general, the dihedral torsional angle ϕ is defined between the planes of the atoms $(1,2,3)$ and $(2,3,4)$ with the *cis*-configuration at $\phi = 0^\circ$, *trans* otherwise. The symmetric rotational dihedral potential

$$V_{rot}(\phi) = k(1 + \cos(n\phi)) \quad (3.22)$$

with n minima is used in the general case, often (but not necessarily) coupled to an additional 1-4 pair interaction. This potential also describes the torsion of four atoms in a “star” configuration when adhering to the definition of the angle between the two planes defined by two sets of three atoms. For alkanes, the Ryckaert-Bellemans potential

$$V_{RB}(\phi) = \sum_{n=0}^5 C_n (\cos(\phi - 180^\circ))^n \quad (3.23)$$

is used with the *cis*-position by convention at 180° , shown in Figure 3.13 right. Due to their parametrization, Ryckaert-Bellemans dihedrals require the exclusion of 1-4 interactions. The example in Figure 3.13 is calculated with the numerical values for lipid alkane dihedrals as used in this thesis. Lastly, improper dihedrals use a harmonic potential to restrict the torsion to values close to ϕ_0 .

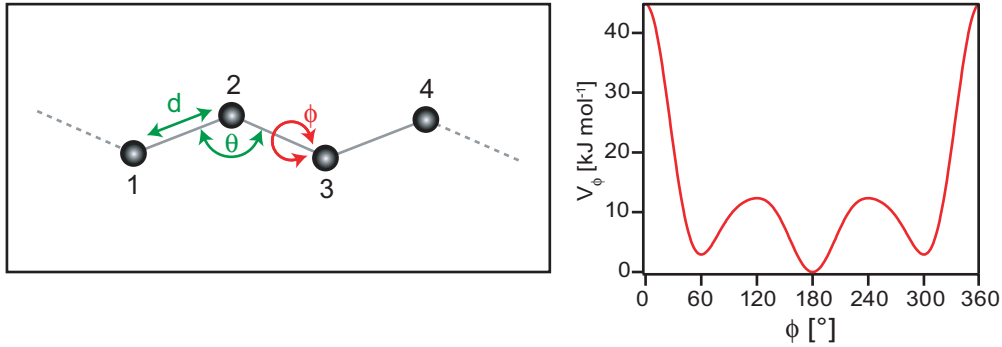


Figure 3.13: Left: Illustration of the bonded interactions. The bond stretching is harmonic in d , as are bond angles in Θ . The dihedral torsion angle ϕ is defined between the planes of the atom sets $(1,2,3)$ and $(2,3,4)$. For alkanes, the Ryckaert-Bellemans potential is used (right).

Once all forces acting on an atom are known, the Newtonian equations of motion are integrated in a Verlet-type leap-frog algorithm, where the next coordinates and velocities are calculated from the current coordinates $r(t)$ and vectorial forces $\mathbf{F}(t)$ as well as the velocities from the previous half-step:

$$v\left(t + \frac{\Delta t}{2}\right) = v\left(t - \frac{\Delta t}{2}\right) + \frac{\mathbf{F}(t)}{m} \Delta t \quad (3.24)$$

$$r(t + \Delta t) = r(t) + v\left(t + \frac{\Delta t}{2}\right) \Delta t \quad (3.25)$$

In this thesis, pressure and temperature are controlled with Berendsen-type [136] strongly damped exponential functions. The target conditions are set with T_0 and \mathbf{P}_0 and the scaling kinetics are controlled with the user-defined parameters τ_T and τ_P through:

$$\frac{dT}{dt} = \frac{T_0 - T}{\tau_T} \quad (3.26)$$

$$\frac{d\mathbf{P}}{dt} = \frac{\mathbf{P}_0 - \mathbf{P}}{\tau_P} \quad (3.27)$$

with the velocity scaling factor

$$\lambda = \left[1 + \frac{\Delta t}{\tau_T^*} \left\{ \frac{T_0}{T(t - \frac{\Delta t}{2})} \right\} \right]^{0.5} \quad \text{using } \tau_T^* = \frac{N_{df} k \tau_T}{2c_V}, \quad (3.28)$$

and the coordinate scaling matrix

$$\mu_{ij} = \delta_{ij} - \frac{\Delta t}{3\tau_P} \beta_{ij} \{P_{0,ij} - P_{ij}(t)\}, \quad (3.29)$$

where c_V is the system heat capacity, N_{df} is the total degrees of freedom, k is Boltzmann's constant, β is the isothermal compressibility of the system. Imprecise values e.g. for the compressibility affect the scaling, not the final conditions reached.

4 Materials and Experiments

4.1 Materials

Chemicals If not stated otherwise, chemicals were purchased from Sigma-Aldrich (Munich, Germany) and used without further purification.

Buffers For all aqueous solutions, water from a Millipore purification system ($\rho > 18 \text{ M}\Omega\text{cm}$, Millipore, Molsheim, France) was used. If not stated otherwise, experiments used phosphate buffered saline (PBS) at pH 7.5–8.0 with 10 mM NaH_2PO_4 and 100 mM NaCl .

Lipids The following lipids were purchased from Avanti Polar Lipids (Alabaster, Ala, USA) (see also Figure 4.1):

- 1,2-dimyristoyl-*sn*-glycero-3-phosphocholine (14:0, DMPC),
- 1,2-dipalmitoyl-*sn*-glycero-3-phosphocholine (16:0, DPPC),
- 1,2-di-O-hexadecyl-*sn*-glycero-3-phosphocholine (16:0, DHPC),
- 1-octadecanoyl-2-(9Z-octadecenoyl)-*sn*-glycero-3-phosphocholine (18:0-18:1, SOPC).

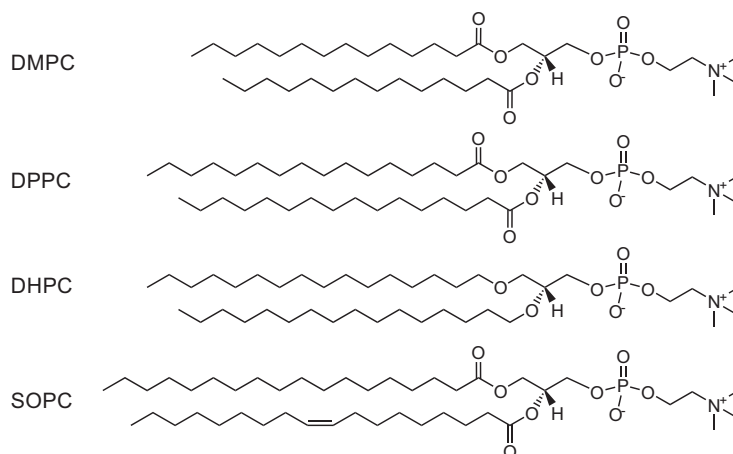


Figure 4.1: Structures of the two-chain phospholipids lipids used in this thesis.

Synthetic cyclic tetraether lipids were kindly provided by the group of Moto Shibakami (Institute of Biological Resources and Functions, AIST, Tsukuba, Japan), synthesized according to previously published protocols [137, 138]. The ether-linked lipids are based

on the 2,3-di-*O*-*sn*-glycerol backbone structure (see also Appendix A.1) The headgroups are either phosphatidylcholine (PC), an OH-group, or a sugar (glucofuranosid). The structures are shown in Figure 4.2.

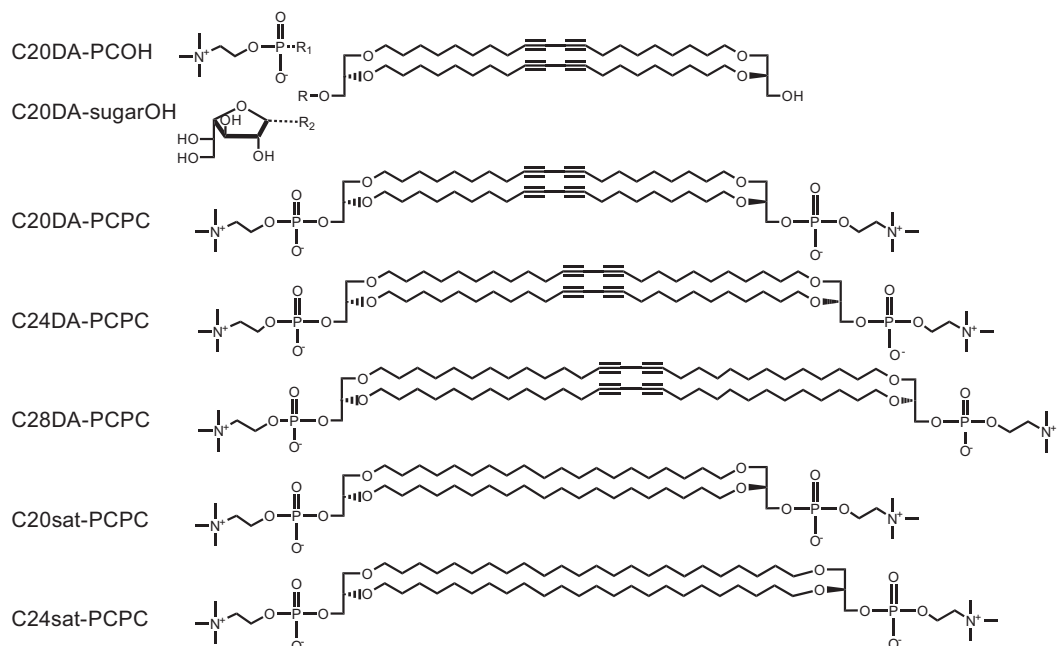


Figure 4.2: Structures of the synthetic cyclic lipids used in this thesis. Shown (from the top) are the asymmetric diacetylenic lipids C20DA-PCOH and C20DA-sugarOH, the symmetric diacetylenic lipids C20DA-PCPC, C24DA-PCPC, C28DA-PCPC, and the symmetric saturated lipids C20sat-PCPC and C24sat-PCPC. The “C” nomenclature refers to the number of carbon atoms per chain.

Fluorescent Dyes Fluorescent dyes were used in the form of the head-labeled lipids TexasRed-DHPE (Molecular Probes, Germany), Alexa Fluor 555 conjugated with streptavidin (Sigma-Aldrich, Germany), and TAMRA-SE for protein conjugation (Invitrogen, Germany). The absorption and emission maxima are listed in Table 4.1.

Table 4.1: Absorption and emission maxima of fluorescent chemical dyes used in this thesis. The listed values can vary depending on solvent, pH, conjugation, and proximity to other dyes. Values taken from company sources.

	Alexa Fluor 555	TAMRA	TexasRed
abs max [nm]	555	540	596
em max [nm]	565	565	615

4.2 Preparation of Samples

Substrates For optical fluorescence microscopy (including single-molecule fluorescence and FRAP) the used substrates were standard microscope cover slips ($24 \times 24 \text{ mm}^2$ or $24 \times 60 \text{ mm}^2$, Karl Hecht AG, Sondheim, Germany). X-ray reflectivity and GID experiments used silicon wafers covered with native oxide (SiMat, Landsberg am Lech, Germany) in a self-built liquid cell.

The standard cleaning procedure for substrates was by ultrasonication and rinsing in acetone, ethanol and methanol, and subsequently immersion in a solution of 1:1:5 (v/v/v) H_2O_2 (30 %) : NH_4OH (25 %) : water at 60 °C for 30 min (RCA standard clean 1) [139]. Finally, substrates were rinsed intensively with water and dried at 70 °C.

Substrates for single-molecule fluorescence experiments were additionally cleaned in an oxygen plasma for 2 min just prior to experiments.

Solid-Supported Membrane Preparation by Vesicle Fusion To prepare supported membranes by vesicle fusion, lipids were dried into thin films either under a stream of nitrogen or with a rotary evaporator, stored in vacuum overnight and then resuspended in water/buffer. Standard lipids suspensions were incubated at 40 °C for 2 h, then sonicated with a titanium micro-tip sonicator to form small-unilamellar vesicles (SUVs). Before use, the samples were centrifuged to remove titanium particles. The vesicle suspension was incubated on the sample for 1 h and afterwards the samples were vigorously rinsed with buffer.

For cyclic lipids with high melting temperatures, the vesicle suspension was first incubated at 70 °C for 2 h, and then on the glass or silicon substrates at 70 °C for at least 1 h. In general, the solubility of these long-chained ether lipids in water is low and resuspension of a dried film can be difficult.

Langmuir-Blodgett transfers [140] were performed on a self-built Langmuir trough with motorized lift and Wilhelmy sensor. Substrates were immersed and then lipids were spread on the subphase from chloroform solution, with >10 min allowed for solvent evaporation. The film was compressed to 30 mN/m, and then the substrates extracted under constant pressure conditions and left to dry in air. Bilayer membranes were formed from the monolayers by vesicle fusion as described above.

Solid-Supported Membrane Preparation by Solvent Exchange To prepare supported membranes by solvent exchange, the lipids were dried from chloroform, then dissolved in pure ethanol at 1 mg/ml. This mixture was then injected into a fluid cell containing the cleaned hydrophilic substrate. The solvent was then slowly exchanged for buffer using a peristaltic pump.

Solid-Supported Membrane Multilayer Stacks Oriented aligned multi-lamellar membrane stacks were obtained by spreading lipids from organic solvents on solid (silicon) substrates [141]. Approximately 1 mg of lipids was deposited on the substrates. These were placed in falcon tubes, dried overnight in vacuum, and then thermally cycled by

Table 4.2: Properties of Cy3/Cy5 and analog fluorescent chemical dyes from the Alexa Fluor and Atto series. The listed values can vary depending on solvent, pH, conjugation, and proximity to other dyes.

	Alexa 555	Alexa 647	Atto 550	Atto 647N	Cy3	Cy5
abs max [nm]	555	650	554	644	550	649
em max [nm]	565	665	576	669	570	670
ϵ [$\text{cm}^{-1}\text{M}^{-1}$]	150.000	239.000	120.000	150.000	150.000	250.000
QY [%]	10	33	80	65	4	28

exposure to alternatively 4 °C and 70 °C. These samples were used for X-ray and neutron reflectivity as well as GID.

Membrane Multilayers in Dispersion Multi-lamellar vesicles [29] in dispersion were used for SAXS/WAXS measurements. Aqueous lipid suspensions (pure water) with a concentration of ~ 20 wt % were filled into quartz capillaries (Hilgenberg, Malsfeld, Germany), centrifuged and flame-sealed. Measurements were performed after conducting several heating/cooling cycles to cancel the thermal history of each sample.

Reconstituted Prion Protein (PrP^c) Prion Protein (PrP^c) samples were kindly provided by M. Bärmann and M. Rusp (Lehrstuhl für Biophysik E22, Physik-Department, TU München). The purification protocol used is given in Appendix A.4. Reconstitution into DMPC vesicles did not control orientation. The PrP^c-vesicle samples for experiments were diluted with pure DMPC vesicles when needed for SDT experiments, or used directly otherwise. The vesicles were spread on glass substrates coated with lipid monolayers deposited by Langmuir-Blodgett transfer [140, 142] to improve upright protein orientation. SDT experiments were performed at $\sim 28^\circ\text{C}$ in the sample holder shown in Figure 4.5.

Surface-Immobilized Streptavidin Streptavidin conjugated with Alexa Fluor 555 was used to immobilize fluorescent dyes on a glass surface. First, the substrate was exposed to a bovine serum albumin (BSA) solution with 1% BSA-biotin (Sigma-Aldrich Germany) for 30 min, then vigorously rinsed with buffer. Streptavidin was then added in concentrations ranging from 1 nM to 10 pM, depending on the desired surface density. After a short incubation time (< 5 min) the samples were rinsed with buffer as the final step.

4.3 Optical Instruments

4.3.1 Single-Molecule TIRF Microscopy

The microscope setup developed for this thesis was based on through-the-objective TIRF (see Section 3.1) and is illustrated in Figure 4.4. The design allows it to be used either

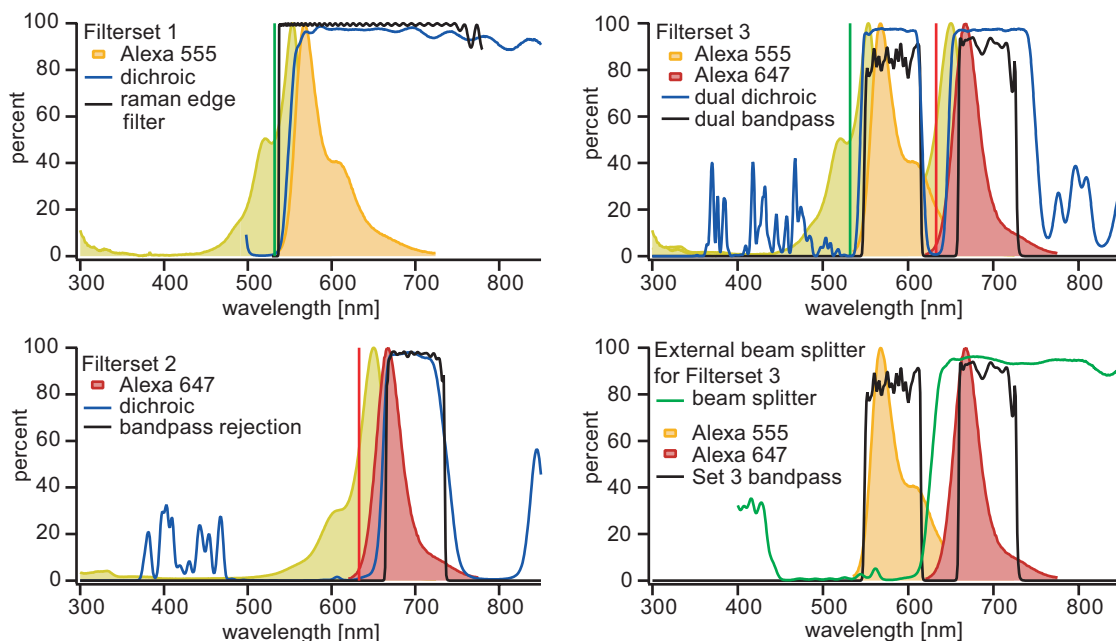


Figure 4.3: The spectra of the filter sets selected for the single-molecule fluorescence setup, optimized for single-molecule fluorescence microscopy using Cy3/Cy5 or analog dyes.

in a single-color or a dual-color mode of illumination and single or dual-imaging (see Figure 4.4).

The setup was assembled around a Zeiss Axiovert 200 main body with open rear illumination port (standard lamp removed) to couple in the free laser illumination beams from a 5 mW HeNe laser at 633 nm and an 80 mW 532 nm Nd:YAG laser. The lasers are expanded to approximately 2 cm diameter and combined at a dichroic mirror with ensuing iris aperture. Also at this stage the convergence of the expanded beam is adjusted to achieve focusing into the objective back focal plane (see Figure 3.1). Switching between epi-illumination and TIRF mode (including TIRF angle setting) is achieved with a shift/tilt mirror assembly before the microscope rear port.

As in a conventional inverted fluorescence microscope, the separation of excitation light and sample signal is made with a filter set in the standard filter cube revolver of the microscope. All filter sets were optimized for the widely used dye combination Cy3/Cy5 [105, 143], or modern analogs such as Alexa Fluor 555/647 and Atto 550/647N (see Figure 4.3 and Table 4.2). The dyes TRITC or TAMRA are spectrally similar to Cy3, while TexasRed is not suitable for these filter sets (see Table 4.1).

Images are recorded with a Peltier and water cooled EMCCD camera iXon BV887 (Andor, Dublin, Ireland) with 512×512 pixels. EMCCD (electron multiplying charge-coupled device) cameras [144, 145] possess an on-chip amplification stage before the analog amplification circuitry, in principle allowing the signal of a single photon to be lifted above the electronic noise floor. Cooling reduces the dark current to negligible levels.

A microfluidic sample environment was developed for use with SDT, shown in Figure 4.5. The main sample substrate is a 24 mm \times 60 mm glass coverslip ($d = 0.17$ mm) which

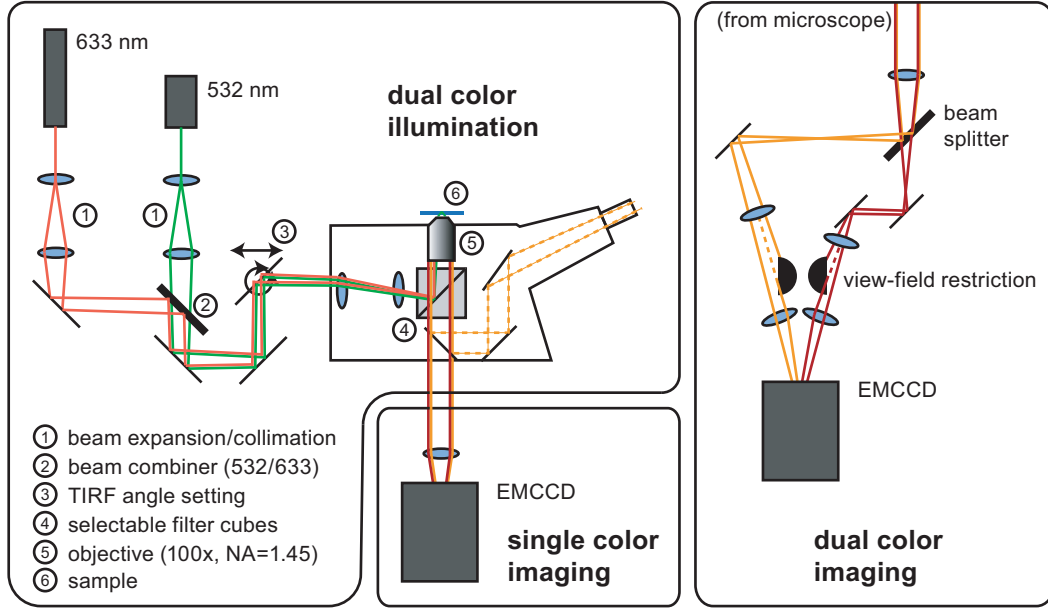


Figure 4.4: The microscope setup with single and dual color illumination (left) and either a single (bottom inset) or a dual color (right inset) imaging pathway. Illumination can also be switched between TIRF and wide-field epi-illumination.

forms the lower half of a “sandwich” with a parafilm spacer ($d \sim 0.1$ mm) and a microscope slide ($d = 1$ mm) cover. The parafilm spacer possesses a 40 mm \times 5 mm cut-out canal and is sealed to the glass by short heating to 70 °C. The reusable microscope slide cover has drilled holes ($\varnothing \sim 1$ mm) for connection to the tubing. The tubing is inserted tightly into hollow screws in the aluminium holder and pressed onto/over the microscope slide holes for contact and sealing. The sample holder in Figure 4.5 possesses a large cut-out viewing area for visual inspection from the sample backside (top). For temperature control a similar holder was used without viewing window, instead equipped with a Peltier element and embedded PT100 thermometer.

Single color imaging For single-color operation, the EMCCD camera is attached directly to the microscope body, thus using its full sensor area. There is a choice between excitation with either 532 nm (green) or 633 nm (red), with matching filter-sets for imaging using the full viewfield of the EMCCD camera directly attached at the microscope. The spectra of the filters and mirrors are shown in Figure 4.3. All filters and dichroic mirrors purchased from AHF Analysentechnik (Tübingen, Germany). Filter set (1) is suitable for 532 nm excitation and long-pass (orange to deep red) imaging. Filter set (2) is used for 633 nm excitation and band-pass (deep red) imaging. Without pixel binning, the image resolution is 245 nm/pixel.

Dual color imaging Two-color simultaneous imaging is possible with an external split-image pathway, spectrally separating the image and projecting side-by-side onto the camera sensor (see also Section 5.3.3). The filter set (3) in Figure 4.3 is a dual-illumination/dual-imaging bandpass set and is used in combination with an external

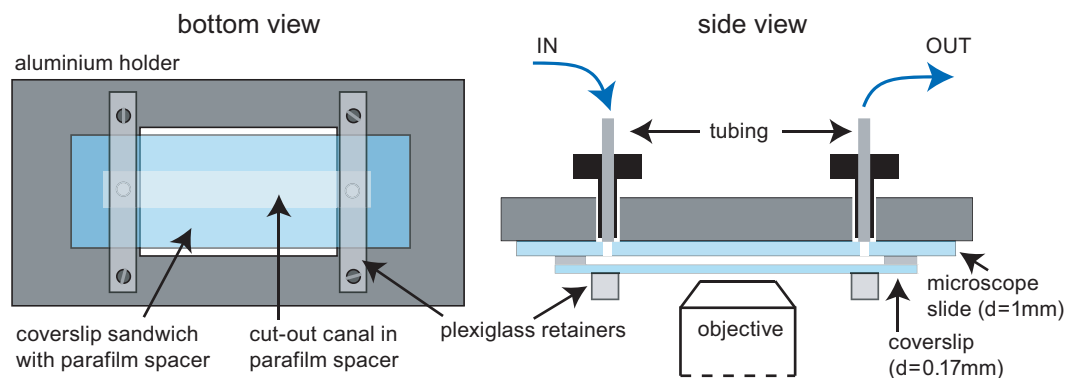


Figure 4.5: The microfluidic sample holder built for use with SDT. A parafilm spacer with cut-out canal creates the microfluidic channel between the coverslip substrate and the microscope slide covering. Full exchange of sample volume needs as little as $\sim 150\mu\text{l}$ (depending on connection tubing).

beam splitter (632 nm) to separate the optical paths of the color channels before projection onto the camera (see Figure 4.4). The alignment is performed so that for both colors the center of the full image is projected into the center of each image half on the camera. To prevent image overlap, optical blocks are inserted in the pathway at an optical plane conjugated with the image plane, so that the edges of each half-image are sharp (similar to the placement of a standard field aperture). This mode of operation allows simultaneous excitation with two lasers and imaging of two emission wavelengths for co-localization experiments, or excitation with the shorter wavelength only for FRET-type experiments [143]. The optical pathway allows additional magnification, so that the image resolution is $\sim 60\text{--}70\text{ nm/pixel}$ (without binning), depending on the exact optical alignment.

4.3.2 FRAP

Fluorescence recovery after photobleaching (FRAP) was measured with a self-built setup (Figure 3.5), also described previously [45, 146]. A wave-length selectable strong laser pulse (Ar-ion laser, Innova70C, Coherent) at $\sim 700\text{ mW}$ is used to bleach the sample for 200 - 500 ms through a pinhole and 100x oil-immersion objective (Fluar NA 1.3, Carl-Zeiss, Göttingen). The sample (e.g. supported membrane containing fluorescently labeled molecules) is bleached in a circular spot with a diameter of $9.3\mu\text{m}$. The recovery of the fluorescence signal by lateral diffusive exchange of bleached by unbleached molecules is observed with an attenuated beam ($\times 1/1000$) on a photomultiplier. The data fitting and evaluation is described in Section 3.4.

4.3.3 Epi-Fluorescence Microscopy

Epi-fluorescence images were taken on an inverted fluorescence microscope Axiovert 200 (Zeiss, Oberkochen) with standard fluorescence filtersets for TRITC and TexasRed, illumination was by a high-pressure mercury lamp (HBO 100, Osram). Image acquisition software was the custom program OpenBox (by J. Schilling, TU München).

4.4 X-Ray and Neutron Scattering Experiments

SAXS/WAXS SAXS/WAXS experiments were conducted at the A2 beamline at HASYLAB (DESY, Hamburg, Germany) using a photon energy of 8 keV (see also Section 3.6). For SAXS, data was recorded on a 2D detector and radially integrated. WAXS was recorded on a position-sensitive detector (PSD). Calibration was performed with well-defined reference samples (rat tail and tripalmitin). Sample capillaries were inserted into a temperature-controlled copper block to enable precise thermal scans. Waiting time between a temperature step and measurement was at least 1 min per degree of the step.

X-Ray Reflectivity and GID Specular reflectivity and GID measurements at the solid/air and solid/liquid interface (see also Section 3.5 and 3.7) were performed at the ID10B beamline at the European Synchrotron Radiation Facility (ESRF, Grenoble, France). Energy of the illumination was 22 keV ($\lambda = 0.56 \text{ \AA}$, $k = 11.2 \text{ \AA}^{-1}$). For GID, the incident angle was chosen at $\sim 80\%$ of the critical angle (see Section 2.2.3) and the signal was recorded using a Soller collimator with an angular resolution of $\Delta\delta = 0.05^\circ$ ($\Delta q = 0.02 \text{ \AA}^{-1}$).

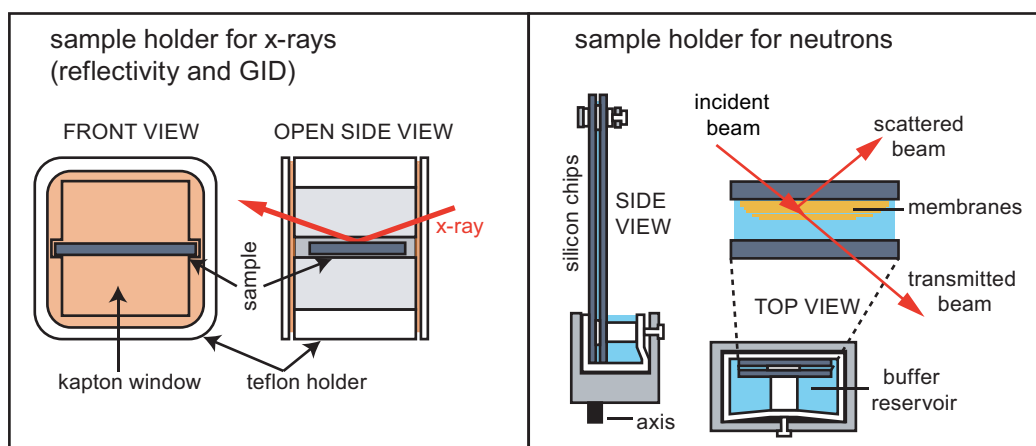


Figure 4.6: Sample holders used for X-ray and neutron scattering experiments.

Sample wafers were inserted into a self-built teflon fluid cell with kapton windows (see Figure 4.6). For experiments with membranes under bulk water, vesicle fusion was performed directly in this fluid cell (see also Section 4.2 for the general procedure). Samples with membrane multilayer stacks were prepared previously by drying from organic solvent, and inserted into the fluid cells (used as sample holders).

All samples were measured at ambient temperature ($\sim 22^\circ\text{C}$). Multilayer samples were measured either at high humidity or in ambient air. High humidity was achieved by inserting a water reservoir (wet tissue) into the sealed chamber and equilibrating for at least 30 min.

For evaluation of reflectivity curves the Motofit [147] software package was used, which implements a Parratt/Abelès formalism (see Section 3.5) with a genetic minimization

algorithm. Evaluation of GID data was performed based on the model described in Section 3.8 with self-written software.

Neutron Scattering Neutron scattering experiments were performed at the Institute Laue-Langevine (ILL, Grenoble, France) at the beamline D16 in cooperation with E. Schneck (Uni Heidelberg). The samples (silicon wafers with lipid multilayers) were inserted into the teflon holder (see Figure 4.6) in an upright position and placed in a climate chamber. For experiments under bulk water/buffer a wafer sandwich was used as shown in Figure 4.6 which provided wetting by capillary forces.

4.5 MD Software and Simulations

Force fields and Software The OPLS-based united-atom lipid force field and DPPC topology used here (dppc.itp and lipid.itp, [148]) was developed in the works of Berger *et al.*, Chiu *et al.*, and Tieleman *et al.* [149–152] and used here with the ffgmx force field and TIP3P water. Simulations were run with Berendsen anisotropic pressure coupling, and selected runs with surface tension coupling did not show significant differences. Temperature was coupled with the Berendsen thermostat. To reduce calculation time, H-angle restraints and a time step of 0.004 ps was used. Electrostatics were treated with PME, where passing the parameter *-rcon 1.0* to *mdrun* ensures sufficient minimal decomposition cell size.

Simulations were performed with the free GROMACS software package, version 4 (pre-release version 200800503 and version 4.0.3) [121–128]. Selected runs were compared with version 3.3.3 without finding any differences. Evaluation of the simulations was performed with the GROMACS toolset and self written scripts.

Starting Systems For all gel phase construction methods, a small membrane block with 32 lipids in a bilayer configuration was made as a starting point. For each monolayer, an energy-minimized upright single lipid was multiplied on a hexagonal lattice with random rotations around the z-axis. This system was then hydrated with GROMACS tools and afterwards misplaced water was removed, with at least 35 water molecules per lipid remaining. If required, modified topologies were used for initial system equilibration as described in the text (Section 7.3.1). In all cases, the 32 lipid building blocks were equilibrated for 20 ns at 270 K with the original unmodified topology and then multiplied into 288 lipid systems ($3 \times 3 \times 32$). These were equilibrated for another 25 ns, and finally evaluated for another 25 ns. Heating scans were performed by single continuous annealing runs, with rates as described in the text.

3D-Autocorrelation The 3D autocorrelations were calculated using a linear overlap function going to zero at a radius of 0.15 nm. With this function, the overlap from each atom in the reference dataset to each atom in the (dx,dy,dz)-displaced dataset is measured. Overlap values are summed for each (dx,dy,dz) and normalized. The autocorrelation software was written in C using the MPI framework and was run on the

large compute clusters where the scaling was nearly 100%. The maps were evaluated with self-written scripts.

Computing Hardware The runs were performed on HELICS II (IWR, Universität Heidelberg) and the Heidelberg cluster of the bwGRiD initiative. HELICS II uses 4-CPU nodes with AMD quad-core Opterons at 2.8 GHz and 10G Myrinet, while bwGRiD uses 8-cpu nodes with 2×Intel Xeons at 2.83 GHz and Infiniband interconnects. Systems with 288 lipids could be run at approximately 80 ns/day using 64 CPUs.

5 Diffusion of Membrane-Anchored Prion Protein

5.1 Introduction

The power of single-particle tracking (SPT) lies in its ability to reveal information hidden in ensemble measurements like FRAP, such as the presence of subpopulations or obstacles in membranes (see also Section 3.2). In an early seminal study, kinesin motors labeled with fluorescent beads could be tracked in live cells [153]. In another pioneering study, the diffusion of individual lipids carrying single rhodamine dyes was studied in supported membranes [101, 154]. Recently, SPT has been used for many *in vivo* studies of diffusion in cell membranes [82, 86, 92, 155–157]. For a good overview of SPT in membranes see also [52] and references therein.

In this chapter, the lateral diffusion of individual GPI-anchored bovine prion proteins (PrP^c) in supported model membranes is studied by single-molecule fluorescence. To minimize the influence of labeling, the prion proteins were conjugated with single chemical dyes (TAMRA) rather than brighter but larger labels such as quantum dots [102]. Therefore, the term single-dye tracking (SDT) is used, rather than the generic term SPT. In a previous study, solid supported membranes were established as a tool to investigate PrP^c diffusion [142]. There, a protocol using pre-deposited lipid monolayers on planar glass substrates was designed which enabled a protein mobile fraction of $> 90\%$ when spreading vesicles containing PrP^c (see Figure 5.1). This strategy is also applied in this thesis for studies of PrP^c at the level of single molecules.

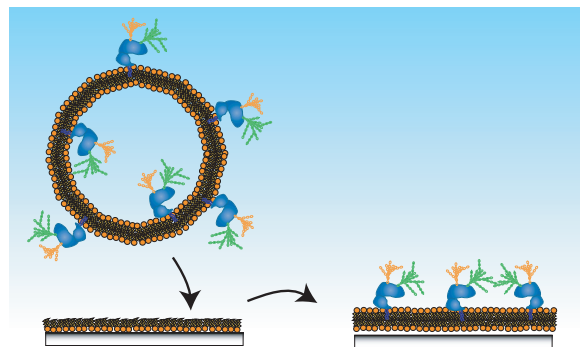


Figure 5.1: Preparation of PrP^c in supported membranes. The PrP^c containing liposomes are spread on a monolayer of lipids, pre-deposited on the solid support by a Langmuir-Blodgett transfer [140] from an air-water interface. As established in a previous study [142], this monolayer helps to achieve an upright orientation of PrP^c in the supported bilayer membrane. The lateral density of the PrP^c is adjusted to be low enough for resolution of single proteins.

A novel simulation-based method is developed for the analysis of the experimentally obtained distribution of diffusion coefficients D . This quantitative method aims to separate the influence of statistical scatter (inherent in random walks) from the influence of sub-populations or variations in the physical properties of the diffusing particles. In contrast to previous simulations of random walks [107, 108], this new approach is directly applicable to actual experimental results.

Even with modern camera technology (electron multiplying CCD, EMCCD [158]) and laser illumination, single-dye tracking is still a very challenging proposition. Thus, for the experiments in this thesis a dedicated TIRF microscope setup (see Section 3.1) was constructed and optimized for single-dye tracking in solid-supported membranes, together with the necessary specialized video analysis and particle tracking software. As a further technical challenge, a two-color single-molecule colocalization microscope is developed (see Section 5.3 and Section 4.3.1). Here, the major target is to achieve a colocalization accuracy by image registration which matches or surpasses the localization accuracy of the individual molecules which is on the order of ~ 20 nm.

5.2 Single Dye Tracking (SDT) of Membrane-Anchored Prion-Protein (PrP^c)

5.2.1 SDT Results

The (low) density of PrP^c in the supported membranes was optimized for single-molecule tracking. The PrP^c were labeled with the chemical dye TAMRA (see Appendix A.4) at a ratio of approximately one labeled in four unlabeled proteins. Indeed, experimental traces did not show multiple bleaching events, confirming the observation of single dye fluorescence (see Figure 5.2).

The setup used was the one-color configuration as described in Section 4.3.1, using excitation at 532 nm. The evaluation of the individual traces was performed as *internal averaging over all pairs* as described in Section 3.3. To treat all data uniformly, the maximum time difference used was $\Delta t \leq 1$ s, corresponding to 20 frames, and the minimum trace length for inclusion was 1 s. Traces of obviously immobile particles were discarded. An example trace and its internally averaged mean square displacement (MSD) are shown in Figure 5.3.

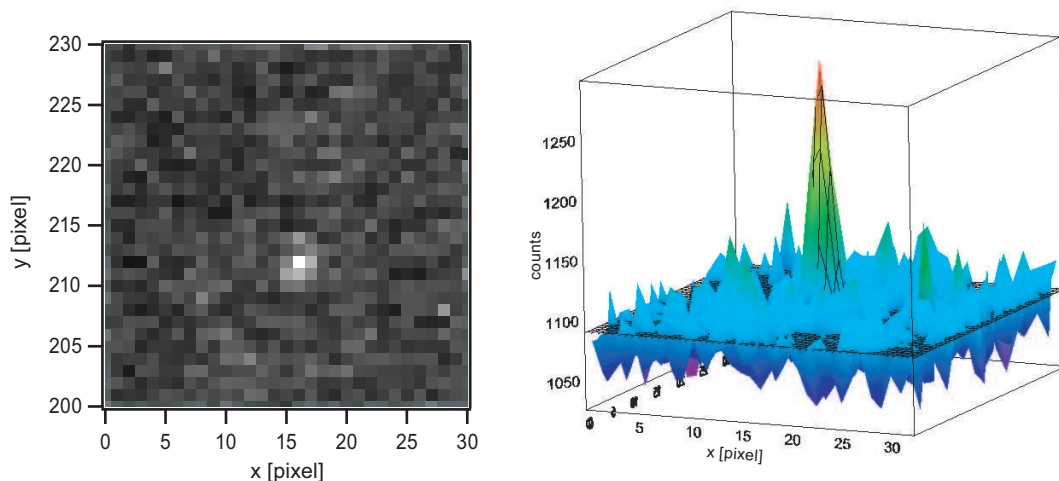


Figure 5.2: Left: An experimental video frame containing a single TAMRA-labeled PrP^c molecule. Under the experimental conditions the signal of the single dye can be clearly separated from the background noise. Right: 3D representation of the video frame. The peak is fitted with a 2D-Gaussian to localize its center position.

The distribution of the experimentally obtained diffusion coefficients for 50 traces is shown in Figure 5.4A. A Gaussian fit to the data is also shown, which is centered at $0.84 \mu\text{m}^2/\text{s}$ with a width (Gaussian standard deviation) $w_{\text{data}} = 0.42 \mu\text{m}^2/\text{s}$. In Figure 5.4B the distribution of trace lengths is shown. The length of traces is of course limited by bleaching (exponential in time). The center of the distribution lies slightly below the value obtained by FRAP ($D_{\text{FRAP}} = 1.6 \mu\text{m}^2/\text{s}$, see [142]), but the match is satisfactory considering the statistical deviations for this sample size and the strongly differing techniques.

Furthermore, the average ensemble displacement was calculated by using all available

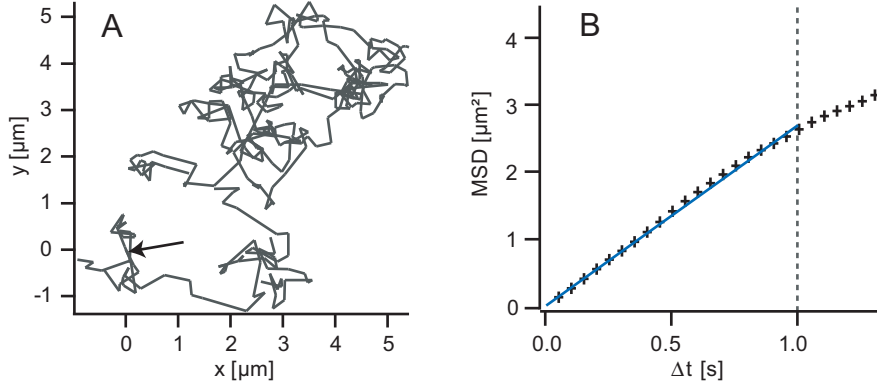


Figure 5.3: A) An example PrP^c diffusion trace over 20 s. The start of the trace is indicated by an arrow. B) The MSD of the trace (averaged over all pairs) and a linear fit. For all traces the linear fit was limited to below 1 s to exclude scatter by long-range fluctuations. In this example, the diffusion coefficient from the fit was $0.7 \mu\text{m}^2/\text{s}$.

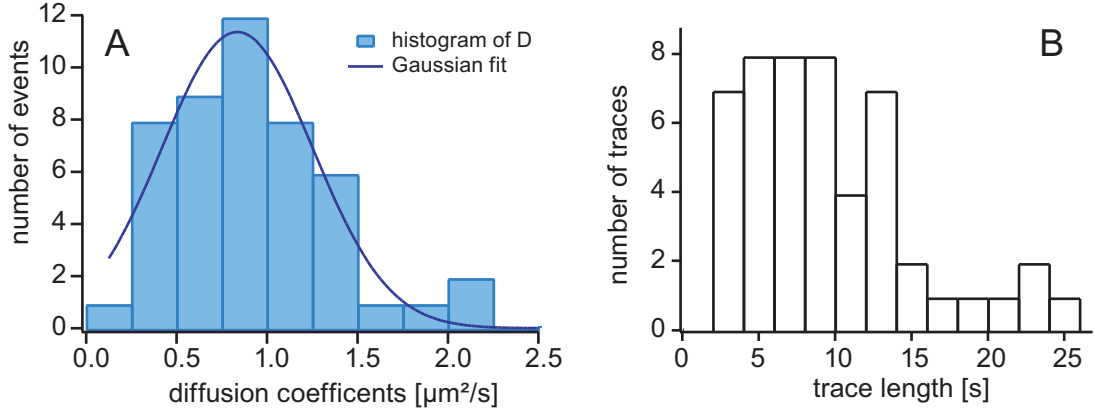


Figure 5.4: A) Distribution of diffusion coefficients calculated from 50 PrP^c traces. The Gaussian fit is centered at $D = 0.84 \mu\text{m}^2/\text{s}$ with a width of $w_{data} = 0.42 \mu\text{m}^2/\text{s}$. B) Distribution of experimental trace lengths.

displacements from the experimental traces to construct a single MSD curve (see Figure 5.5). For consistency this curve is evaluated for $\Delta t < 1$ s. A power-law fit to the ensemble average MSD for $dT < 1$ s has an exponent $\gamma = 0.96$, indicating almost no sign of sub-diffusion for these time (\sim s) and length (\sim μm) scales. Moreover, a linear fit to times smaller than 1 s (not shown) results in an ensemble diffusion coefficient of $D = 0.97 \mu\text{m}^2/\text{s}$, which agrees well with the center of the distribution of individual coefficients.

5.2.2 Simulation-Based Analysis of the Diffusion Coefficients

As stated above, a central aim in the study of PrP^c was to separate the inherent statistical scatter of diffusion coefficients of single molecule random walks from the actual presence of sub-populations or other molecular variations. The effects encountered in this study were seen to be subtle, necessitating very careful analysis. In this section a

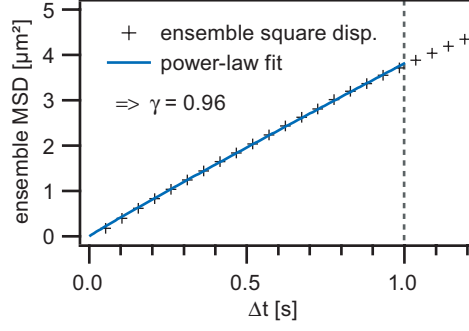


Figure 5.5: A power-law fit ($\sim t^\gamma$) to the ensemble MSD for times up to 1 s returned an exponent of $\gamma = 0.96$, which indicates free diffusion ($\gamma_{free} \equiv 1.0$) within one standard deviation accuracy (see text for derivation of the accuracy).

simulation-based method is developed to quantitatively analyze the scatter in experimental single molecule diffusion traces, taking effects such blinking and bleaching into account.

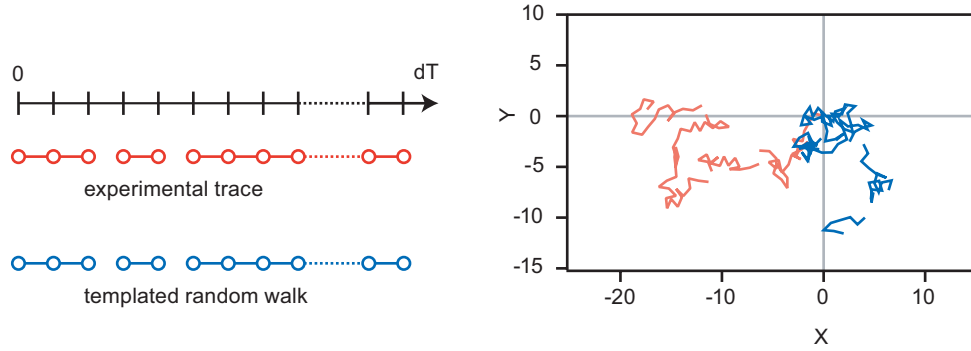


Figure 5.6: Illustration of templated computer generated random walks (tCGRW). Left: The tCGRW is matched to an experimental trace in length and gaps. Right: The tCGRW random walk is of course different from the experimental trace, but matches its relative statistical weight in a whole set.

Non-Uniform Population is Necessary to Explain the Experimental Data. As discussed in the literature [107, 108] and in Section 3.3 of this work, the distribution of D depends strongly on the method of evaluation. For ideal random walks of identical length and number of steps, it is possible to calculate the variance (standard deviation) for the displacements at time t as well as for the width of the distribution of D . However, experimental data are not ideal random walks. Traces can lack intermediate steps due to blinking [159] or failed position acquisition and traces lengths will be unequal. For example, a single long trace has a statistically better defined D than a short trace (due to more contributing displacement pairs), but in a simple distribution histogram of D both would have the same weight. Consequently, the expected width of the distribution of D is undefined when based on a set of traces with an undefined length distribution. In this case, one would not be able to decide easily whether an experimental distribution is composed of differing sub-populations or not.

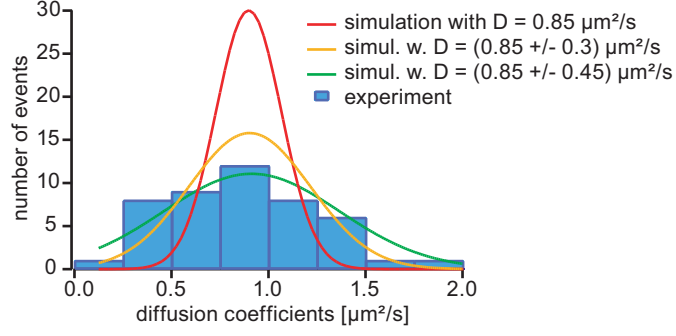


Figure 5.7: Distributions of D compared from different simulations for uniform populations, and for populations including a spread of physical D , superimposed on the experimental data.

To resolve this situation the experimental data can be compared to computer-generated random walks (CGRW) modeled to match the experimental traces in their statistically relevant properties. This is achieved by “templating” the set of CGRW on the experimental trace set. Each CGRW is matched directly to an experimental trace regarding its length and defects/gaps. This is achieved easily by generating a set of CGRW of maximum needed length, and then modifying each by deleting time points not available in its experimental data template (see Figure 5.6). These templated CGRW (tCGRW) are then evaluated in exactly the same fashion as the data traces to deliver a distribution of D . Running a set of tCGRW multiple times gives an estimation of the statistical fluctuations of the distribution of D .

The PrP^c data were then compared with such simulations. As described above, multiple runs were performed with templated simulation sets using exactly the central value of the data fit $D_{center} = 0.85 \mu\text{m}^2/\text{s}$ for each individual diffusion coefficient in generating each random walk (making a uniform population), and the parameters for Gaussian fits to the D distributions of these runs were averaged to give the final results of the simulation. The simulation distribution for a uniform population is shown as the red curve in Figure 5.7 and it is seen that it is significantly sharper than the experimental distribution ($w_{sim} \sim 0.17 \mu\text{m}^2/\text{s}$ compared to $w_{data} \sim 0.42 \mu\text{m}^2/\text{s}$). Immobile obstacles and pinning centers in the membrane are not likely the cause, since FRAP experiments confirmed that almost all PrP^c molecules are freely diffusive. In fact, according to the theoretical framework [107], the presence of obstacles would sharpen the distribution of D and shift the distribution to lower values. Also, the ensemble diffusion exponent ($\gamma = 0.96$) did not indicate any significant subdiffusion.

Having demonstrated that a uniform population cannot reproduce the experimental data, a population spread is introduced (PrP^c modeled as non-uniformly diffusing particles). This is accounted for by introducing randomly selected per-particle diffusion coefficients D_{part} . The functional shape of the population spread is chosen as Gaussian as there are no obvious sub-peaks indicating sharply separated sub-populations and there is no basis for any specific other functional shape. The probability distribution of D_{part} is centered at D_{cen} with a standard deviation w_{pop} . In the simulations, each random walk was generated with a random D_{part} selected from this probability distribution.

Such templated simulations with population spread were compared to the experimental PrP^c data. It is seen that the simulations match the experimental data best with $D_{cen} = 0.85 \mu\text{m}^2/\text{s}$ and $w_{pop} = 0.45 \mu\text{m}^2/\text{s}$. This means that indeed fast and slow proteins were observed, and not just statistical scatter. Based on these results, it can be concluded that the population of PrP^c was not uniform.

Statistical Uncertainties and Justification of $N=50$ Traces. In the simulations some variation is present from run to run (each with $N = 50$ random walks), i.e. under identical starting conditions Gaussian fits to the histograms (per run) of simulated D will have an error bar/standard deviation both for its central value D_{cen} and its width w_{pop} (area under curve is kept constant $\equiv 1$). By performing many runs of tCGRW sets (i.e. many times 50 tCGRWs), the standard deviation for the properties (center and width) of the distribution of D for the specific tCGRW set can be determined.

As stated above, for the case of PrP^c the experimental distribution of D was best matched by simulations using $D_{cen} = 0.85 \mu\text{m}^2/\text{s}$ and $w_{pop} = 0.45 \mu\text{m}^2/\text{s}$. Exploring this aspect, it was seen that when fitting the distributions of D from simulations made with $D_{cen} = 0.85 \mu\text{m}^2/\text{s}$ and $w_{pop} = 0.45 \mu\text{m}^2/\text{s}$, the center of the fit $D_{simfit,cen}$ had a standard deviation of $\sigma_{cen} = 0.14 \mu\text{m}^2/\text{s}$, and the width had a standard deviation of $\sigma_{width} = 0.10 \mu\text{m}^2/\text{s}$.

Performing the analogous simulations using spreads of $w_{pop} = 0.35 \mu\text{m}^2/\text{s}$ and $w_{pop} = 0.55 \mu\text{m}^2/\text{s}$ showed that the experimental distribution width was also within one standard deviation of the widths using these population spreads. From this observation a rough estimation of the precision of proposed population spread was made as $\sigma_{pop} = (0.55 - 0.45) \mu\text{m}^2/\text{s} = 0.1 \mu\text{m}^2/\text{s}$ (not to be confused with σ_{width} which describes the error of the width of the distribution of D). Therefore, using these results as an error approximation one can conclude that $w_{pop} = (0.45 \pm 0.10) \mu\text{m}^2/\text{s}$. This again strongly excludes $w_{pop} = 0$.

These standard deviations obtained above (σ_{cen} and σ_{width}) are the correct error bars for a set of traces modeled exactly like the experimental PrP^c dataset. Thus, applying these results to the data gives an error margin for the center and width of the fit to the experimental distribution of D , so that one can state that $D_{data,cen} = (0.84 \pm 0.14) \mu\text{m}^2/\text{s}$ and $w_{data} = (0.42 \pm 0.10) \mu\text{m}^2/\text{s}$.

In a directly analogous fashion, evaluating the ensemble properties of the simulations with power-law fit to the ensemble average resulted in $\gamma_{sim} = 0.98 \pm 0.1$. For PrP^c, the experimental power law exponent of the ensemble MSD (see Section 5.2.1) can be thus endowed with the error estimation of $\gamma = 0.96 \pm 0.1$, confirming free diffusion for $\Delta t < 1 \text{ s}$ within one standard deviation error margin.

Finally, an important question is whether the distribution of D is already well-defined and “stable” for $N = 50$ traces. On the one hand, as seen from the discussion above, the number of $N = 50$ traces was sufficient to discriminate the random walks of a uniform free population from a non-uniform population. The error for the width of the distribution $\sigma_{width} = 0.10 \mu\text{m}^2/\text{s}$ is quite small and sufficient for most purposes. But on the other hand, the relative error is in fact $\sim 25\%$ of the experimentally observed width $w_{data} = 0.42 \mu\text{m}^2/\text{s}$. Thus, depending on the accuracy necessary for any specific

statement or conclusion one wishes to make, the number of $N = 50$ might need to be increased or at least checked for sufficiency using simulations.

5.2.3 Discussion

In a previous study [142], FRAP measurements excluded significant contributions of immobile obstacles and pinning centers for the used preparation protocol. Also, they showed an unusual pH dependency of the PrP^c diffusion coefficient (ranging from $1.1 \mu\text{m}^2/\text{s}$ to $1.8 \mu\text{m}^2/\text{s}$ from pH 5 to pH 8.5). Interestingly, in 2D-electrophoresis experiments, the accumulation of mobile PrP^c molecules under an electric field against a barrier in the supported membrane did not result in an exponential concentration profile. Even after long times a linear shape was retained, possibly indicating that the implicit assumption of a uniform population of diffusing particles was not fulfilled. These previous observations match the non-uniform population observed by SDT.

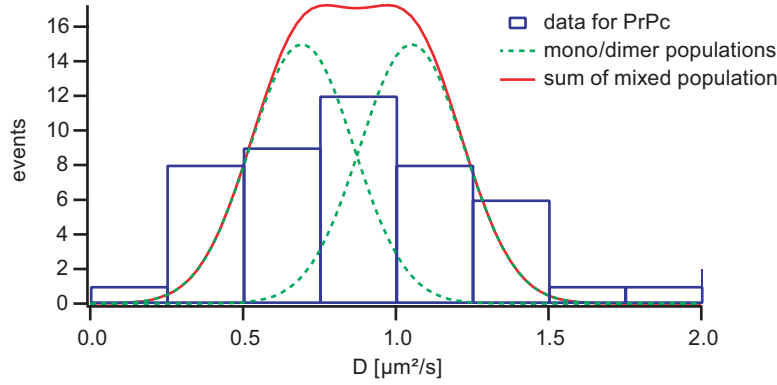


Figure 5.8: Hypothetical distribution of D from a mixed population of PrP^c monomers and dimers, superimposed on the experimental data. The diffusion coefficients used here ($D_{\text{dimer}}/D_{\text{monomer}} \approx 0.67$) are estimated using free volume theory. The combined width ($w_{\text{mixed}} = 0.3 \mu\text{m}^2/\text{s}$) of such a mixed population does not fully match the experimentally observed distribution width ($w_{\text{data}} = 0.42 \mu\text{m}^2/\text{s}$).

One scenario to consider is the formation of dimers of PrP^c [67] or larger aggregates. As discussed in Section 2.1.2 lateral diffusion coefficients are sensitive to the frictional drag experienced by a particle in a lipid membrane [160]. In case of transmembrane proteins and lipid-anchored proteins, their diffusion coefficients are considered to be dominated by the radius r of the segments immersed in the viscous hydrocarbon chain region. Very roughly, two anchor lipids instead of one results in approximately twice the anchor area and $\sqrt{2}$ times the monomer radius r . However, commonly used hydrodynamic continuum theories such as Saffmann-Delbrück cannot be directly applied to the friction of individual lipid anchors in a lipid membrane. Considering free-volume theory (Section 2.1.2.1) and assuming a constant activation energy, an upper limit estimate for the critical free area of a dimer is two times the critical free area of a monomer, $a_{\text{dim}}^* = 2a_{\text{mon}}^*$. Galla *et al.* [79] have used $\gamma a^*/a_f = 0.4$ for DPPC, and using this value Equation 2.5 then predicts

$$\frac{D_{\text{dimer}}}{D_{\text{monomer}}} \approx 0.67 \quad (5.1)$$

From this qualitative estimation one would expect a mixed monomer/dimer populations of diffusing particles to have diffusion coefficients of approximately $D_{monomer} = 1.0 \mu\text{m}^2/\text{s}$ and $D_{dimer} = 0.7 \mu\text{m}^2/\text{s}$ if their average value is to match the center of the experimental PrP^c distribution of $D_{data, cen} = 0.84 \mu\text{m}^2/\text{s}$. The sum of their distributions of D as shown in Figure 5.8 would have a width broadened to $0.3 \mu\text{m}^2/\text{s}$, which is less than the distribution width seen in the PrP^c data ($w_{data} = 0.42 \mu\text{m}^2/\text{s}$). Furthermore, the distribution of D sum of two such well-defined populations with diffusion coefficients separated far enough to fully match the experimental distribution width (not shown) would also have a distinct minimum between their respective probability maxima (which is not evident in the data).

In the previous estimations the hydrodynamic drag of the protein in the aqueous buffer was considered small against the drag in the highly viscous membrane. However, taking this extra hydrodynamic influence into account makes it plausible to attribute the observed scatter to large variations in glycosylation occurring in native (i.e. not recombinant) proteins, since such variations should also modify the effective hydrodynamic radius of the PrP^c moiety immersed into the solvent. As supporting evidence for the existence of PrP^c molecular variations, the previously obtained electrophoretic steady state concentration profile of PrP^c [142] suggests that PrP^c molecules might possess non-uniform net charges, attributed to different degrees of glycosylation. Although the exact molecular origin of differences in diffusive behavior cannot be concluded, the presented single-molecule experiments allow much more detailed investigations than ensemble measurements.

5.3 Construction of a Two-Color Dual-Imaging TIRF Microscope

5.3.1 Target Application of Instrument Design

The setup for single-molecule fluorescence microscopy as developed in this thesis is described in detail in Section 4.3.1. It allows simultaneous imaging of the fluorescent dyes Cy3/Cy5 (or analogs) in two color channels (see Figure 5.14 on page 59 for an example). Such a setup can have multiple uses, these mainly being single molecule colocalization or FRET.

In FRET (fluorescence energy resonance transfer, see [143] for an introduction), the observation of emission from the acceptor dye is a very strong indicator of very close proximity (< 10 nm) to the donor, and thus between their carriers, e.g. the receptor/ligand pair. However, single molecule FRET experiments can be difficult to perform due to many problematic factors such as the difficulty in performing exact site-specific labeling of proteins.

Without using FRET, one can perform colocalization of dyes by observing their position in two color channels and calculating the distance between them [105, 161–163]. In order to gain knowledge about the relative position between two fluorophores observed in two different camera color channels one has to first perform image registration. In single molecule colocalization for biological purposes the relevant length scales are on the order of nanometers, and with image resolutions on the camera of ~ 100 – 500 nm/pixel the image registration has to provide subpixel accuracy. In this thesis, a simple method to perform image registration is developed with very high accuracy on the order of 10 nm.

5.3.2 Localization Accuracy and Noise

As discussed in Section 3.2, background noise and sample emission statistics are the fundamental limitation in single molecule localization microscopy. Here, some basic experiments are performed to characterize the background, noise and localization accuracy of the setup.

Noise and background are best defined by the average signal and the fluctuation of single pixels over time. The pixels used for evaluation should be representative of the actual background (e.g. free from fluorescent sample). The intensity over time yields an average value which is taken as the background signal level, and a standard deviation which is taken as the (single pixel) noise level. The thresholding parameters used to detect particles are then based on these values. Contributions to the background are ambient light, detector noise (dark current, amplification, etc), sample autofluorescence, and direct laser signal due to imperfect filters and dichroic mirrors.

The dependency of background signal and noise on laser power for a blank glass sample in water is shown in Figure 5.9 (left), using the dual-imaging mode (separated orange and deep red channels). The relative laser power is set with the aid of (imperfect) rotating polarizers, so that in practice the relative power of 0.0 does not correspond to absolute zero transmitted laser power. It can be clearly seen that excitation with

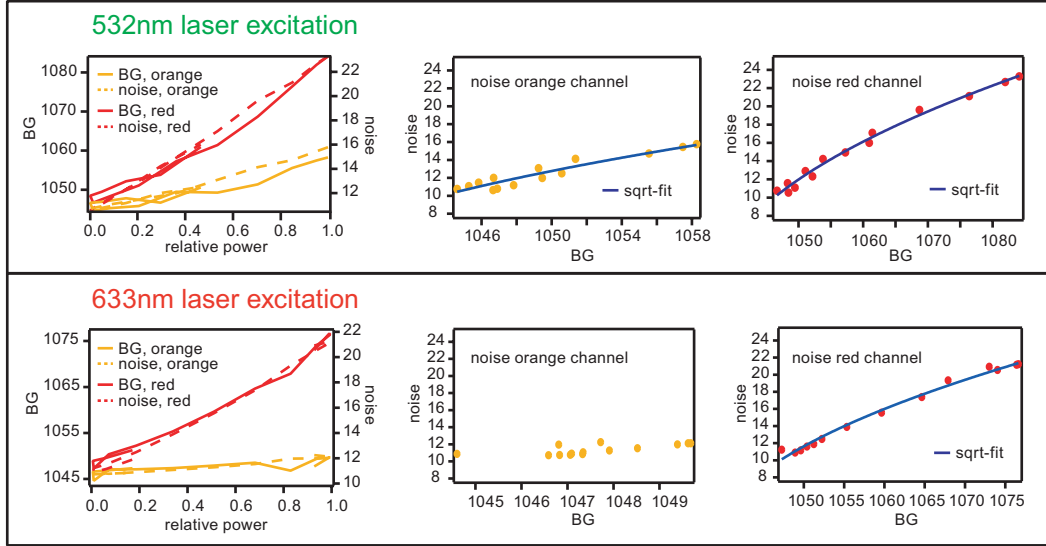


Figure 5.9: Background level (BG) and noise for the dual-imaging setup characterized for excitation at 532 nm (top) and 633 nm (bottom), with a blank glass sample under water. Top/Left: Excitation at 532 nm leads to a noticeable background in the orange channel, and a strong background in the red channel. Bottom/Left: Excitation at 633 nm has no significant background in the orange channel, but strong background in the red. These observations can be explained by red-shifted glass autofluorescence. Middle and Right: The dependency of the noise on the background signal (with a constant offset) follows a square-root function.

532 nm leads to a noticeable background in the orange channel and a strong background in the red channel. Excitation with 633 nm leads to a comparable background in the red channel but no significant background in the orange channel. There is a dark current offset of ~ 1000 counts which is intrinsic to the CCD readout. When glass/sample autofluorescence is the major contributor to the observed background signals, the noise will be dominated by the statistical fluctuation of number of photons received per time and pixel. For a higher signal, i.e. number of photons/s, a square-root dependency is expected for a normally distributed property. This is also illustrated in Figure 5.9 (center and right), where fits using a square-root function match the trend of noise plotted over background well.

In Figure 5.10 the trace of an immobilized particle over time is shown, recorded in the dual-imaging setup with high resolution on the CCD (~ 128 nm/pixel at 2×2 pixel binning). Besides photon emission/detection fluctuations, other factors such as sample drift or setup vibrations also contribute (see Section 3.2). The standard deviation of the radial displacement was $\delta \sim 20$ nm (defined as the localization accuracy), which is a typical value for signal levels obtained with chemical dyes. The average width of the Gaussian fits in this example was $w_\sigma = 120$ nm, equivalent to the first minimum of the Airy disc being at $R_{\text{airy}} \sim 350$ nm. The minimum attainable ideal Airy disc would be expected to have a radius $R_{\text{airy,ideal}} = 0.61\lambda/NA = 0.61 \times 565\text{nm}/1.45 = 238$ nm, which points towards minor focus or alignment issues.

A systematic investigation of the localization accuracy δ was performed for the single-color configuration, which has a CCD resolution 245 nm/pixel resolution without bin-

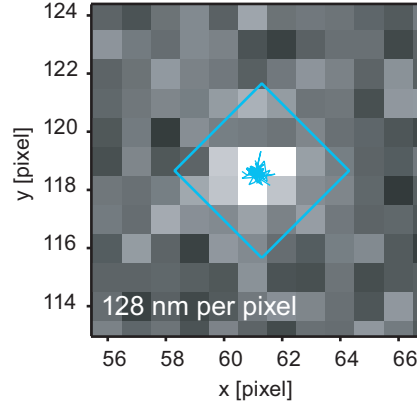


Figure 5.10: The trace of an immobile particle illustrates the typical localization accuracy δ . The image resolution on the CCD was 128 nm per pixel (using 2×2 pixel binning). The immobile particle (surface-adsorbed streptavidin labeled with Alexa Fluor 555, emission maximum at $\lambda = 565$ nm) was traced over 100 frames (5 s) and localized by 2D Gaussian fits, revealing the standard deviation of the displacement to be $\sigma_{pos} = 19.4$ nm. This is defined as the localization accuracy.

ning. The results are shown in Figure 5.11 for 1×1 binning (top) and 2×2 binning (bottom). The wide range of the SNRs stem from the fact that the surface-adsorbed particles (streptavidin) can carry between one and four fluorescent dyes. Laser power was set with a rotating polarizer, and approximately 25 traces were recorded per setting.

The case of 1×1 binning (245 nm/pixel) is shown in Figure 5.11(top). The functional form of the the accuracy δ plotted over the SNR (Figure 5.11, left) and over relative laser power (Figure 5.11, right) is predicted by the Equations 3.2 and 3.1 on page 19, but the spread is too large to distinguish between the two. The accuracy δ increases with SNR as well as with laser power, and the average localization accuracy at maximum laser power was (27 ± 7) nm. The large spread in accuracy for the lowest laser power indicates that the lowest limit for particle localization is $\text{SNR} > 2$.

Different observations were made for the case of 2×2 binning (490 nm/pixel, Figure 5.11, bottom). While the shape of the distribution of accuracy over SNR appears similar, the spread for a given relative laser power is larger. Most strikingly, the maximum localization accuracy does not increase with increasing laser power, there appears to be a hard limit around $\delta \sim 60\text{--}70$ nm. The limit is imposed by the large pixel size of 490 nm compared to the expected Airy disc diameter of 250 nm. Not surprisingly, if high localization accuracies are required in an experiment, the pixel size (resolution of the image on the CCD) must be smaller than the diffraction limited spot size.

5.3.3 Image Registration for Two-Color Co-Localization Microscopy

5.3.3.1 Introduction to Image Registration

Image registration in a technical or medical imaging context is separated into several steps, including feature detection and feature matching with a custom mapping function. The mapping can be rigid, affine or arbitrarily complex, and it can be global or

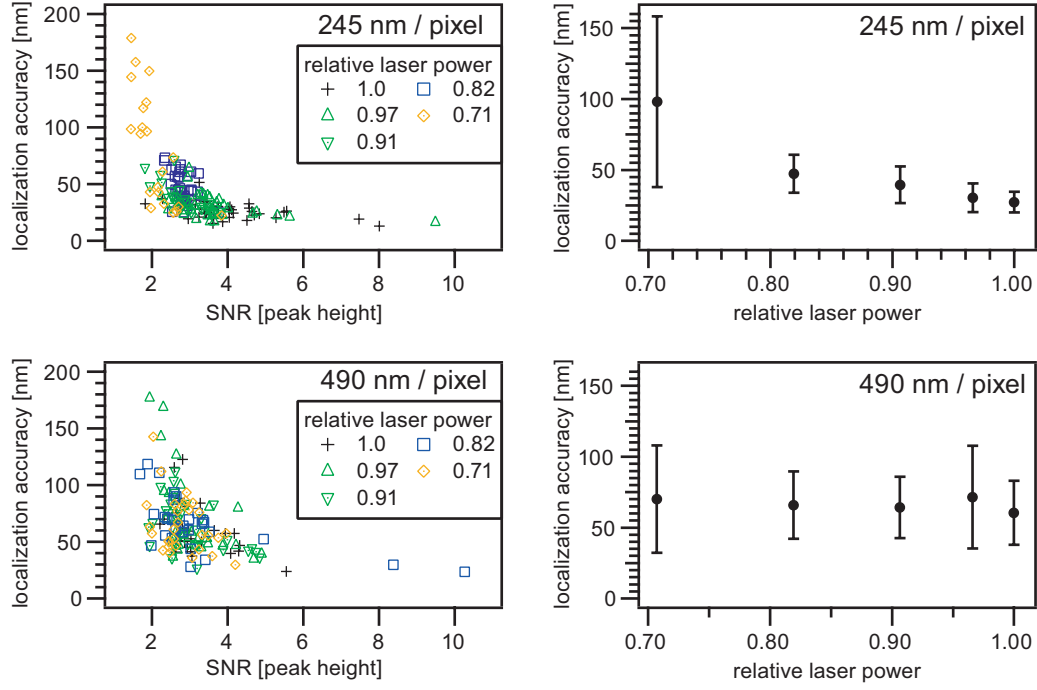


Figure 5.11: Accuracy of sub-diffraction single-molecule localization. Immobile surface adsorbed fluorescent particles (streptavidin labeled with Alexa Fluor 555) were traced over time for different laser powers and for 1×1 binning (top) and 2×2 binning (bottom). Left: Localization accuracy plotted over the signal-to-noise ratio (SNR, defined as the average peak height of the Gaussian fit divided by the noise). Higher SNRs correlate with better localization. Right: Localization accuracy plotted over the relative laser power. The 2×2 binning results in an accuracy limited by the large pixel size (490 nm compared to the expected Airy disc diameter of 250 nm).

local [164]. Typically a set of correlated control points (CPs) are determined in both images, with the goal that the mapping function will project one set of CPs onto their counterpart CPs with suitable parameters to the function. These parameters are then obtained from a fit minimizing the least-square distance of the CPs.

The mapping function for the dual-view microscope described here must include contributions from multiple mirrors and lenses. The sum of these effects leads to an unknown mapping function which is approximated by using low order polynomials to include shift, tilt, stretching and non-linear distortion. In the following, the “*comparative measure*” and the *mapping function* are discussed, where the former describes the nature of the CPs (i.e. “how do I pick similar bits in each image?”), while the latter is the function describing the mathematical projection (i.e. “is a polynomial sufficient to project one image onto the other?”).

Two different “comparative measures” were used, both using fluorescent beads which are so bright that they are visible in both channels:

- One measure used discrete CPs from the Gaussian fits to diffraction limited spots of correlated bead images (see Figure 5.14). These CPs are guaranteed to pinpoint the exact same physical location with nanometer precision. The difference in loca-

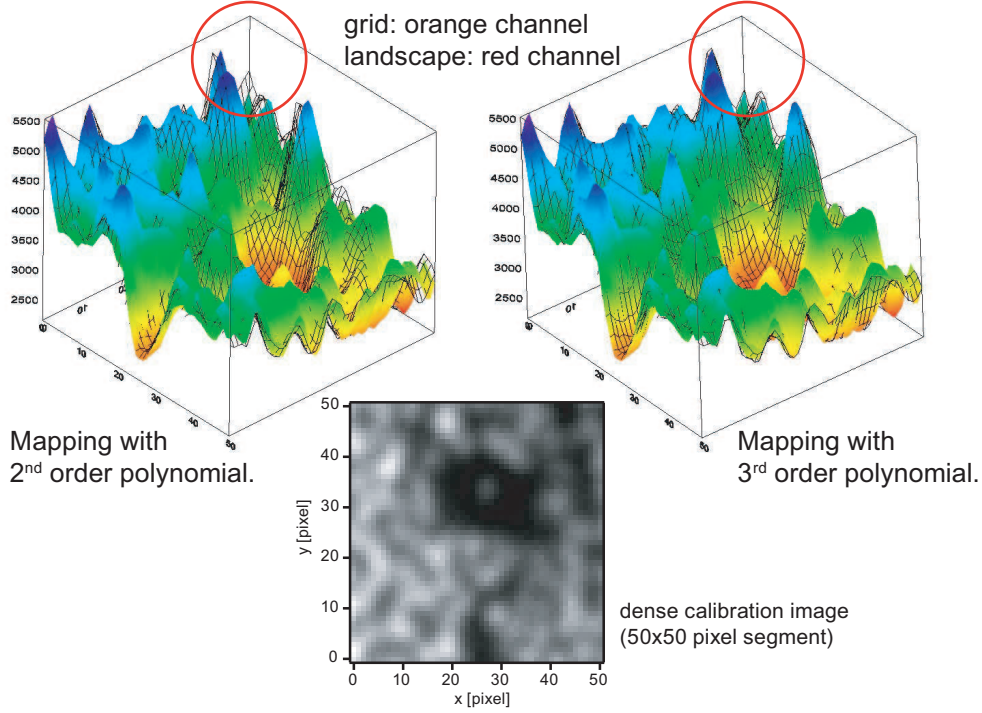


Figure 5.12: Image registration by pixel intensity fitting. Top/Left: The orange channel (grid) is mapped and fitted onto the red channel (landscape) using a 2D polynomial. Some insufficiencies are highlighted by the red circle. Top/Right: Accuracy is improved by 3rd order polynomial mapping. Bottom: The images used for this calibration were densely packed with highly fluorescent beads visible in both channels.

tion is used during minimization/fitting. Obtaining the CPs from such Gaussian fits to beads require some operator effort.

- The other “comparative measure” used was quasi-continuous without discrete CPs, using dense images of the beads visible in both channels which provide an intensity landscape (see Figure 5.12). The test region can be the whole image or a local sub-region of one channel, which is mapped onto the other channel (using interpolation). The pixel intensity difference chi-square between the test region and its target image region in the other channel delivers a single chi-square value which is used minimization/fitting. This pixel-based method requires little operator interaction and can be convenient in application.

Two types of mapping function were tested, a global analytical form and a local model free form:

- The analytical form describes the mathematical image transform and projection (the mapping) in a closed two dimensional analytical form as $\vec{r}_1(x, y) \rightarrow \vec{r}_2(x, y)$ for all \vec{r} .
- The model free form determines empirical shift maps, which define the shift in x and y direction necessary to bring the two color channels locally into overlap, i.e. the shift $\Delta\vec{r}(x, y)$ which is necessary to project the local small area (several

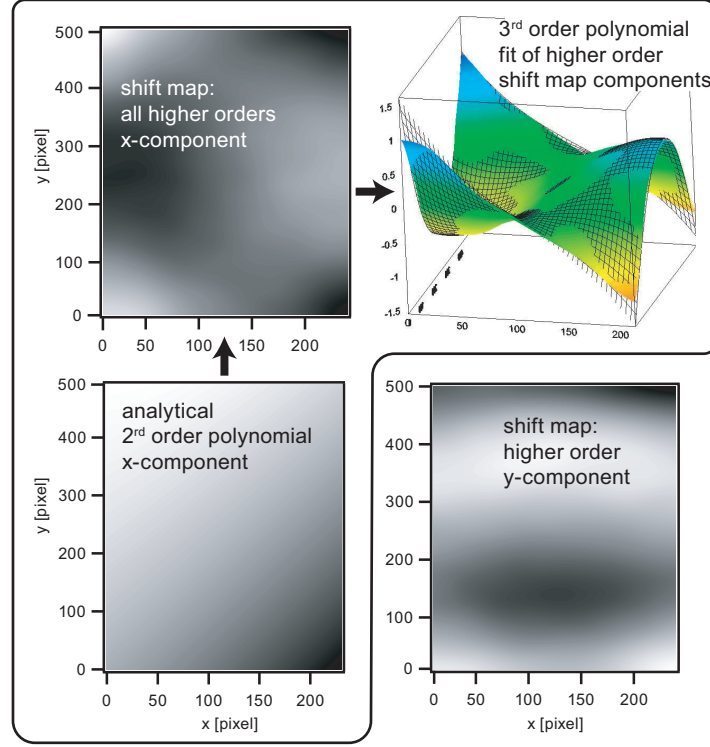


Figure 5.13: Shift maps obtained from pixel-based interpolated intensity fitting (see text) for the mapping of the orange camera channel (250×512 pixels) onto the red channel. Left and Top: Shown are the x-shift components for the 2nd order analytical polynomial, the higher order shift map, and a 2D polynomial fit of 3rd order to the higher order x-shifts. The good fit quality of the latter demonstrates that no significant contributions from orders higher than 3 are present in the image distortion. Bottom/Right: For comparison, the higher order shift map of the y-component is shown. This could also be fitted well with a 3rd order polynomial.

pixels) at \vec{r} onto its target area in the other image channel as $\vec{r}_1(x, y) + \vec{\Delta}r(x, y) \rightarrow \vec{r}_2(x, y)$. With smoothing one obtains continuous shift maps over all pixels (see Figure 5.13). The necessary shift is determined from chi-square minimization of the pixel intensity differences (with interpolation).

5.3.3.2 Determination of the Mapping Function

As a first step, the type of distortions present in the image and the mapping were determined empirically. For simplicity, the pixel-intensity based “comparative measure” was used.

1. A shift map was calculated which produced a good mapping by visual inspection. This map was then investigated for its analytical components. The strongest components in the map appeared to be second order.
2. A second order polynomial was used as mapping function, determined by pixel intensity as CPs. In general, the second order polynomial produced an adequate mapping, but with some clearly visible insufficiencies (Figure 5.12 top left).

3. A shift map was calculated on top of a second order polynomial, so that this shift map would contain third order and any higher terms. The second order (analytical) 2D polynomial for the x-component is visualized as 2D image for comparison with the shift maps in Figure 5.12 (bottom left). The higher-order shift map (Figure 5.13 top left) was seen to be fitted very well by a 2D polynomial of exactly third order (Figure 5.13 top right). In no case did 4th order or higher polynomials show any improvement.

Consequently, the appropriate mapping functions for this specific setup were seen to be third-degree 2D polynomials for the x and y components:

$$\begin{aligned} dx(x, y) &= a_1 + a_2x + a_3y + a_4x^2 + a_5xy + a_6y^2 + a_7x^3 + a_8x^2y + a_9xy^2 + a_{10}y^3 \\ dy(x, y) &= b_1 + b_2x + b_3y + b_4x^2 + b_5xy + b_6y^2 + b_7x^3 + b_8x^2y + b_9xy^2 + b_{10}y^3 \end{aligned}$$

5.3.3.3 Achieving 10 nm Accuracy in Image Registration

As determined above, the image distortions are described well by 3rd degree polynomials. The question remains which strategy is best to achieve highest quality in image registration.

To judge the image registration quality, the accuracy of the image registration was analyzed in detail with images of sparsely spread latex beads which are visible in both channels. The Gaussian fit position of a bead in the orange channel was mapped to its red projection position, and compared with the fit of the signal from same bead in the red channel. The difference between the “projected-from-orange” and “fitted-in-red” position is the local mapping function error. The distribution histogram of the local mapping errors is the final quality measure, where both the average and maximum error are of interest as well as their spatial distribution. In the following, at least 50 beads which were not used in calculating the mapping function were used to test image registration accuracy (see Figure 5.14).

Several strategies for image registration were tested for registration accuracy. Where Gaussian bead-fitting is used sparse images with few beads visible are necessary (see Figure 5.14). For pixel intensity difference chi-square minimization very full images with many beads were used (see Figure 5.12).

Some representative strategies were:

1. 2nd order polynomial analytical mapping function obtained using manually-fitted CPs from beads, plus additional non-analytical shift maps for higher order contributions => ~ 15 nm avg error.
2. 3rd order polynomial analytical mapping function obtained from global intensity chi-square minimization (no manual CPs, no shift maps) => ~ 16 nm avg error.
3. Fitting 3rd order polynomials exclusively using CPs from Gaussian fitted bead positions => Best results! Accuracy was 8.5 nm avg with 18 nm max error (see Figure 5.15).

Methods (1) and (2) involve pixel-intensity chi-square minimization, either in the determination of the shift maps or in fitting the polynomial mapping function. Both appear

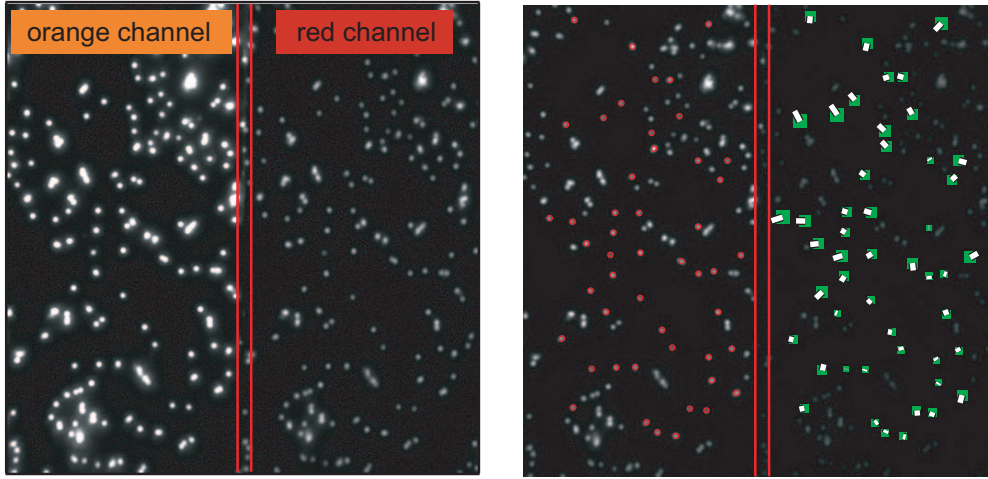


Figure 5.14: Left: Typical sparse image with fluorescent latex beads (visible in both channels), for image registration using CPs from Gaussian fits to the diffraction limit bead images. Right: The quality/accuracy of a mapping function can be obtained by fitting a bead in the orange channel (red dots), and then comparing its calculated position in the red channel with the fitted position in the red channel. The magnitude of the error is encoded in the green square size and the directional offset in the white lines.

limited to ~ 15 nm precision, corresponding to $1/4$ pixel at the used magnification. Pixel-based methods might be limited by the necessary interpolation and the resolution of the image.

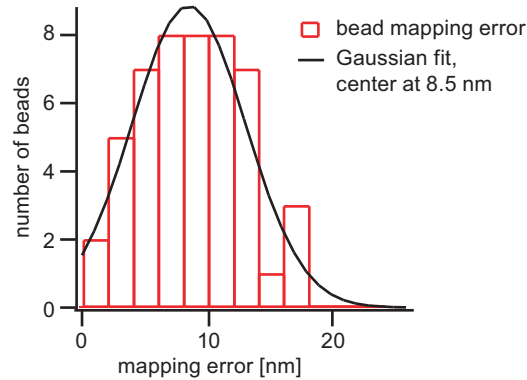


Figure 5.15: Mapping error histogram between the orange and red channel, with a 3rd order polynomial mapping function fit using Gaussian fits of manually selected beads as control points (CPs). The average mapping (registration) accuracy is 8.5 nm, which is better than localization accuracy of a normal weakly fluorescent particle such as a chemical dye.

The highest image registration accuracy was achieved with an analytical 3rd order polynomial mapping function parametrized using CPs from Gaussian fits to single highly fluorescent beads. Here, the localization of each bead is sub-pixel precise within a few nm. The final obtained average mapping precision of 8.5 nm is very high and corresponds to only $1/8$ pixel, with a maximum error of ~ 18 nm over the entire view area ($35\text{ }\mu\text{m} \times 17\text{ }\mu\text{m}$). The error here also includes the sum of the individual localization

errors of the fits in the orange and red channel. Importantly, there is no strong systematic spatial variation or correlation of the error magnitude or direction. The mapping precision achieved here is higher than the localization accuracy of a normal weakly fluorescent particle (~ 20 nm). Thus, the image registration is not a limiting factor for any future single-molecule colocalization experiments.

6 Structure and Dynamics of Archaea-Mimetic Cyclic Lipid Membranes

6.1 Introduction

Some studies on natural archaea lipids (e.g. reconstituting membrane proteins [165, 166]) have been made, but are limited by the challenging growth conditions necessary for the extremophiles in cell culture as well as complicated lipid extraction [167, 168]. Therefore, much more than for non-archaea lipids, it is desirable to establish and characterize synthetic archaea-mimetic lipids and membranes thereof. Previously, synthetic cyclic lipids have been designed [23, 169, 170] to mimic the key structural motifs of archaeal membranes. Rigid diacetylenes were successfully used as a structural moiety to avoid bending of the backbone into a “U-shape” at the air-water interface [171, 172]. However, full characterization of such monolayers and the application to solid supported membranes is missing.

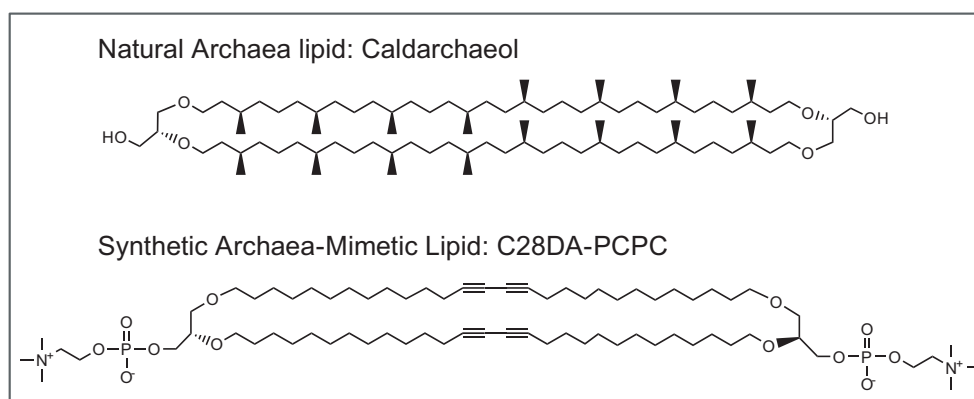


Figure 6.1: Top: The cyclic tetraether lipid *caldarchaeol* is a building block of archaea membranes. It is shown here in its basic form with OH-terminated headgroups, but variants with phosphatidylcholine headgroups exist as well. Bottom: C28DA-PCPC, one of the archaea-mimetic cyclic lipids used in this study. In the center of its hydrocarbon chains, this C28 lipid possesses triple-bonds (diacetylenes) to rigidify its structure.

In this chapter, investigations from multiple angles aim to give a fundamental understanding of lipid membrane monolayers of archaea-mimetic cyclic lipids. The synthetic cyclic lipids used here [137, 173] are controlled in their stereochemistry, thus providing a more accurate biological model (see Figure 6.1). As do their natural archaea templates, these cyclic lipids possess ether-linked hydrocarbon chains. Cyclic lipids with

chain lengths between 20 and 28 carbon atoms are investigated, which are either fully saturated (e.g. C20sat) or contain rigid diacetylenic cores (e.g. C20DA) as shown in Figure 4.2 on page 34. In order to further highlight the effects of ether links, the C16 lipid DHPC (the ether-linked analog of DPPC) is included in some of the experiments.

The basic archaeol headgroup motif is a polar OH-group, but there exist archaea lipids with phosphatidylcholine (PC) headgroups, as well as glycolipid or sulfolipid variants [17, 22]. The basic headgroup motif used for the cyclic lipids in this thesis is the zwitterionic phosphatidylcholine, which is also used in the most widely studied two-chain model lipids (e.g. DMPC or DPPC). The influence of lipid asymmetry (C20DA-PCOH) and headgroup chemistry (C20DA-sugarOH) is investigated and compared to the symmetrical counterpart (C20DA-PCPC).

First, the formation, homogeneity and fluidity of self-assembled cyclic lipid membranes on solid supports is probed by fluorescence microscopy and fluorescence after photobleaching (FRAP). The structure of supported membrane monolayers in bulk water is investigated using specular X-ray reflectivity, where the use of high energy X-ray radiation (22 keV) is necessary to achieve sufficient transmission in water (see Section 2.2.1). It was demonstrated only very recently [49, 174, 175] that this technique can be used as an alternative to the commonly used specular neutron reflectivity for characterizing biological membranes at the solid/liquid interface with a much higher throughput rate and a higher spatial resolution.

The lateral ordering and vertical membrane structure is investigated by various complementary X-ray scattering experiments. Small and wide-angle scattering (SAXS/WAXS) of unoriented multi-lamellar samples in dispersion reveal information about chain-chain correlations and the lamellar spacings. Full Q-range fitting [114] of SAXS data is used as the appropriate method to extract electron density profiles perpendicular to the membrane plane. A systematic investigation of the lamellar spacings and the inter-membrane water gaps highlights their dependency on structural features and chain lengths. Complementary to WAXS, grazing-incidence diffraction (GID) is used to probe chain-chain correlations of oriented membranes as a powerful technique to gain full information on unit cell and chain tilt in solid ordered phases.

6.2 Supported Membranes of Cyclic Lipids

6.2.1 Macroscopic Homogeneity

As previously outlined, solid-supported membranes are a very versatile and robust platform for use in the study of fundamental membrane physics and in complex applications, for instance integrating biological membrane functionality with physical or electrochemical biosensors. Consequently, the first question to ask about the archaea-mimetic synthetic lipids was whether they could form self-assembled solid supported membranes. This can simply and effectively be explored by fluorescence microscopy. A fluorescent tracer lipid is added to the lipid mixture at low concentrations, so that imaging in an optical fluorescence microscope gives information about the presence and homogeneity of the membrane at the surface. Here, the standard two-chain tracer lipid TR-DHPE is used, a C16:0 saturated lipid with chemical fluorescent dye Texas Red (TR) linked to the headgroup.

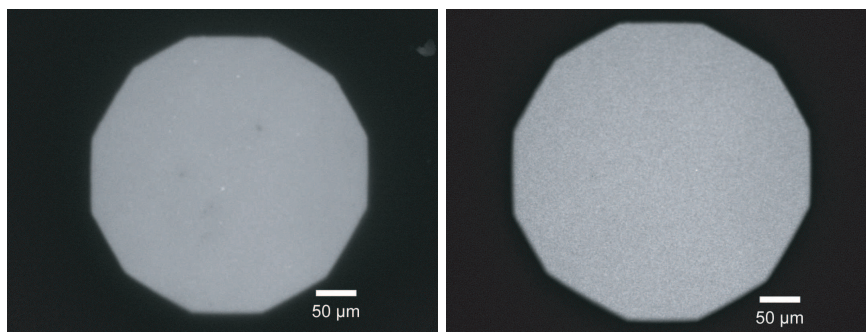


Figure 6.2: Fluorescence micrographs of solid supported membranes of C20-PCPC-DA (left) and C24-PCPC-DA (right). The membranes display macroscopically homogeneous surface coverage, and homogeneous distribution of the fluorescent tracer lipid TexasRed-DHPE within the cyclic lipid monolayers.

Solid-supported membrane formation was tested for C20DA-PCPC, C24DA-PCPC, C28DA-PCPC, C20sat-PCPC, C24sat-PCPC, and the asymmetric C20DA-PCOH. Membrane preparation was by vesicle fusion, as described in Section 4.2. For all cyclic lipid types, a well-defined macroscopically homogeneous surface coverage was observed. Example images are shown in Figure 6.2. Whether the observed membranes are indeed monolayers is investigated by under-water X-ray reflectivity in Section 6.3.

6.2.2 Fluidity of Cyclic Lipid Membranes (FRAP)

Depending on the purpose of a supported membrane experiment or application, either a solid phase with no lipid mobility or a fluid phase with high mobility can be desirable. For instance, the integration of functional membrane proteins in most cases requires the membrane to be in a fluid phase, as observed in biological membranes.

A well-established and quantitative method to examine the fluidity of membranes (especially solid supported membranes) is Fluorescence Recovery After Photobleaching (FRAP, see Section 3.4 and Section 4.3). In the following the influence of chain lengths, chain saturation, temperature and head group chemistry on the membrane fluidity will be presented for C20DA-PCPC, C24DA-PCPC, C28DA-PCPC, C20sat-PCPC, C24sat-PCPC, and the asymmetric C20DA-PCOH.

6.2.2.1 Diacetylenic Cyclic Lipids: Influence of Chain Length

The long-chain symmetric diacetylenic lipids C24DA-PCPC and C28DA-PCPC were seen to be immobile over the entire investigated temperature range up to 70 °C (see Figure 6.3). The immobility clearly indicates a solid phase, but not necessarily a gel or crystal phase by conventional definition (see Section 2.1.1). The nature of the ordering of cyclic lipid solid phases and the influence of the diacetylenic core is investigated by X-ray scattering experiments in Section 6.4).

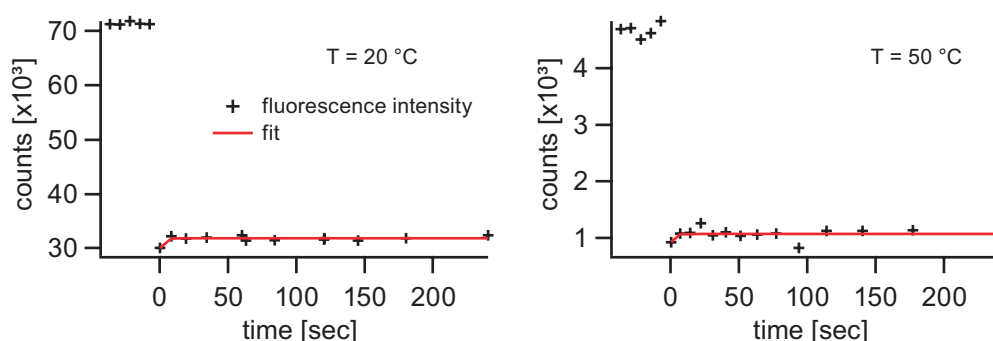


Figure 6.3: FRAP data and fits for C24DA-PCPC at 20 °C (left) and 50 °C (right). No recovery of fluorescence is observed. Similar results are obtained for C28DA-PCPC.

By contrast, the shorter lipid C20DA-PCPC formed membranes which were at least partially fluid. Some FRAP curves for C20DA-PCPC and the extracted R over the temperature T are shown in Figure 6.4. The maximum diffusion coefficient reached at 70 °C is $D = 0.04 \mu\text{m}^2/\text{s}$ which is two orders of magnitude slower than for two-chain lipid membranes in a fluid state ($D = 1\text{--}10 \mu\text{m}^2/\text{s}$). However, a continuous increase of the relative recovery R over temperature was observed, with no clear phase transition temperature. Also, the recovery curves do not follow the expected functional form at long times, and could be fitted satisfactorily with the standard FRAP model only for times < 15 min (longer times not shown).

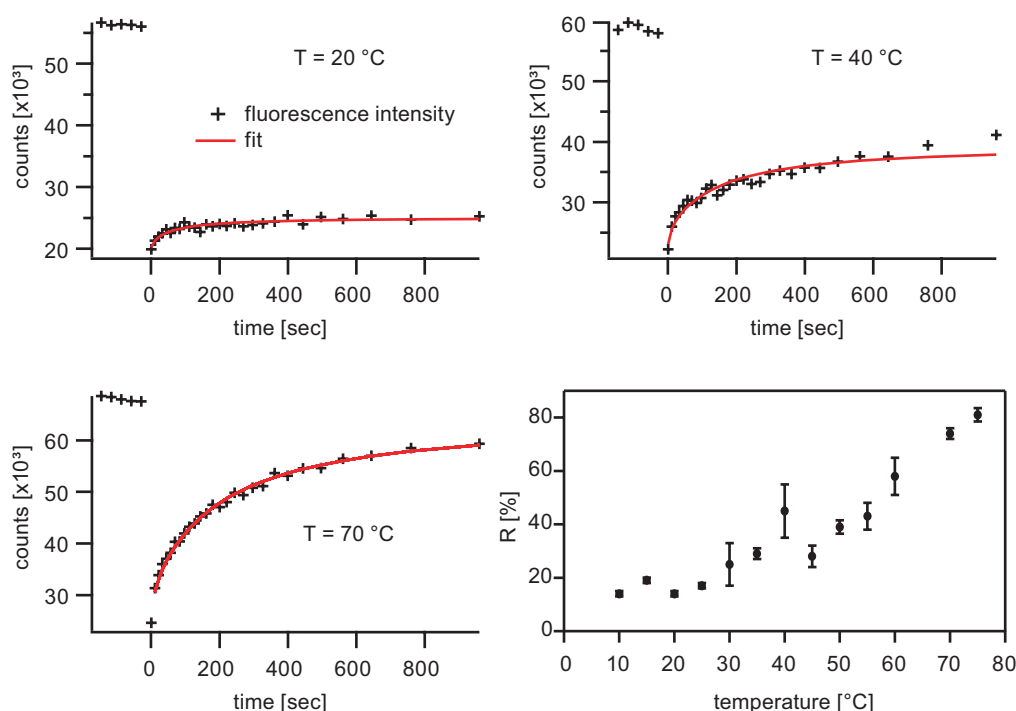


Figure 6.4: Top and Bottom/Left: FRAP data and fits for C20DA-PCPC at different temperatures. Bottom/Right: A continuous increase of the relative recovery R over temperature is observed.

6.2.2.2 Diacetylenic Cyclic Lipids: Influence of Headgroup Asymmetry

In addition to the symmetric molecules presented above, the transmembrane molecular configuration allows for unique asymmetric lipids with two different headgroups. Membranes of C20DA-PCOH with one PC headgroup and one OH headgroup were investigated, with an expected random orientation of the asymmetric lipids in the membrane.

The temperature-dependent FRAP results shown in Figure 6.5 and Table 6.1 for C20DA-PCOH differ clearly from those of the symmetric C20DA-PCPC. Qualitatively, the FRAP curves can be well-fitted with Equation 3.3 (in contrast to C20DA-PCPC) as shown in Figure 6.6. Also, below 30 °C the membrane is immobile, while it is clearly fluid above 50 °C. These observations are consistent with a discontinuous chain melting phase transition around 40 °C. In the fluid state one can observe a temperature dependent increase of the diffusion coefficient D to beyond $0.1 \mu\text{m}^2/\text{s}$. The rate of diffusion is significantly faster than for C20DA-PCPC where $D \sim 0.04 \mu\text{m}^2/\text{s}$, though still one order of magnitude slower than normal two-chain lipids.

6.2.2.3 Saturated Cyclic Lipids

The saturated cyclic lipids C20sat and C24sat were seen to be immobile over the entire examined temperature range up to 70 °C.

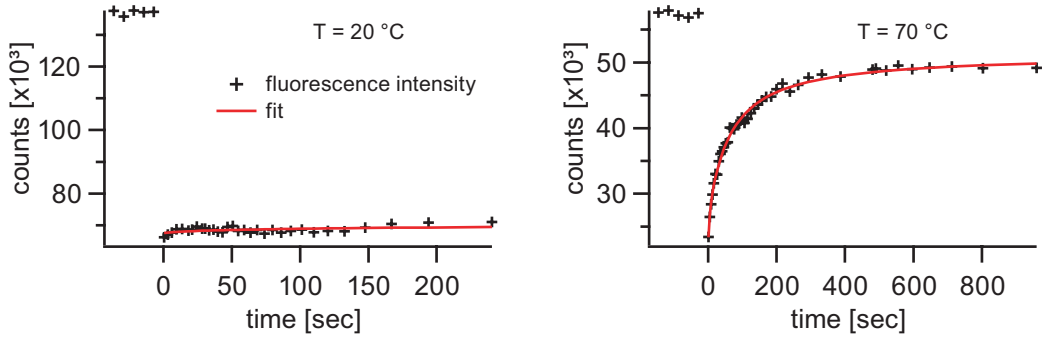


Figure 6.5: FRAP data and fits for C20DA-PCOH at 20 °C (left) and 70 °C (right). At low temperatures ($T = 20^{\circ}\text{C}$) there is no significant recovery of fluorescence, showing that the membrane is in a solid phase. At high temperatures ($T = 50^{\circ}\text{C}$) there is nearly full recovery of fluorescence by diffusion ($R > 90\%$), indicating a fluid phase.

Table 6.1: FRAP results for C20DA-PCOH. Two clear phases are observed. At low temperatures (20°C) there is no significant recovery of fluorescence, the membrane is in a solid phase. At high temperatures ($T > 50^{\circ}\text{C}$) there is nearly full recovery of fluorescence by diffusion ($R > 90\%$). The resulting diffusion coefficient D increases with increasing temperature, but is at least an order of magnitude smaller than values observed in solid-supported phospholipid bilayers [45].

temperature	diffusion coefficient D	relative recovery R
20 °C	-	< 0.05
50 °C	0.05 $\mu\text{m}^2/\text{s}$	0.94
60 °C	0.06 $\mu\text{m}^2/\text{s}$	0.94
70 °C	0.11 $\mu\text{m}^2/\text{s}$	0.92

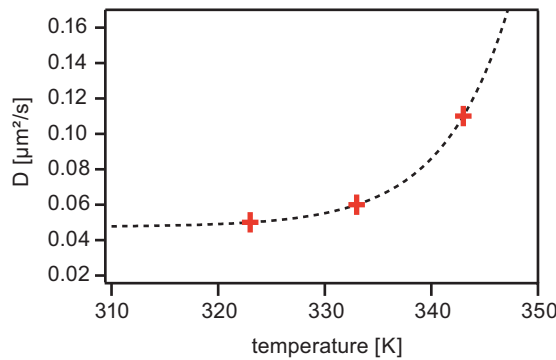


Figure 6.6: Influence of temperature on the diffusion coefficient D for C20DA-PCOH. An exponential fit according to Equation 2.5 shows the consistency with free volume theory.

6.2.2.4 C20DA-PCPC Solid-Supported Membrane Deposited by Solvent Exchange

For C20DA-PCPC, solvent exchange was tested as a further membrane preparation method. This method avoids the difficult resuspension of the cyclic ether lipids and could allow creation of higher quality supported membranes in a simpler fashion. For details of the preparation, see Section 4.2.

A solid-supported C20DA-PCPC monolayer was deposited by this method using ethanol as solvent, and the resulting homogeneous membrane is shown in Figure 6.7. FRAP measurements revealed a very fast diffusion coefficient $D \sim 2.5 \mu\text{m}^2/\text{s}$ in the membrane at room temperature. The mobile fraction was very high with $R = 0.98$. These observations indicate a significantly higher fluidity compared to a membrane prepared by vesicle fusion (see above).

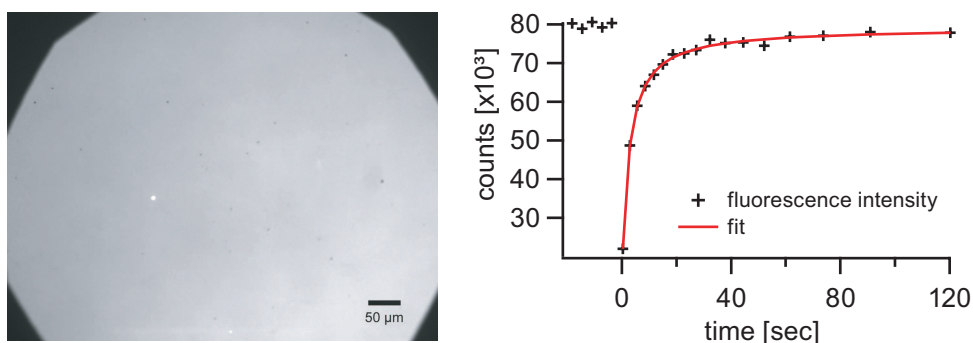


Figure 6.7: Left: Membrane of C20DA-PCPC prepared by solvent exchange. Right: FRAP measurement at room temperature. Recovery is nearly 100%, and the diffusion is very fast ($D \sim 2.5 \mu\text{m}^2/\text{s}$).

The effect is most likely due to residual solvent molecules in the membrane interfacial region, as an increase in fluidity in the presence of alcohol has been reported for lipid bilayer membranes [176, 177]. However, the magnitude of the effect is large and points either to a very strong partitioning of ethanol into the membrane or an unusual sensitivity of the physico-chemically unique monolayer membrane to the effects of ethanol incorporation. While the dramatic fluidifying effect of ethanol could be useful for some specialized applications, in general the solvent exchange method appears not ideally suited for studies of fundamental physics of solid-supported cyclic lipid monolayers.

6.2.2.5 Diffusion of Transmembrane Lipids in a DMPC Membrane

The diffusion of the fluorescent tracer C20DA-PC-TAMRA was also studied in a matrix of the standard phospholipid DMPC in the fluid phase. Here, the transmembrane probe is expected to penetrate both leaflets of the DMPC bilayer and thus experience a different frictional coupling than the two-chain matrix lipids. Indeed, the FRAP results (Table 6.2) very clearly show an order of magnitude slower fluorescence recovery for the transmembrane tracer compared to the two-chain tracer TR-DHPE, while the mobile fraction is comparable.

Table 6.2: Comparison of the diffusion coefficients for C20DA-PC-TAMRA and TR-DHPE in a fluid DMPC matrix.

Temp.	Tracer Lipid (in DMPC)	Diffusion Coef. D	Rel. Recovery R
30 °C	TR-DHPE	$1.7 \mu\text{m}^2/\text{s}$	0.94
	C20DA-PC-TAMRA	$0.14 \mu\text{m}^2/\text{s}$	0.89
60 °C	TR-DHPE	$3.6 \mu\text{m}^2/\text{s}$	0.96
	C20DA-PC-TAMRA	$0.31 \mu\text{m}^2/\text{s}$	0.96

The strong decrease of the diffusion coefficient D can be explained by free volume theory (Equation 2.5 on page 9), where D is exponentially dependent on the critical free area a^* . This critical free area is approximately doubled as the diffusion is coupled to two leaflets. Also, the DMPC bilayer is slightly thicker than the length of C20 lipid, so that the bulky headgroups are partially immersed in the membrane and thus requiring a greater a^* .

6.2.2.6 Discussion

These FRAP results for the cyclic lipids highlight the interplay of the chain-length dependent attractive forces and the strain from the presence of a diacetylenic core, as well as the additional effects of headgroup packing strain.

The symmetric diacetylenic lipid C20DA-PCPC exhibited a temperature-dependent mobility with no clear phase transition, while the asymmetric diacetylenic C20DA-PCOH showed a clear contrast between a solid and a fluid phase. Apparently for C20DA-PCPC, in addition to the kinked diacetylenic core which C20DA-PCOH also possesses, the symmetric large PC headgroups contribute to prevent a tight chain packing at low temperatures. This view is supported by the fact that the C20DA-PCPC membrane is partially mobile at temperatures where a shorter two-chain saturated PC lipid is fully immobile. For comparison, the saturated C16 phospholipid DPPC is immobile up to $\sim 42^\circ\text{C}$, whereas C20DA-PCPC has a mobile fraction of $R \sim 30\text{--}40\%$ at this temperature. Although C20DA-PCPC exhibits an increased mobile fraction at higher temperatures, clearly the melting is different from a first-order chain melting transition. This is consistent with a disordered type of packing.

The asymmetric diacetylenic lipid C20DA-PCOH exhibited a clear phase transition. At low temperatures, a fully immobile solid phase exists and one observes a first order melting transition around $\sim 45^\circ\text{C}$. The markedly different behavior compared to the symmetric C20DA-PCPC lipid can be explained in terms of reduced headgroup packing strain which allows more favorable chain packing, despite the presence of the kinked diacetylenic core. Also, the mobile fraction of C20DA-PCOH at 70°C is higher ($R > 90\%$) and the diffusion is faster than for C20DA-PCPC ($0.11 \mu\text{m}^2/\text{s}$ vs $0.04 \mu\text{m}^2/\text{s}$). This can be explained by reduced headgroup friction and a minor contribution from the slightly lower molecular weight of the asymmetric lipid.

It must be noted that the observed diffusion coefficients for cyclic lipid membranes in the

fluid phase are at least one order of magnitude smaller than those observed in standard bilayers of two-chain phospholipids. Furthermore, the longer chain cyclic lipids C24DA-PCPC and C28DA-PCPC showed no mobility at all investigated temperature. Although these lipids also possess a stiff kinked diacetylenic core and symmetric headgroups, the flexible saturated hydrocarbon chain fraction is greater, possibly allowing more favorable packing. Also, longer chains means stronger van der Waals attraction. The saturated lipids C20sat and C24sat also showed no mobility at all investigated temperatures. These lipids do not possess a kinked diacetylenic core, which enables the compact chain packing of a true gel phase. For comparison, a high melting temperature is observed for two-tail saturated PC lipids with comparable hydrocarbon chain length ($T_m \sim 80^\circ\text{C}$ for lipids with 24-carbon chains, see [9, 31]). Thus for applications of supported membranes where fluidity is required, these findings motivate further optimizations of the cyclic lipid structure.

Finally, one should considering the validity of extrapolating C16-lipid tracer diffusion to self-diffusion of the C20 and longer cyclic lipid monolayer matrix. In the free volume model of diffusion a smaller/shorter molecule will require a smaller critical free volume and diffuse faster in a matrix of larger molecules than the matrix molecules themselves. In this light, the observed diffusion of the tracer lipid might overestimate the magnitude of matrix self-diffusion. However, the hydrocarbon chain length of the C16 tracer lipid TR-DHPE is greater than half the length even of the C28 cyclic lipid. Consequently, its diffusion should be coupled strongly the matrix and represent the membrane fluidity well.

6.3 X-Ray Reflectivity of Supported Monolayer Membranes

6.3.1 Results

Here, the structure of fully hydrated single solid-supported cyclic lipid membranes (under bulk water) is presented, determined from X-ray reflectivity measurements (see Section 3.5). Measuring under water is the ideal condition to study membrane structure at full hydration, closing the large gap to experiments at high humidity [178]. Such experiments have become possible only quite recently [49] and still pose a technological challenge. The signal strength is limited due to scattering from only a single membrane and due to the X-ray absorption in water, which necessitates selection of an X-ray energy with low absorption (see Section 2.2.1 and Equation 2.12). Here, 22 keV ($\lambda = 0.56 \text{ \AA}$) was chosen.

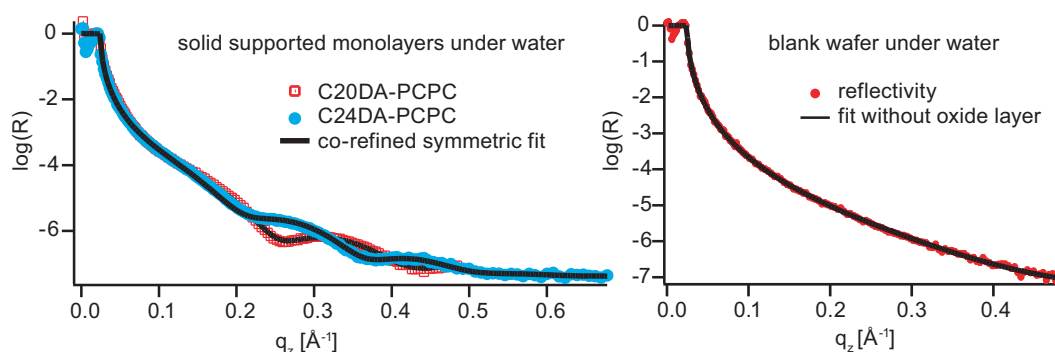


Figure 6.8: Left: X-ray reflectivity of solid-supported monolayers of C20DA-PCPC and C24DA-PCPC under water. The co-refined fits are superimposed on the data. Right: Reflectivity of a blank wafer under water. The lack of Kiessig fringes shows that under the experimental conditions there is no resolvable contrast between silicon and silicon-dioxide, so that no oxide layer was included in the slab model.

The reflectivity experiments were performed with C20DA-PCPC and C24DA-PCPC. As established above (Section 6.2.2. see also Sections 6.4 and Sections 6.6), at 20 °C the membranes of all transmembrane lipids investigated in this study are in an immobile state with gel-phase characteristics. Figure 6.8 represents the specular X-ray reflectivities of C20DA-PCPC (red squares) and C24DA-PCPC (blue circles). Both curves exhibit two pronounced minima, indicating the presence of layers with high electron density contrast. The fact that the first and second minima of C24DA-PCPC appear at lower q -values than those of C20DA-PCPC further indicates that C24PCPC forms thicker layers than C20PCPC (see Section 3.5 Equation 3.11).

To fit the measured reflectivity curves, the supported membranes were modeled with three slabs, consisting of two slabs of head groups (layers 1 and 3) that sandwich one slab of hydrocarbon chains (layer 2). The model reflectivity was calculated with a Parratt-type algorithm (see Section 3.5 and Section 4.4).

Owing to the unique structural symmetry of the transmembrane lipids, a strongly symmetric fit strategy could be employed. This is in contrast to normal phospholipid bilayers that consist of two independent monolayer leaflets. Also, the two different types of

transmembrane monolayers are expected to share most features except for chain length, which motivated links between the two datasets during fitting, referred to as *co-refining*. This symmetrically-linked and co-refined approach is especially powerful as it reduces the number of free parameters and helps to perform the modeling without choosing arbitrary constraints. The used software (Motofit) can perform such a fit linked across several datasets.

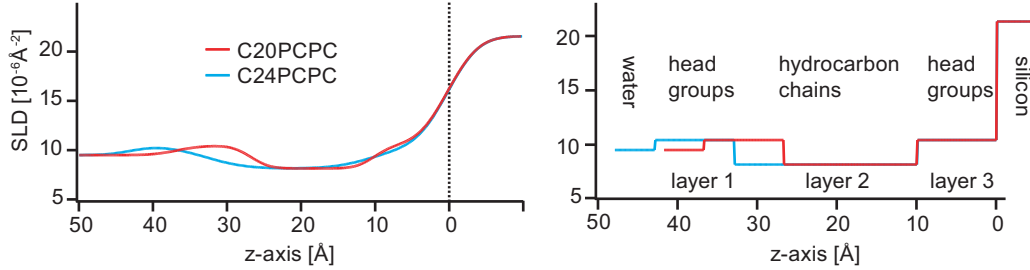


Figure 6.9: Slab models of the co-refined symmetric fit to the reflectivity data as electron density profile (left) and box model (right). The electron density of both headgroups and hydrocarbon chain region is low, indicating monolayers with low packing density. Also, the hydrocarbon chain electron density ($8.0 \times 10^{-6} \text{ \AA}^{-3}$, see Table 6.3) is not raised towards the water level ($9.4 \times 10^{-6} \text{ \AA}^{-3}$), so that significant water penetration into the membrane can be excluded.

For instance, the slabs of head groups were required to have the same density and thickness for both the inner leaflet (in contact to the solid substrates) and the outer leaflet in contact with bulk water, across both membrane types. A different roughness was allowed however. The links and constraints used were:

- the thickness and scattering length density (SLD) of the head groups (layers 1 and 3) were linked within and between datasets,
- the SLD of hydrocarbon chains (layer 2) was linked between both datasets,
- the interface roughness below and above the chain region were linked within each dataset, and
- background and bulk silicon/water SLD were set constant.

The best fits achieved with this co-refined, symmetric slab model are presented as solid lines in Figure 6.8. The high global fit quality confirms the validity of the boundary conditions and parameter links. The thickness d , scattering length density $\text{SLD} = r_e \sigma_e$, and RMS roughness σ of individual slabs and interfaces are summarized in Table 6.3, where r_e is the Compton radius and σ_e is the electron density. The corresponding SLD profiles of C20DA-PCPC and C24DA-PCPC are presented in Figure 6.9. It should be noted that neither a silicon oxide layer nor a water gap between the substrate and the membrane could be clearly identified. The contrast between silicon and silicon oxide was low (see Figure 6.8, right) and the thin water gap is likely hidden in the interfacial roughness between head groups and silicon.

Table 6.3: Summary of slab model parameters from the co-refined fit to the supported monolayer reflectivity data. The headgroup thickness and density as well as the hydrocarbon chain density were linked between the two datasets. The hydrocarbon layer thickness was free.

	layer	D [Å]	SLD [10^{-6} Å^{-3}]	σ [Å]
C20DA-PCPC	1	10.0	10.4	2.6
	2	16.7	8.0	2.0
	3	10.0	10.4	2.0
C24DA-PCPC	1	10.0	10.4	2.6
	2	22.9	8.0	4.3
	3	10.0	10.4	4.3

6.3.2 Discussion

The thickness of the head group regions (10 Å) agrees well with previous reports on dimyristoylphosphatidylcholine (DMPC). The total thicknesses of C20DA-PCPC and C24DA-PCPC membranes are calculated to be 36.7 Å and 42.9 Å, respectively, indicating that both lipids form monolayers at the solid/liquid interface. The thickness difference $\Delta d = 6.2 \text{ Å}$ can reasonably be attributed to the difference in length of the hydrocarbon chains. The RMS roughness values between water and outer head groups ($\sigma = 2.6 \text{ Å}$) are even smaller than the $\sigma = 6 \text{ Å}$ reported for fluid phosphocholine membranes, indicating the formation of smooth, homogeneous membranes.

However, the model results for solid supported monolayers for both C20DA and C24DA are less dense than expected. The scattering length densities of head groups ($10.4 \times 10^{-6} \text{ Å}^{-2}$) and hydrocarbon chains ($8.0 \times 10^{-6} \text{ Å}^{-2}$) are slightly lower than reported for DMPC membranes in $L_{\beta'}$ phase ($13 \times 10^{-6} \text{ Å}^{-2}$ and $9.3 \times 10^{-6} \text{ Å}^{-2}$) [113]. It is notable that the electron density of the chain slab is lower than that of water, indicating that the penetration of water into the hydrocarbon core is negligible. Even though very clearly a single well-defined monolayer is formed, it is simply less dense than for conventional bilayers. A reasonable assumption is that membrane formation from vesicle fusion and subsequent self-healing are hindered by the high melting temperatures of the lipids and the slow lateral diffusivity.

6.4 X-Ray Scattering of Unoriented Samples (SAXS/WAXS)

SAXS and WAXS as described in Section 3.6 are well-suited to give information on complementary length-scales about the structural characteristics of membranes (especially membrane multilayers) related to their thermodynamic phases and phase transitions. A peak seen in WAXS stems from correlations on the length scale of chain-chain distances, which is indicative of a solid-ordered phase with long-range in-plane chain ordering. SAXS gives information about the lamellar repeat distance as a product by membrane thickness and inter-membrane interactions, as well as the vertical electron density (the membrane form factor).

Temperature-controlled SAXS and WAXS experiments with aqueous suspensions of lipid (see Section 4.4) were performed between 20 °C and 70 °C for the symmetric diacetylenic lipids C28DA-PCPC, C24DA-PCPC and the two short asymmetric lipids C20DA-PCOH and C20DA-sugarOH¹. See also Table 6.5 on page 79.

6.4.1 Results

6.4.1.1 Asymmetric C20DA lipids

Shown in Figure 6.10 are SAXS/WAXS measurements during temperature scans for the asymmetric C20DA lipids. As shown in Figure 4.2, the lipid molecules each have an OH-termination on one side, and either a PC or sugar headgroup on the other (with similar dimensions). Orientation in the membrane is expected to be random.

C20DA-PCOH At 20 °C one can observe two orders of SAXS peaks for C20DA-PCOH at q_r values of 0.129 \AA^{-1} and 0.258 \AA^{-1} , corresponding to a lamellar spacing of $d = 48.6 \text{ \AA}$. The existence of the WAXS peak at $q_r = 1.53 \text{ \AA}^{-1}$ indicates a solid phase with chain-chain correlations at a spacing of $d = 4.1 \text{ \AA}$. Furthermore, one can observe a weak WAXS satellite peak at $q_r \sim 1.4 \text{ \AA}^{-1}$ ($d \sim 4.4 \text{ \AA}$).

Between 42 °C–46 °C a drastic change in SAXS is observed. The ordering remains lamellar, but on the one hand the correlation peaks drastically lose intensity (correlation length), and on the other hand one observes a jump of the spacing to $q_r = 0.067 \text{ \AA}^{-1}$ ($d = 93.6 \text{ \AA}$, at 50 °C). Still, two lamellar SAXS peaks can be discerned with decreasing spacing upon increasing temperature. Consistent with the SAXS measurements, the WAXS peak is lost between 42 °C and 46 °C, indicating a loss of chain-chain correlation.

C20DA-sugarOH Comparable observations were made for C20DA-sugarOH. Here, sharp lamellar SAXS peaks were observed until 40 °C, with the first order at $q_r = 0.152 \text{ \AA}^{-1}$ ($d = 41.4 \text{ \AA}$) and suppressed second orders (see Section 6.4.2). In this temperature range one also observes a WAXS peak similar in position and shape to C20DA-PCOH, indicating chain-chain correlations.

¹Due to limited sample availability it was not possible to measure full temperature scans for C24DA-PCPC, or a sample of C20DA-PCPC.

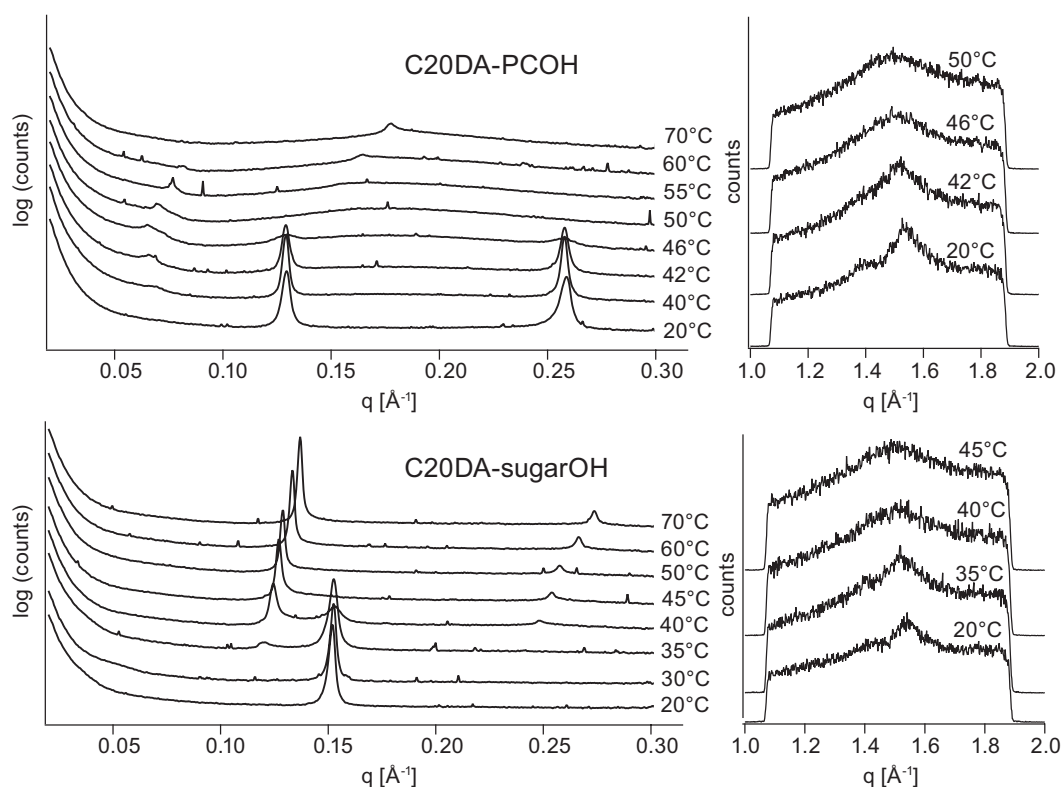


Figure 6.10: SAXS/WAXS curves for the C20 asymmetric lipids C20DA-PCOH (top) and C20DA-sugarOH (bottom). Results for both lipids show clear indications for a phase melting transition around 40–45°C. For both lipids below this temperature, a peak exists in the WAXS curves (indicating chain-chain correlations), which disappears upon heating. At the same temperature, the equidistant peaks in SAXS (indicating lamellar correlation) change discontinuously to larger spacings.

Between 35 °C to 40 °C there is a jump to larger lamellar spacings visible in SAXS $q_r = 0.127 \text{ \AA}^{-1}$ ($d = 49.5 \text{ \AA}$, at 45 °C), comparable to C20DA-PCOH. Beyond 40 °C the spacing decreases with increasing temperature. As the SAXS peaks shift to higher q -values, the overlap of the form-factor minimum with the second order peak appears to decrease and the latter becomes more prominent. The change in SAXS features is accompanied by a loss of the WAXS peak between 35 °C to 40 °C.

6.4.1.2 C24DA-PCPC and C28DA-PCPC

Shown in Figure 6.11 are the SAXS/WAXS curves for the longer symmetric lipids C24DA-PCPC and C28DA-PCPC. Due to experimental limitations, the obtained scattering patterns for C24DA-PCPC were of low quality and no full temperature scan could be performed. The data shown in Figure 6.11 is an average over several individual data sets between 20 °C and 25 °C. In SAXS, two lamellar orders can be observed (first order at $q_r = 0.172 \text{ \AA}^{-1}$) indicating a spacing of $d = 49.4 \text{ \AA}$. In WAXS, a weak peak can be discerned.

For C28DA-PCPC one observes SAXS peaks with three orders at temperatures up to

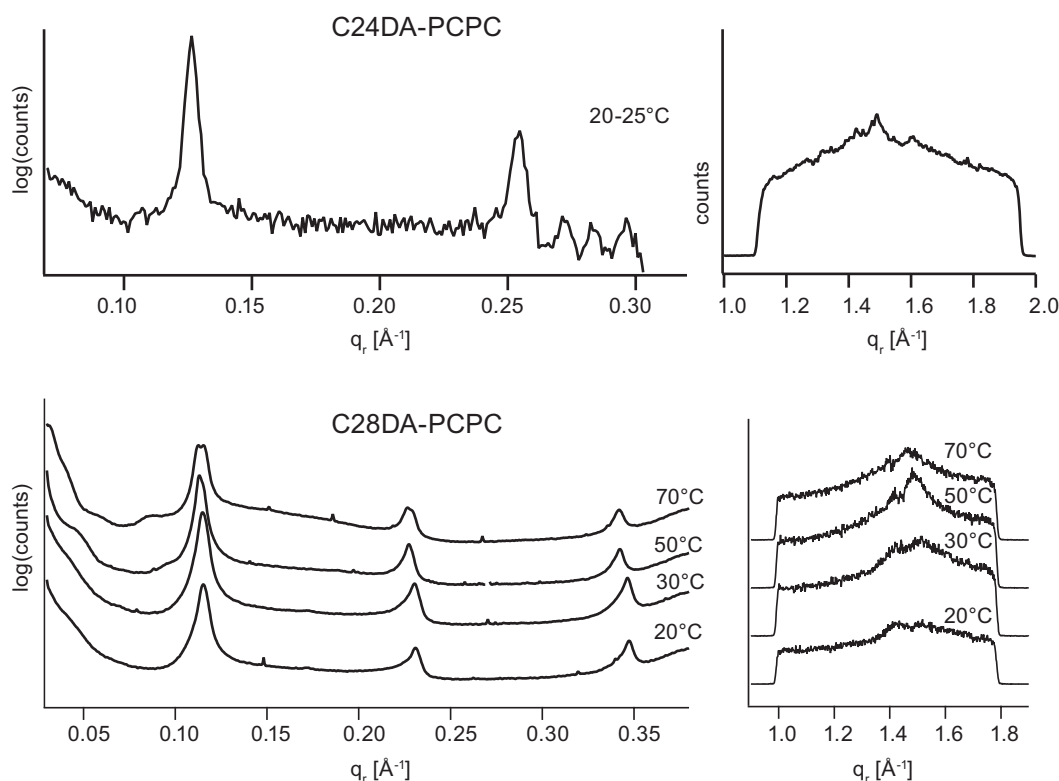


Figure 6.11: SAXS/WAXS curves for C24DA-PCPC (top) and C28DA-PCPC (bottom). The C24DA-PCPC curves are an average over several individual data sets between 20 °C and 25 °C. The C28DA-PCPC curves do not show any evidence of melting up to 70 °C. For both lipids, the equidistant SAXS peaks indicate lamellar correlation, while the presence of a peak in WAXS indicates chain-chain correlations and the existence of a solid phase.

70 °C, indicating a lamellar phase with 54.5 Å spacing. There is no change of these features up to 70 °C. A WAXS peak is visible, indicating a solid phase with long-range chain-chain correlation.

6.4.2 Electron Density Modeling

The electron density profile of the lamellar unit cell (in z direction) can be extracted from SAXS data by full- q -range fitting, as discussed in Section 3.6. Importantly, the electron density profile as a function of z also encodes the thickness of the inter-membrane water gap. This information is valuable, as it allows conclusions to be drawn about hydration effects and inter-membrane forces.

The SAXS data at 20 °C for the four diacetylenic cyclic lipids C20DA-PCOH, C20DA-sugarOH, C24DA-PCPC and C28DA-PCPC was fitted with the model, using some constraints. Due to the limited q -range and number of Bragg peaks, only few free parameters should be fitted. At 20 °C the membranes of all lipid types were shown to be in a solid phase by FRAP experiments (Section 6.2.2) and by the observation of WAXS peaks. This knowledge guided the model design:

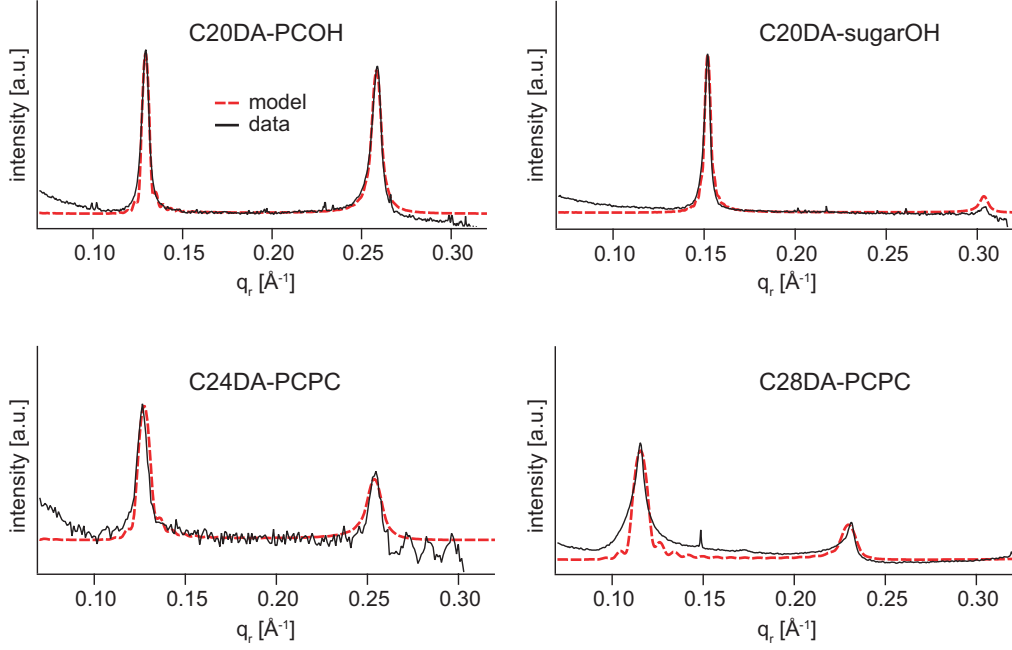


Figure 6.12: The SAXS model fits superimposed on the SAXS data of the cyclic lipids in dispersion at 20 °C. The models are able to capture most features well. Note that even though C20DA-PCOH and C20DA-sugarOH have similar membrane thickness and molecular structure, the second order lamellar peak is suppressed for C20DA-PCOH as the different lamellar periodicity moves the Bragg peak onto a form factor minimum.

- For symmetric PC cyclic lipids, the headgroup electron density profile was taken from DMPC/DPPC results [30, 113] which explicitly resolve the choline and phosphate groups as separate slabs. The z-resolution of this headgroup profile is higher than could be obtained from fitting of the present SAXS data, but without negative consequences for the subsequent modeling/fitting.
- For the asymmetric C20DA-PCOH a PC headgroup electron density profile was used, scaled down by 50% relative to water.
- For the asymmetric C20DA-sugarOH the headgroup was assumed as a single slab with the width and electron density determined from the subsequent fitting.
- The electron density of the hydrocarbon chain region was fixed at a reasonable value for gel phase hydrocarbon chains ($\sim 95\%$ of water electron density [113]) and assumed constant over the whole length.

Consequently, the main focus was on obtaining the length of the hydrocarbon region and the membrane thickness independently from the lamellar spacing (and water gap). These boundary conditions were sufficient to model all datasets at 20 °C satisfactorily (see Figure 6.12) with the electron density profiles shown in Figure 6.13. Two fits decomposed into structure factor and form factor are shown in Figure 6.14, illustrating the suppression of the second order lamellar Bragg peak. Results are presented in detail in Table 6.4). Major results were:

- The fit results for membrane thickness are consistent with the molecular struc-

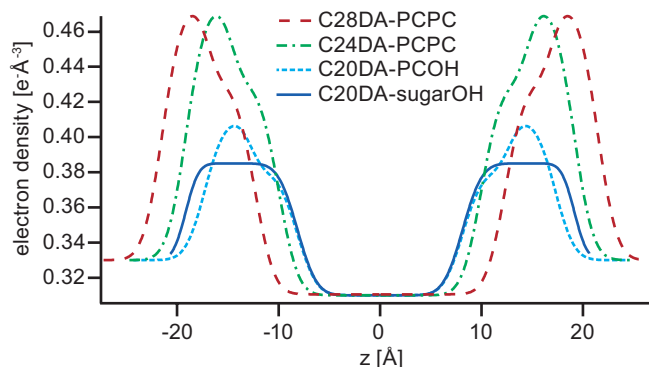


Figure 6.13: The electron density profiles extracted from the SAXS model fits for the di-acetylenic lipid membrane at 20 °C. The differences of the water gaps are clearly visible. The asymmetric C20DA-PCOH has the largest gap, while the also asymmetric C20DA-sugarOH has the smallest.

tures, with a progression from the shortest to the longest molecules. To give an example for comparison, the C28DA-PCPC membrane has approximately the same thickness as a membrane bilayer of the widely-used lipid DMPC (saturated C14 phospholipid) [113].

- Both C20DA membranes have approximately the same thickness.
- The symmetric PCPC membrane stacks have an inter-membrane water gap of $\sim 11.5 \text{ \AA}$, which is very similar to values reported for DPPC in the gel phase ($\sim 11 \text{ \AA}$ [31]).
- The asymmetric PCOH membrane multilayers have a water gap of $\sim 14 \text{ \AA}$, indicating weaker inter-membrane attraction and greater hydration levels. This is consistent with the observation in SAXS that C20DA-PCOH decouples upon melting.
- The asymmetric glycolipid (sugar-OH) membrane stacks show a much thinner water gap of $\sim 3 \text{ \AA}$, which means that the membranes have a very low hydration level and are practically in contact. This is consistent with the fit also indicating a high number of correlated lamellae and the observation that the glycolipid membranes do not decouple upon melting.

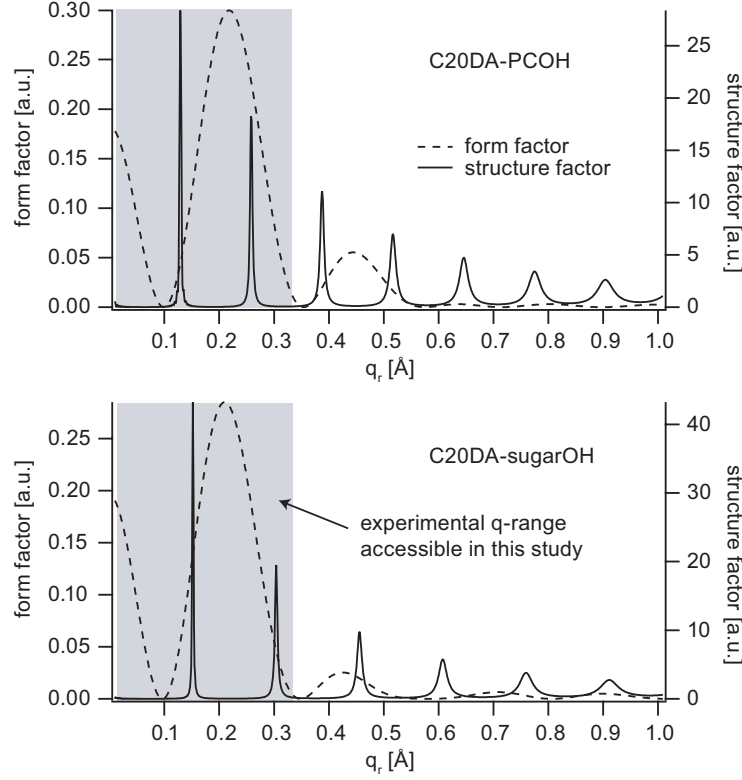


Figure 6.14: The form factor F and structure factor S for the models of C20DA-PCOH (top) and C20DA-sugarOH (bottom), where the final signal is $F \times S$. The possibility of a Bragg peak being suppressed by a form factor minimum is evident.

Table 6.4: SAXS modeling results, at 20 °C. The parameters listed are the total membrane thickness d_{mem} , the hydrocarbon chain thickness d_{hc} and electron density δ_{hc} , the headgroup thickness d_{hg} and density δ_{hg} , the lamellar repeat distance l , the number of correlated layers n_{correl} and the layer roughness σ_{mem} .

	C20DA-PCOH	C20DA-sugarOH	C24DA-PCPC	C28DA-PCPC
Slab Model Parameters				
d_{mem} [Å]	34.5	38.3	38.2	42.9
d_{hc} [Å]	16.3	16.3	20.0	24.7
δ_{hc} [e ⁻ Å ⁻³]	0.31	0.31	0.31	0.31
d_{hg} [Å]	4.6/4.5	11.0	4.6/4.5	4.6/4.5
δ_{hg} [e ⁻ Å ⁻³]	0.41/0.38	0.385	0.48/0.43	0.48/0.43
Lamellar Correlation Parameters				
l [Å]	48.6	41.4	49.4	54.5
n_{correl}	32	60	20	15
σ_{mem} [Å]	1.4	1.4	2.0	2.0

Table 6.5: SAXS and WAXS peak positions as q -values [in \AA^{-1}] and as correlation spacings [in \AA]. Values in parentheses are of limited accuracy (see figures with data curves). For WAXS, the position of the main peak and the satellite peak is given. For SAXS, the position of the first order peak is given, before and after melting (if applicable).

	WAXS, main	WAXS, satellite	SAXS, 1 st order	SAXS, after melt.
C20DA-PCOH	$q_r = 1.53 \text{ \AA}^{-1}$ $d = 4.1 \text{ \AA}$	$(\sim 1.4 \text{ \AA}^{-1})$	$q_r = 0.129 \text{ \AA}^{-1}$ $d = 48.6 \text{ \AA}$	0.067 \AA^{-1} $93.6 \text{ \AA} (50^\circ\text{C})$
C20DA-sugarOH	$q_r = 1.53 \text{ \AA}^{-1}$ $d = 4.1 \text{ \AA}$	$(\sim 1.4 \text{ \AA}^{-1})$	$q_r = 0.152 \text{ \AA}^{-1}$ $d = 41.4 \text{ \AA}$	0.127 \AA^{-1} $49.5 \text{ \AA} (45^\circ\text{C})$
C24DA-PCPC	$(q_r \sim 1.5 \text{ \AA}^{-1})$	$(\sim 1.4 \text{ \AA}^{-1})$	$q_r = 0.172 \text{ \AA}^{-1}$ $d = 49.4 \text{ \AA}$	-
C28DA-PCPC	$q_r = 1.50 \text{ \AA}^{-1}$ $d = 4.21 \text{ \AA}$	1.43 \AA^{-1} $d = 4.4 \text{ \AA}$	$q_r = 0.115 \text{ \AA}^{-1}$ $d = 54.5 \text{ \AA}$	-

6.4.3 Discussion

The presence of a WAXS peak for all cyclic DA lipids at 20°C indicates that the membranes are in a solid phase at 20°C for all lipid types. Furthermore, in SAXS all samples exhibit a clear lamellar spacing at 20°C . The results are summarized in Table 6.5.

Interestingly, in most cases the WAXS peaks in the solid phase appear to possess a satellite peak². The main peak at $q_r \sim 1.5 \text{ \AA}^{-1}$ indicates a chain-chain spacing of $d \sim 4.2 \text{ \AA}$, while the satellite peak at $q_r \sim 1.4 \text{ \AA}^{-1}$ corresponds to a second spacing at $d \sim 4.4 \text{ \AA}$. These features could correspond to a distorted unit cell, where a molecular tilt leads to a symmetric distortion with the existence of a second spacing (see Section 3.8). The presence of multiple WAXS peaks is in accordance with the observation of multiple peaks in grazing-incidence X-ray diffraction (GID) experiments presented in Section 6.6.

During temperature scans differences between the lipid types were observed. For the longest lipid C28DA-PCPC no change in the WAXS features were observed up to 70°C , i.e. no phase transition or melting. It appears to be in a solid phase at all investigated temperatures. Similar observations were made for the shorter C24DA-PCPC, although the available data was of limited quality.

By contrast, both asymmetric C20DA lipids exhibited a loss of chain-chain correlation at temperatures around 45°C , consistent with a chain-melting transition to a fluid phase. However, in the WAXS data the contrast between solid and fluid phase is low. The WAXS peaks are not very pronounced in the solid phase, and one still observes a very

²While the diacetylenic bonds are to some extent prone to X-ray beam damage (observed as orange discoloration), no influence on scattering patterns was observed (e.g. on the satellite peaks). Repeating some measurements and performing temperature scans in inverse direction did not show any significant variations.

broad feature in the fluid phase. For conventional two-chain PC lipids such as DMPC the contrast is much clearer, as shown in Appendix A.2.

Accompanying the chain-chain correlation loss upon melting, a change in lamellar correlation is visible in SAXS for the asymmetric C20DA lipids, i.e. a jump to larger spacings (+45 Å for C20DA-PCOH and +8 Å C20DA-sugarOH). For comparison, bilayers of DPPC show an increase in spacing from gel ($L_{\beta'}$) to the fluid (L_{α}) phase of +4 Å [179], where the number of water molecules per lipid increases from ~ 12 at 20 °C ($L_{\beta'}$) to ~ 30 at 50 °C (L_{α}). For C20DA-PCOH the dramatic increase of lamellar spacing upon melting indicates a strong decoupling of the membrane lamellae. By contrast, the moderate increase of spacing for C20DA-sugarOH upon melting and small spacing in the solid phase appear to reflect a stronger inter-membrane attraction by sugar headgroups when compared to PC headgroups. Such carbohydrate-mediated attraction has been observed for example in glycolipid model membranes [34].

The electron density modeling of SAXS data confirms these results. The membrane thicknesses could be distinguished clearly from the water gap, also indicating stronger inter-lamellar coupling for the sugar headgroup and weaker coupling for the asymmetric lipids. Overall, the electron density profiles $\rho(z)$ obtained from SAXS modeling possess sufficient resolution to systematically link the scattering patterns to the structural features of the cyclic lipids.

Furthermore, the total thickness and the relative differences compare well to the results obtained from X-ray reflectivity of supported membranes (Section 6.3). The hydrocarbon core thickness for C20DA lipids from SAXS is 16.3 Å, compared to 16.7 Å from reflectivity, while for C24DA it is 21.1 Å and 22.9 Å for SAXS and reflectivity respectively. Notably, in the SAXS models the electron density is higher than in the reflectivity models, indicating that the membrane equilibration and self-healing is much improved in multi-lamellar vesicles compared to the solid supported membranes.

6.5 X-Ray and Neutron Scattering of Oriented Multilayer Samples

In addition to the lamellar spacings gained from SAXS experiments of multilayers in suspension (Section 6.4), spacings were measured with X-ray reflectivity and small angle neutron scattering³ (SANS) for solid-supported oriented multilayer stacks at low and high relative humidities as well as under bulk water. These spacings are summarized in Table 6.6.

6.5.1 Results

6.5.1.1 Neutrons

Small angle neutron scattering (SANS) is ideally suited to determine membrane spacings under bulk water in direct comparison to results under controlled humidity in air. Additionally, the off-specular scattering gives information on mechanical properties such as the membrane rigidity. Neutron scattering measurements in air were performed in a climate chamber with controlled humidity. Bulk conditions were achieved by capillary force wetting in a silicon wafer sandwich [34], also in the climate chamber.

First, the cyclic lipid C20sat was compared to the two-chain C16 ether lipid DHPC (see Figure 4.1), at high relative humidity ($RH \sim 95\%$) and under bulk water. As can be seen in Figure 6.15, at 20°C both C20sat and DHPC are highly aligned at high relative humidity with two and three Bragg peaks visible, respectively. The lamellar repeat distances (spacings) are 45.4 \AA for C20sat and 62.1 \AA for DHPC.

Under bulk water, the interpretation of the scattering patterns is not so clear (Figure 6.15, right). C20sat shows a weakening of lamellar correlation and loss of alignment, seen in the lack of a specular first order Bragg peak. Two Bragg sheet features can be seen. The Bragg sheet at higher Γ is assigned as the first order sheet, which reflects the existence of fragments with lamellar ordering and spacing $D = 47.7 \text{ \AA}$ (compared to 45.4 \AA in the dry state), but no alignment to the substrate. The other sheet at lower Γ is considered to be the signal of membrane multilayers in the process of fully unbinding.

DHPC in bulk water also had two Bragg sheet contributions, where the sheet at lower Γ and $D = 90.5 \text{ \AA}$ possesses a well-defined specular Bragg peak and is assigned as first order. The membrane stacks appear correlated and aligned to the substrate but with a surprisingly large spacing. At larger Γ and $D = 48.4 \text{ \AA}$ there is a Bragg sheet contribution from unaligned sample fragments with rather strong intensity whose position does not exactly match a lamellar second order. A time-dependent effect due to insufficient equilibration can be excluded as the time axis of the scan is along Ω . However, this spacing can also be assigned as the interdigitated gel phase of DHPC, the thermodynamically stable structure for the gel phase at full hydration [180]. Previous works [181] reported a spacing at full hydration and 22°C of $D \sim 47 \text{ \AA}$. The spacing $D = 90.5 \text{ \AA}$ obtained from the specular peak could thus be interpreted as a meta-stable “over-hydrated” state of the non-interdigitated bilayers.

³The neutron measurements and data analysis were performed in cooperation with Emanuel Schneck (Biophysical Chemistry, Uni Heidelberg)

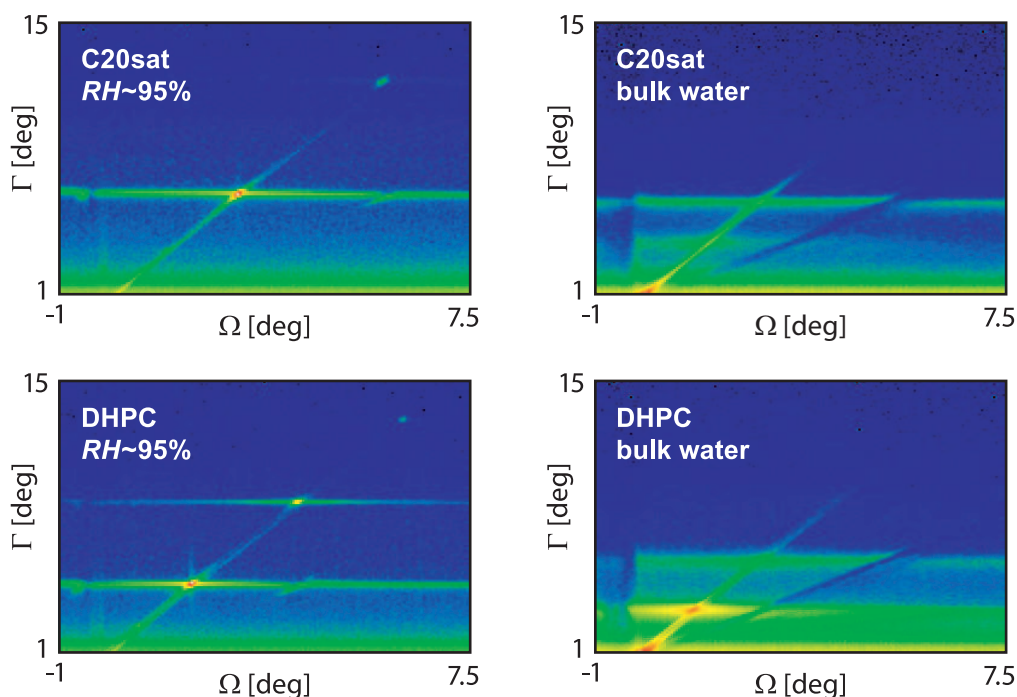


Figure 6.15: Neutron scattering intensity maps for C20sat (top) and DHPC (bottom) at 20°C, both at high relative humidity $RH \sim 95\%$ (left) and under bulk water (right). Left: At high RH both samples exhibit multiple orders of well-defined specular Bragg peaks clearly above the with off-specular Bragg-sheet contributions. This indicates well-aligned samples. Right/Top: C20sat in bulk water does not possess a clear specular Bragg peak in the first order Bragg sheet, indicating a weakly aligned sample. Right/Bottom: DHPC in bulk water has a well-defined first-order specular Bragg peak, indicating an aligned sample. However, there is an unaligned Bragg sheet at higher Γ angles (higher q -values) which does not perfectly match the position of a lamellar second order. This spacing can be interpreted as the DHPC interdigitated gel phase.

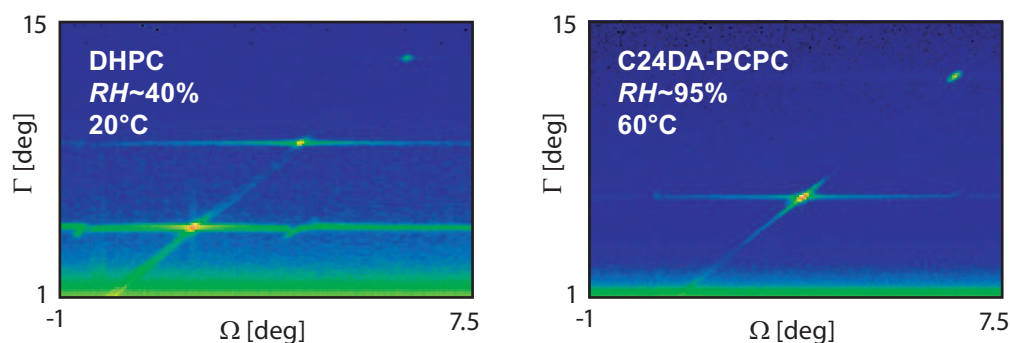


Figure 6.16: Additional neutron scattering experiments. Left: DHPC at 20°C and low relative humidity ($RH \sim 40\%$). The results are similar to those at high RH (see Figure 6.15) but the specular Bragg peaks are more pronounced, indicating better lamellar alignment. Right: C24DA-PCPC at 20°C in high relative humidity ($RH \sim 95\%$). The sample is extremely well aligned with rigid lamellae, seen in the negligible off-specular contributions.

Additionally, two other neutron reflectivity experiments were performed, as shown in Figure 6.16. DHPC was measured at 20°C and low relative humidity ($RH \sim 40\%$), with quite similar results and slightly lower spacings compared to high relative humidity (see Figure 6.15). Three lamellar orders are visible, corresponding to a spacing of $D = 61.8 \text{ \AA}$. Also, the diacetylenic C24DA-PCPC was measured at 20°C and high relative humidity ($RH \sim 95\%$). Only two lamellar orders fall within the detector range, but the Bragg peaks are extremely well defined with negligible off-specular contributions indicating rigid crystalline ordering.

6.5.1.2 X-Ray

For X-ray reflectivity, spacings were measured at room temperature ($\sim 22^\circ\text{C}$) at ambient ($\sim 30\% RH$) for C20DA-PCPC, C24DA-PCPC, C28DA-PCPC, C20sat, C24sat, DHPC and DPPC. At this temperature, all membranes are expected to be in a solid phase.

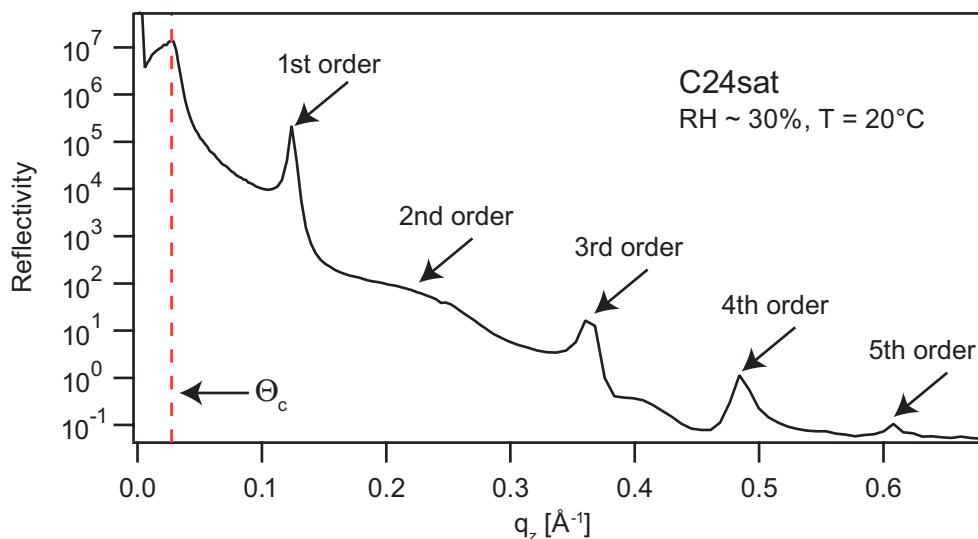


Figure 6.17: X-ray reflectivity of solid-supported multilayer stacks of C24sat at ambient conditions. Five orders of peaks are visible, with a suppressed second order. The lamellar periodicity is extracted from the equidistant peak positions.

Up to five orders of peaks could be obtained in the dry state, shown for example in Figure 6.17 for C24sat. However, the membrane stacks of saturated cyclic lipids showed greater spacings than their diacetylenic counterparts. The observed spacings were 43.4 \AA for C20sat but only 38.3 \AA for C20DA-PCPC, and 51.6 \AA for C24sat but only 43.5 \AA for C24DA-PCPC.

6.5.2 Discussion

The results using neutrons were consistent within the set of experiments, and with previous SAXS results. At high humidity, the spacing for C20sat matches the results from SAXS for other C20 cyclic lipids (see Table 6.5), and the DHPC spacing matches the value for bilayers of its ester-analogue DPPC [30, 31]. The results under bulk buffer

Table 6.6: All experimentally determined spacings D [\AA] with data from S SAXS, X X-ray reflectivity, N neutron reflectivity (all at 20 °C), except N2 neutron reflectivity at 60 °C.

lipid	low	high	bulk
C20DA-PCPC	38.3 ^X	-	-
C20DA-PCOH	-	-	48.6 ^S
C20DA-sugarOH	-	-	41.4 ^S
C20sat	43.4 ^X	45.4 ^N	47.8 ^N
C24DA-PCPC	43.5 ^X	43.5 ^{N2}	49.4 ^S
C24sat	51.6 ^X	-	-
C28DA-PCPC	48.2 ^X	-	54.5 ^S
DHPC	61.8 ^N 62.7 ^X	62.1 ^N	48.4/90.5 ^N
DPPC	57.1 ^X	-	-

can be explained by partial unbinding, and the DHPC interdigitated phase. Furthermore, the negligible off-specular contributions especially for C24DA-PCPC show that the monolayer membranes are extremely well aligned and rigid. This is consistent with the X-ray reflectivity of single solid supported monolayers (Section 6.3), where very low roughnesses were observed.

For the results using X-rays at ambient humidity, within each “family” of lipids (i.e. with and without DA core) the spacings systematically matched the expected membrane thickness depending on the number of carbon atoms in the chains (see Table 6.6). The DA lipids showed an increase in spacing of $\sim 5 \text{ \AA}$ from C20DA to C24DA, while the saturated lipids showed a increase of $\sim 8 \text{ \AA}$ from C20sat to C24sat. The spacings of saturated lipids were $\sim 5 \text{ \AA}$ and $\sim 8 \text{ \AA}$ (*sic*) greater, for chain lengths of 20 and 24 respectively, when compared to the DA lipids. These differences can be explained by a lower molecular tilt of the saturated lipids, where the more upright configuration leads to thicker membranes.

Overall, the spacings of the cyclic lipid membranes are consistent with stable monolayers, with a systematic dependency on structure. The spacings match the chain lengths, as measured with three independent techniques (SAXS, X-ray reflectivity and neutron scattering).

6.6 Grazing Incidence X-Ray Diffraction (GID) of Oriented Samples

To complement and expand the WAXS measurements (Section 6.4), X-ray grazing incidence diffraction (GID, Section 3.7) experiments were performed with solid supported oriented membrane stacks. With GID, the X-ray scattering from oriented samples can be resolved in q_z and q_{xy} (out-of-plane and in-plane components). Information on the length-scale of chain-chain distances can be gained, for studies of the chain packing, molecular tilt and the unit cell of membranes in a solid ordered phase.

In addition to the diacetylenic lipids C20DA-PCPC and C24DA-PCPC used in the WAXS experiments, GID was also performed for the saturated lipids variants C20sat and C24sat. Furthermore, the two-chain ether lipid DHPC was investigated as a reference for the saturated cyclic lipids. See Figure 4.2 and Figure 4.1 for the chemical structures.

The measurements were performed at ambient humidity ($\sim 30\%$) and at saturated vapor conditions⁴, both at room temperature ($\sim 20^\circ\text{C}$) (see also Section 4.2). Saturated vapor conditions were achieved by including a water reservoir in the sealed sample holder (see also Section 4.4).

In the following, the GID maps are presented together with their integration in q_z and q_{xy} direction. The model used for interpretation is discussed in Section 3.8 and in most cases assumes a hexagonal unit cell with next-neighbor tilt. For idealized cylinders, this type of distortion leads to two unique reflections. These reflections are indicated with green markers in the GID maps and green lines in the integrated plots. Due to the often broad peaks and thus limited resolution in q_{xy} , in the simplest model applied here a distortion of the unit cell is not considered, i.e. the (1,1) reflection is not shifted in q_{xy} from the (2,0) reflection. This does not imply an absence of unit cell distortion in a membrane sample, just the limits of the evaluation. Results are summarized in Table 6.7.

6.6.1 Results

6.6.1.1 C20DA-PCPC and C24DA-PCPC

C20DA-PCPC, dry The GID scattering pattern of C20DA-PCPC under dry (ambient) conditions displays remarkable multiple peaks (Figure 6.18), with the main in-plane reflection at $(q_{xy}/q_z) = (1.42/0.0 \text{ \AA}^{-1})$ and the main out-of-plane reflection at $(q_{xy}/q_z) = (1.42/0.90 \text{ \AA}^{-1})$. There are satellite peaks at $(q_{xy}/q_z) = (1.26/0.91 \text{ \AA}^{-1})$ and $(q_{xy}/q_z) = (1.26/1.75 \text{ \AA}^{-1})$.

In the the q_z integration (Figure 6.18 top center) the main peak at $q_{xy} = 1.42 \text{ \AA}^{-1}$ and the satellite peak at $q_{xy} = 1.27 \text{ \AA}^{-1}$ are very clearly resolved, corresponding to in-plane spacings of 4.43 \AA and 4.95 \AA , respectively. In the q_{xy} integration (Figure 6.18) the main out-of-plane peak can be clearly observed.

Assuming the simplest GID model without unit cell distortion but including tilt, the positions of the main reflections would allow calculation of the orthorhombic unit cell

⁴Under bulk water conditions no scattering signal could be obtained for any sample.

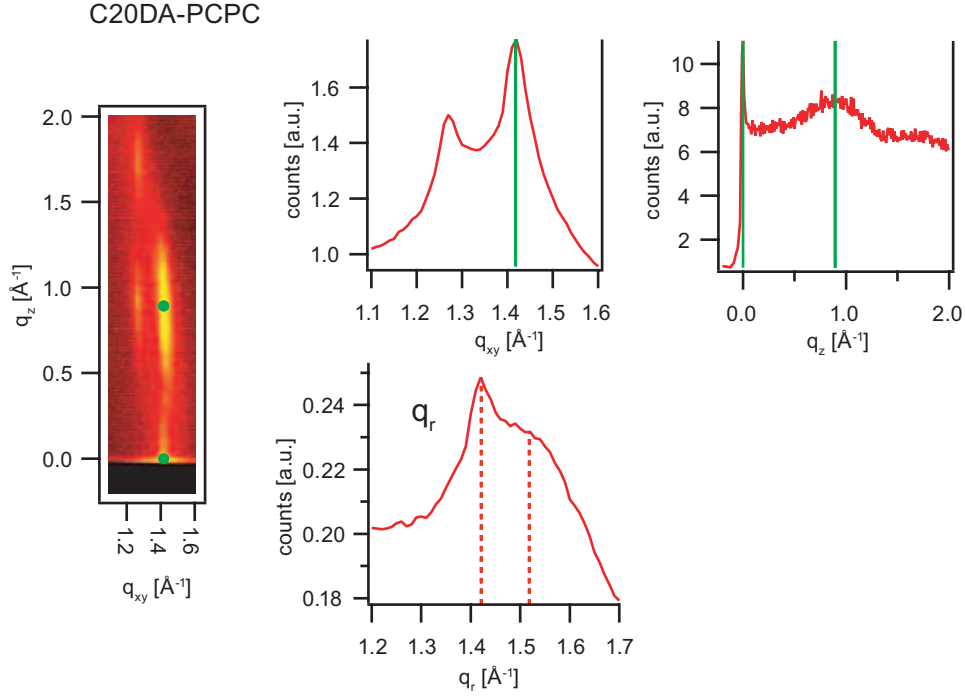


Figure 6.18: C20DA-PCPC at ambient humidity and room temperature exhibits multiple GID reflections (left). The simplest GID model with nn -tilt and no unit cell distortion is indicated with green markers and solid green lines (left and top). The pattern with four reflections cannot be accommodated in a single model of packed cylinders. The strong out-of-plane reflections show the presence of a molecular tilt. The reflections are well-defined in q_z direction, with low Debye-Scherrer contributions from unaligned sample fragments. The radial integration of the GID map is also shown (bottom), with the dotted lines indicating two possible q_r peak positions. See also Figure 6.19.

vectors $a = 8.86 \text{ \AA}$ and $b = 5.11 \text{ \AA}$ (see Figure 6.18 top, and Section 3.8), a chain tilt of $\alpha \sim 36^\circ$ and the in-plane area per molecule to $A_H \sim 45 \text{ \AA}^2$ with Equation 3.20. However, this model clearly cannot accommodate the scattering pattern observed.

Instead, two alternative models are proposed (Figure 6.19):

- A hybrid lattice, where each molecule has two segments with differing tilt vectors but identical in-plane projections of the unit cell. The unit cell is obliquely distorted, with one tilt vector towards the nearest-neighbor (nn , 40° tilt to the membrane normal), and the other towards the next-nearest-neighbor (nnn , 55° tilt). The oblique unit cell stretching follows the nnn -tilt direction. The in-plane area per molecule is 49 \AA^2 . A possible interpretation for the hybrid lattice would assume that the saturated hydrocarbon chains are strongly nnn tilted at 55° leading to the unit cell distortion, while the diacetylenic core is nn tilted but less strongly (39°) and “out-of-line” with the saturated chains. It is conceivable that very low hydration could lead to such unusual packing conditions [32].
- A lateral phase separation, where two unit cells coexist. The tilt vectors are the same as in (1), as is the oblique unit cell. Only the nn -tilt now exists in a separate orthorhombic unit cell with stretching distortion and the undistorted in-plane

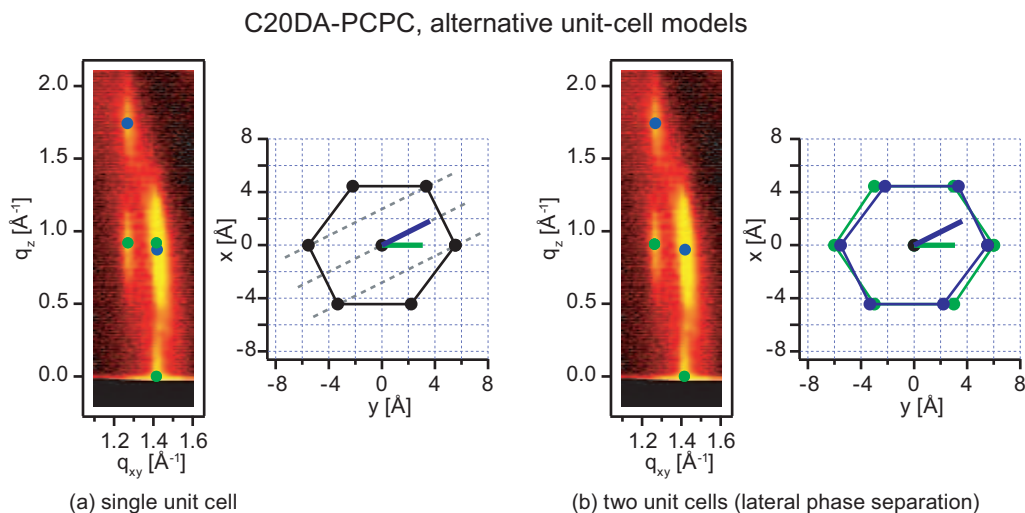


Figure 6.19: Alternative models for interpretation of the GID map of C20DA-PCPC (Figure 6.18). (a) A hybrid lattice is assumed, with a single oblique unit cell but with different tilt vectors for different segments of each lipid (e.g. chains, core). (b) Two unit cells with lateral phase separation are assumed: one oblique with nnn tilt, and one with an orthorhombic stretching and nn tilt.

spacing identical to the oblique cell. The in-plane areas per molecule are 49 \AA^2 and 53 \AA^2 for the oblique and orthorhombic unit cells, respectively. The lateral phase separation might be explained by laterally inhomogeneous partial hydration, where probably the less hydrated phase exhibits a strong 55° nnn tilt of the whole molecule as a single “cylinder”. The other phase exhibits a 40° nn tilt of the whole molecule with “standard” orthorhombic stretching with a larger area per molecule, consistent with higher hydration. The orthorhombic lattice is described by $a = 8.88 \text{ \AA}^{-1}$ and $b = 5.96 \text{ \AA}^{-1}$ with a distortion $\epsilon = 0.14$ (Equation 3.21). These values compare favorably to the results obtained with molecular dynamics simulations in Chapter 7.

However, without further experimental evidence these scenarios cannot be conclusively distinguished.

The multiple peaks are also reminiscent of the satellite peaks seen in WAXS curves of diacetylenic lipids (see Section 6.4). Therefore a radial integration was also performed for the GID map of C20DA-PCPC, shown in Figure 6.18 (top right) as integrated intensity over q_r . In this integration the GID satellite peak becomes invisible, the main peak at $q_z = 0$ remains sharp at $q_r = 1.42 \text{ \AA}^{-1}$ and the out-of-plane components form a broad peak around $q_r \sim 1.51 \text{ \AA}^{-1}$. The WAXS satellite peak q_r position matches the sharp main GID peak q_r position, while the major WAXS peak position is quite consistent with the broad GID q_r peak (see Table 6.5 for WAXS). For these comparisons of GID with WAXS one has to keep in mind that the WAXS results are obtained from samples in bulk water and are expected to be fully hydrated.

C24DA-PCPC, dry The C24DA-PCPC diffraction pattern under dry ambient conditions does not exhibit satellite peaks. In general, its features are slightly more smeared

out and diffuse than for C20DA-PCPC, corresponding to reduced in-plane ordering and reduced sample homogeneity/orientation. Unoriented sample crystallites lead to Debye-Scherrer type diffraction rings.

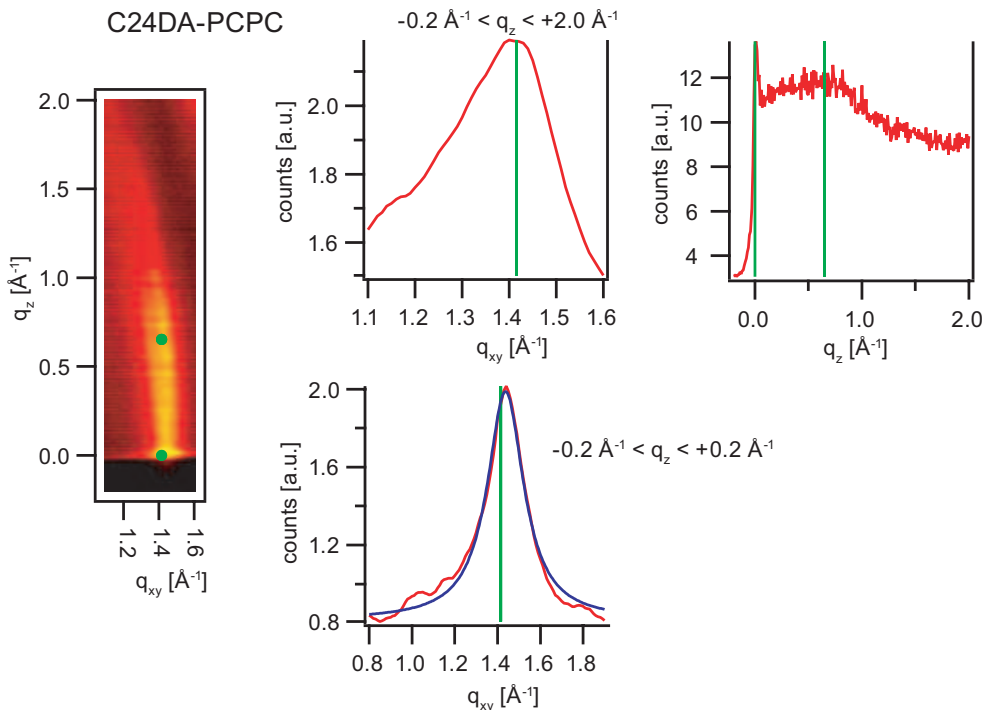


Figure 6.20: GID for C24DA-PCPC at ambient humidity and room temperature. The simple GID model with nn -tilt and no unit cell distortion is indicated with green markers and solid green lines (left and top). Bottom: A Lorentzian fit (blue) matches the peak from a short integration range $q_z < 0.2 \text{ \AA}^{-1}$ well (see also Figure 6.22). The peak broadening when integrating to greater q_z is due to Debye-Scherrer contributions which are not parallel to the q_z axis.

For the full integration q_z range, the main GID peak occurs at a minimally smaller q -value/spacing ($q_{xy} = 1.41 \text{ \AA}^{-1}$) than C20DA-PCPC, but for the short integration range $q_z < 0.2 \text{ \AA}^{-1}$ the in-plane peak is resolved more sharply at $q_{xy} = 1.44 \text{ \AA}^{-1}$ (see Table 6.7 and Figure 6.20 bottom). A Lorentzian fit shows excellent agreement with the peak shape when integrated over this short range.

Also, a distinct out-of-plane peak is visible at $q_z = 0.65 \text{ \AA}^{-1}$. In the simplest model, the q_z position indicates a molecular tilt of $\sim 28^\circ$ and a more upright configuration than C20DA-PCPC. Overall, the C24DA-PCPC GID scattering is consistent with the simple cylindrical model with tilt. Radial integration of C24DA-PCPC (not shown) results in a single broad peak at $q_r = 1.46 \text{ \AA}^{-1}$, also with no satellite features.

C20DA- and C24DA-PCPC, humid Under humid conditions (Figure 6.21), both C20DA-PCPC and C24DA-PCPC display comparable diffraction patterns with only a single broad peak observed at $q_{xy} = 1.42 \text{ \AA}^{-1}$ and $q_{xy} = 1.40 \text{ \AA}^{-1}$, respectively. For the short integration range one finds $q_{xy} = 1.47 \text{ \AA}^{-1}$ for both (not shown). These findings indicate

a minimal change from the dry state, with slightly smaller spacing at high humidity. For both lipids, no out-of-plane reflection could be resolved clearly, due to increasingly unaligned sample crystallites at higher hydration. However, features especially in the map of C24DA-PCPC appear reminiscent of the features observed for C20DA-PCPC in the dry state (Figure 6.19).

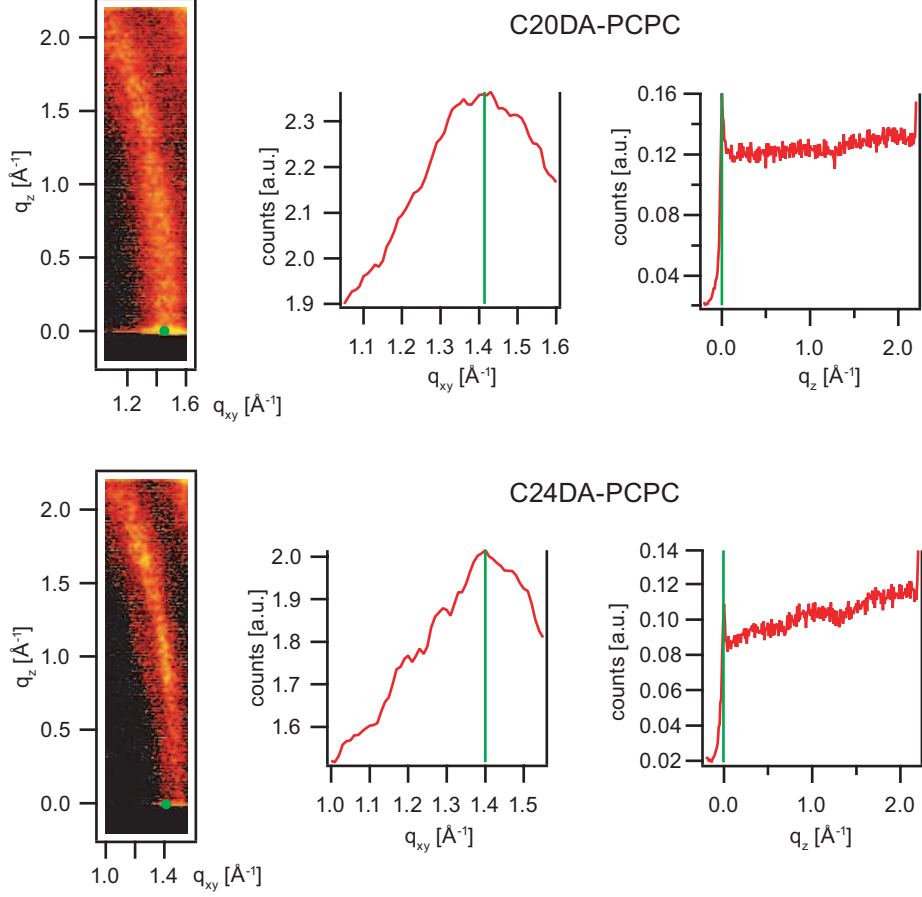


Figure 6.21: GID for C20DA-PCPC (top) and C24DA-PCPC (bottom) at high humidity and room temperature. For both lipids, the q_z -integrated peaks (middle) are slightly broadened compared to the dry state (reduced in-plane correlation length), and no distinct reflections at $q_z > 0$ (right) can be distinguished from the Debye-Scherrer contributions. Compared to the dry state, the samples appear much less aligned.

Peak widths and in-plane correlation lengths An analysis of the integrated-peak widths ($q_z < 0.2 \text{ \AA}^{-1}$) with the Scherrer equation Equation 3.18 shows a sequence of decreasing correlation lengths (increasing peak widths) from C20DA (dry), C24DA (dry), C24DA (humid) to C20DA (humid) (see Table 6.7). In the dry state, C24DA appears less ordered than C20DA, while in the humid state both are approximately equal. Higher hydration leads to worse sample alignment. Overall, the humid conditions reduced the resolution and increased the background diffuse signal.

6.6.1.2 C20sat, C24sat, and the Ether-Lipid DHPC

Dry The GID maps of saturated lipids C20sat and C24sat (Figure 6.23) show some clear differences to the DA cyclic lipids. In general appearance they are also consistent with the structurally similar ether lipid DHPC (see Figure 4.2). The peak position ($q_{xy} \sim 1.49 \text{ \AA}^{-1}$) is similar for these three lipid types, and is greater than for the DA lipids ($\sim 1.42 \text{ \AA}^{-1}$), indicating a tighter packing for the saturated lipids. There is a tendency towards broader peaks (shorter correlation length) for increasing chain length, where DHPC displays the sharpest peak (see also Table 6.7) and largest calculated lateral correlation distance. No clear out-of-plane peaks could be resolved. If the features in q_z are the shoulders of a peak symmetrical around $q_z = 0$, this would indicate fully upright molecules. One can roughly estimate [119] the expected width in q_z for a reflection of a cylindrical molecules as $\text{FWHM} = 2\pi/L$, where L is the length of the cylindrical molecule. Assuming $L = 2 \text{ nm}$ for DHPC, this results in an expected FWHM of 0.3 \AA^{-1} . However, the FWHM in q_z of the DHPC peak extracted from a Gaussian fit to the shoulder (symmetric around $q_z = 0$) is 0.88 \AA^{-1} , indicating that either the peak is broadened by poor sample microcrystalline alignment (Debye-Scherrer) or that the shoulder is partly formed by an out-of-plane peak with $q_z > 0$. For the latter case, possible peak positions are indicated in Figure 6.23 on the right. With these estimates one can give a limit for the molecular tilt angle as $\sim 10^\circ$ or less.

Humid Under humid conditions all samples showed a broadening of the chain-correlation peak and a strong increase of the out-of-plane scattering, partially in the form of Debye-Scherrer rings (Figure 6.24). The peaks shift to slightly lower q_{xy} values (higher spacings) than in the dry state, with increasing spacing from DHPC over C20sat to C24sat (see Table 6.7). For DHPC it seems reasonable to assign an out-of-plane reflection at $q_z = 0.52 \text{ \AA}^{-1}$, which can be modeled with a molecular tilt of $\sim 22^\circ$. A notable feature for C20sat and C24sat compared to DHPC is the presence of a shoulder in q_{xy} at higher q values. This is highlighted in Figure 6.22.

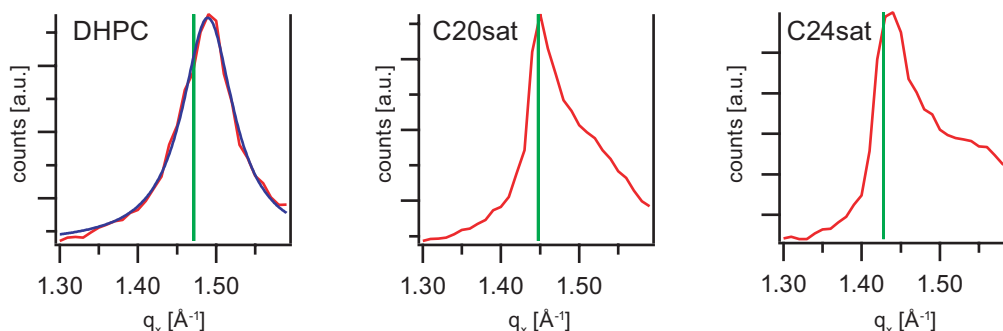


Figure 6.22: GID integrated in q_z for DHPC, C20sat and C24sat, at high humidity and room temperature. The green lines indicate the peak position matching the broad peaks from the full q_z range integration in Figure 6.24. The reduced q_z integration range emphasizes the difference between DHPC (symmetric Lorentzian shape) and the saturated lipids (strong shoulder at higher q -values).

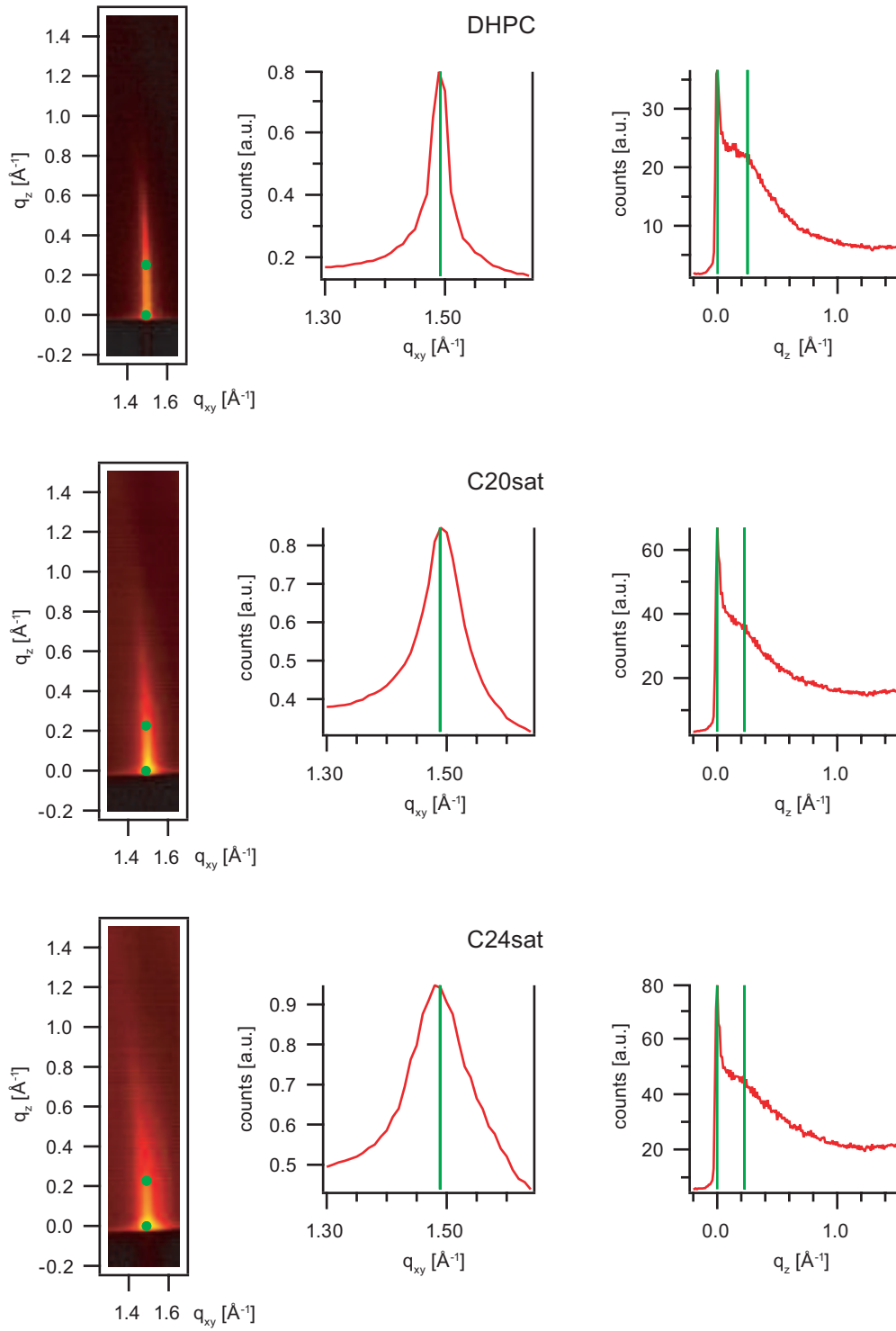


Figure 6.23: GID for DHPC (top), C20sat (middle) and C24sat (bottom) at ambient humidity and room temperature. The integrations are shown for the q_z (middle) and q_{xy} (right) direction. The peaks are well-defined in q_{xy} , and no clear reflection at $q_z > 0$ can be distinguished. The out-of-plane q_z positions (indicated in the figures on the left and right) are maximum estimates as described in the text.

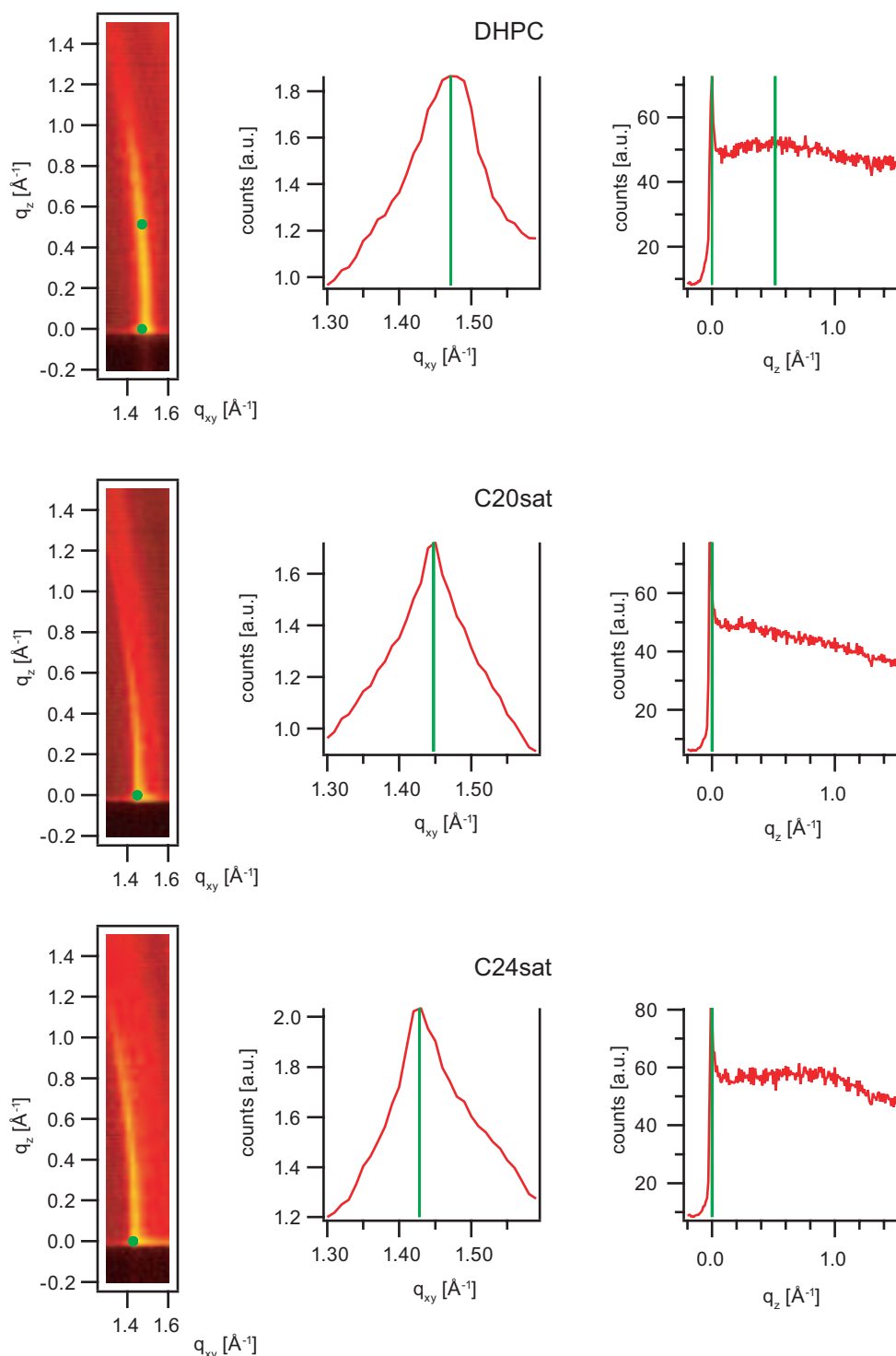


Figure 6.24: GID for DHPC (top), C20sat (middle) and C24sat (bottom) at high humidity and room temperature. The integrations are shown for the q_z (middle) and q_{xy} (right) direction. The peaks are broadened in q_{xy} due to strong Debye-Scherrer contributions from unaligned fragments (see also Figure 6.22). While no clear reflection at $q_z > 0$ can be distinguished, for DHPC (top, right) a tentative assignment of an out-of-plane q_z positions is indicated corresponding to a tilt of $\sim 22^\circ$.

Table 6.7: Summary of GID results for the simplest model which does not consider unit cell distortion due to limited resolution in q_{xy} . Shown are the q_{xy} position of the main reflection at $q_z = 0$, the equivalent spacing (d), the GID peak width (σ), the correlation length extracted from the Scherrer equation (l_{correl}), the q_z position of the main out-of-plane reflection, and the extracted chain tilt angle α . Values which could not be determined are omitted (“-”).
^avalues for the main peak, see text and Figure 6.18. ^bvalues are for the integration range $q_z < 0.2 \text{ \AA}^{-1}$

lipid	$q_{xy} [\text{\AA}^{-1}]$	$d [\text{\AA}]$	$\sigma [\text{\AA}^{-1}]^b$	$l_{correl} [\text{\AA}]$	$q_z [\text{\AA}^{-1}]$	$\alpha [^\circ]$
C20DA, dry ^a	1.42 (1.42 ^b)	4.43	0.107	53	0.90	36
C24DA, dry	1.41 (1.44 ^b)	4.46	0.207	27	0.65	28
C20DA, humid	1.42 (1.47 ^b)	4.43	0.332	17	-	-
C24DA, humid	1.40 (1.47 ^b)	4.49	0.290	20	-	-
DHPC, dry	1.49 (1.49 ^b)	4.22	0.032	175	0.25	≤ 11
C20sat, dry	1.49 (1.50 ^b)	4.22	0.067	84	0.23	≤ 10
C24sat, dry	1.49 (1.50 ^b)	4.22	0.108	52	0.23	≤ 10
DHPC, humid	1.47 (1.49 ^b)	4.27	0.080	71	0.52	(22)
C20sat, humid	1.45 (1.46 ^b)	4.33	-	-	-	-
C24sat, humid	1.43 (1.44 ^b)	4.39	-	-	-	-

6.6.2 Discussion

For all cyclic lipids at room temperature clear peaks in the GID could be observed at $q_{xy} \sim 1.4\text{--}1.5 \text{ \AA}^{-1}$, assigned to chain-chain correlations with a repeat distance of $d \sim 4.2\text{--}4.4 \text{ \AA}$ (see Table 6.7). At low humidity, these peaks are well-defined, and even allowed assignment of the out-of-plane reflections in some cases. Especially for C20DA-PCPC a complex pattern with four reflections could be interpreted with a hybrid lattice. These multiple-reflections features also resembled the more weakly resolved and diffuse features of the other samples. A clear homology could be observed in the “families” of lipids. The DA lipids showed broader peaks and more complex scattering patterns than the saturated lipids and DHPC. For example, the peak width for C24DA-PCPC in the dry state ($\sigma = 0.2 \text{ \AA}^{-1}$) is twice as large as for C24sat ($\sigma = 0.1 \text{ \AA}^{-1}$). Where possible, the extraction of a molecular tilt showed greater tilt values for the DA lipids ($\sim 30^\circ$ vs $\sim 10^\circ$ for the dry state). The greater lamellar spacings observed for the saturated cyclic lipid membranes in X-ray reflectivity (Section 6.5) match the lower tilt angle obtained by GID. The saturated two-chain ether lipid DHPC matched the saturated cyclic lipids in the appearance of its weakly tilted, highly aligned scattering patterns. The Debye-Scherrer contributions of the DA lipids were stronger, indicating less well aligned samples.

7 Structure and Thermodynamics of Lipid Membranes in Molecular Dynamics Simulations with Atomistic Detail

7.1 Introduction

There have been many molecular dynamics (MD) studies with atomistic detail simulating lipid membranes in the fluid L_α phase [150, 151, 182–184], mainly due to the relevance for simulations of biological membranes including proteins [185]. However, studies of fundamental lipid membrane properties must include the solid phases, especially the L_β gel phase. There have been studies of the gel phase at the level of atomic detail, but relying on construction of membranes by hand using crystallographic information [186–189]. Also, some commonly used force fields required a external surface tension to achieve an adequately large area per molecule in a fluid phase [184], which introduced a physically problematic and arbitrary parameter. Studies using coarse-grained simulations have been able to investigate solid phases and phase transitions on a large scale [190–193], but lack the detail to correctly reproduce features such as the tilt angle [194].

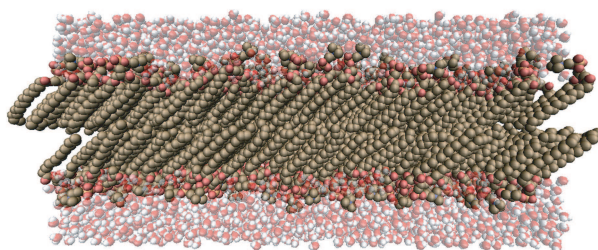


Figure 7.1: A snapshot of 800 DPPC lipids in a bilayer configuration in water, equilibrated at 300 K. The chains are well-ordered and nearly all-trans, indicating that the membrane is in the gel phase. The tilt induced by the head/chain cross-sectional area mismatch is clearly visible.

In this chapter, new approaches in MD simulations are used to study ordering of lipid membranes in solid and fluid phases and the associated phase transitions. The membranes investigated by MD consist of the standard phospholipid DPPC as well as synthetic cyclic lipids. Emphasis is put on developing the link between simulating lipid membranes and the modeling of experimental data from techniques such as differential scanning calorimetry (DSC) or X-ray and neutron scattering. The simulations are performed with atomistic detail using a united atom model (see Section 3.9) in the free simulation software package GROMACS.

As a first step, new methods to create DPPC membranes in the gel phase are investigated (see Figure 7.1). The use of the well-known lipid DPPC allows rigorous testing of basic MD simulation models against a wealth of precise experimental results and paves the way for simulations of “non-standard” membranes. Furthermore, the approaches introduced here for simulations of membranes in the gel phase do not require *a priori* knowledge of the membrane structure and allow extension to new lipids with unknown membrane ordering. Also, 3D autocorrelation of the atomic coordinates is introduced as a new tool for evaluating membrane simulations.

As the second focus besides gel phase structure, heating scans of highly ordered gel phase systems are performed to obtain details of the melting transitions. The enthalpy of the transition is investigated as a prime indicator of a first order transition. There has been a previous report on simulations which observed melting/freezing transitions of DPPC membranes using atomistic detail, however the authors used strongly disordered systems and could not reproduce first order transitions [195].

Building on the results obtained with DPPC membranes, the simulations are extended to cyclic lipid monolayer membranes. These simulations are quite unique, as only very few previous simulation studies have dealt with systems relevant to archaea membranes [196–198]. In this thesis, monolayer membranes of saturated and diacetylenic lipids in the gel phase are simulated to highlight the influence of the diacetylenic core. The results are also compared with the experimental results of Chapter 6.

7.2 3D-Autocorrelation for Membrane Simulations

As introduced in Section 2.1.1, the ordering especially of the hydrocarbon chains of lipid membranes is closely linked to their thermodynamic phases. In this section, the 3D-autocorrelation of the atomic coordinates of simulated membranes is introduced as a novel method to quantify the ordering in lipid membranes and determine the unit cell of membranes in an ordered phase, utilizing the information uniquely available from the atomic detail of MD simulations.

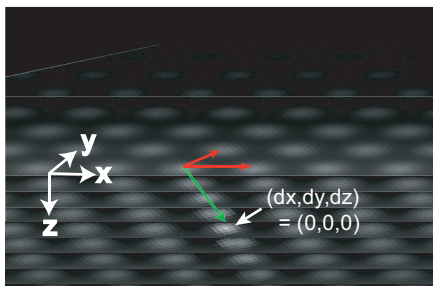


Figure 7.2: The 3D-autocorrelation of a highly ordered DPPC membrane monolayer. The red arrows indicate the in-plane vectors of the 2D unit cell, while the green arrow indicates the molecular tilt vector. The $dz = 0$ plane is in the center of the stack, each plane is a step of $\Delta z = 1 \text{ \AA}$. Note that there are no periodicities in z -direction, the apparent gaps stem from the calculation and display as a stack of XY -planes.

Determination of the Unit Cell The result of the autocorrelation of atomic positions is a 3D map (in $dx/dy/dz$, see Figure 7.2), which is normalized to unity at the central self-correlation at $(0,0,0)$. For an ordered system with certain characteristic repeat distances the map will exhibit periodic correlation maxima. The 3D-autocorrelation maps for a membrane in an ordered solid state include the full information about the 2D (in-plane) unit cell as well as the molecular tilt. As the two leaflets of a simulated bilayer are not necessarily correlated, calculations are performed separately for each leaflet (see also Section 3.8). Note that there are no periodicities in z -direction, the apparent gaps in Figure 7.2 stem from the display of the stack in discrete z -steps.

For evaluation of the unit cell from a map, one determines the in-plane vectors (at $dz = 0$) from the self-correlation peak to two linearly independent first-order peaks which fully describe the 2D unit cell (see Figure 7.2 and Figure 7.7). Exact peak positions are determined from 2D-Gaussian fits to the peaks. The molecular tilt vector is determined by the tilt angle and the tilt direction in the xy -plane projection (relative to the 2D unit cell). Both aspects are extracted from 2D Gaussian fits to the self-correlation peak at different dz (see Figure 7.2).

Quantification of Ordering The autocorrelation can be calculated from all atoms or any subselection within a single monolayer. This allows a direct test for the existence

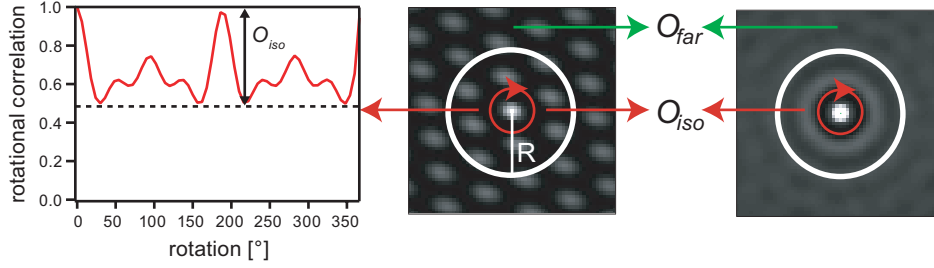


Figure 7.3: Illustration of the new order coefficients O_{far} and O_{iso} for a highly ordered and an isotropic melted system. The rotational correlation of the first order (left) produces peaks and valleys for an ordered system (middle), leading to a high value for O_{iso} . A disordered system (right) is isotropic and has low values for O_{far} and O_{iso} .

of headgroup and chain correlations (see Figure 7.6). Due to the relevance for the gel phase, in the following discussion of ordering we use the autocorrelation of all carbon chain atoms but no glycerol or head group atoms.

In the following, the distinction is made between “near” and “far” ordering. Near ordering is used here to refer to an isotropic average proximity to a neighbor, such as might occur in a viscous fluid. Conversely, far ordering refers to a crystalline (or paracrystalline) anisotropic ordering with a well-defined unit cell. As mentioned above, the existence of lateral in-plane far ordering of the chains is a major discriminating parameter between solid and melted membrane phases. To extract relevant quantitative values from the maps, we introduce two new order coefficients, O_{iso} and O_{far} (Figure 7.3), applied in the XY -plane at $dz = 0$.

O_{far} is a direct measure of far ordering, defined as the standard deviation of the $XY = 0$ plane of an autocorrelation map beyond a given radius R excluding the nearest neighbor. In this work, we used $R = 0.85$ nm. O_{far} essentially measures the “spikiness” of the autocorrelation map: a highly ordered system has strong correlations and anti-correlations leading to a large standard deviation and a large value of O_{far} . By contrast, a fully disordered system will produce a uniform level in the autocorrelation with no spikes so that the standard deviation and thus O_{far} will be equal to zero.

O_{iso} represents the rotational (an)isotropy in the autocorrelation map. As the effect is most prominent within the first order, the calculation of O_{iso} is restricted again to within the radius R . In detail, O_{iso} is obtained by rotating the map by an angular step, multiplying the pixel values with the original reference map and summing over the result within R . For absolute comparison between maps of different resolution and different R the values are normalized per pixel of the summation. O_{iso} is then defined as the maximum amplitude difference over a full rotation (Figure 7.3 left). The alternation of peak and valley overlaps of an ordered system results in an oscillating rotational correlation function (shown in Figure 7.3) with a high value of O_{iso} , whereas a smooth isotropic near order ring results in an essentially flat curve with $O_{iso} = 0$.

Often, membrane simulations are compared with H_2 -NMR S_{CD} order parameters [199]. However, these parameters can be difficult to obtain for united-atom or coarse-grain simulations, due to the lack of explicit hydrogens. Furthermore, these order parameters are obtained relative to the membrane plane, not the molecular axis. Thus, for strongly

tilted molecules in the gel phase the NMR order parameters are not ideal and are not used in this thesis.

7.3 DPPC

7.3.1 Creating Highly Ordered Gel Phase Membranes

First, ways to obtain highly ordered equilibrated DPPC gel phase system were explored. A main goal was that the membrane gel phase systems should represent experimental results while using as little *a priori* information as possible, in order to establish methods for tackling systems less well known than DPPC. Previously, best ordering has been achieved by constructing membranes using crystallographic information approach, which is in contrast to the demand here for little *a priori* information. So, in the following, the focus lies on methods that rely to a large extent on self-ordering.

Self-organization effectively implies a kind of freezing process. However, some drawbacks of creating a gel phase system by simple cooling (“natural freezing”) will be highlighted, especially in view of the fact that only extremely fast cooling rates are accessible due to computational limits. As a consequence, two “assisted freezing” methods are introduced, which effectively bypass a nucleation stage and significantly accelerate equilibration to high ordering compared to the method of “natural freezing”. It will be shown that one can obtain highly ordered systems which match many known experimental parameters.

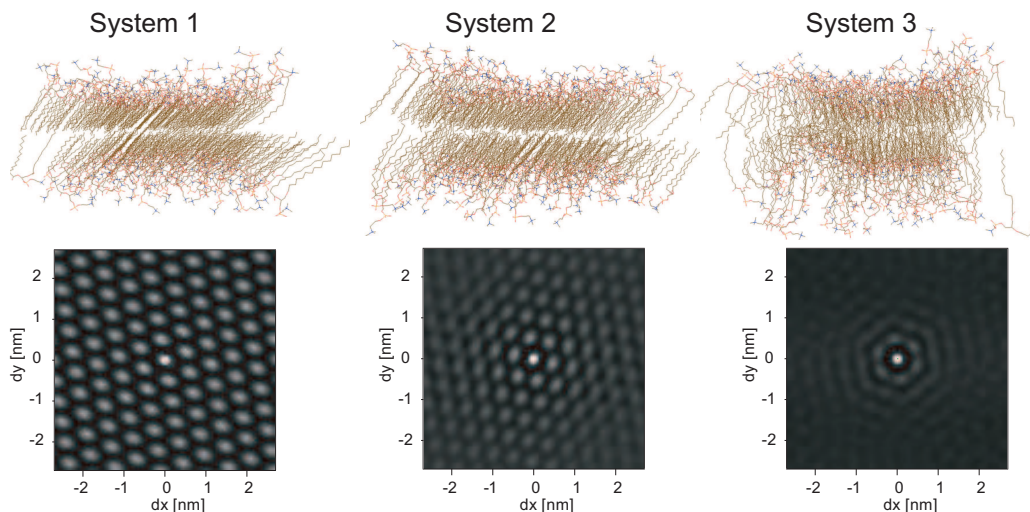


Figure 7.4: The three systems with 288 DPPC molecules which were used to compare the gel phase construction methods and their corresponding autocorrelation maps. System 1 (left) was made using initially fixed chain dihedrals, system 2 (middle) was made with an artificially compact topology, and system 3 (right) was made by cooling/freezing. The autocorrelation maps highlight the different levels of ordering achieved.

All three methods started with 32 upright lipids randomly rotated around the z -axis, placed in a 4×4 bilayer configuration (see also Section 4.5). To maximize ordering, 270 K was chosen as the starting temperature and the systems made with the three

methods are compared at this temperature. In Section 7.3.2 a system constructed and equilibrated at 300 K is also discussed. The bias in methods (1) and (2) is considered small compared to explicit construction, so that one might consider them as “assisted freezing”, while (3) is “natural freezing”. The presented strategies are:

1. Initially all chain dihedrals are fixed in all-trans configuration by definition as improper (non-rotating) dihedrals in the topology (see also Section 3.9). Temporarily fixing the chain dihedrals reduces the conformational space the lipid molecules have to sample in order to find a packing minimum, which is expected to reduce the necessary equilibration times. In practice, equilibrating with this topology lead to a very compact system, which remained highly ordered upon exchange for the unmodified lipid topology with normal chain dihedrals.
2. One starts with a dedicated topology that exhibits a tendency to form compact ordered systems due to a severely mismatched attraction/repulsion and hydration balance. A DPPC topology generated by PRODRG [200] tends towards this behavior, as do some standard CHARMM force fields [184]. Here, a PRODRG-generated topology was used, further modified by removing all partial charges. The lack of partial charges lead to even more compact systems, but for use of the system with the correct topology a stepwise reintroduction of charges was necessary, performed in multiple short equilibration steps to avoid system explosion.
3. Here, the standard unmodified lipid topology was used for slowly cooling a melted bilayer system of 32 lipids over 600 ns at 0.1 K/ns from 330 K to 270 K. The system was thus kept for 450 ns at temperatures below the expected melting temperature for DPPC of $T_m = 315$ K.

The 32 lipid starting systems created by methods (1)-(3) were multiplied into the desired final system size (here 288 lipids), and equilibrated with the correct standard topology for 25 ns. The resulting equilibrated membranes are shown in Figure 7.4. In the following, these 288 lipid starting systems created by these methods at 270 K are denoted by system (1), system (2) and system (3), respectively¹. A visual inspection of the systems shows the clear trend (see also Table 7.1) that system (1) has the highest ordering, followed by system (2) and last system (3).

In the following, we will focus on quantifying correlation and ordering, not on structural details. Comparison to experimental results are made where possible, taken from Nagle [28] if not mentioned otherwise. Comparison was made for different aspects:

- Looking at the total fraction of gauches in the hydrocarbon chains, one sees that system (1) is nearly all-trans with 0.71 gauche/chain. For system (2), one sees an overall higher level of gauche rotamers with 1.14 gauche/chain, while system (3) is very disordered with 2.11 gauche/chain, which is close to the value of 3.30 gauche/chain observed for a melted system. Experimentally, values of 1.0 gauche/chain or less are observed [69, 202, 203].
- The fraction of gauches depending on the position of the bond in the carbon chains is shown in Figure 7.5. Only for system (1) a clear maximum of gauches is observed

¹In general, the results as presented here are typical and reproducible, though naturally there is a certain random component. Not every construction run will result in a perfectly acceptable system, where the selection is at the discretion of the investigator.

Table 7.1: Selected parameters for different systems of 288 DPPC. System (1) displays the highest ordering and greatest tilt angle.

	tilt	$O_{iso} [\times 10^2]$	$O_{far} [\times 10^2]$	gauche/chain
270 K, method (1)	45°	2.0	10.7	0.71
270 K, method (2)	32°	0.71	3.4	1.14
270 K, method (3)	4°	0.12	1.4	2.11
300 K, method (1)	37°	1.4	7.5	0.94
330 K, fluid	0°	0.02	0.5	3.30

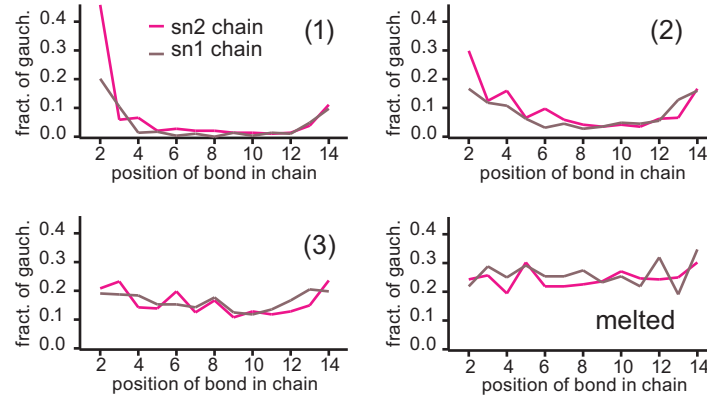


Figure 7.5: Comparison of the distribution of gauche dihedrals along the *sn1* and *sn2* hydrocarbon chains for the 288 lipid systems (1), (2), (3) at 270 K and a melted system at 330 K. The data were extracted from a snapshot of the final frame after 50 ns at 270 K. System (1) shows a strong increase of gauche torsions at the first position in the *sn2* chain.

at the start of the *sn2* chain [189, 199, 202, 204, 205].

- Furthermore, we could confirm for all systems that we have a gel phase with chain correlation but no headgroup correlation [201], as shown in Figure 7.6.
- The highly ordered system (1) has a chain tilt value of 45°, whereas in the less ordered system (2) the chain tilt is 32°. System (3) is weakly ordered and shows a very small average molecular tilt.
- The area per molecule is 0.55 nm², 0.52 nm² and 0.52 nm² for systems (1), (2) and (3) respectively. All values are slightly high compared to the experimental value of 0.48 nm².

Quite striking is that the chain tilt angle appears to be correlated with the system order/disorder. The greater tilt and lattice strain in system (1) apparently correlates with the greater area per molecule. However, the area per molecule and the chain tilt are interdependent factors. Remaining pockets of disorder in system (3) are reminiscent of previously reported simulation results [195, 206], but appear rather artefactual. Highly ordered systems did not show any remaining significant disorder in the simulation box, and no interdigitation.

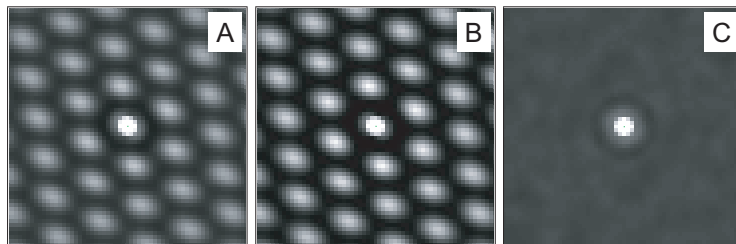


Figure 7.6: Autocorrelation of system (1) with different atom subsets: (A) All lipid atoms. (B) Chain carbons. (C) All lipid atoms except chain carbons. It can be clearly seen that only chain-chain correlations exist with no trace of headgroup correlations. This is the definition of an L_β gel phase (as compared to an L_c crystalline phase) [201].

7.3.2 Unit Cell of Gel Phase Membranes

Maybe the strongest feature of the 3D autocorrelation (Figure 7.2) is that it becomes possible to quantitatively compare the simulation unit cell to experimental unit cell parameters obtained with high accuracy from scattering experiments such as wide angle X-ray scattering (WAXS) or grazing incidence X-ray diffraction (GID) (see also Chapter 6 and Section 3.8). Previously suggested approaches to use simulations for modeling of scattering data [51, 188, 206, 207] are not based on the unit cell.

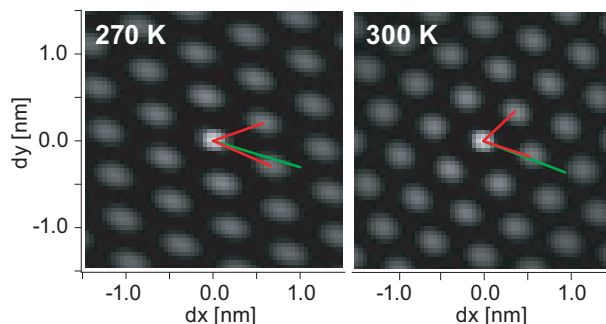


Figure 7.7: XY-plane at $dz = 0$ from 3D autocorrelation of two systems of 288 DPPC, at 270 K (left) and 300 K (right), independently constructed with method (1). Red lines indicate the in-plane unit cell vectors, while the green line indicates the tilt vector projection (see also Figure 7.2). At 300 K, the chains are tilted at 37° , compared to 45° at 270 K. The increased tilt leads to the stronger unit cell distortion.

In order to avoid extremely long equilibration times in the gel phase system after temperature changes, a 300 K system was constructed separately and equilibrated directly at 300 K and compared with the system (1) at 270 K. Both systems exhibited less than one gauche rotamer per chain with an increased fraction at the first position of the *sn*2 chain, and were highly ordered (see Table 1). Also in both cases a parallel co-linearity was observed between chains in the two monolayers. These features are expected and required for fully hydrated DPPC [28].

The 3D autocorrelation maps are shown in Figure 7.7 at $dz = 0$ where the oblique in-plane unit cell vectors and the tilt vector are indicated. A chain tilt of 45° was observed at 270 K, and a tilt of 37° was observed at 300 K, which is close to the experimentally

Table 7.2: DPPC simulation and experimental unit cell parameters. Experimental parameters taken from Sun *et al.* [30]. Values concerning chain-packing perpendicular to the tilt (a and d_{20}) are slightly smaller in the simulation than in experiment, indicating a minor deficiency of the lipid topology. Values with components in direction of the tilt (b and d_{11}) are greater, due to the greater tilt and unit cell distortion observed in the simulations.

	a [Å]	b [Å]	d_{20} [Å]	d_{11} [Å]	ϵ
simulation @ 270 K	8.18	6.65	4.09	5.16	+0.291
simulation @ 300 K	8.36	5.85	4.18	4.79	+0.175
experiment	8.488	5.64	4.244	4.182	+0.131

observed value of 32° at room temperature [30, 31, 208, 209].

For DPPC in the gel phase at full hydration a tilt in direction of the nearest neighbor is expected, and in the simulations we do indeed observe that the tilt vectors are approximately directed towards the nearest neighbor. In both cases the unit cell is distorted as a consequence of the tilt, and distorted more at 270 K than at 300 K. In general, nearest-neighbor tilt is expected to induce a stretching distortion of the hexagonal lattice which can be described by orthorhombic (more accurately face-centered rectangular) unit cell vectors a and b with stretching in direction of b . See also Section 2.1.1 and Section 3.8. The vectors indicated in Figure 7.7 describe the unit cell for arbitrary symmetry.

However, in the simulations slightly oblique unit cells were observed, with three distinct spacings. The small deviations from an orthorhombic unit cell are considered a meta-stability issue of the simulations [188]. For comparison with orthorhombic unit cell parameters from experiment, two spacings are extracted from the simulation: the spacing along the stretching (equal to the d_{20} spacing) and the approximate perpendicular spacing $d_{11} = (d_{1,+1} + d_{1,-1})/2$. From these, we find the in-plane orthorhombic unit cell vectors according to Equation 3.19. At 300 K we find the in-plane vectors $a = 8.36$ Å and $b = 5.85$ Å, and at 270 K $a = 8.18$ Å and $b = 6.65$ Å (see also Table 7.2). For DPPC at 24°C (297 K) Sun *et al.* [30] reported in-plane orthorhombic unit cell vectors of $a = (8.488 \pm 0.0008)$ Å and $b = (5.64 \pm 0.02)$ Å. From the small differences seen for the vector a (perpendicular to the tilt) it appears that the simulation chains pack slightly more densely than seen in experiment. The larger values of b seen in the simulations are consistent with the larger tilt angles.

From the simulation unit cells we can obtain the distortions ϵ and ϵ_{chain} (see Section 3.8 Equation 3.21 and Figure 3.12). The calculated in-plane distortions are $\epsilon(300 \text{ K}) = +0.175$ and $\epsilon(270 \text{ K}) = +0.291$. From Sun *et al.* one can calculate an experimental in-plane distortion of $\epsilon(297 \text{ K}) = +0.131$, which is smaller than the simulation value and consistent with the lower experimental tilt. In both simulations we find for the distortion perpendicular to the chains $\epsilon_{chain}(300 \text{ K}, 270 \text{ K}) \sim -0.03$, which matches $\epsilon_{chain}(298 \text{ K}) \sim -0.03$ reported by Sun *et al.* This indicates that the molecular shape is well-represented by the simulation lipid topology.

The area per molecule at 300 K is less than at 270 K (0.50 nm^2 and 0.55 nm^2 , respectively) which correlates with the lower tilt angle at 300 K. At both temperatures the area per molecule and tilt angle is higher than experimental values at room temperature (0.48 nm^2

and 32°). One possible cause for the discrepancies of area and tilt between simulation and experiment could be non-equilibrium headgroup hydration. Indeed, the observed ratio of area/tilt matches a predicted tendency for combinations of area/tilt/hydration very closely [209]. In general, the expected dependency of chain tilt on the effective headgroup/chain cross-sectional areas is calculated according to:

$$\cos \alpha = \frac{2A_c}{A_H} \quad (7.1)$$

where α is the chain tilt relative to the membrane normal, A_c is the cross-sectional area of a single chain and A_H is the in-plane (interfacial) area of the headgroups (see also Section 3.8 Equation 3.20). In experiment, the tilt is seen to be temperature dependent [31] as a consequence of the chain cross-sectional area A_c increasing for higher temperatures compared to a more or less constant headgroup area A_H . One can calculate the area per chain A_c from

$$A_c = \frac{ab \cos \alpha}{2}. \quad (7.2)$$

In the simulations, the results were $A_c(300 \text{ K}) = 19.5 \text{ \AA}^2$ and $A_c(270 \text{ K}) = 19.2 \text{ \AA}^2$. The simulations correctly predicted a reduced area per chain at lower temperatures and matched the experimental values of $A_c(300 \text{ K}) \sim 20.1 \text{ \AA}^2$ and $A_c(270 \text{ K}) \sim 19.6 \text{ \AA}^2$ within 3 %. Also, an area per chain which is slightly too small in the simulations relative to experiment matches the observation of an increased chain tilt. This observation is directly linked to the values of a reported above, which underestimated the experimental value for a slightly.

7.3.3 Chain Melting Transitions

7.3.3.1 Phase Transition Enthalpy

In analogy to differential scanning calorimetry (DSC) experiments, heating scans of the gel phase systems were performed (see Section 2.1.1). In Figure 7.8 the total energy for a heating scan of system (1) with 0.5 K/ns is shown. The system energy exhibited a discontinuous jump during melting at 321 K, identified as the phase transition enthalpy (pV terms are small). At the same time, a loss of chain ordering is observed (see Section 7.3.3.2), confirming the observation of first-order chain melting transition. The transition for this heating scan occurred close to the experimental main transition temperature for DPPC at 314.5 K, but statistical variations and the heating rate dependency of the simulation melting temperature will be discussed later.

The plot of the total energy over temperature can be fitted with an analytical function composed of a sigmoid and two independent linear components to extract the phase transition enthalpy. Furthermore, if the energy plot is smoothed it is possible to directly plot its derivative (excess heat capacity) in a fashion analogous to DSC experiments. Alternatively, the derivative of the sigmoidal fit to the energy can be used. The plots for both methods are shown in Figure 7.8 with subtracted constant offset.

Note that the peak width of this microscopic transition does not correspond to macroscopic calorimetric peak widths, which are described by the equilibrium occupation (frozen/melted) of an ensemble of cooperative units. Rather, the microscopic transition is a single system melting event, which is expected to be quasi-instantaneous and appears to be broadened due to limited equilibration at fast heating rates.

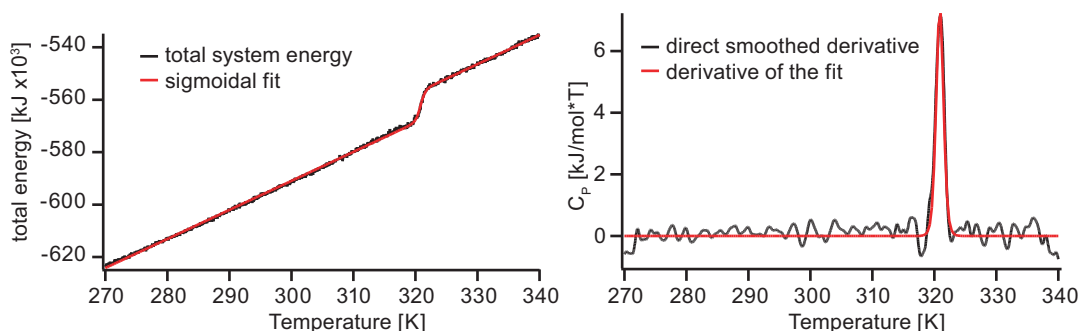


Figure 7.8: Total energy over temperature for a heating scan of system (1) at 0.5 K/ns. Left: The total system energy and a sigmoidal fit with sloped baseline. Right: The derivative of the smoothed total system energy H (equal to the excess heat capacity c_p) and the derivative of the sigmoidal fit to the energy show excellent agreement (both with subtracted constant offset). The full-width at half-maximum (FWHM) of this transition is 1.5 K. Note that this cannot be directly compared to DSC peak widths.

The phase transition enthalpy per mole lipid can be compared with experimental values simply by normalizing to the number of DPPC molecules. An enthalpy of $\Delta H = 40$ kJ/mol was obtained for the highly ordered system (1), but only $\Delta H = 24$ kJ/mol for the less ordered system (2). The values were taken from scans where no distinct pre-transitions (see Section 2.1.1) were observed, and ΔH should thus include the pre-transition enthalpy and be ~ 10 – 20% higher than expected for the main transition

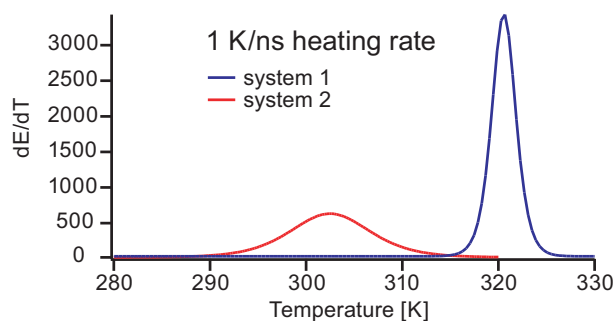


Figure 7.9: Comparison of excess heat capacity scans at 1 K/ns for systems (1) and (2). System (2) shows a broad, early melting transition with low transition enthalpy (24 kJ/mol), while system (1) shows a sharp transition with a high enthalpy (40 kJ/mol).

alone. $\Delta H = 40$ kJ/mol matches both literature values for the DPPC main transition of $\Delta H = 30$ – 40 kJ/mol [9, 73, 74] and the reference measurement shown in Appendix A.3 where $\Delta H = 39.7$ kJ/mol.

The melting transitions for system (1) and (2) are compared in Figure 7.9. It was consistently observed that the lower ordering of system (2) prevented a sharp melting transition. Instead, a nearly continuous transition around 305 K was observed, which differs strongly from the known lipid phase transition behavior. The broad transition of system (2) resembles melting transitions reported previously [195], both in width and position. System (3) is much more disordered and displays practically no first-order transition (not shown). As a consequence, only the details of the phase transition for system (1) will be discussed in the following.

7.3.3.2 Details of the Transition

Beyond enthalpic considerations, some structural features of the melting transition were investigated in detail. These were the area per molecule, the fraction of gauches, the chain tilt angle and the new order coefficients O_{far} and O_{iso} (see Section 7.2). Note that the chain tilt was extracted from the 3D autocorrelation maps. This definition gives the same quantity which would be observed in X-ray diffraction experiments and avoids assigning the molecular axis between arbitrary atoms.

In Figure 7.10 the development of these parameters is shown during a heating scan at 0.5 K/ns. There is a distinct sequence of melting and there are different relaxation times of the individual parameters. The area per molecule showed a slow and small but continuous increase below the melting transition, similar to the fraction of gauches. The order coefficients showed a clear reduction of correlation in the system below the phase transition, until an abrupt complete loss of order at the phase transition (Figure 7.10 and Figure 7.11). Both order coefficients showed similar trends, but the isotropy O_{iso} showed the clearest contrast to the fluid phase. The molecular tilt angle was quite stable until the melting transition, even while the system lost ordering.

Below the melting transition a tilt angle reduction of approximately $-0.06^\circ/\text{K}$ was observed, which is nearly consistent with the experimentally determined temperature

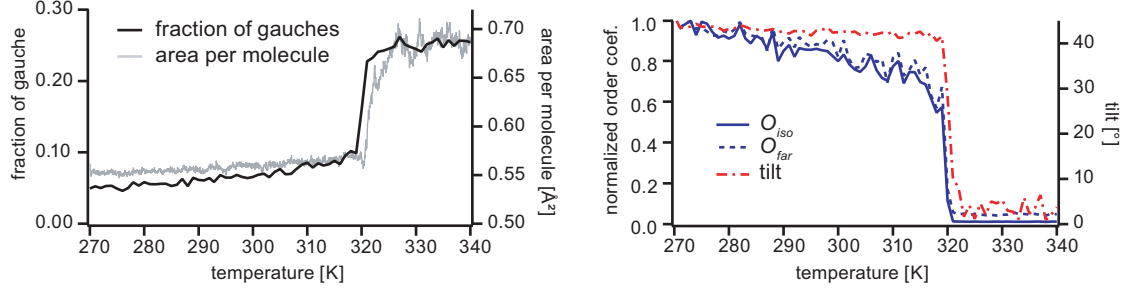


Figure 7.10: An exemplary melting transition of system (1) at 0.5 K/ns. For better comparison, the order coefficients are normalized. The changes in area per molecule and tilt angle trail the change of ordering by $\sim 1 \text{ K} = 2 \text{ ns}$.

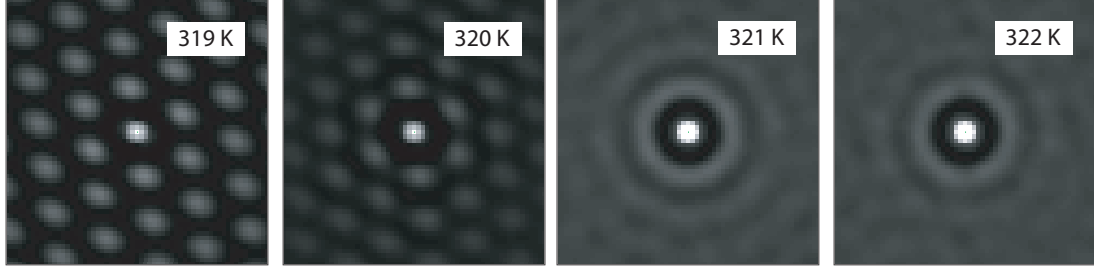


Figure 7.11: Autocorrelation of the chain carbon atoms of the top monolayer of system (1) during melting, at 0.5 K/ns. The intensity of the images at 321 K and 322 K is scaled by a factor of two to highlight their features.

dependence of the tilt of $-0.10^\circ/\text{K}$ to $-0.16^\circ/\text{K}$ [31]. Also, the tilt angle remained higher at 300 K than for a system constructed directly at 300 K (see Section 7.3.2). These observation again indicate that equilibration can take exceedingly long in the gel phase.

Moreover, a distinct sequence of melting events was observed. The fraction of gauches as well as O_{iso} and O_{far} transitioned approximately $\sim 1 \text{ K}$ ($\triangleq 2 \text{ ns}$) before the area per molecule and tilt angle. This observation is consistent with the line of thought that parameters directly related to entropy and ordering (fraction of gauches, O_{iso} and O_{far}) are the primary factors in a melting transition, while parameters such as area per molecule and tilt are secondary relaxation processes. The time difference of 2 ns is probably dominated by the intrinsic relaxation time of the system, and will vary with system size, simulation parameters, etc.

Finally, it was observed that the entire membrane melted instantaneously, indicating a single cooperative unit. This was confirmed in all heating scans discussed below, as well. One can pose the question whether it might be possible to resolve multiple discrete melting events in future studies using larger systems and slower scan rates, and determine an equilibrium cooperative unit size for the simulation systems.

7.3.3.3 Statistical Nature of T_m and Effect of the Heating Rate

To gain some insight into the statistical nature and the rate dependency of the microscopic T_m , we performed multiple runs at scan rates of $r = 5$ K/ns, 2 K/ns, 1 K/ns and 0.5 K/ns. At these scan rates one observes non-equilibrium effects such as a rate dependency of the melting transition and the equilibration time to the melted phase (see Figure 7.12). In the following, the area per molecule is used as the indicator of transition temperature. The melting point of a single melting event is defined at the onset of the transition, denominated by T_m . This definition excludes most effects of slow box equilibration after melting begins. Important to note is also the absence of re-freezing events. As also seen during system construction, freezing cannot lead to correct system ordering on the timescales investigated here.

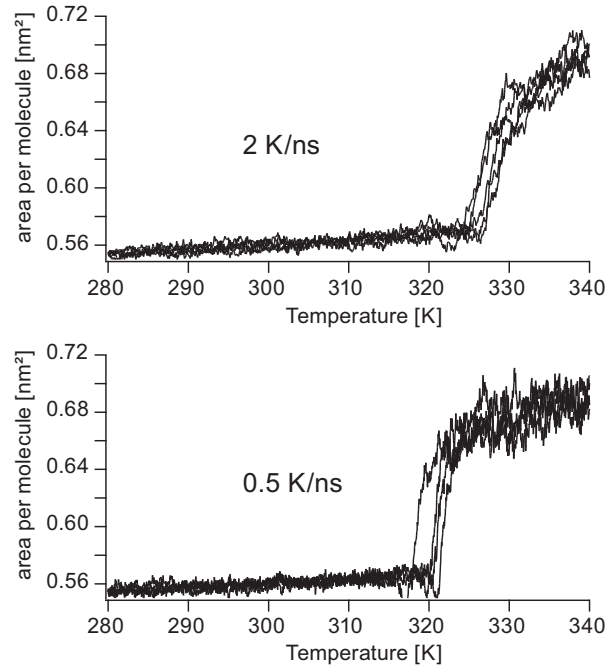


Figure 7.12: Area per molecule during heating scans for system (1) displaying melting events. For a given scan rate one finds a distribution of the microscopic T_m . For the faster scan rate one observes a higher average melting temperature. Also, the equilibration process after begin of the melting event is spread over a considerably greater temperature range for faster scan rates.

Qualitatively, delayed melting for faster scan rates is observed. The obtained values of T_m are shifted significantly upwards for fast scanning rates and it was observed that melting events can occur over a temperature range of several degrees around the average value. The average microscopic melting temperature as well as its standard deviation for each rate r are shown in Figure 7.13. It is found empirically that T_m follows an approximately logarithmic behavior. For the slowest scan rate, an average transition temperature of $T_{m,avg} = 320$ K was found.

For very slow scan speeds (which are inaccessible with current computational power), a melting/refreezing equilibrium should appear, which should lead to a deviation from

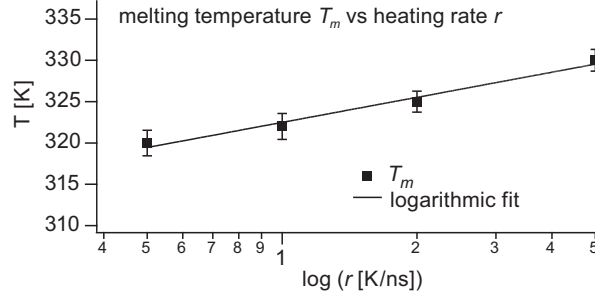


Figure 7.13: The dependency of T_m on the heating rate was empirically found to be logarithmic, but must deviate towards a finite average melting temperature for very slow scan speeds. The error bars are the standard deviations.

the logarithm and to a saturation of T_m at the equilibrium transition temperature determined by the molecular force field. The current simulations provide an upper bound estimate for the equilibrium phase transition temperature, so that the value defined by the lipid topology used in this thesis should be below 320 K and close to the experimental value of 314.5 K.

Furthermore, the distribution of T_m for a single scan rate was investigated in more detail. T_m was extracted from a total of 15 runs at 0.5 K/ns (not shown), from which a standard deviation of ~ 1.5 K (FWHM ~ 3.5 K) around 320 K was obtained. This distribution is not analogous to the temperature-width of the melting transition of an experimental system with an ensemble of independent cooperative units, as the simulated distribution is a non-equilibrium property for fast heating rates without refreezing (and the cooperative unit limited by the system size). As a consequence, it is not directly comparable to the quasi-static peak widths (~ 0.2 K FWHM) obtained from DSC experiments.

7.3.4 Pre-Transition and Ripple Phase

As discussed in Section 2.1.1, for most phosphatidylcholine (PC) lipids, below the main phase transition a solid phase with a distinct rippled appearance is observed experimentally. The wavelength of the stable ripple phase is given as $\sim 13 - 15$ nm for DPPC [71, 210, 211]. The first-order pre-transition from the gel phase to the ripple phase has a transition enthalpy of $\sim 2 - 10$ kJ/mol (see [9, 73, 212] and Section A.3).

For the highly ordered and stable system (1) with 288 lipids no pre-transition or ripple phase was observed at any system size or scan rate. By contrast, during heating scans with the less ordered system (2) some distinctly rippled structures formed spontaneously below the main melting transition as shown in Figure 7.14. As the simulation with 288 lipids had a box side length of only around 8 nm, a larger system with 800 lipids was also simulated with a box side length of around 14 nm. For both system sizes ripple formation was observed with similar amplitude and with wavelengths determined by the box dimensions. During main transition melting, the small system showed artefactual behavior and collapsed due to the increasingly high curvature. The large system transitioned smoothly into a fluid phase.

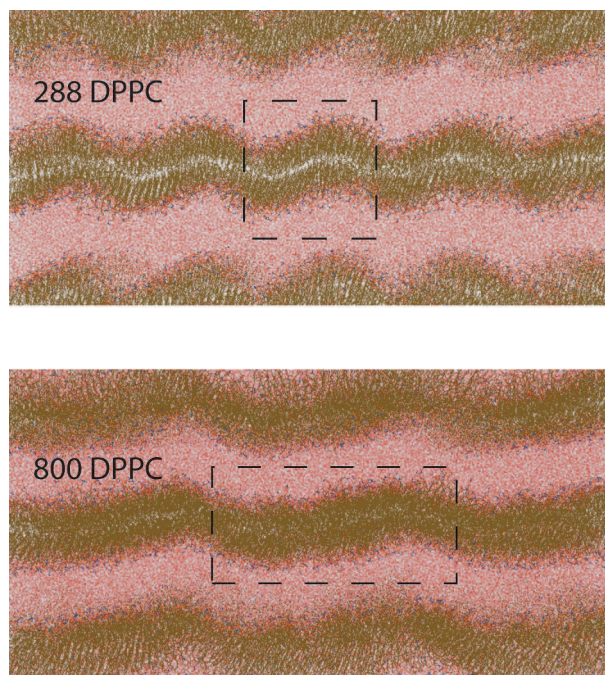


Figure 7.14: Ripples observed in simulations with 8 nm and 14 nm box side lengths, here at 300 K. The structures formed during heating scans with 0.5 K/ns of the less ordered system (2). The simulation boxes are indicated in the figures.

For both system sizes, the ripples were asymmetric with a long and short arm, compatible with experimental findings. During formation of the ripple, the average molecular tilt angle decreased, and the ripple vector formed parallel to the molecular tilt angle. Visual inspection showed that local melting at defects present in the membrane drives membrane bending or rippling. It appears that local melting in one leaflet induces curvature towards the side of that leaflet. The energy changes involved are shown in Figure 7.15, and are to a large extent analogous to the experimental DSC scans (see Appendix A.3). The observed pretransition energies were on the order of 7-15 kJ/mol, which is slightly larger but still comparable to the experimentally found values.

7.3.5 Discussion

Overall, it could be shown that even without using *a priori* knowledge, construction of systems that satisfactorily represent DPPC gel phase membranes is possible using the method with initially fixed chain dihedrals. This approach produced highly ordered gel phase systems in a simple fashion. Comparing the construction methods for gel phase membranes, it appears that creating a gel phase starting system by freezing a small building block is very unlikely to yield useful results without extremely long equilibration. It is conceivable that freezing a larger system than 32 lipids could lead to better partial ordering due to facilitated nucleation, but this is beyond the scope of this work.

A second important observation is that disorder correlates with a reduced average chain

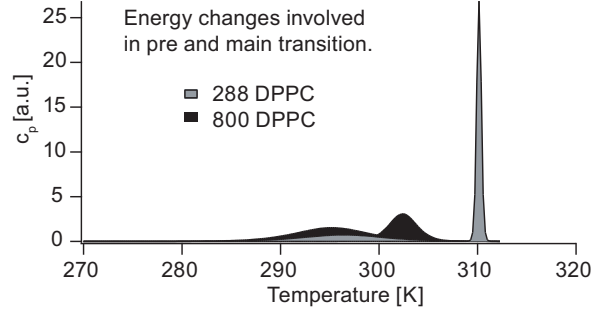


Figure 7.15: Energy changes involved in formation of ripples. The peaks are obtained from double-sigmoid fits to the total system energy over temperature, capturing the pretransition and main transition enthalpies.

tilt angle. In this light, one has to conclude that the average equilibrium tilt angle determined by the lipid topology (for given simulation parameters) will only become visible in a highly ordered gel phase system. In order to judge the equilibrium structure defined by a topology for the gel phase (or any other solid phase) only highly ordered systems should be used. The root cause is of course the slow equilibration or even metastability of simulation of membranes in a solid phase. In any case, one might have to also consider other limitations such system size effects [152, 213].

Looking in detail at the unit cell at 270 K and 300 K, the match between simulation and experiment can be considered to be quite good. The results closely reproduced the experimental lattice when taking into account the systematic effects correlated with the tilt. Considering the findings on tilt, area per molecule and area per chain, it appears that the area per chain is represented best, while the area per headgroup is too large. Reasons for this effect might include: (1) insufficiently equilibrated molecular arrangement or packing, (2) excessive hydration caused by the topology or insufficient equilibration, and (3) a suboptimal headgroup topology parametrization for the given simulation conditions. In the future, more detailed studies should be able to differentiate between these effects.

The question remains whether the unit cell observed in the simulation (especially at 300 K) is the equilibrium structure defined by the molecular force field (and simulation parameters) considering that extremely long simulation times are likely necessary for a membrane in the gel phase to reach its final equilibrium structure. If so, the small discrepancies we observed would motivate further specific optimizations. The differences between the systems at 300 K and 270 K hint at the necessity of using longer equilibration times. In practical use, it appears that the obtained gel phase structures will be strongly affected by the preparation of the membrane in addition to the employed force field.

The ripple structures observed in the simulations matched models obtained from experiments for the ripple phase $P_{\beta'}$ well. However, some structural details of this phase are still under discussion, as it does not lend itself well to experimental analysis by X-ray scattering or similar techniques [70, 71, 210, 214]. Thus, the information gained by simulations with high detail is valuable to modeling and interpreting experiments. The fact that the rippling/bending process appeared to be driven by partial melting below T_m linked to local defects is compatible with experimental models. Previously, another

study using atomistic detail has reported the formation of ripple structures upon cooling [206], but the structures presented there are not consistent with any standard models of the ripple phase.

However, the observed ripple structures are not in a full equilibrium, as the scan rates are not quasi-static and it is beyond the scope of this study to evaluate these structures over longer times for stability and equilibration. Interestingly, the formation of ripples was not observed for the highly ordered system, attributed to the lack of defects as nucleation points for local melting. Further dedicated studies will hopefully answer more questions in detail.

In general the interpretation of MD simulations has to be done with some care, as: (1) in all cases MD simulations are based on simplified models and require significant human-expert input, and (2) the accessible time and length scales are limited in atomistic MD. Especially simulations of membranes in solid phases will require very long times for equilibration. Therefore, a critical comparison of simulation results with experimental results has to be made at all times.

7.4 C20 Cyclic Lipids

7.4.1 Structure and Ordering in the Gel Phase

Building on the methodological basis established above using DPPC, the simulations were extended to the unique cyclic lipids investigated in Chapter 6. To enable a systematic comparison, three C20 cyclic lipids were chosen: C20sat, C20DA-PCPC, and the asymmetric C20DA-PCOH (Figure 7.16). This choice highlights the influence of headgroup symmetry as well as a rigid diacetylenic core on gel phase ordering.

The cyclic lipid topologies used here were based on the DPPC topology used in the first part of this chapter. A C10 ether lipid was created by reducing the carbon chain length, changing ester to ether links (double-bonded ester oxygens removed) and modifying the partial charges appropriately to preserve total charge neutrality. Headgroup partial charges were not modified. C20sat was then created by directly linking the hydrocarbon chains of two such ether lipids. C20DA-PCPC was created from C20sat by modifying the central chain atom types and bonds to make the diacetylenic core. C20DA-PCOH was created from C20DA-PCPC by removing the PC headgroup and replacing it by an OH group while preserving total charge neutrality.

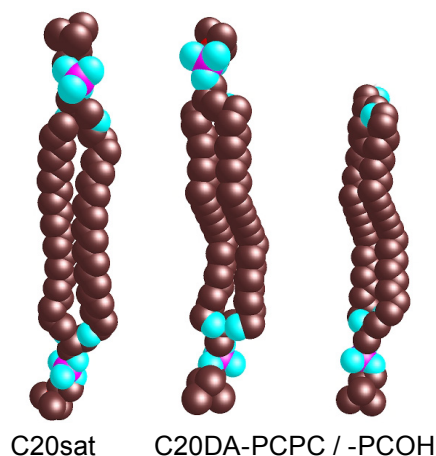


Figure 7.16: 3D representations of the C20 cyclic lipid models. The kink at the diacetylenic cores for C20DA-PCPC and C20DA-PCOH is the energy-minimized conformation in vacuum.

Membranes of cyclic lipids were made using the Method (1) as described for DPPC in Section 7.3.1, initially fixing the chain dihedrals to facilitate tight packing. Membranes of the asymmetric C20DA-PCOH were made by flipping every second lipid in a square initial lattice (“chess board”) by 180° and aligning the hydrocarbon regions at one height. The final membrane size was 256 lipids in a monolayer. For heating scans with cyclic lipid membranes very high final temperatures are expected to be necessary, so that in order to reduce the temperature range the starting temperature was chosen to be 285 K (higher than the 270 K for DPPC). At this temperature, the membranes were equilibrated for 50 ns, then evaluated for 25 ns.

As shown in Figure 7.17, all three cyclic lipids formed stable membrane monolayers. The C20sat membrane was highly ordered, with an area per molecule of 0.61 Å² and a

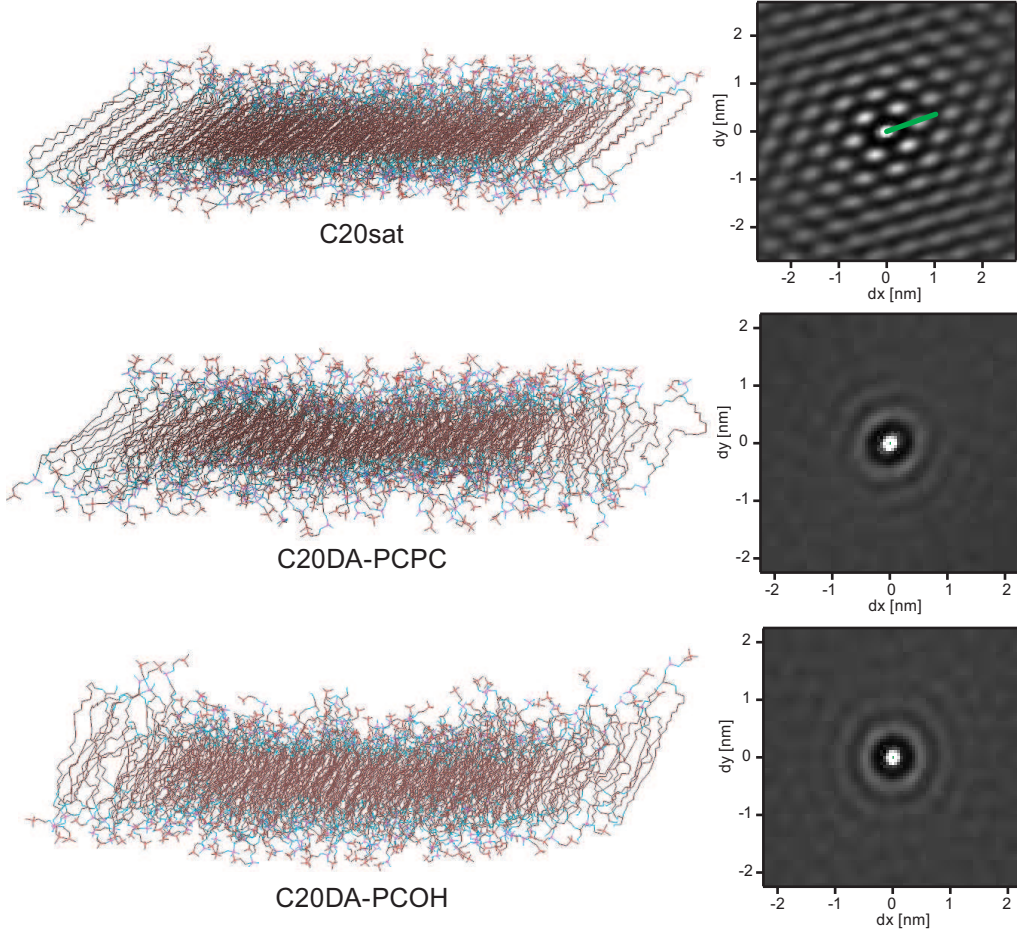


Figure 7.17: Simulated membranes with 256 lipids at 285 K (12 °C) for C20sat, C20DA-PCPC and C20DA-PCOH, as well as the chain carbon autocorrelations at $dz = 0$. The green line in the correlation for C20sat indicates the nearest-neighbor (nn) tilt vector, while due to lack of ordering no clear tilt vector could be obtained for either C20DA membrane from the autocorrelation. However, the correlation map for the C20DA-PCPC membrane appears distorted while for C20DA-PCOH it does not, indicating less strain in the latter due to relaxed headgroup packing.

chain tilt of 48° in direction of the next neighbor. The order coefficients O_{iso} and O_{far} for all three membranes are summarized in Table 7.3. A clear far ordering is visible in the autocorrelation with a strong distortion of the hexagonal unit cell. The correlation length was greater in direction of the tilt than perpendicular to it. The orthorhombic unit cell vectors were determined to $a = 8.05 \text{ \AA}$ and $b = 7.15 \text{ \AA}$, so that the unit cell distortion was calculated to $\epsilon = 1 - a/\sqrt{3}b = +0.35$. The spacings were $d_{20} = 4.03 \text{ \AA}$ and $d_{11} = 5.35 \text{ \AA}$ (Section 3.8 Equation 3.19). Compared to the DPPC simulations, the tilt of 48° is greater and the unit cell distortion is stronger. The d_{20} spacing (perpendicular to the tilt direction) is slightly smaller ($\sim 4.1 \text{ \AA}$ for DPPC), while the tilt-dependent d_{11} spacing is greater. The smaller d_{20} spacing can be explained by the stronger attraction of the longer C20 chains. The area per chain $A_c = a \cdot b / \cos(\Theta) = 19.3 \text{ \AA}^2$ is close to that seen in the DPPC simulations (19.2 \AA^2 to 19.6 \AA^2).

Table 7.3: Order coefficients for C20 cyclic lipid simulations at 285 K. The saturated lipid C20sat is significantly better ordered than the diacetylenic lipids, but slightly less ordered than a comparable DPPC system (10.7×10^{-2} and 7.5×10^{-2} for O_{far} of DPPC at 270 K and 300 K, respectively). The diacetylenic lipids exhibit similar absolute numbers for the order coefficients. The higher anisotropy value O_{iso} for C20DA-PCPC compared to C20DA-PCOH stems from the distortion of the first order, while the visually minimally higher ordering for C20DA-PCOH (see Figure 7.17) is reflected in the values of O_{far} .

lipid	$O_{iso} [\times 10^2]$	$O_{far} [\times 10^2]$
C20sat	1.39	5.03
C20DA-PCPC	0.074	0.57
C20DA-PCOH	0.037	0.64

By contrast, the C20DA-PCPC and C20DA-PCOH membranes did not form any clear ordering. To some extent, a first and second periodic order can be discerned in the autocorrelation maps in Figure 7.17, but the patterns are quasi-isotropic. Qualitatively, the autocorrelation map of the C20DA-PCPC membrane shows some strain and distortion, while the map of the asymmetric C20DA-PCOH membrane appears more symmetric. The C20DA-PCPC membrane had an area per molecule of 0.63 \AA^2 , while C20DA-PCOH had a significantly smaller area per molecule of 0.52 \AA^2 , which is reasonable considering the headgroup asymmetry. A tilt direction and angle could not be extracted from either autocorrelation map due to the limited vertical correlation. However, C20DA-PCPC had a geometrically determined² tilt angle of $(40 \pm 17)^\circ$, whereas the asymmetric C20DA-PCOH exhibited an average tilt angle of $(0 \pm 27)^\circ$ (large variations but on average upright). These observations are consistent with the expected relaxation of headgroup packing strain for asymmetric lipids, and consequently leading to a reduced tilt or even upright configuration.

7.4.2 Electron Density Profiles

For comparison with the experimental results in Chapter 6 the electron density (ED) profiles for the C20 lipid membranes were calculated. In Figure 7.18, the profiles are shown, averaged from 100 frames over 25 ns at 285 K.

The C20sat membrane has an overall higher electron density than the diacetylenic lipids and the profile is sharper and more well-defined. The headgroup width is smaller and a shoulder is visible which is also seen in gel phase PC lipid membranes [113]. For the case of the diacetylenic lipids, the hydrocarbon region does not reach a sharp plateau and it has a minimum at lower density than C20sat. The maximum headgroup density is also significantly lower for C20DA-PCPC than for C20sat even though both possess the same headgroup structure. Therefore, the lower density must be attributed to the larger area per molecule, lower tilt angle and greater thickness of the C20DA-PCPC membrane, which in turn are caused by the diacetylenic core disturbing the chain packing.

²The geometrical tilt angle was defined between the first and last atom of each chain.

The membrane of the asymmetric C20DA-PCOH lipids displays similar ordering and packing characteristics as the symmetric C20DA-PCPC, with the same electron density of the hydrocarbon region but lower headgroup density (as expected). However, the membrane is slightly thicker corresponding to a more upright configuration. These results very clearly highlight the influence of the headgroup asymmetry and the order-breaking presence of a diacetylenic core.

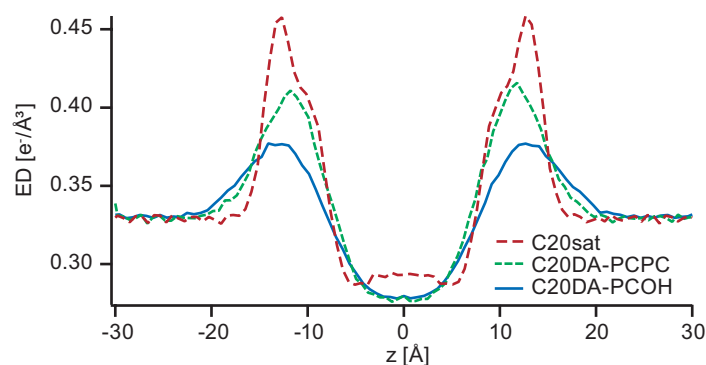


Figure 7.18: Comparison of electron density profiles of the C20 cyclic lipid membranes equilibrated at 285 K. The profiles are the averages of 100 frames over 25 ns.

7.4.3 Comparison to Experiments

The electron density profiles obtained from the simulations were also compared to the experimental profiles obtained from SAXS and reflectivity modeling at 20 °C (in Chapter 6). The total membrane thicknesses obtained from the MD simulation electron density profiles at 285 K are 30 Å, 31 Å and 34 Å for C20sat, C20DA-PCPC and C20DA-PCOH respectively, defined between the headgroup outer half-maximum positions. These values are a good match to the experimentally obtained thickness for C20DA-PCOH of 34.5 Å obtained from SAXS (see also Table 6.4), but slightly less than the value of 36.7 Å obtained for C20DA-PCPC from reflectivity of a single solid-supported monolayer. However, these values reflect different experimental conditions of fully equilibrated membrane multilayers in suspension and the solid-supported membranes formed by vesicle fusion.

In Figure 7.19 (left) the electron density profile from the simulation of C20DA-PCOH is overlaid with the profile obtained from SAXS modeling (Section 6.4.2). The profile obtained from the MD simulation is less dense than the model from SAXS experiments but is a match in thickness. Shown in Figure 7.19 (right) is a model SAXS curve calculated from the simulation ED profile and superimposed on the experimental SAXS data. The significant deviation of the first order peak intensity is a consequence of the different form factor of the less dense membrane in the simulation.

In Figure 7.20 (left) the electron density profile from the simulation of C20DA-PCPC is overlaid on the profile obtained from the reflectivity of a solid-supported monolayer (Section 6.3). The profile obtained from the MD simulation displays higher electron density in the headgroup region while matching the density of the hydrocarbon core region. The membrane thickness obtained from MD is 6 Å less, and to some extent this is

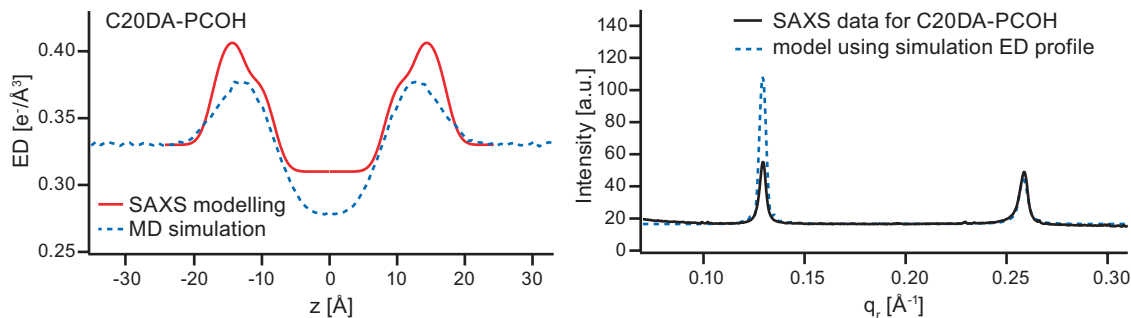


Figure 7.19: Left: Comparison of the electron density profiles for C20DA-PCOH as obtained from SAXS modelling (Section 6.4.2) and as extracted from the MD simulations. Right: The SAXS pattern calculated from the MD electron density profile superimposed on the experimental SAXS data.

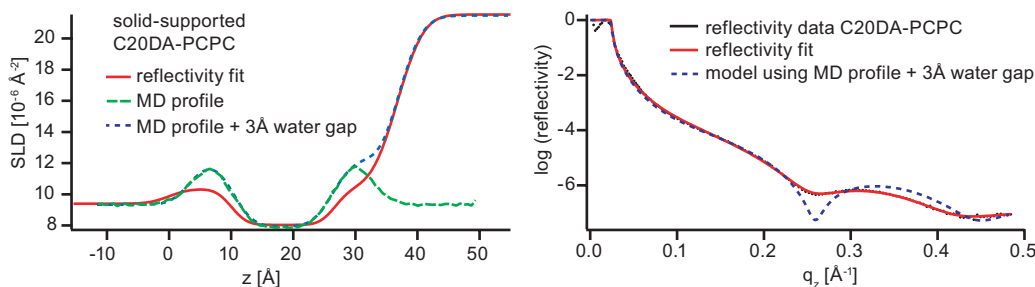


Figure 7.20: Left: Comparison of the electron density profiles for C20DA-PCPC as obtained from the fit to the reflectivity of the solid-supported monolayer (Section 6.3) and as extracted from the MD simulation. The MD profile is also shown adapted for the scenario of a solid-supported membrane, with a 3 \AA water gap and a bulk silicon substrate. Right: The reflectivity calculated from the MD electron density profile plus 3 \AA water gap overlaid on the experimental reflectivity data and the fit.

consistent with a greater tilt in simulations than in experiment. However, during modeling of the experimental data a water gap could not be resolved and was not included in the slab model, leading to a possible overestimation of membrane layer thickness. Accordingly, the MD electron density profile is shown in Figure 7.20 adapted to the scenario of a supported membrane with an added water gap of 3 \AA on a bulk silicon substrate. The reflectivity calculated from this modified profile is shown in Figure 7.20 (right) superimposed on the reflectivity data and the original fit. The position of the first minimum is well matched, with the higher electron density of the MD model leading to more pronounced features. The sum of smaller membrane thickness plus the water gap appears to correctly reproduce the total layer thickness of the experiment. This interesting observation could lead to a modified fitting strategy for experimental reflectivity data using MD results.

The discrepancies between simulation and experiment are small and show that the simulations capture the fundamental membrane properties well without systematic errors. Rather, several specific factors contribute to the deviations. The SAXS experiments show that for C20DA-PCOH lipids a membrane with well-ordered hydrocarbon chain packing can be obtained in experiments, which is not observed in simulations. This can

most likely be explained by insufficient equilibration times in the simulations. Also, an equilibrium packing configuration must exist which apparently cannot be reached easily from randomly rotated lipid molecules in a simulation. Conversely, the experimental density of the solid-supported C20DA-PCPC monolayer appears to be limited by slow self-healing, so that the MD results naturally overestimate the electron density.

7.4.4 Outlook to Fluid Phase Simulations of Cyclic Lipid Membranes

Some preliminary fluid phase simulations were performed extending the work on gel phase systems. Heating scan simulations of C20DA-PCPC and C20DA-PCOH up to 370 K did not show any clear phase transitions (not shown). Considering the disorder of the gel phase starting systems, this finding is consistent with the lack of a phase transition for disordered DPPC systems (e.g. System (3) as discussed in Section 7.3.3). By contrast, C20sat exhibited a broad transition around 355 K (82 °C) with ~ 40 kJ/mol transition enthalpy. However, these preliminary results were inconclusive as the membrane artefactually collapsed after melting.

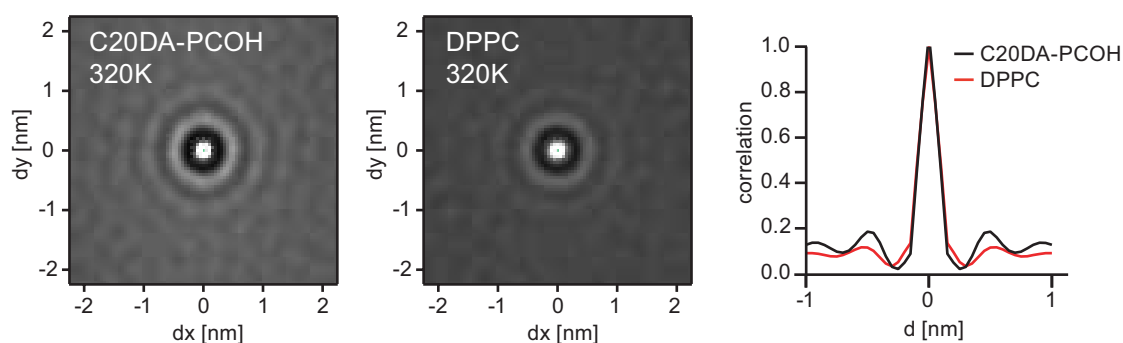


Figure 7.21: Left and Center: Autocorrelation maps of 256 C20DA-PCOH and 512 DPPC in the fluid phase at 320 K. The lower average correlation value of DPPC indicates a lower average overlap and thus a lower average density of the DPPC membrane. Right: Line profiles at $dy = 0$ through the autocorrelation maps (equivalent to a radial distribution function for isotropic systems).

A comparison of fluid phase ordering between C20DA-PCOH and DPPC is shown in Figure 7.21, both at 285 K. The autocorrelation map of DPPC has a slightly lower average level, corresponding to a lower membrane density for fluid DPPC. The position of the first near order maximum is closer to zero for the cyclic lipid. Moreover, the ratio of isotropic first order intensity to average level is greater for the cyclic lipid (1.52 vs 1.37), indicating greater isotropic near-ordering and closer average proximity to the nearest neighbor. Also, the autocorrelation map of the cyclic lipid hints at multiple (isotropic) orders beyond the nearest neighbor. This might be linked to the low mobility of the cyclic lipids in experimental FRAP results (Section 6.2) and the presence of a broad diffuse WAXS peak in the fluid phase (Section 6.4).

8 Conclusions

In this thesis, the influence of structural variations in lipids and proteins on the structure and dynamics of model membranes were probed from the ensemble viewpoint down to single molecules using a variety of complementary experiments and simulations.

The diffusion of membrane-anchored prion proteins (PrP^c) was investigated by single-dye tracking in Chapter 5. A microscope setup was constructed and optimized for single-molecule fluorescence in supported membranes. The distribution of diffusion coefficients D of individual PrP^c could be determined, and the center value of $D_{cen} = 0.84 \mu\text{m}^2/\text{s}$ matched previously obtained ensemble results obtained by FRAP. Single-molecule tracking is especially well suited to investigate the mode of motion (free diffusion, subdiffusion, etc). Here, the obtained power-law exponent $\gamma = 0.96 \pm 0.1$ of a fit to the ensemble mean-square displacement indicated linearity and thus free diffusion of PrP^c in the supported membranes within the investigated times ($< 1 \text{ s}$). As the particle traces from experiments did not possess identical lengths (due to fluorophore bleaching and blinking), “templated random walks” simulations were developed to quantify the expected errors and accuracies of the results. It could be determined that with a high probability the distribution of D is incompatible with a single uniform PrP^c population. These observations can be explained by non-uniform glycosylation of the proteins influencing their hydrodynamic drag, possibly in combination with formation of dimers. The detection of subtle structural variations in PrP^c and their influence on the dynamics of the diffusion is a prime example of the capability and suitability of single-molecule experiments. The challenging experimental conditions in single-dye tracking make these findings non-trivial achievements. Moreover, the experimental setup was further upgraded for future two-color single-molecule fluorescence experiments in a dual-imaging mode. A model-free analysis was introduced to enable high precision image registration between the two color channels for single-molecule colocalization. The final accuracy of the image registration was 8.5 nm on average, which is better than the average localization precision for single dyes. With this level of accuracy, single-molecule colocalization experiments are only limited by the dye performance.

The structure and fluidity of archaea-mimetic cyclic lipid monolayers were investigated in Chapter 6. First, it was established by fluorescence microscopy that planar solid-supported membranes can be formed from cyclic lipids by vesicle fusion. FRAP experiments showed all cyclic lipids membranes were seen to be in a solid state at room temperature. Melting transitions upon heating were only observed for the shortest lipids with diacetylenic cores (C20DAs), while no melting was observed for the cyclic lipids C20sat with fully saturated chains or any cyclic lipids with longer chains than C20. The kinked diacetylenic core appears to lower the phase transition temperature and promote fluidity due to sterically disturbed chain packing, similar to double-bonds in acyl chains

of conventional lipids. Strikingly, the observed diffusion coefficients in the fluid state were more than an order of magnitude lower than those observed in conventional bilayer membranes. Furthermore, high energy X-ray reflectivity experiments were used to obtain the vertical electron density profiles of supported membranes of C20DA-PCPC and C24DA-PCPC at the solid-liquid interface, which showed a thickness difference matching the difference in chain length and confirmed the presence of single monolayers with very low roughness. For multi-lamellar samples a series of X-ray and neutron scattering experiments was used to obtain the lamellar spacings and vertical electron density profiles under various hydration conditions. Moreover, full-q-range fitting of small-angle X-ray scattering (SAXS) data allowed to distinguish membrane thickness and water gap. While the lamellar spacings strongly deviated between lipid species (depending on headgroup chemistry), the extracted membrane thicknesses and electron density profiles correlated closely with the chain lengths. These measurements confirmed formation of stable membrane monolayers for all investigated lipids without indications of “U-shape” bending. In the solid phase, all membranes exhibited chain-chain correlation peaks in wide-angle X-ray scattering (WAXS) patterns. GID experiments with oriented samples allowed for the quantitative separation of momentum transfer parallel and perpendicular to the membrane surfaces, which provides quantitative information about the unit cells. In general, the chain-chain correlation peaks for the saturated lipids were seen to be much sharper when compared to those possessing diacetylenic cores. This can be interpreted as packing frustration caused by the kinked rigid diacetylenic core, consistent with its effects on membrane phase behavior.

Molecular dynamics (MD) simulations were used to study lipid membranes on the level of atomic detail in Chapter 7, focusing on ordering in the gel phase as well as melting transitions. In contrast to previous reports, these simulations did not rely on *a priori* knowledge of crystal structures to create the starting systems. Instead, a detailed comparison was made between different self-ordering methods to obtain membranes in the gel phase, with a focus on avoiding the problems associated with the extremely long equilibration times necessary for membranes in a solid phase. As a new tool for analysis of MD simulations, 3D autocorrelation of the atomic coordinates enabled quantitative studies of system ordering and the unit cell of membranes in a solid phase. One of the main achievements in this study is the first successful representation with atomistic detail of the first order phase transition of conventional phospholipids, which can be characterized with a discontinuous nature and a phase transition enthalpy. It could be demonstrated that only highly ordered gel phase membranes exhibit a clear phase transition, whose melting temperature T_m and the transition enthalpy ΔH are comparable to the corresponding values obtained from calorimetry experiments. However, as suggested by the dependence of the phase transition on the heating rate, it should be noted that even the slowest heating rates currently accessible in such simulations are still far from quasi-static conditions. In order to examine the potential use of atomistic MD simulation to anticipate the ordering and dynamics of molecules with unique structural motifs, monolayers of the C20 cyclic lipids were simulated. A clear difference in ordering could be observed between the diacetylenic and saturated variants in the gel phase. The saturated lipids formed tightly packed tilted membranes, closely resembling the type of ordering observed in DPPC simulations. The diacetylenic lipids did not exhibit well-

defined ordering in the simulations, which can be explained by the packing strain at the rigid core. The results achieved in this thesis will allow more detailed investigations of the complex phase behavior of cyclic lipids in future studies. Already, the simulations of cyclic lipid monolayers could be used directly for modeling of experimental results from Chapter 6. The differences between the electron density profiles extracted from the gel phase simulations compared to those obtained from SAXS and reflectivity experiments are well explained by the specific experimental conditions.

Overall, the combination of optical ensemble and single-molecule techniques with scattering experiments is a powerful tool to investigate the ordering and dynamics of biological molecules in different length and time scales. The interpretation and modeling of such experiments can be supported effectively by computer simulations as demonstrated in this thesis.

9 Outlook

The complementary combination of experiments and simulations applied in this thesis holds much promise for future studies of model and biological membranes, both from a fundamental viewpoint as well as in application.

For instance, the strategy established here for single-molecule experiments with prion proteins can be extended towards studies of the interaction of individual prion proteins. As mentioned previously, these protein interactions in or at membranes appear to be a critical step in the progression of prion disease [13, 14]. Furthermore, one might consider a dual-labeling strategy to observe prion conformational changes. By directed labeling of specific residues large scale rearrangements of tertiary structure can be observed using single-dye FRET. Similar strategies have led to progress in understanding the kinetics of the Hsp90 protein [215].

The integration of experiments such as X-ray scattering with molecular dynamics simulations is promising for deepening the understanding of structural and molecular details. Experimental data can be modeled in an unbiased context using information from MD simulations as performed in this thesis. The demonstrated suitability of the framework established in this thesis will allow the extension to other systems in the future, where molecular detail is critically relevant to structure and function.

From the application side, a potential use of archaea-type membranes is in wet electrochemical biosensors [216, 217], where the solid-supported membrane allows integration of biological soft matter functionality with hard semiconductor or metal devices. Especially for conductive membrane-based biosensors an excellent electrical isolation of the sensor surface from the electrolyte is required, putting stringent requirements on the preparation of the membrane and the choice of lipids. Here, archaea-type membranes hold much promise due to their proven robustness in extreme environments, especially against large gradients of salt and pH.

A Appendix

A.1 Stereochemistry of Archaeol and Related Lipids

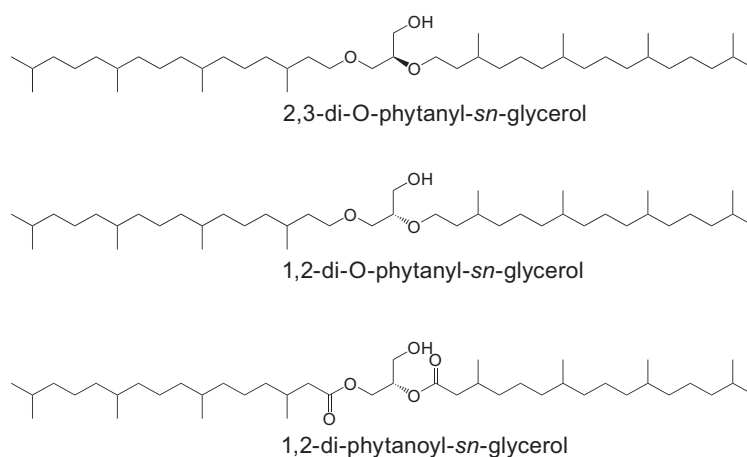


Figure A.1: Stereochemistry of archaeol and related lipids, specified using the stereospecific numbering (*sn*) system. Top: Archaeol, with ether-linked phytanyl at the *sn*-2,3 positions of glycerol. Middle: A phytanyl ether lipid, linked at the *sn*-1,2 positions of glycerol. Bottom: A phytanoyl ester lipid, linked at the *sn*-1,2 positions of glycerol.

Only archaea possess lipids with *sn*-2,3 linkage [17, 21]. Non-archaea organisms can possess ether and/or phytan(o)yl lipids, but only at the *sn*-1,2 positions. Three example configurations are shown in Figure A.1. The hydrocarbon chains are spread apart to highlight the stereochemical differences.

A.2 SAXS/WAXS of DMPC

In Figure A.2 a SAXS/WAXS measurement of the standard two-chain phospholipid DMPC is shown for comparison with cyclic lipid results. In the SAXS curves below 24 °C we can observe two orders of lamellar peaks with the typical “extra” peaks of the ripple phase (correlations at the ripple wavelength). The $L_{\beta'}$ phase is not visible in this temperature range. Clear WAXS chain-chain correlation peaks are seen with correlation peaks at $q = 1.5 \text{ \AA}^{-1}$ equal to a spacing of 4.2 \AA , which do not show any satellite peaks.

Melting occurs at 23–24 °C, and afterwards the SAXS peaks exhibit pure lamellar ordering with no visible WAXS peaks. The SAXS lamellar spacing decreases continuously with temperature (q increases). There is no jump in spacing at the transition from $P_{\beta'}$ to L_{α} phase.

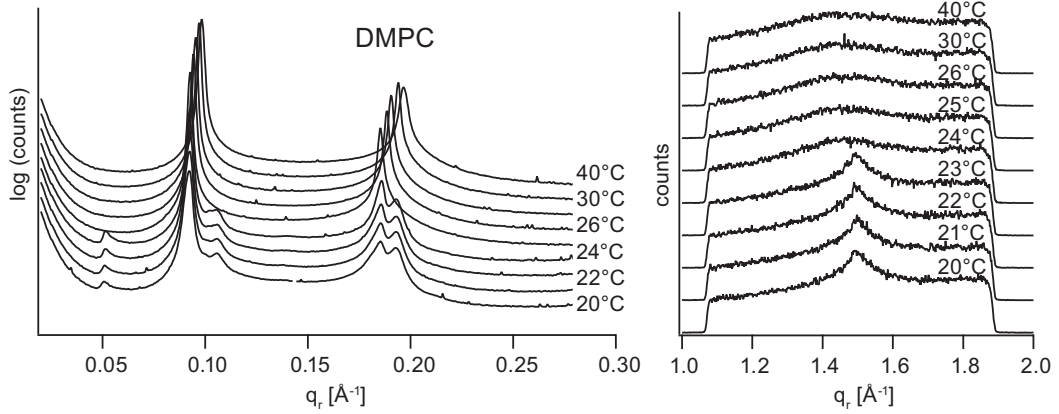


Figure A.2: SAXS/WAXS temperature scan for DMPC.

A.3 DSC Measurement of DPPC

As experimental reference to the MD simulations in Chapter 7, we performed differential scanning calorimetry measurements for DPPC in pure double-distilled water ($\rho > 18 \text{ M}\Omega\text{cm}$) to obtain values for ΔH and T_m for the pre-transition and main transition (Figure A.3). The scans were performed at 10 K/hour from 20 °C to 50 °C using a VP-DSC calorimeter (Microcal, USA). The samples were prepared by drying from DPPC chloroform stock solution under a stream of nitrogen and storing in vacuum overnight, then resuspending in water to 1 mg/ml. This suspension was incubated at 40 °C for 4 h, vortexed and stored at 4 °C overnight, then equilibrated at room temperature for 4 h before measuring.

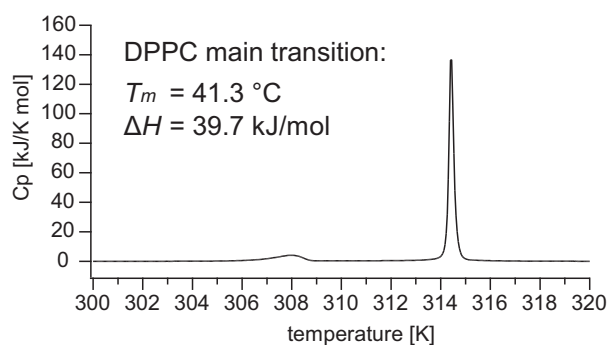


Figure A.3: DSC measurement of DPPC in pure water. For the main transition $T_m = 314.5 \text{ K}$ (41.3°C) and $\Delta H = 39.7 \text{ kJ/mol}$. The pre-transition is at $T_p = 308 \text{ K}$ (35°C) with $\Delta H = 7.3 \text{ kJ/mol}$.

A.4 Prion Protein Preparation

Materials For prion protein preparation, following material was used: Zwittergent 3-12 and protease inhibitor cocktail, EDTA-free, were from Calbiochem (Merck, Darmstadt, Germany), lipids from Avanti Polar Lipids (Alabaster, Ala), monoclonal anti-PrP antibody 6H4 from Prionics (Zurich, Switzerland). Hitrap Chelating HP, Mono-S and PD-10 columns were purchased from Amersham Biosciences (GE Healthcare, Munich). Bio-Beads SM-2 were from BioRad (Munich, Germany), and 5-carboxytetramethylrhodamin succinimide ester (TAMRA) from Molecular Probes (Invitrogen).

Prion Protein Purification Bovine brains were extracted from BSE-negative tested animals less than 2.5 years old at a state institute of animal health control, shock-frozen in liquid nitrogen, and stored at -20 °C. PrP^c was isolated in principle according to the method of Turk *et al.* [218] and Pan *et al.* [219]. In short, 90 g of frozen brain were homogenized in 810 ml ice-cold PBS (10 mM sodium phosphate, pH 7.0, 150 mM NaCl), containing 250 mM sucrose and 5 vials protease inhibitor cocktail, and 1 % zwittergent 3-12, by 4 × 10 s strokes in a Warring blender. The homogenate was centrifuged for 30 min at 3,500 rpm in a Beckman Type 19 rotor at 4 °C. To the supernatant fraction, 4 % PEG 8000 (w/v) was added under stirring on ice. After standing for 10 min, the precipitate was collected by centrifugation for 10 min at 12,500 rpm in the same rotor. The pellet was homogenized in a Dounce homogenizer into PBS containing protease inhibitors and 8 % zwittergent 3-12, and stirred on ice for 1 h. From here on, all further steps were performed at 4 °C. After centrifugation of the solution for 1 h at 34,000 rpm in a Beckman rotor type 50.2-Ti, the supernatant was applied to a 5 ml Hitrap NTA-Cu⁺⁺ column, pre-equilibrated with 15 mM imidazole, 10 mM sodium phosphate, pH 7.0 and 0.2 % zwittergent, and eluted with an imidazole gradient of 100-500 mM. The PrP-containing peak was adjusted to pH 6.4 and loaded onto a 5 ml Mono-S column pre-equilibrated with 150 mM NaCl, 2 mM MOPS, pH 6.4 and 0.2% zwittergent, washed with the same buffer at pH 7.0, and eluted with a 150–500 mM NaCl gradient. The PrP-containing peak was concentrated over a 1 ml HiTrap-Co⁺⁺ column. Up to the last step, all procedures were performed in a bio-safety lab (L3**). After each purification step, the PrP^c-containing fraction was identified with a dot blot test with the PrP specific antibody 6H4. As a control, PrP^c-containing fractions were treated with proteinase K. All were proteinase K sensitive.

Fluorescence labelling of PrP^c. An aliquot of PrP^c solution was dialyzed against bicarbonate buffer (150 mM NaHCO₃, pH 8.3, 150 mM NaCl, 0.2% zwittergent) and incubated at room temperature with a 60 × molar excess of TAMRA. After passage over a pre-equilibrated PD10 column, the labelling efficiency was calculated to be 1 labeled in 10 unlabeled protein molecules using a molar extinction coefficient of 80 000 M⁻¹ cm⁻¹.

PrP^c reconstitution in phospholipids vesicles. In principle, reconstitution into lipid vesicles followed the method of Hu *et al.* [58] based on Erb *et al.* [56]. Proteins in zwittergent 3-12 dispersion were mixed with PBS containing 1 mM DMPC under gentle

shaking for 30 min at 37 °C, then 90 min at 30 °C. Zwittergent was removed by adding twice 50 mg/ml Bio-Beads for 30 min. The Bio-Beads were removed by centrifugation with an Eppendorf centrifuge. The resulting vesicle solution was layered on top of a 4-step sucrose gradient (2 M / 1.2 M / 0.8 M / 0.4 M) in PBS and centrifuged for 24 h at $27,500 \times g$. In order to detect the fraction that contained PrP^c in the membrane-anchored version, the protein was labeled with TAMRA prior to the reconstitution, and the lipid content determined by measuring the phosphate content of the TAMRA-labeled fraction according to Bartlett [220]. The PrP^c-containing fraction was collected from the top of the 1.2 M sucrose layer and identified by western blotting with the anti-PrP monoclonal antibody 6H4.

Bibliography

- [1] B. Alberts, A. Johnson, J. Lewis, M. Raff, K. Roberts, and P. Walter. *Molecular Biology of the Cell*. Garland Science, New York, 4th edition, 2002. 1
- [2] Charles Tanford. *Physical Chemistry of Macromolecules*. Wiley, New York, 1961. 1
- [3] T. S. Tillman and M. Cascio. Effects of membrane lipids on ion channel structure and function. *Cell Biochemistry and Biophysics*, 38(2):161–190, 2003. 1
- [4] E. A. Clark and J. S. Brugge. Integrins and signal transduction pathways: the road taken. *Science*, 268(5208):233–239, 1995. 1
- [5] S. D. Marlin and T. A. Springer. Purified intercellular adhesion molecule-1 (ICAM-1) is a ligand for lymphocyte function-associated antigen 1 (LFA-1). *Cell*, 51(5):813–819, 1987. 1
- [6] S.J. Singer and G.L. Nicolson. The fluid mosaic model of the structure of cell membranes. *Science*, 175:720–731, 1972. 1
- [7] Mariana Ruiz Villarreal. Biomembrane, August 2009. 1
- [8] Julie A. Pitcher, Neil J. Freedman, and Robert J. Lefkowitz. G protein-coupled receptor kinases. *Annual Review of Biochemistry*, 67(1):653–692, 1998. 1
- [9] Rumiana Koynova and Martin Caffrey. Phases and phase transitions of the phosphatidylcholines. *Biochimica et Biophysica Acta-Reviews on Biomembranes*, 1376(1):91–145, 1998. 1, 7, 8, 69, 106, 109
- [10] S. B. Prusiner. Prions - novel infectious pathogens. *Advances in Virus Research*, 29:1–56, 1984. 1
- [11] S. B. Prusiner. Prions. *Proceedings of the National Academy of Sciences of the United States of America*, 95(23):13363–13383, 1998. 1
- [12] N. Stahl, D. R. Borchelt, K. Hsiao, and S. B. Prusiner. Scrapie prion protein contains a phosphatidylinositol glycolipid. *Cell*, 51(2):229–240, 1987. 2
- [13] B. Chesebro, M. Trifilo, R. Race, K. Meade-White, C. Teng, R. LaCasse, L. Raymond, C. Favara, G. Baron, S. Priola, B. Caughey, E. Masliah, and M. Oldstone. Anchorless prion protein results in infectious amyloid disease without clinical scrapie. *Science*, 308(5727):1435–1439, 2005. 2, 123
- [14] D. L. Cox, R. R. P. Sing, and S. C. Yang. Prion disease: Exponential growth requires membrane binding. *Biophysical Journal*, 90(11):L77–L79, 2006. 123
- [15] L. Breydo, Y. Sun, N. Makarava, C. I. Lee, V. Novitskaia, O. Bocharova, J. P. Y. Kao, and I. V. Baskakov. Nonpolar substitution at the C-terminus of the prion protein, a mimic of the glycosylphosphatidylinositol anchor, partially impairs amyloid fibril formation. *Biochemistry*, 46(3):852–861, 2007. 2

- [16] R. Lipowsky and E. Sackmann. *Structure and Dynamics of Membranes. From Cells to Vesicles*, volume 1. North Holland Publishing Corp., Amsterdam, 1995. 2, 3
- [17] Riccardo Cavicchioli, editor. *Archaea: Molecular and Cellular Biology*. ASM Press, Washington, 2007. 2, 62, 125
- [18] C. R. Woese, O. Kandler, and M. L. Wheelis. Towards a natural system of organisms - proposal for the domains archaea, bacteria, and eucarya. *Proceedings of the National Academy of Sciences of the United States of America*, 87(12):4576–4579, 1990. 2
- [19] C. R. Woese and G. E. Fox. Phylogenetic structure of the prokaryotic domain: the primary kingdoms. *Proceedings of the National Academy of Sciences of the United States of America*, 74(11):5088–5090, 1977. 2
- [20] G. E. Fox, E. Stackebrandt, R. B. Hespell, J. Gibson, J. Maniloff, T. A. Dyer, R. S. Wolfe, W. E. Balch, R. S. Tanner, L. J. Magrum, L. B. Zablen, R. Blakemore, R. Gupta, L. Bonen, B. J. Lewis, D. A. Stahl, K. R. Luehrsens, K. N. Chen, and C. R. Woese. The phylogeny of prokaryotes. *Science*, 209(4455):457–463, 1980. 2
- [21] J. L. C. M. van de Vossenberg, A. J. M. Driessen, and W. N. Konings. The essence of being extremophilic: the role of the unique archaeal membrane lipids. *Extremophiles*, 2(3):163–170, 1998. 2, 3, 125
- [22] Morris Kates, editor. *Glycolipids, Phosphoglycolipids and Sulfoglycolipids*. Handbook of Lipid Research. Plenum Press, New York, 1990. 2, 62
- [23] D. H. Thompson, K. F. Wong, R. Humphrybaker, J. J. Wheeler, J. M. Kim, and S. B. Rananavare. Tetraether bolaform amphiphiles as models of archaeobacterial membrane-lipids - Raman-spectroscopy, P-31 NMR, x-ray-scattering, and electron-microscopy. *Journal of the American Chemical Society*, 114(23):9035–9042, 1992. 3, 61
- [24] M. G. L. Elferink, J. G. Dewit, A. J. M. Driessen, and W. N. Konings. Stability and proton-permeability of liposomes composed of archaeal tetraether lipids. *Biochimica et Biophysica Acta-Biomembranes*, 1193(2):247–254, 1994.
- [25] E. L. Chang. Unusual thermal stability of liposomes made from bipolar tetraether lipids. *Biochemical and Biophysical Research Communications*, 202(2):673–679, 1994. 3
- [26] H. Lindsey, N.O. Petersen, and S.I. Chan. Physicochemical characterization of 1,2-diphytanoyl sn-glycero-3-phosphocholine in model membrane systems. *Biochimica et Biophysica Acta*, 555:147–167, 1979. 3
- [27] W. C. Hung, F. Y. Chen, and H. W. Huang. Order-disorder transition in bilayers of diphytanoyl phosphatidylcholine. *Biochimica et Biophysica Acta-Biomembranes*, 1467(1):198–206, 2000. 3
- [28] J. F. Nagle and S. Tristram-Nagle. Structure of lipid bilayers. *Biochimica et Biophysica Acta-Reviews on Biomembranes*, 1469(3):159–195, 2000. 3, 7, 100, 102
- [29] A. D. Bangham, M. M. Standish, and J. C. Watkins. Diffusion of univalent ions across the lamellae of swollen phospholipids. *Journal of Molecular Biology*, 13(1):238–252, IN26–IN27, 1965. 3, 36

- [30] W. J. Sun, R. M. Suter, M. A. Knewton, C. R. Worthington, S. Tristramnagle, R. Zhang, and J. F. Nagle. Order and disorder in fully hydrated unoriented bilayers of gel phase dipalmitoylphosphatidylcholine. *Physical Review E*, 49(5):4665–4676, 1994. 3, 7, 28, 76, 83, 103
- [31] W. J. Sun, S. TristramNagle, R. M. Suter, and J. F. Nagle. Structure of gel phase saturated lecithin bilayers: Temperature and chain length dependence. *Biophysical Journal*, 71(2):885–891, 1996. 3, 28, 69, 77, 83, 103, 104, 107
- [32] J. Katsaras. Structure of the subgel ($L_{\alpha'}$) and gel ($L_{\beta'}$) phases of oriented dipalmitoylphosphatidylcholine multibilayers. *Journal of Physical Chemistry*, 99(12):4141–4147, 1995. 3, 7, 86
- [33] Tim Salditt. Thermal fluctuations and stability of solid-supported lipid membranes. *Journal of Physics: Condensed Matter*, 17(6):R287–R314, 2005. 3
- [34] Emanuel Schneck, Florian Rehfeldt, Rafael G. Oliveira, Christian Gege, Bruno Deme, and Motomu Tanaka. Modulation of intermembrane interaction and bending rigidity of biomembrane models via carbohydrates investigated by specular and off-specular neutron scattering. *Physical Review E*, 78(6):061924–9, 2008. 3, 80, 81
- [35] T. M. Bayerl and M. Bloom. Physical-Properties of Single Phospholipid-Bilayers Adsorbed to Micro Glass-Beads - a New Vesicular Model System Studied by H-2-Nuclear Magnetic-Resonance. *Biophysical Journal*, 58(2):357–362, 1990. 3
- [36] S. A. Tatulian, P. Hinterdorfer, G. Baber, and L. K. Tamm. Influenza hemagglutinin assumes a tilted conformation during membrane-fusion as determined by attenuated total-reflection FTIR spectroscopy. *EMBO Journal*, 14(22):5514–5523, 1995. 3
- [37] L. K. Tamm and H. M. McConnell. Supported phospholipid bilayers. *Biophysical Journal*, 47(1):105–113, 1985. 3
- [38] E. Sackmann. Supported membranes: Scientific and practical applications. *Science*, 271(5245):43–48, 1996. 3
- [39] E. Kalb, S. Frey, and L. K. Tamm. Formation of supported planar bilayers by fusion of vesicles to supported phospholipid monolayers. *Biochimica et Biophysica Acta*, 1103(2):307–316, 1992. 3
- [40] J. Rädler, H. Strey, and E. Sackmann. Phenomenology and kinetics of lipid bilayer spreading on hydrophilic surfaces. *Langmuir*, 11(11):4539–4548, 1995.
- [41] P. S. Cremer and S. G. Boxer. Formation and spreading of lipid bilayers on planar glass supports. *Journal of Physical Chemistry B*, 103(13):2554–2559, 1999.
- [42] Ralf Richter, Anneke Mukhopadhyay, and Alain Brisson. Pathways of lipid vesicle deposition on solid surfaces: A combined QCM-D and AFM study. *Biophysical Journal*, 85(5):3035–3047, 2003. 3
- [43] E. S. Wu, K. Jacobson, and D. Papahadjopoulos. Lateral diffusion in phospholipid multibilayers measured by fluorescence recovery after photobleaching. *Biochemistry*, 16(17):3936–3941, 1977. 3

- [44] D. Axelrod, D.E. Koppel, J. Schlessinger, E. Elson, and W.W. Webb. Mobility measurement by analysis of fluorescence photobleaching recovery kinetics. *Biophysical Journal*, 16:1055–1069, 1976. 22
- [45] R. Merkel, E. Sackmann, and E. Evans. Molecular friction and epitactic coupling between monolayers in supported bilayers. *Journal de Physique II*, 50:1535–1555, 1989. 3, 4, 39, 66
- [46] S. J. Johnson, T. M. Bayerl, D. C. McDermott, G. W. Adam, A. R. Rennie, R. K. Thomas, and E. Sackmann. Structure of an adsorbed dimyristoylphosphatidylcholine bilayer measured with specular reflection of neutrons. *Biophysical Journal*, 59(2):289–294, 1991. 3
- [47] M. Ferrand, A. J. Dianoux, W. Petry, and G. Zaccai. Thermal motions and function of bacteriorhodopsin in purple membranes - effects of temperature and hydration studied by neutron-scattering. *Proceedings of the National Academy of Sciences of the United States of America*, 90(20):9668–9672, 1993.
- [48] R. Henderson. The potential and limitations of neutrons, electrons and x-rays for atomic-resolution microscopy of unstained biological molecules. *Quarterly Reviews of Biophysics*, 28(2):171–193, 1995.
- [49] C. E. Miller, J. Majewski, T. Gog, and T. L. Kuhl. Characterization of biological thin films at the solid-liquid interface by x-ray reflectivity. *Physical Review Letters*, 94(23):238104, 2005. 62, 70
- [50] Jens Als-Nielsen and Des McMorrow. *Elements of Modern X-Ray Physics*. Wiley, 2006. 12, 23
- [51] J. S. Hub, T. Salditt, M. C. Rheinstader, and B. L. de Groot. Short-range order and collective dynamics of dmpc bilayers: A comparison between molecular dynamics simulations, x-ray, and neutron scattering experiments. *Biophysical Journal*, 93(9):3156–3168, 2007. 3, 102
- [52] M. J. Saxton and K. Jacobson. Single-particle tracking: Applications to membrane dynamics. *Annual Review of Biophysics and Biomolecular Structure*, 26:373–399, 1997. 4, 43
- [53] N. L. Thompson, K. H. Pearce, and H. V. Hsieh. Total internal-reflection fluorescence microscopy - application to substrate-supported planar membranes. *European Biophysics Journal with Biophysics Letters*, 22(5):367–378, 1993. 4
- [54] A. A. Brian and H. M. McConnell. Allogeneic stimulation of cytotoxic T cells by supported planar membranes. *Proceedings of the National Academy of Sciences of the United States of America*, 81(19):6159–6163, 1984. 4
- [55] P. Y. Chan, M. B. Lawrence, M. L. Dustin, L. M. Ferguson, D. E. Golan, and T. A. Springer. Influence of receptor lateral mobility on adhesion strengthening between membranes containing Lfa-3 and Cd2. *Journal of Cell Biology*, 115(1):245–255, 1991.
- [56] E. M. Erb, K. Tangemann, B. Bohrmann, B. Muller, and J. Engel. Integrin alpha iib beta 3 reconstituted into lipid bilayers is nonclustered in its activated state but clusters after fibrinogen binding. *Biochemistry*, 36(24):7395–7402, 1997. 128

- [57] A. Kloboucek, A. Behrisch, J. Faix, and E. Sackmann. Adhesion-induced receptor segregation and adhesion plaque formation: A model membrane study. *Biophysical Journal*, 77(4):2311–2328, 1999.
- [58] B. Hu, D. Finsinger, K. Peter, Z. Guttenberg, M. Barmann, I. Kessler, A. Escherich, L. Moroder, J. Bohm, W. Baumeister, S. F. Sui, and E. Sackmann. Intervesicle cross-linking with integrin $\alpha(\text{iib})\beta(3)$ and cyclic-rgd-lipopeptide. a model of cell-adhesion processes. *Biochemistry*, 39(40):12284–12294, 2000. 128
- [59] S. Y. Qi, J. T. Groves, and A. K. Chakraborty. Synaptic pattern formation during cellular recognition. *Proceedings of the National Academy of Sciences of the United States of America*, 98(12):6548–6553, 2001.
- [60] O. Purrucker, S. Gonnennwein, A. Fortig, R. Jordan, M. Rusp, M. Barmann, L. Moroder, E. Sackmann, and M. Tanaka. Polymer-tethered membranes as quantitative models for the study of integrin-mediated cell adhesion. *Soft Matter*, 3(3):333–336, 2007. 4
- [61] M. Tanaka and E. Sackmann. Polymer-supported membranes as models of the cell surface. *Nature*, 437(7059):656–663, 2005. 4
- [62] S. Gönennwein, M. Tanaka, B. Hu, L. Moroder, and E. Sackmann. Functional incorporation of integrins into solid supported membranes on ultrathin films of cellulose - impact on adhesion. *Biophysical Journal*, 48(6):646–655, 2003. 4
- [63] M. Tanaka, A. P. Wong, F. Rehfeldt, M. Tutus, and S. Kaufmann. Selective deposition of native cell membranes on biocompatible micropatterns. *JACS*, 126(10):3257–3260, 2004.
- [64] O. Purrucker, A. Fortig, R. Jordan, E. Sackmann, and M. Tanaka. Control of frictional coupling of transmembrane cell receptors in model cell membranes with linear polymer spacers. *Physical Review Letters*, 98(7):078102, 2007. 4
- [65] A. R. Walmsley, F. N. Zeng, and N. M. Hooper. Membrane topology influences N-glycosylation of the prion protein. *EMBO Journal*, 20(4):703–712, 2001. 4
- [66] P.M. Rudd, A.H. Merry, M.R. Wormald, and R.A. Dwek. Glycosylation and prion protein. *Current Opinion in Structural Biology*, 12:578–586, 2002. 4
- [67] R. K. Meyer, A. Lustig, B. Oesch, R. Fatzer, A. Zurbriggen, and M. Vandevelde. A monomer-dimer equilibrium of a cellular prion protein (PrPc) not observed with recombinant PrP. *Journal of Biological Chemistry*, 275(48):38081–38087, 2000. 5, 50
- [68] K. Miyawaki, A. Harada, T. Takagi, and M. Shibakami. Design, synthesis, and self-assembly of parallel cyclobolaphile that contains four amide groups as a linkage between polar head groups and hydrocarbon chain: A mimetic of archaeal membrane lipid. *Synlett*, 3(3):349–352, 2003. 5
- [69] D. Marsh. General features of phospholipid phase-transitions. *Chemistry and Physics of Lipids*, 57(2-3):109–120, 1991. 7, 100
- [70] W. J. Sun, S. TristramNagle, R. M. Suter, and J. F. Nagle. Structure of the ripple phase in lecithin bilayers. *Biophysical Journal*, 70(2):Wp227–Wp227, 1996. 7, 111

- [71] K. Sengupta, V. A. Raghunathan, and J. Katsaras. Structure of the ripple phase of phospholipid multibilayers. *Physical Review E*, 68(3):–, 2003. 7, 109, 111
- [72] Kurt Binder. Theory of first-order phase transitions. *Rep. Prog. Phys.* 50, 50: 783–859, 1987. 8
- [73] Susan Mabrey and Julian M. Sturtevant. Investigation of phase transitions of lipids and lipid mixtures by high sensitivity differential scanning calorimetry. *Proceedings of the National Academy of Sciences of the United States of America*, 73(11):3862–3866, 1976. 8, 106, 109
- [74] M.J. Janiak, D.M. Small, and G.G. Shipley. Nature of the thermal pretransition of synthetic phospholipids: dimyristoyl- and dipalmitoyllecithin. *Biochemistry*, 15 (21):4575–4580, 1976. 8, 106
- [75] A. Einstein. Über die von der molekularkinetischen Theorie der Wärme geforderte Bewegung von in ruhenden Flüssigkeiten suspendierten Teilchen. *Annalen der Physik*, 322(8):549–560, 1905. 9
- [76] P. G. Saffman and M. Delbrück. Brownian motion in biological membranes. *Proceedings of the National Academy of Sciences of the United States of America*, 72: 3111–3113, 1975. 9
- [77] R. Peters and R. J. Cherry. Lateral and rotational diffusion of bacteriorhodopsin in lipid bilayers - experimental test of the saffman-delbruck equations. *Proceedings of the National Academy of Sciences of the United States of America-Biological Sciences*, 79(14):4317–4321, 1982. 9
- [78] E. Evans and E. Sackmann. Translational and rotational drag coefficients for a disk moving in a liquid membrane associated with a rigid substrate. *Journal of Fluid Mechanics*, 194:553–561, 1988. 9
- [79] H.-J. Galla, W. Hartmann, U. Theilen, and E. Sackmann. On two-dimensional passive random walk in lipid bilayers and fluid pathways in biomembranes. *Journal of Membrane Biology*, 48:215–236, 1979. 9, 10, 50
- [80] W. L. C. Vaz, R. M. Clegg, and D. Hallmann. Translational diffusion of lipids in liquid crystalline phase phosphatidylcholine multibilayers. a comparison of experiment with theory. *Biochemistry*, 24:781–786, 1985.
- [81] P. F. F. Almeida, W. L. C. Vaz, and T. E. Thompson. Lateral diffusion in the liquid-phases of dimyristoylphosphatidylcholine cholesterol lipid bilayers - a free-volume analysis. *Biochemistry*, 31(29):6739–6747, 1992. 9
- [82] A. Kusumi, C. Nakada, K. Ritchie, K. Murase, K. Suzuki, H. Murakoshi, R. S. Kasai, J. Kondo, and T. Fujiwara. Paradigm shift of the plasma membrane concept from the two-dimensional continuum fluid to the partitioned fluid: High-speed single-molecule tracking of membrane molecules. *Annual Review of Biophysics and Biomolecular Structure*, 34:351–U54, 2005. 9, 11, 43
- [83] M. H. Cohen and D. Turnbull. Molecular transport in liquids and glasses. *Journal of Chemical Physics*, 31:1164–1169, 1959. 9
- [84] P. B. Macedo and T. A. Litovitz. On the relative roles of free volume and activation energy in the viscosity of liquids. *Journal of Chemical Physics*, 42:245–256, 1965. 9

- [85] W. L. C. Vaz and P. F. Almeida. Microscopic versus macroscopic diffusion in one-component fluid phase lipid bilayer-membranes. *Biophysical Journal*, 60(6):1553–1554, 1991. 9
- [86] A. Sonnleitner, G. J. Schutz, and T. Schmidt. Free brownian motion of individual lipid molecules in biomembranes. *Biophysical Journal*, 77(5):2638–2642, 1999. 10, 43
- [87] M. J. Saxton. Single-particle tracking - models of directed transport. *Biophysical Journal*, 67(5):2110–2119, 1994. 11
- [88] M. J. Saxton. Single-particle tracking - effects of corrals. *Biophysical Journal*, 69(2):389–398, 1995.
- [89] M. J. Saxton. Anomalous diffusion due to binding: a monte carlo study. *Biophysical Journal*, 70(3):1250–1262, 1996.
- [90] T. J. Feder, I. BrustMascher, J. P. Slattey, B. Baird, and W. W. Webb. Constrained diffusion or immobile fraction on cell surfaces: A new interpretation. *Biophysical Journal*, 70(6):2767–2773, 1996. 11
- [91] T. Fujiwara, K. Ritchie, H. Murakoshi, K. Jacobson, and A. Kusumi. Phospholipids undergo hop diffusion in compartmentalized cell membrane. *Journal of Cell Biology*, 157(6):1071–1081, 2002. 11
- [92] K. Ritchie, X. Y. Shan, J. Kondo, K. Iwasawa, T. Fujiwara, and A. Kusumi. Detection of non-brownian diffusion in the cell membrane in single molecule tracking. *Biophysical Journal*, 88(3):2266–2277, 2005. 19, 43
- [93] K. Suzuki, K. Ritchie, E. Kajikawa, T. Fujiwara, and A. Kusumi. Rapid hop diffusion of a G-protein-coupled receptor in the plasma membrane as revealed by single-molecule techniques. *Biophysical Journal*, 88(5):3659–3680, 2005.
- [94] N. Meilhac, L. Le Guyader, L. Salome, and N. Destainville. Detection of confinement and jumps in single-molecule membrane trajectories. *Physical Review E*, 73(1), 2006. 11
- [95] B. J. Sung and A. Yethiraj. Lateral diffusion and percolation in membranes. *Physical Review Letters*, 96(22), 2006. 11
- [96] Eugene Hecht and Alfred Zajac. *Optics*. Addison-Wesley, 1998. 14
- [97] A. Egner, S. Jakobs, and S. W. Hell. Fast 100-nm resolution three-dimensional microscope reveals structural plasticity of mitochondria in live yeast. *Proceedings of the National Academy of Sciences of the United States of America*, 99(6):3370–3375, 2002. 18
- [98] T. A. Klar, S. Jakobs, M. Dyba, A. Egner, and S. W. Hell. Fluorescence microscopy with diffraction resolution barrier broken by stimulated emission. *Proceedings of the National Academy of Sciences of the United States of America*, 97(15):8206–8210, 2000. 18
- [99] M. Dyba and S. W. Hell. Focal spots of size $\lambda/23$ open up far-field fluorescence microscopy at 33 nm axial resolution. *Physical Review Letters*, 88(16):163901, 2002. 18

- [100] E. Betzig, G. H. Patterson, R. Sougrat, O. W. Lindwasser, S. Olenych, J. S. Bonifacino, M. W. Davidson, J. Lippincott-Schwartz, and H. F. Hess. Imaging intracellular fluorescent proteins at nanometer resolution. *Science*, 313(5793):1642–1645, 2006. 18
- [101] T. Schmidt, G. J. Schutz, W. Baumgartner, H. J. Gruber, and H. Schindler. Characterization of photophysics and mobility of single molecules in a fluid lipid-membrane. *Journal of Physical Chemistry*, 99(49):17662–17668, 1995. 18, 43
- [102] X. Michalet, F. F. Pinaud, L. A. Bentolila, J. M. Tsay, S. Doose, J. J. Li, G. Sundaresan, A. M. Wu, S. S. Gambhir, and S. Weiss. Quantum dots for live cells, in vivo imaging, and diagnostics. *Science*, 307(5709):538–544, 2005. 18, 43
- [103] R. J. Ober, S. Ram, and E. S. Ward. Localization accuracy in single-molecule microscopy. *Biophysical Journal*, 86(2):1185–1200, 2004. 19
- [104] Norman Bobroff. Position measurement with a resolution and noise-limited instrument. *Review of Scientific Instruments*, 57(6):1152–1157, 1986. 19
- [105] L. S. Churchman, Z. Okten, R. S. Rock, J. F. Dawson, and J. A. Spudich. Single molecule high-resolution colocalization of Cy3 and Cy5 attached to macromolecules measures intramolecular distances through time. *Proceedings of the National Academy of Sciences of the United States of America*, 102(5):1419–1423, 2005. 19, 37, 52
- [106] D. S. Martin, M. B. Forstner, and J. A. Kas. Apparent subdiffusion inherent to single particle tracking. *Biophysical Journal*, 83(4):2109–2117, 2002. 19
- [107] M. J. Saxton. Single-particle tracking: The distribution of diffusion coefficients. *Biophysical Journal*, 72(4):1744–1753, 1997. 20, 21, 44, 47, 48
- [108] Q. A. Hong, M. P. Sheetz, and E. L. Elson. Single-particle tracking - analysis of diffusion and flow in 2-dimensional systems. *Biophysical Journal*, 60(4):910–921, 1991. 21, 44, 47
- [109] D.M. Soumpasis. Theoretical analysis of fluorescence photobleaching recovery experiments. *Biophysical Journal*, 41:95–97, 1983. 22
- [110] Florin Abelès. La théorie générale des couches minces. *J. Phys. Radium*, 11(7):307–309, 1950. 24
- [111] L.G. Parratt. Surface studies of solids by total reflection of x-rays. *Physical Review*, 95(2):359–369, 1954. 24
- [112] O. Glatter and O. Kratky, editors. *Small Angle X-ray Scattering*. Academic Press, 1982. 24
- [113] S. Tristram-Nagle, Y. F. Liu, J. Legleiter, and J. F. Nagle. Structure of gel phase dmpc determined by x-ray diffraction. *Biophysical Journal*, 83(6):3324–3335, 2002. 25, 72, 76, 77, 115
- [114] Georg Pabst, Michael Rappolt, Heinz Amenitsch, and Peter Laggnier. Structural information from multilamellar liposomes at full hydration: Full q-range fitting with high quality x-ray data. *Physical Review E*, 62(3):4000, 2000. 25, 62

- [115] Georg Pabst, Richard Koschuch, Beatriz Pozo-Navas, Michael Rappolt, Karl Lohner, and Peter Laggner. Structural analysis of weakly ordered membrane stacks. *Journal of Applied Crystallography*, 36(6):1378–1388, 2003. 25
- [116] R. Zhang, S. Tristram-Nagle, W. Sun, R.L. Headrick, T.C. Irving, R.M. Suter, and J.F. Nagle. Small-angle x-ray scattering from lipid bilayers is well described by modified Caillé theory but not by paracrystalline theory. *Biophysical Journal*, 70(1):349–357, January 1996. ISSN 0006-3495. 25
- [117] A. Guinier. *Crystals, Imperfect Crystals and Amorphous Bodies*. Freeman, San Francisco, 1963. 27
- [118] J. Oelke, A. Pasc, A. Wixforth, O. Konovalov, and M. Tanaka. Highly uniform, strongly correlated fluorinated lipid nanodomains embedded in biological membrane models. *Applied Physics Letters*, 93(21):–, 2008. 27
- [119] K. Kjaer. Some simple ideas on x-ray reflection and grazing-incidence diffraction from thin surfactant films. *Physica B*, 198(1-3):100–109, 1994. 27, 28, 90
- [120] E. B. Sirota, H. E. King, D. M. Singer, and H. H. Shao. Rotator phases of the normal alkanes - an x-ray-scattering study. *Journal of Chemical Physics*, 98(7):5809–5824, 1993. 28
- [121] S. Miyamoto and P. A. Kollman. Settle - an analytical version of the shake and rattle algorithm for rigid water models. *Journal of Computational Chemistry*, 13(8):952–962, 1992. 30, 41
- [122] R. Vandrunen, D. Vanderspoel, and H. J. C. Berendsen. Gromacs - a software package and a parallel computer for molecular-dynamics. *Abstracts of Papers of the American Chemical Society*, 209:49–Comp, 1995.
- [123] U. Essmann, L. Perera, M. L. Berkowitz, T. Darden, H. Lee, and L. G. Pedersen. A smooth particle mesh ewald method. *Journal of Chemical Physics*, 103(19):8577–8593, 1995. 30
- [124] H. J. C. Berendsen, D. Vanderspoel, and R. Vandrunen. Gromacs - a message-passing parallel molecular-dynamics implementation. *Computer Physics Communications*, 91(1-3):43–56, 1995.
- [125] D. Van der Spoel, E. Lindahl, B. Hess, G. Groenhof, A. E. Mark, and H. J. C. Berendsen. Gromacs: Fast, flexible, and free. *Journal of Computational Chemistry*, 26(16):1701–1718, 2005.
- [126] E. Lindahl, B. Hess, and D. van der Spoel. Gromacs 3.0: a package for molecular simulation and trajectory analysis. *Journal of Molecular Modeling*, 7(8):306–317, 2001.
- [127] B. Hess, C. Kutzner, D. van der Spoel, and E. Lindahl. Gromacs 4: Algorithms for highly efficient, load-balanced, and scalable molecular simulation. *Journal of Chemical Theory and Computation*, 4(3):435–447, 2008.
- [128] B. Hess. P-lincs: A parallel linear constraint solver for molecular simulation. *Journal of Chemical Theory and Computation*, 4(1):116–122, 2008. 41
- [129] gromacs.org, 2009. 30

- [130] A. R. Vanbuuren, S. J. Marrink, and H. J. C. Berendsen. A molecular-dynamics study of the decane water interface. *Journal of Physical Chemistry*, 97(36):9206–9212, 1993. 30
- [131] A. R. Vanbuuren and H. J. C. Berendsen. Molecular-dynamics simulation of the stability of a 22-residue alpha-helix in water and 30-percent trifluoroethanol. *Biopolymers*, 33(8):1159–1166, 1993.
- [132] A. E. Mark, S. P. Vanhelden, P. E. Smith, L. H. M. Janssen, and W. F. Vangunsteren. Convergence properties of free-energy calculations - alpha-cyclodextrin complexes as a case-study. *Journal of the American Chemical Society*, 116(14):6293–6302, 1994.
- [133] H. Y. Liu, F. Mullerplathe, and W. F. Vangunsteren. A force-field for liquid dimethyl-sulfoxide and physical-properties of liquid dimethyl-sulfoxide calculated using molecular-dynamics simulation. *Journal of the American Chemical Society*, 117(15):4363–4366, 1995. 30
- [134] P. P. Ewald. Die Berechnung optischer und elektrostatischer Gitterpotentiale. *Annalen der Physik*, 369(3):253–287, 1921. 30
- [135] T. Darden, D. York, and L. Pedersen. Particle mesh ewald - an $n\log(n)$ method for Ewald sums in large systems. *Journal of Chemical Physics*, 98(12):10089–10092, 1993. 30
- [136] H. J. C. Berendsen, J. P. M. Postma, W. F. van Gunsteren, A. DiNola, and J. R. Haak. Molecular dynamics with coupling to an external bath. *The Journal of Chemical Physics*, 81(8):3684–3690, 1984. 32
- [137] K. Miyawaki, T. Takagi, and M. Shibakami. Efficient synthesis of parallel cyclobolaphiles having two diacetylenes: Mimetics of archaeal membrane lipids. *Synlett*, 8(8):1326–1328, 2002. 33, 61
- [138] M. Shibakami, R. Goto, and M. Nakamura. Phase separation of binary membranes composed of artificial cyclic lipid and distearoyl phosphatidylcholine. *Japanese Journal of Applied Physics Part 1-Regular Papers Brief Communications & Review Papers*, 46(8B):5617–5620, 2007. 33
- [139] W. Kern and D. Puotinen. Cleaning solutions based on hydrogen peroxide for use in silicon semiconductor technology. *RCA Review*, 31:187–206, 1970. 35
- [140] G. G. Roberts. Langmuir-Blodgett films. *Contemporary Physics*, 25(2):109–128, 1984. ISSN 0010-7514. 35, 36, 43
- [141] J. Katsaras. Highly aligned lipid membrane systems in the physiologically relevant "excess water" condition. *Biophysical Journal*, 73(6):2924–2929, 1997. 35
- [142] T. Schubert, M. Barmann, M. Rusp, W. Granzer, and M. Tanaka. Diffusion of glycosylphosphatidylinositol (GPI)-anchored bovine prion protein (PrPc) in supported lipid membranes studied by single-molecule and complementary ensemble methods. *Journal of Membrane Science*, 321(1):61–68, 2008. 36, 43, 45, 50, 51
- [143] R. Roy, S. Hohng, and T. Ha. A practical guide to single-molecule FRET. *Nature Methods*, 5(6):507–516, 2008. 37, 39, 52

- [144] W. E. Moerner and D. P. Fromm. Methods of single-molecule fluorescence spectroscopy and microscopy. *Review of Scientific Instruments*, 74(8):3597–3619, 2003. 37
- [145] X. Michalet, O. H. W. Siegmund, J. V. Vallerga, P. Jelinsky, J. E. Millaud, and S. Weiss. Detectors for single-molecule fluorescence imaging and spectroscopy. *Journal of Modern Optics*, 54(2-3):239–281, 2007. 37
- [146] M. Kühner, R. Tampe, and E. Sackmann. Lipid mono- and bilayer supported on polymer films: Composite polymer-lipid films on solid substrates. *Biophysical Journal*, 67:217–226, 1994. 39
- [147] A. Nelson. Co-refinement of multiple-contrast neutron/x-ray reflectivity data using motofit. *Journal of Applied Crystallography*, 39:273–276, 2006. 40
- [148] Peter Tieleman. Website of the Tieleman group, 2008. 41
- [149] S. W. Chiu, M. Clark, V. Balaji, S. Subramaniam, H. L. Scott, and E. Jakobsson. Incorporation of surface-tension into molecular-dynamics simulation of an interface - a fluid-phase lipid bilayer-membrane. *Biophysical Journal*, 69(4):1230–1245, 1995. 41
- [150] D. P. Tieleman and H. J. C. Berendsen. Molecular dynamics simulations of a fully hydrated dipalmitoyl phosphatidylcholine bilayer with different macroscopic boundary conditions and parameters. *Journal of Chemical Physics*, 105(11):4871–4880, 1996. 95
- [151] O. Berger, O. Edholm, and F. Jahnig. Molecular dynamics simulations of a fluid bilayer of dipalmitoylphosphatidylcholine at full hydration, constant pressure, and constant temperature. *Biophysical Journal*, 72(5):2002–2013, 1997. 95
- [152] E. Lindahl and O. Edholm. Mesoscopic undulations and thickness fluctuations in lipid bilayers from molecular dynamics simulations. *Biophysical Journal*, 79(1):426–433, 2000. 41, 111
- [153] J. Gelles, B. J. Schnapp, and M. P. Sheetz. Tracking kinesin-driven movements with nanometre-scale precision. *Nature*, 331(6155):450–453, 1988. 43
- [154] T. Schmidt, G. J. Schutz, W. Baumgartner, H. J. Gruber, and H. Schindler. Imaging of single molecule diffusion. *Proceedings of the National Academy of Sciences of the United States of America*, 93(7):2926–2929, 1996. 43
- [155] E. D. Sheets, G. M. Lee, R. Simson, and K. Jacobson. Transient confinement of a glycosylphosphatidylinositol-anchored protein in the plasma membrane. *Biochemistry*, 36(41):12449–12458, 1997. 43
- [156] M. Sonnleitner, G. J. Schutz, H. Kahr, N. M. Soldatov, C. Romanin, T. Schmidt, and H. Schindler. Localization of L-type Ca^{2+} -channels by two photon laser scanning microscopy. *Biophysical Journal*, 78(1):445A–445A, 2000.
- [157] A. Kusumi, H. Ike, C. Nakada, K. Murase, and T. Fujiwara. Single-molecule tracking of membrane molecules: plasma membrane compartmentalization and dynamic assembly of raft-philic signaling molecules. *Seminars in Immunology*, 17(1):3–21, 2005. 43

- [158] P. Jerram, P. J. Pool, R. Bell, D. J. Burt, S. Bowring, S. Spencer, M. Hazelwood, I. Moody, N. Catlett, and P. S. Heyes. The LLCCD: low-light imaging without the need for an intensifier. *Proceedings of SPIE*, 4306:178–186, 2001. 44
- [159] M. Lippitz, F. Kulzer, and M. Orrit. Statistical evaluation of single nano-object fluorescence. *ChemPhysChem*, 6(5):770–789, 2005. 47
- [160] M. Tanaka, J. Hermann, I. Haase, M. Fischer, and S. G. Boxer. Frictional drag and electrical manipulation of recombinant proteins in polymer-supported membranes. *Langmuir*, 23(10):5638–5644, 2007. 50
- [161] K. Kinoshita, H. Itoh, S. Ishiwata, K. Hirano, T. Nishizaka, and T. Hayakawa. Dual-view microscopy with a single camera - real-time imaging of molecular orientations and calcium. *Journal of Cell Biology*, 115(1):67–73, 1991. 52
- [162] L. Cognet, G. S. Harms, G. A. Blab, P. H. M. Lommerse, and T. Schmidt. Simultaneous dual-color and dual-polarization imaging of single molecules. *Applied Physics Letters*, 77(24):4052–4054, 2000.
- [163] I. Koyama-Honda, K. Ritchie, T. Fujiwara, R. Iino, H. Murakoshi, R. S. Kasai, and A. Kusumi. Fluorescence imaging for monitoring the colocalization of two single molecules in living cells. *Biophysical Journal*, 88(3):2126–2136, 2005. 52
- [164] B. Zitova and J. Flusser. Image registration methods: a survey. *Image and Vision Computing*, 21(11):977–1000, 2003. 55
- [165] G. I. Veld, M. G. L. Elferink, A. J. M. Driessen, and W. N. Konings. Reconstitution of the leucine transport-system of lactococcus-lactis into liposomes composed of membrane-spanning lipids from sulfolobus-acidocaldarius. *Biochemistry*, 31(49):12493–12499, 1992. 61
- [166] M. G. L. Elferink, J. G. Dewit, R. Demel, A. J. M. Driessen, and W. N. Konings. Functional reconstitution of membrane-proteins in monolayer liposomes from bipolar lipids of sulfolobus-acidocaldarius. *Journal of Biological Chemistry*, 267(2):1375–1381, 1992. 61
- [167] M. Nishihara and Y. Koga. Extraction and composition of polar lipids from the archaebacterium, methanobacterium-thermoautotrophicum - effective extraction of tetraether lipids by an acidified solvent. *Journal of Biochemistry*, 101(4):997–1005, 1987. 61
- [168] F.A. Rainey and A. Oren, editors. *Extremophiles*. Methods in Microbiology. Elsevier, London, 2006. 61
- [169] J. M. Kim and D. H. Thompson. Tetraether bolaform amphiphiles as models of archaebacterial membrane-lipids - synthesis, differential scanning calorimetry, and monolayer studies. *Langmuir*, 8(2):637–644, 1992. 61
- [170] A. P. Patwardhan and D. H. Thompson. Efficient synthesis of 40-and 48-membered tetraether macrocyclic bisphosphocholines. *Organic Letters*, 1(2):241–243, 1999. 61
- [171] S. Dante, M. De Rosa, O. Francescangeli, C. Nicolini, F. Rustichelli, and V. I. Troitsky. Supramolecular ordering of bipolar lipids from archaea in langmuir-blodgett films by low-angle x-ray diffraction. *Thin Solid Films*, 284-285:459–463, 1996. 61

- [172] A. P. Patwardhan and D. H. Thompson. Novel flexible and rigid tetraether acyclic and macrocyclic bisphosphocholines: Synthesis and monolayer properties. *Langmuir*, 16(26):10340–10350, 2000. 61
- [173] K. Miyawaki, R. Goto, T. Takagi, and M. Shibakami. Convergent synthesis of antiparallel cyclobolaphiles having two diacetylenes: Mimetics of membrane components that are found in archaea. *Synlett*, 9(9):1467–1470, 2002. 61
- [174] E. Novakova, K. Giewekemeyer, and T. Salditt. Structure of two-component lipid membranes on solid support: An x-ray reflectivity study. *Physical Review E*, 74(5):051911, 2006. 62
- [175] E. Schneck, E. Papp-Szabo, B. E. Quinn, O. V. Konovalov, T. J. Beveridge, D. A. Pink, and M. Tanaka. Calcium ions induce collapse of charged O-side chains of lipopolysaccharides from *Pseudomonas aeruginosa*. *Journal of The Royal Society Interface*, 2009. 62
- [176] S. Y. Chen, B. Yang, K. Jacobson, and K. K. Sulik. The membrane disordering effect of ethanol on neural crest cells in vitro and the protective role of GM1 ganglioside. *Alcohol*, 13(6):589–595, 1996. 67
- [177] A. N. Dickey and R. Faller. How alcohol chain-length and concentration modulate hydrogen bond formation in a lipid bilayer. *Biophysical Journal*, 92(7):2366–2376, 2007. 67
- [178] J. F. Nagle and J. Katsaras. Absence of a vestigial vapor pressure paradox. *Physical Review E*, 59(6):7018–7024, 1999. 70
- [179] J. F. Nagle, R. T. Zhang, S. TristramNagle, W. J. Sun, H. I. Petrache, and R. M. Suter. X-ray structure determination of fully hydrated l(alpha) phase dipalmitoylphosphatidylcholine bilayers. *Biophysical Journal*, 70(3):1419–1431, 1996. 80
- [180] J. T. Kim, J. Mattai, and G. G. Shipley. Gel phase polymorphism in ether-linked dihexadecylphosphatidylcholine bilayers. *Biochemistry*, 26(21):6592–6598, 1987. 81
- [181] J. T. Kim, J. Mattai, and G. G. Shipley. Bilayer interactions of ether-linked and ester-linked phospholipids - dihexadecylphosphatidylcholines and dipalmitoylphosphatidylcholines. *Biochemistry*, 26(21):6599–6603, 1987. 81
- [182] D. P. Tieleman, S. J. Marrink, and H. J. C. Berendsen. A computer perspective of membranes: molecular dynamics studies of lipid bilayer systems. *Biochimica et Biophysica Acta-Reviews on Biomembranes*, 1331(3):235–270, 1997. 95
- [183] S. E. Feller and A. D. MacKerell. An improved empirical potential energy function for molecular simulations of phospholipids. *Journal of Physical Chemistry B*, 104(31):7510–7515, 2000.
- [184] J. Sonne, M. O. Jensen, F. Y. Hansen, L. Hemmingsen, and G. H. Peters. Reparameterization of all-atom dipalmitoylphosphatidylcholine lipid parameters enables simulation of fluid bilayers at zero tension. *Biophysical Journal*, 92(12):4157–4167, 2007. 95, 100
- [185] D. P. Tieleman and H. J. C. Berendsen. A molecular dynamics study of the pores formed by *Escherichia coli* OmpF porin in a fully hydrated palmitoylphosphatidylcholine bilayer. *Biophysical Journal*, 74(6):2786–2801, 1998. 95

- [186] H. Heller, M. Schaefer, and K. Schulten. Molecular-dynamics simulation of a bilayer of 200 lipids in the gel and in the liquid-crystal phases. *Journal of Physical Chemistry*, 97(31):8343–8360, 1993. 95
- [187] U. Essmann, L. Perera, and M. L. Berkowitz. The origin of the hydration interaction of lipid bilayers from md simulation of dipalmitoylphosphatidylcholine membranes in gel and liquid-crystalline phases. *Langmuir*, 11(11):4519–4531, 1995.
- [188] K. Tu, D. J. Tobias, J. K. Blasie, and M. L. Klein. Molecular dynamics investigation of the structure of a fully hydrated gel-phase dipalmitoylphosphatidylcholine bilayer. *Biophysical Journal*, 70(2):595–608, 1996. 102, 103
- [189] R. M. Venable, B. R. Brooks, and R. W. Pastor. Molecular dynamics simulations of gel (l-beta i) phase lipid bilayers in constant pressure and constant surface area ensembles. *Journal of Chemical Physics*, 112(10):4822–4832, 2000. 95, 101
- [190] J. C. Shelley, M. Y. Shelley, R. C. Reeder, S. Bandyopadhyay, and M. L. Klein. A coarse grain model for phospholipid simulations. *Journal of Physical Chemistry B*, 105(19):4464–4470, 2001. 95
- [191] M. Kranenburg, M. Venturoli, and B. Smit. Phase behavior and induced interdigitation in bilayers studied with dissipative particle dynamics. *Journal of Physical Chemistry B*, 107(41):11491–11501, 2003.
- [192] M. J. Stevens. Coarse-grained simulations of lipid bilayers. *Journal of Chemical Physics*, 121(23):11942–11948, 2004.
- [193] S. J. Marrink, H. J. Risselada, S. Yefimov, D. P. Tieleman, and A. H. de Vries. The martini force field: Coarse grained model for biomolecular simulations. *Journal of Physical Chemistry B*, 111(27):7812–7824, 2007. 95
- [194] S. J. Marrink, J. Risselada, and A. E. Mark. Simulation of gel phase formation and melting in lipid bilayers using a coarse grained model. *Chemistry and Physics of Lipids*, 135(2):223–244, 2005. 95
- [195] S. Leekumjorn and A. K. Sum. Molecular studies of the gel to liquid-crystalline phase transition for fully hydrated DPPC and DPPE bilayers. *Biochimica et Biophysica Acta-Biomembranes*, 1768(2):354–365, 2007. 96, 101, 106
- [196] T. Husslein, D. M. Newns, P. C. Pattnaik, Q. F. Zhong, P. B. Moore, and M. L. Klein. Constant pressure and temperature molecular-dynamics simulation of the hydrated diphytanolphosphatidylcholine lipid bilayer. *Journal of Chemical Physics*, 109(7):2826–2832, 1998. 96
- [197] Jerome L. Gabriel and Parkson Lee Gau Chong. Molecular modeling of archaeobacterial bipolar tetraether lipid membranes. *Chemistry and Physics of Lipids*, 105(2):193–200, 2000.
- [198] Wataru Shinoda, Keiko Shinoda, Teruhiko Baba, and Masuhiro Mikami. Molecular dynamics study of bipolar tetraether lipid membranes. *Biophysical Journal*, 89(5):3195–3202, 2005. 96
- [199] L. S. Vermeer, B. L. de Groot, V. Reat, A. Milon, and J. Czaplicki. Acyl chain order parameter profiles in phospholipid bilayers: computation from molecular

- dynamics simulations and comparison with H-2 NMR experiments. *European Biophysics Journal*, 36:919–931, 2007. 98, 101
- [200] A. W. Schuttelkopf and D. M. F. van Aalten. PRODRG: a tool for high-throughput crystallography of protein-ligand complexes. *Acta Crystallographica Section D-Biological Crystallography*, 60:1355–1363, 2004. 100
- [201] V. A. Raghunathan and J. Katsaras. $L_{\beta'}$ -> L_c phase transition in phosphatidylcholine lipid bilayers: A disorder-order transition in two dimensions. *Physical Review E*, 54(4):4446–4449, 1996. 101, 102
- [202] J. P. Douliez, A. Leonard, and E. J. Dufourc. Conformational order of DMPC sn-1 versus sn-2 chains and membrane thickness: An approach to molecular protrusion by solid state H-2-NMR and neutron diffraction. *Journal of Physical Chemistry*, 100(47):18450–18457, 1996. 100, 101
- [203] M. Picquart and T. Lefevre. Raman and fourier transform infrared study of phytol effects on saturated and unsaturated lipid multibilayers. *Journal of Raman Spectroscopy*, 34(1):4–12, 2003. 100
- [204] H. Hauser, I. Pascher, and S. Sundell. Preferred conformation and dynamics of the glycerol backbone in phospholipids - an nmr and x-ray single-crystal analysis. *Biochemistry*, 27(26):9166–9174, 1988. 101
- [205] J. P. Douliez, A. Leonard, and E. J. Dufourc. Restatement of order parameters in biomembranes - calculation of C-C bond order parameters from C-D quadrupolar splittings. *Biophysical Journal*, 68(5):1727–1739, 1995. 101
- [206] A. H. de Vries, S. Yefimov, A. E. Mark, and S. J. Marrink. Molecular structure of the lecithin ripple phase. *Proceedings of the National Academy of Sciences of the United States of America*, 102(15):5392–5396, 2005. 101, 102, 112
- [207] J. B. Klauda, N. Kucerka, B. R. Brooks, R. W. Pastor, and J. F. Nagle. Simulation-based methods for interpreting x-ray data from lipid bilayers. *Biophysical Journal*, 90(8):2796–2807, 2006. 102
- [208] J. Katsaras, D. S. C. Yang, and R. M. Epand. Fatty-acid chain tilt angles and directions in dipalmitoyl phosphatidylcholine bilayers. *Biophysical Journal*, 63(4):1170–1175, 1992. 103
- [209] S. Tristramnagle, R. Zhang, R. M. Suter, C. R. Worthington, W. J. Sun, and J. F. Nagle. Measurement of chain tilt angle in fully hydrated bilayers of gel phase lecithins. *Biophysical Journal*, 64(4):1097–1109, 1993. 103, 104
- [210] J. Katsaras, S. Tristram-Nagle, Y. Liu, R. L. Headrick, E. Fontes, P. C. Mason, and J. F. Nagle. Revisiting the ripple phase using fully hydrated, aligned dppc multibilayers. *Biophysical Journal*, 78(1):20a–20a, 2000. 109, 111
- [211] T. Kaasgaard, C. Leidy, J. H. Crowe, O. G. Mouritsen, and K. Jorgensen. Temperature-controlled structure and kinetics of ripple phases in one- and two-component supported lipid bilayers. *Biophysical Journal*, 85(1):350–360, 2003. 109
- [212] HJ Hinz and J. M. Sturtevant. Calorimetric studies of dilute aqueous suspensions of bilayers formed from synthetic l-agr-lecithins. *Journal of Biological Chemistry*, 247(19):6071–6075, 1972. 109

- [213] S. E. Feller and R. W. Pastor. On simulating lipid bilayers with an applied surface tension: Periodic boundary conditions and undulations. *Biophysical Journal*, 71(3):1350–1355, 1996. 111
- [214] G. Cevc. Polymorphism of the bilayer-membranes in the ordered phase and the molecular-origin of the lipid pretransition and rippled lamellae. *Biochimica et Biophysica Acta*, 1062(1):59–69, 1991. 111
- [215] Moritz Mickler, Martin Hessling, Christoph Ratzke, Johannes Buchner, and Thorsten Hugel. The large conformational changes of Hsp90 are only weakly coupled to ATP hydrolysis. *Nature Structural & Molecular Biology*, 16(3):281–286, March 2009. ISSN 1545-9993. 123
- [216] O. Purrucker, H. Hillebrandt, K. Adlkofer, and M. Tanaka. Deposition of highly resistive lipid bilayer on silicon-silicon dioxide electrode and incorporation of gramicidin studied by ac impedance spectroscopy. *Electrochimica Acta*, 47(5):791–798, 2001. 123
- [217] D. Gassull, A. Ulman, M. Grunze, and M. Tanaka. Electrochemical sensing of membrane potential and enzyme function using gallium arsenide electrodes functionalized with supported membranes. *Journal of Physical Chemistry B*, 112(18):5736–5741, 2008. 123
- [218] E. Turk, D. B. Teplow, L. E. Hood, and S. B. Prusiner. Purification and properties of the cellular and scrapie hamster prion proteins. *European Journal of Biochemistry*, 176(1):21–30, 1988. 128
- [219] K. M. Pan, M. Baldwin, J. Nguyen, M. Gasset, A. Serban, D. Groth, I. Mehlhorn, Z. W. Huang, R. J. Fletterick, F. E. Cohen, and S. B. Prusiner. Conversion of alpha-helices into beta-sheets features in the formation of the scrapie prion proteins. *Proceedings of the National Academy of Sciences of the United States of America*, 90(23):10962–10966, 1993. 128
- [220] G. Bartlett. Phosphorus assay in column chromatography. *Journal of Biological Chemistry*, 234(3):466–468, 1958. 129